MULTI-WAVELENGTH POLARISING INTERFEROMETER FOR IN-PROCESS METROLOGY

SAIF AL-BASHIR

A thesis submitted to the University of Huddersfield in partial fulfilment of the requirements for the degree of Doctor of Philosophy

The University of Huddersfield

April 2019

Copyright statement

i. The author of this thesis (including any appendices and/or schedules to this thesis) owns any copyright in it (the "Copyright") and he has given The University of Huddersfield the right to use such copyright for any administrative, promotional, educational and/or teaching purposes.

ii. Copies of this thesis, either in full or in extracts, may be made only in accordance with the regulations of the University Library. Details of these regulations may be obtained from the Librarian. This page must form part of any such copies made.

iii. The ownership of any patents, designs, trademarks and any and all other intellectual property rights except for the Copyright (the "Intellectual Property Rights") and any reproductions of copyright works, for example graphs and tables ("Reproductions"), which may be described in this thesis, may not be owned by the author and may be owned by third parties. Such Intellectual Property Rights and Reproductions cannot and must not be made available for use without the prior written permission of the owner(s) of the relevant Intellectual Property Rights and/or Reproductions

Acknowledgements

First of all, I would like to thank Allah, the almighty, for creating me and granting me hearing, seeing, understanding and giving me the strength to complete the project. Secondly I would like to thank my beloved country Iraq who gave me so much.

I would like to offer my special thanks to my supervisor Professor Xiangqian Jiang for her encouragement and support during my PhD. I really appreciate her motivating me to undertake this research and encouraging me to attended conferences outside the UK.

I would like to express my deepest appreciation to my supervisor Dr. Hussam Muhamedsalih for his sincere effort throughout the development of this project. Dr. Hussam Muhamedsalih dedicating much of his time to help me solve some problems that occurred during the research. Also a special thanks for the effort that he made in helping with my academic work including this thesis and conference papers.

I want to thank Dr. Feng Gao for his valuable advice during my Ph.D. study. He has always offered me great help and support.

My special thanks to all staff in the EPSRC Centre for Innovative Manufacturing in Advanced Metrology including Professor Liam Blunt, Dr. Haydn Martin, Dr. Paul Bills and Dr Hussein Abdul-Rahman; you all made a tremendous impact on my research.

I would like to show my deep gratitude to my family for financial and emotional support. I'm forever grateful to my father , mother , my brothers (Bilal and Muhammed) , my sisters , my wife and my brother-in-law Dr. Mohammed Aal-Nouman for their prayers and love that helped me in this challenging time of my life.

I would like to express my appreciation to my sponsor, the higher committee for education development in Iraq (HCED), for giving me the opportunity for full-sponsorship in order to pursue my PhD study at the University of Huddersfield. My special thanks are extended to everyone including the Iraqi cultural attaché, university staff, colleagues who supported me during the years of study.

Abstract

Micro-scale and nano-scale surfaces are now fabricated to serve in many fields: from optics needed in telescope/microscope imaging to semiconductors integrated in electronic devices such as smart phones and micro sensors. The production of these surfaces is inspiring the development of new metrology instrumentation that can not only ensure the quality but also optimise the manufacturing process. However, the state-of-the-art offline metrology instruments suffer from a main limitation, namely the inability to operate in the manufacture environment. The industry evolution requires in-process and metric metrology instrumentation that can provide rich surface information within harsh manufacture environment. The specification of such instruments has to be non-destructive, fast, and highly accurate; such instruments have to be combined with a production line. Interferometers offer non-destructive and parallel fashion measurement with nanometre accuracy.

A well-established phase-shift interferometer (PSI) is widely used for high measurement accuracy; however, it has two limitations. Firstly, the height difference between two adjacent points on the sample should be smaller than quarter of wavelength ($\lambda/4$), and secondly, a PSI is slow and not suitable for in-process measurements, if a mechanical scanning is used for phase shifting. In order to utilise PSI for in-process measurements, data capturing at single exposure should be used to overcome the environmental disturbances and advanced phase unwrapping methods need to be employed to extend the measurement range beyond ($\lambda/4$).

This research aimed to develop a multi-wavelength polarising phase-shift interferometer (MPI) for surface measurement and to investigate the possibility of its use for in-process metrology applications. The target specifications of the proposed instrument are as follows: a vertical measurement range greater than ($\lambda/4$) (i.e. greater than 1 μm) with the resolution of a single wavelength interferometer (i.e. less than 10 nm). The MPI requires no mechanical scanning to obtain the phase shift with an extended measurement range using a single shot technique. This represents an improvement over the conventional single wavelength interferometer in terms of the measurement range and speed.

The methodology followed to achieve this study's aims included reviewing the literature and implementing proof-of-concept experiments using mechanical and non-mechanical methods to acquire phase-shifted colour interferograms, hence determining algorithms for fringe analysis. Finally a novel MPI setup using polarisation technique and Red-Green-Blue (RGB) illumination source was developed that can be used for in-process measurement with extended range.

An acousto-optics tuneable filter (AOTF) was successfully employed to simultaneously provide RGB wavelengths with approximately 2 nm linewidth. Several fringe analyses and phase unwrapping algorithms, such as fringe order and best-match methods, were explored to retrieve areal surfaces. Colour crosstalk between cameras' pixels was also investigated. It was found that the crosstalk is significant. A mathematical model and AOTF tuning capability were used to achieve minimum crosstalk. A spatial two dimensional image filtration was used to enhance the interferograms, hence signal-to-noise improvement. The proposed MPI has successfully measured samples (from 40 nm to 4 μm) with few nanometres accuracy and with single exposure (less than 0.3 second). This MPI has the potential for use in the measurement of surfaces produced by ultra-fast manufacturing such as roll-to-roll (R2R) manufacturing process. In the R2R process, structured surfaces are fabricated on large-area substrates (on the scale of several metres squared) at high speed exceeding several meters per minute. As such, MPI can be potentially used to measure moving surfaces within the manufacturing environment at speed limited only to the single exposure of the cameras.

Contents

List of Figures

List of Tables

List of Abbreviations

AM	Additive manufacturing
AOTF	Acousto-optic tunable filter
BS	Beam splitter
CCD	Charge-coupled device
CCI	Coherence correlation interferometry
CCM	Chromatic confocal microscopy
CMOS	Complementary metal-oxide semiconductor
CPU	Central processing unit
CR	Contrast Ratio
CSI	Coherence scanning interferometer
DAQ	Data acquisition card
DMD	Digital micrometer device
DoF	Depth of focus
DPI	Dual wavelength single shot polarised interferometer
EL	Electroluminescence imaging
FFT	Fast Fourier transform
F-operator	Form operator
FWHM	Full width half maximum linewidth of the filtered wavelength
FOV	Field-of-view
IFT	Inverse Fourier transform
IMEC	Hyperspectral imaging camera
IRM	Information-rich surface metrology
ISO	International organization for standardization-filter
LED	Light-emitting diode
L-filter	Large scale filter
LSDI	line-scan dispersive interferometry
MPI	Multi-wavelength polarising interferometer
NA	Numerical Aperture
NPL	National Physical Laboratory
OLED	Organic light-emitting devices
OPD	Optical path difference
PBS	Polarised beam splitter

PD	Photodiode
POL	Polariser
PSI	Phase shifting interferometer
PZT	Piezoelectric translator
QWP	Quarter waveplate
R2R	Roll-to-Roll
Ra	Arithmetic mean of the magnitude of the deviation of the profile from the mean
RGB	Red, green and blue
R' G' B'	Red, green and blue components observed by the camera.
SDSCI	Spatially dispersed short-coherent interferometer
S-filter	Small scale filter
SNR	Signal to noise ratio
SPI	Single shot polarised interferometer
SRWLI	Spectrally resolve white light interferometer
TPI	Triple wavelength single shot polarised interferometer
USAF	U.S. Air Force
WSI	Wavelength scanning interferometers
WVTR	Water vapour transmission rate

List of Nomenclature

A_{bias}	fringe bias
α	phase shift
B_{vis}	fringe visibility for reference and measurement arm
c	speed of light
$\|\gamma\|$	coherence function
D	diattenuation of polariser
$\Delta\theta$	phase difference between reference and sample wavefront
Δn	birefringent crystal refractive index
E	elliptically polarised light
E_o	amplitude of electric field.
f	the frequency of light
fa	frequency of the propagated acoustic wave respectively
ω	angular frequency
h	simulate and measured surface height
H_{12-23}	surface height calculated from longest synthetic wavelength
I	intensity of the light
I_o	intensity of incident light to polariser
Imax	maximum contrast of the fringe (constrictive interference)
Imin	minimum contrast of the fringe (destructive interference)
k	wavenumber of the light source
L	left Hand circular polarised light
l_c	the coherence length
λ	wavelength of the light
λ_s	synthetic wavelength
Λ_{12-23}	longest synthetic
M_{noise}	measurement noise result from subtraction of two measurement
N	fringe order number
Ω	angular frequency
$\emptyset$	polarisation orientation degree
n	refractive index
π	3.14
φ	the phase shift between horizontal and vertical component of light

R	right hand circular polarised light
Sa	arithmetical mean height
Sq	root mean square height
Sp	maximum peak height
Sv	maximum pit height
τ_c	temporal coherence time
θ	phase of the light
ν	fringe visibility for distractive and constrictive interference
va	velocity of the propagated acoustic wave
x	index pixel number in the horizontal direction of the CCD
y	index pixel number in the vertical direction of the CCD
z	the position of wave from the origin

Chapter 1: Introduction

1.1 Application Background

The development of advance technologies, such as semiconductor devices, flexible electronics and fast processors, and the necessity to inspect their micro and nanometre scale engineering surfaces has considerably increased the demands placed on manufacturers. Advanced technology, such as photovoltaics, organic light-emitting devices (OLEDs)/ organic photovoltaics (OPVs), displays, touch panels, and glass-coated devices are produce part-by-part in a highly parallel manner. In several applications, structured surfaces are provided on large-area substrates (on the scale of several metres squared) with high accuracy (down to the fraction of a micrometre) using techniques such as additive manufacturing (AM) and roll-to-roll (R2R) technology (Giusca, 2013). The production process for R2R and AM should be free from defects to ensure a high-quality product, and this presents a challenge to the manufacturer.

Surface scientists, tribologists, and precision engineers have reached a common conclusion that surface topography is a significant factor that affects the functional properties and components of the systems (de Groot, 2015). (Blunt & Jiang, 2003) reported that 90% of all the engineering components fail in practice because of fatigue cracking, stress corrosion, adhesive wear, and other surface defects. Therefore, surface metrology can be a key factor in optimising the manufacturing process to guarantee the performance of a work piece.

In the last few decades, the development in the field of surface metrology has increased exponentially in terms of technology and the range of applications. The development of innovative technology has considerably increased in the fields of measurement and instrumentation, such that even a complex surface with an 80° slope and the deep trend can be measured (Daniel, 2007). The challenge at this point is to apply these metrology instruments to online and in-process measurements that can perform full coverage surface inspection reach to metre-scale areas and with nanometre/micrometre resolution, such as surfaces produced by the R2R process. The in-process metrology for highly parallel manufacturing, for example R2R, has to meet several requirements, such as non-contact, high lateral and vertical measurement resolution, robustness against environmental disturbances, large field-of-view (FOV), and accurate positioning. An example of the in-process metrology application for the R2R process is to inspect the thin film barrier of flexible electronics to identify and register the defects. Achieving this application will allow the manufacturer to develop a repair process to remove these defects to accomplish a reduction in the product costs as well as to guarantee the optimum performance and long lifetime of flexible electronics (Elrawemi *et al.*, 2015; Kimbrough & Novak, 2015).

The interaction of metrology instruments with the surfaces can be classified into contact and non-contact approach (Daniel, 2007; Jaturunruangsri, 2015; Jiang *et al.*, 2007).There are several measurement techniques that emerge from the two approaches, and there is no unique metrology technique that can be used for all applications. The trade-off in measurement specification must typically be made in terms of the type of surface geometry, measurement speed, range, resolution, and environmental robustness (Novak, 2014). Figure 1.1 shows the most used technology and where it fits the best in terms of measuring the vertical and lateral features of different scales.

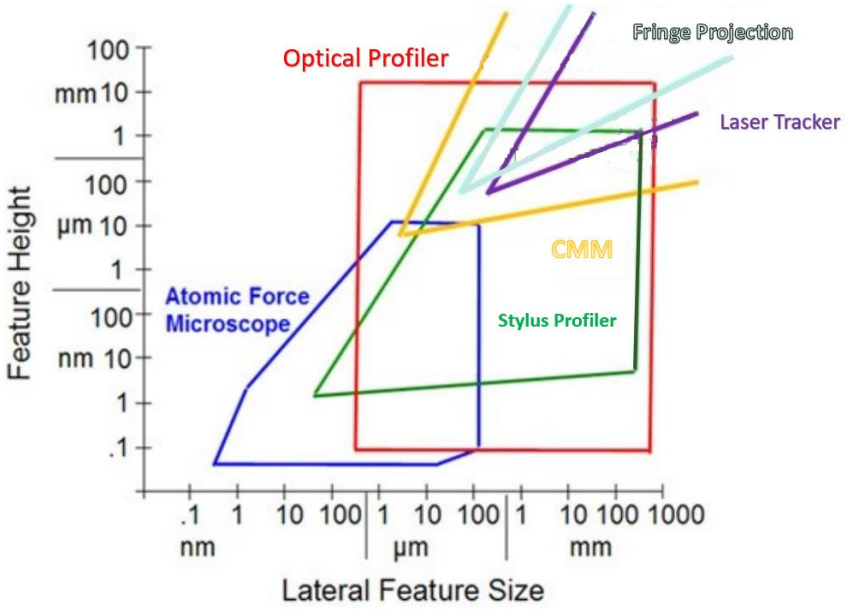

Figure 1.1 Measurement range of various metrology techniques [Adopted from (Novak, 2014)]

The contact approach methods, such as CMM and Stylus Profiler, provide a wide measurement range with resolution down to 0.4 nm, but they are not suitable for in-process measurements because of their slow speed, lack of immunity to vibrations, and tendency to cause defects in soft materials. In contrast, optical surface metrology instruments, such as fringe projection, optical profiler and laser tracker, are suitable for in-process measurements, because they do not damage the sample and provide a good lateral and vertical resolution for specific applications.

Several scholars and companies are focused on developing optical instruments that can be used currently or have the potential for online/in-process surface inspections such as machine vision (Fahlteich et al., 2015), ellipsometers (Huemer et al., 2016), focus variation (R; Danzl *et al.*, 2019), and phase shift interferometers (PSIs) (Brock *et al.*, 2007).

The machine vision technique is used in several applications such as semiconductor inspections and web inspections of paper foils, films, and metals. The function of a machine vision system is based on advanced high-resolution cameras integrated into a specialised lighting and optics high-speed signal processing unit to achieve real-time inspection. All of these elements offer

instant detection and recording of the defects (NDC, 2018). However, the drawback of a machine vision system is that it cannot provide surface metric information.

Interferometry is commonly used to measure surface geometry. Its measurement range depends on the measurement technique. Generally, the measurement ranges between sub-micrometres and hundreds of a micrometre. Several interferometry offers areal measurement and can be used in embedded metrology, such as the one employed in wavelength scanning interferometers (WSI) and phase shifting interferometer (PSI).

Researchers from the University of Huddersfield developed a WSI for areal and online measurement applications. The WSI is integrated with active vibration compensation system that can effectively cancel harsh environmental disturbances (Hussam, 2013; Jiang *et al.*, 2010). The current application of WSI is to detect micro/nano-scale defects on the barrier layer of flexible photovoltaic solar modules (Hussam *et al.*, 2014). However, the scanning mechanism of the WSI has limited this application to static measurement only, restricting its ability to measure moving surfaces.

This thesis describes the development of a novel single shot multi-wavelength polarising interferometer (MPI) for in-process metrology, avoiding any scanning mechanism for the measurement of moving surfaces. This research introduces methods to extend the vertical measurement range using red-green-blue (RGB) illumination along with advanced algorithms. It also introduces an instant phase shifting mechanism using polarisation techniques, providing robust measurement faster than common environmental disturbances.

1.2 Aim

This research aims to investigate and develop a novel MPI for areal surface measurement that can be used for in-process metrology applications. The target specification of the proposed instrument is as follows: a vertical measurement ranges up to 4 μm and vertical resolution comparable to single wavelength interferometer. The MPI should require no mechanical scanning to obtain the required phase shift with an extended measurement range using single-shot technique. This would represent an improvement over the conventional one wavelength single shot interferometer in terms of the measurement range.

1.3 Thesis Objectives

The thesis objectives are summarised as follows:

- Develop and investigate a polarisation technique that can perform instant four phase shift steps without any mechanical movement, generating a single shot polarising PSI.

- Design and investigate an interferometric configuration that integrates the polarising PSI with three colour red-green-blue (RGB) illumination to achieve the accuracy of PSI (i.e., nano-scale vertical resolution) with extended measurement range.
- Develop and investigate an efficient three wavelength phase unwrapping algorithm that can overcome the height ambiguity problem of a conventional phase-shift interferometer by using three colour information.
- Investigate and compensate for the RGB colour crosstalk existing in commercial colour cameras.
- Evaluate the MPI performance by defining the system noise floor, measurement accuracy, and repeatability at different wavelength operation modes (single wavelength, dual wavelength, and triple (three) wavelength).

1.4 Thesis Contribution

The main contribution of the research project is summarised as follows:

- Develop an in-process interferometry that can simultaneously acquire all measurement data at once, as well as overcome the height ambiguity limitations that exist in the commercial phase shift interferometer whilst maintaining the vertical resolution within a few nanometres.
- Design and demonstration of fast MPI, using RGB illumination source filtered by an acousto-optic tuneable filter (AOTF), polarising optics, and four colour complementary metal-oxide semiconductor (CMOS) cameras, all of which together enable the MPI to retrieve high vertical range surface topography at the single shot measurement.
- Employment of several algorithms and techniques, which are suited at different wavelength operation modes, to analyse the colour interference fringe patterns.
- Establishment of an MPI novel instrument for in-process metrology application.

1.5 Thesis Organisation

The thesis is organised into the following chapters:

- Chapter 2 starts with a brief introduction of surface metrology. It then reviews literature related to various on-machine metrology techniques and finally reviews several optical metrology instruments focusing on in-process metrology instrumentation.
- Chapter 3 explains the fundamental concepts that form the foundation for the core chapters. The chapter explains the nature of the light and the interference phenomena. It describes the polarisation principle, including polariser types and their functionality. It also

represents the mathematical presentation for the polarisation using Jones vectors and matrices. The interferometers configurations are also discussed in this chapter.

- Chapter 4 discusses the methodology and the development steps of the MPI. It is divided into five parts: focused literature review, system simulation, and proof-of-concept experiments using mechanical phase-shift interferometry, wedge interferometer, and MPI with four cameras.
- Chapter 5 describes the way MPI is implemented and operated. This chapter describes in detail the operation principle of the MPI light source and the polarised interferometer. Moreover, it illustrates the polarisation mechanism to obtain the required phase shift. The chapter presents the camera calibration and colour camera crosstalk compensation.
- Chapter 6 describes the algorithms used to analyse the fringe recorded by the MPI in order to retrieve the measured surface. The fringe analysis is divided into parts: the wrapped phase determination and the phase unwrapping calculation. The MPI uses a single algorithm for determining the wrapped phase and five algorithms to unwrap the phase.
- Chapter 7 first presents the measurement noise of the MPI for the three operation modes (namely single wavelength single shot polarised interferometer (SPI), dual wavelength single shot polarised interferometer (DPI), and the triple wavelength single shot polarised interferometer (TPI), followed by the measurement results and system performance in terms of accuracy, resolution, and repeatability.
- Chapter 8 presents the conclusions derived from research and suggestions for future investigations.

1.6 Publication

The work on the MPI project has produced three conference papers. Complete details of these publications are provided in the ‘Publications and Awards’ in the final section of the thesis.

Chapter 2: Surface Metrology and Instrumentation

2.1 Introduction

The goal of this thesis is to propose a novel interferometric method to measure micro/nano surface topographies at high speed, allowing on-line inspection within the manufacturing environment. The measurement of moving surfaces currently presents a major challenge to the industry. This chapter reviews different types of measurement techniques to produce a novel instrument that achieves the authors' vision. The chapter starts with an introduction to surface metrology, then briefly classifies the surfaces types and on-machine metrology, and finally reviews several non-contact metrology instruments with a focus on the single shot phase shift interferometer.

2.2 Surface Metrology

Surface metrology is defined as 'the science of measuring small-scale geometrical features of the surface: the topography of the surface' (Jiang et al., 2007). It is focused on the measurements of surface characteristics such as surface texture, surface shape, and surface roughness. The manufactured surface is developed in such a way that it can be designed for a specific function, and it can be classified according to (Stout et al., 2001) into an engineered or a non-engineered surface, as shown in Figure 2.1.

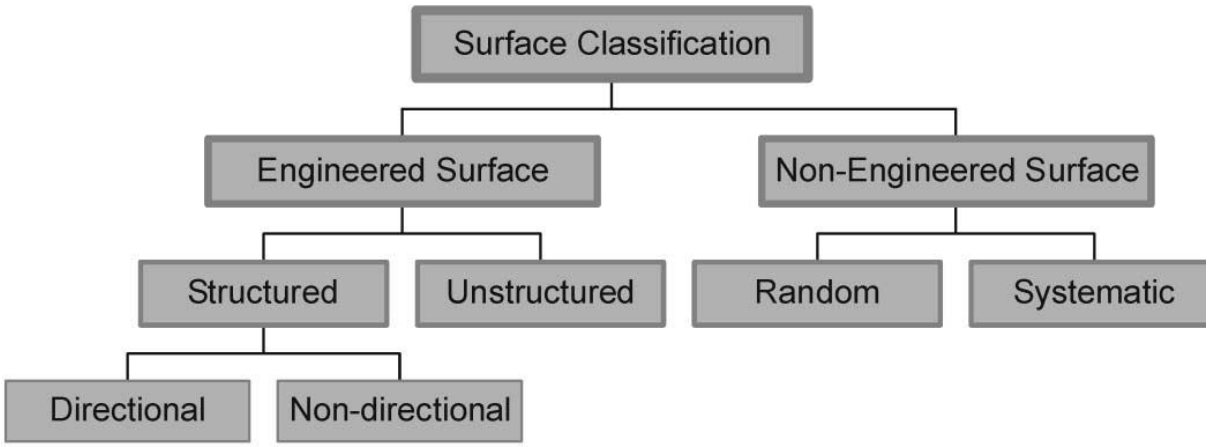

Figure 2.1 Scheme of surface classification [adopted from (Stout *et al.*, 2001)]

The engineered surface is designed and manufactured in practical way which deliberately alters the surface to achieve specific factional performance such as bearing and sealing. A surface assessment is crucial for many products because uncalculated surface friction or corrosion can cause failures in component functionality due to defects in the surface finish.

In the past decades, a considerable amount of research has been conducted on surfaces having roughness values ranging from few micrometres to sub-micrometres that have been manufactured using processes such as polishing, milling, and turning.

Recently, advanced technologies have been applied to fabricate complex structures with lateral dimensions ranging from millimetres to a fraction of a micrometre with nanometre tolerance (de Groot, 2015) .

These surfaces have motivated scholars in the field of surface metrology to develop different instruments for different applications (Mathia et al., 2011). Furthermore, currently, metrology science is trending toward information-rich surface metrology (IRM) by combining several different sources of information such as data acquisition process and the processing pipeline of the measurement process to enhance the quality and efficiency of the measurement (Leach, 2018).

2.3 Surface Characterisation

A surface can be classified according to the following three geometrical features (Hussam, 2013; Whitehouse, 2011):

Roughness: irregularities features often represent signatures of the specific process as an example impression left by grinding or polishing.

Waviness: This term refers to the relatively long wavelength of the irregularities caused by improper manufacturing because of several reasons, such as the vibrations between the sample and the grinding wheel.

Form: Very long waves indicate errors in the form caused by a sideways error in the rotating member or the machine or thermal distortion.

The concept of the scale-limit surface was created for the areal surface characterisation. To this end, (ISO, 2012), (Tang, 2016), and (Jiang et al., 2007) introduced a scale-limited surface. Scale-limited surfaces include S-F surfaces and S-L surfaces as shown in Figure 2.2, which are formed by a mixture of S-Filters, L-Filters, and F-Operators.

- The **S-Filter** filter out the small-scale of lateral parts that unwanted from the surface, resulting in the re-formation of the original surface to produce a primary surface.
- The **L-Filter** removes large-scale lateral parts that unwanted from the primary surface or S-F surface.
- The **F-Operator** filter out the unwanted forms from the primary surface.

The combination of F-operator and an S-Filter produce an S-F surface, while operate the L-filter on S-F surface produced SL surface.

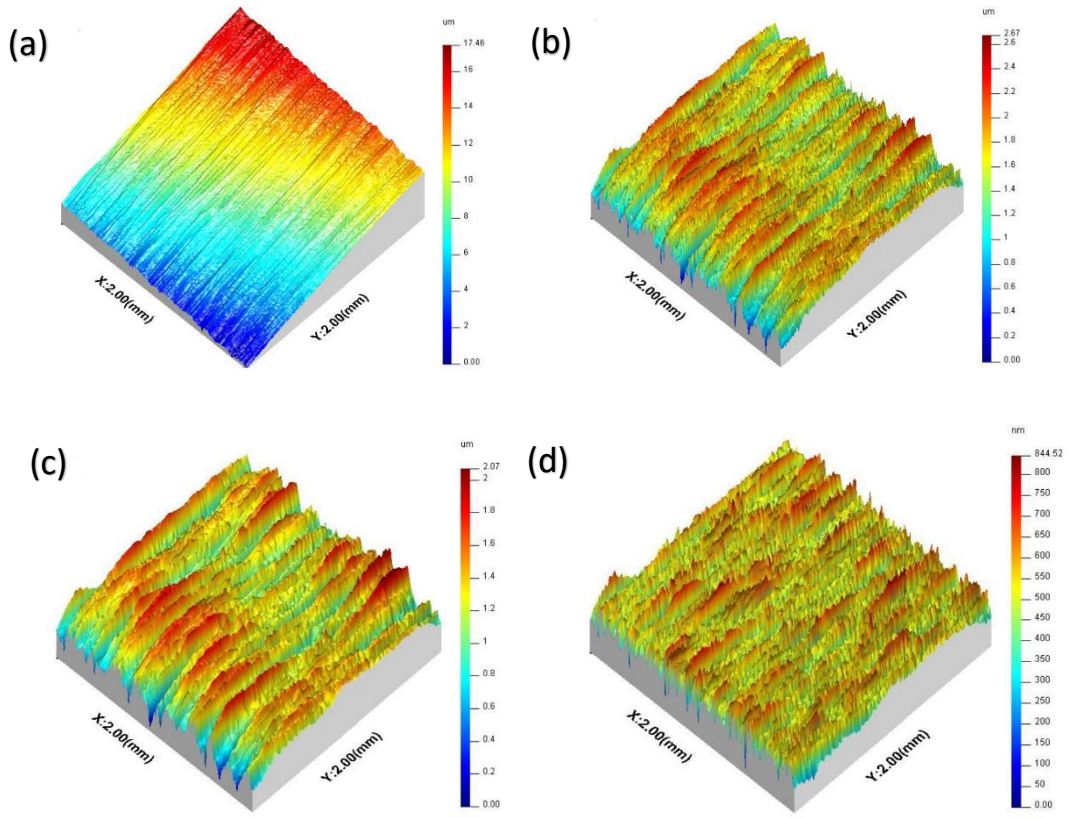

Figure 2.2 ‘’Surface characterisation: (a) extracted (raw) surface, (b) primary surface after S filtering c) S-F surface, and (d) S-L surface’’. [Adopted from (Tang, 2016)]

2.4 Definition of On-Machine Metrology

The surface measurement process can be performed under different conditions according to the requirement application. Therefore, the measurement process of surface metrology can be classified as follows:

In-process is the measurement process performed without halting the manufacturing process irrespective of the measurement technique. In several cases, this metrology is designed as part of the control system during the manufacturing or later in the production process. The in-process metrology challenges are a) fast measurement for inspecting a moving object, b) Robust measurement against environmental disturbances such as external vibration and temperature drifts, and c) measurement that can occur in the presence of fluids and dust. Thin film substrate measurement in roll-to-roll manufacturing process provides a good example of in-process metrology.

On machine, in-situ, embedded, or online metrology is the measurement process of a sample on the manufacturing platform without removing it. The measurement can be included with a machine tool like cutting, grinding, polishing, or moulding, thereby forming a surface. The challenges faced include environmental disturbance and process contamination. The on-machine process faces the same challenges as the in-process, however this process can stop the

manufacturing process during the measurement. The most significant challenges of in-process metrology exist in on-machine metrology as well, such as external disturbance and process contamination. Examples of **on-machine** metrology include the grinding tool wear measurement (Williamson, 2016).

Offline metrology is the process of measuring the sample using an instrument located in a different place from the manufacturing process. Here, moving the sample between the production line and the measurement lab is required. The main drawbacks of the use of offline metrology are high running costs for a separate metrology lab and time consumption. The ability to measure thermally unstable components at constant temperatures is the biggest advantage.

2.5 Surface Metrology Instrumentation

Humans have realised the importance of measurement since man settled from his nomadic lifestyle and started using building material, trading with neighbours, and occupying land. At this point in time, humanity became more technologically oriented with a demand for higher accuracy of measurement. The invention of machine tools followed by industrial revolutions has stimulated the development of inspection tools. Inspection tools have been developed, ranging from simple vision inspection tools to sophisticated measurement instruments that can measure and analyse complex geometries with high accuracy. As mentioned in chapter one, the metrology instruments can be classified into contact and non-contact types according to the physical distance between the probe and the measured. In this chapter, only non-contact devices have been reviewed with an in-depth discussion on on-line metrology.

2.5.1 Machine Vision

Machine vision is considered as a common optical metrology instrument for full coverage surface inspection applied for fast manufacturing throughput, such as the roll-to-roll process for thin film production used in flexible solar cell panels. The basic system configuration of machine vision, shown in Figure 2.3, consists of the light-emitting diode (LED) illumination system, imaging lenses, cameras, and computer processing units.

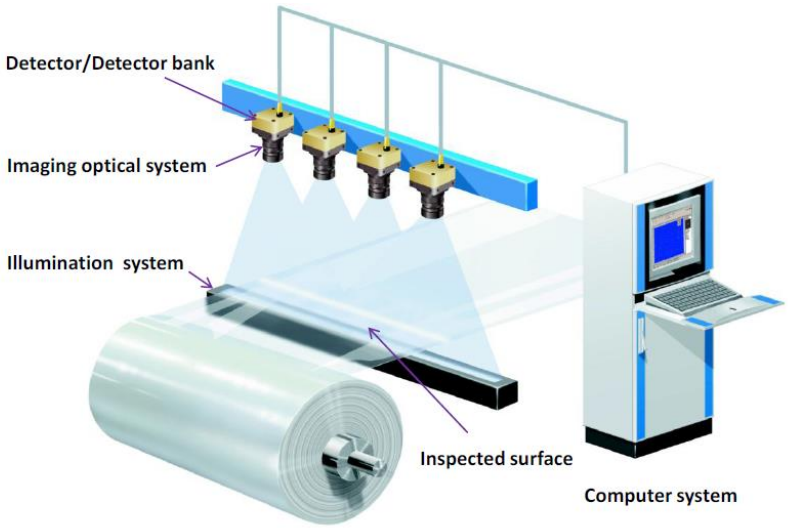

Figure 2.3 Machine vision system [adopted from (Tang, 2016)]

One of the main advantages of using external LED is to provide sufficient light intensity and reduce the exposure time of the camera in order to capture a moving object at high frame rates, as shown in Figure 2.4 (gardasoft, 2018). The measurement process starts with the illumination of the surface. Subsequently, the imaging lens is focused on the surface, and then the images are captured using a high-speed camera. Finally, the recorded data are processed using dedicated image processing algorithm (Harding, 2013)

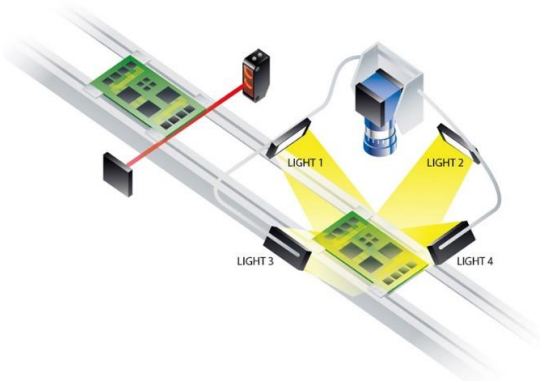

Figure 2.4 Different pulse intensities for individual lights [Adopted from (gardasoft, 2018)]

Dark Field Vision is considered as an important technique in surface metrology because it provides fast measurement and quality assurance in the industry (alliedvision, 2017). DISSEM, the partner of Allied Vision in Korea developed a system for low-cost solar cell inspection based on electroluminescence in the near-infrared spectrum. The system is designed to measure defects such as small cracks and breaks in the solar cell is shown in Figure 2.5. The solar cell system mainly consists of a crystalline silicon layer. Any defect in the micro-size of the crystalline silicon devices, such as cracks, will lead to a fault in the cell and affect the module performance. Therefore, detecting these defects is crucial for the manufacturer.

The inspection system consists of an array of cameras, which is placed in an enclosure free from ambient light to detect defects using an infrared-sensitive camera. The electroluminescence imaging (EL) technique is used to inspect the crystals and thin films in solar cells. This method is based on applying direct current to the solar module and detecting the photoemission by an infrared-sensitive camera (wavelength working range 950 nm–1250nm). With the assistance of reliable inspection software, this image will then be studied for dark defects. The system shows excellent performance in terms of accurately detecting several failures within a short time.

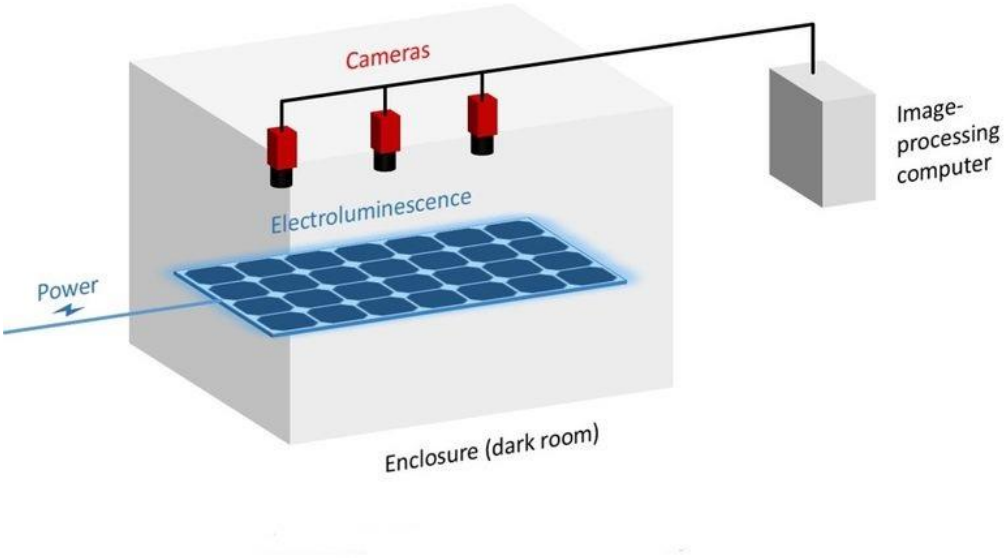

Figure 2.5 Photovoltaic module in-process inspection [adopted from (Allied Vision, 2017)]

Tsai *et al.* (2012) presented a method for the defect inspection in solar cells using EL images. A solar cell emits infrared light after being charged with electrical current. The intensity of the infrared light emitted from the intrinsic crystal grain boundaries and extrinsic defects such as small breaks, cracks, and finger interruptions shows lower value. Such significant defects can be highlighted by the EL image and shown as arbitrary dark regions in the background; this account for difficulty in automatic defect detection in EL images. The author uses a Fourier image reconstruction algorithm with EL imaging. The Fourier image algorithm filters out the frequency components related to the line/bar-shaped defects with back-transformation of spectral image back into a spatial one. Then inverse Fourier transform (IFT) is also used to back-transformed the image spectrum. The resulting image is supposed to be defect-free. The image-processing program will then compare the original image and the defect-free image, and a defect will appear as a clear large grey-level. Experimental results showed that the proposed method is sufficient in terms of inspecting small cracks and breaks.

Neal *et al.* (2011) used a polarised camera for the polarimetry application. The proposed camera was used for a stress inspection in birefringence materials. The same camera is used in a

single shot interferometer, as will be discussed in detail in the next chapter. Until 2018, the technology of such pixelated cameras with a pixelated polarised mask was the monopoly of a few companies (Brock *et al.*, 2014; Yoneyama *et al.*, 2016). In 2018, several companies brought to the market commercialised pixelated polarised cameras equipped with SONY sensors (IMX250MZR/MYR), which provide four different polarisation information with a single snap (thinklucid, 2019a).

The number of applications using polarised cameras is rising such as defect detection, haze removal, and 3D shape reconstruction. Polarised cameras are currently used in the analysis of the internal stress of glass and plastic, which is not visible when a conventional camera is used. This technique is also used to detect scratches on the surface of a transparent object, particularly surfaces that are fabricated from plastic, as shown in Figure 2.6.

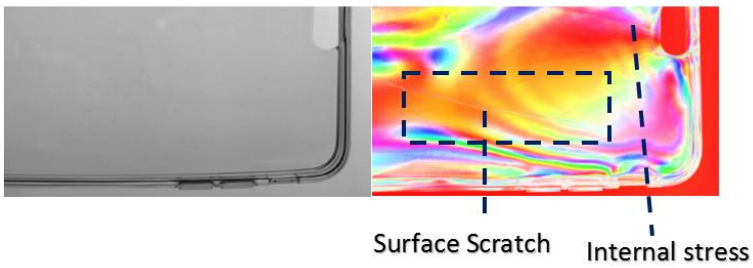

Figure 2.6 Polarisation image showing hidden scratch and stress [adopted from (Thinklucid, 2019)]

2.5.2 Metric Instruments

The machine vision system discussed above can only be used for fast inspection without providing real measurement parameters such as (Sq, Sp and Sv). To characterise surfaces and distinguish the type of defects, the use of metric measurement methods is necessary for on-line inspection. Metric instruments generally classified into interferometric and non-interferometric devices.

The interferometric method can be further classified into interferometers for offline metrology and interferometers for in-process metrology. The non-interferometric techniques reviewed are focus variation, confocal microscopy, and chromatic confocal microscopy, all of which are off-line metrology methods, while the coherence scanning interferometry is only one reviewed as an interferometric technique for offline measurements. The review also includes wavelength scanning interferometry, dispersive interferometry, and phase shift interferometry for in-process measurements.

2.5.2.1 Focus Variation

The focus variation principle based on the integration of several variations of the small depth of focus through the vertical scanning of the optical system provides a 3D topographical area with colour information, as shown in Figure 2.7. The images are captured continuously while the optical head is translated vertically along the Z axis (optical axis). As a result, each part of the sample is sharply focused during the scanning. Dedicated algorithm is used to analyse the sharpness of the images based on the contrast variation between the neighbourhoods of each pixel(Leach, 2011b). The focus position can therefore be determined when the standard deviation of group of pixels is at the highest value along the scan.

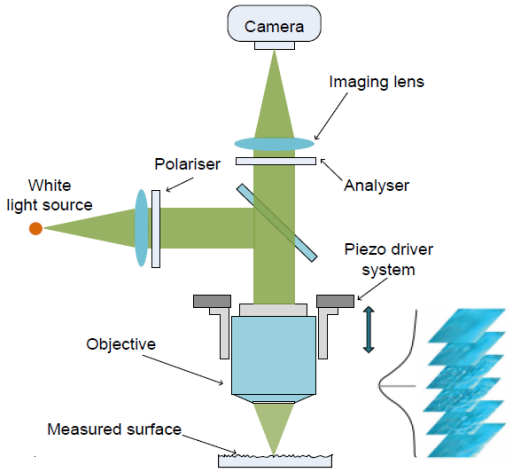

Figure 2.7 Schematic of a focus variation instrument [adopted from (Tang, 2016)]

Focus variation can be equipped with different illumination sources, such as coaxial illumination and ring lights. The ring light allows the objective lens to capture more bounced light from the workpiece even with a limited numerical aperture. As such, the slope measurement of focus variation can be up to 80° (Hiersemenzel *et al.*, 2012), greatly exceeding the slope measurement range of any other optical measurement techniques. As such, the focus variation is preferred to measure rough surfaces, such as surfaces produced by additive manufacturing (AM).

Danzl *et al.* (2009) report that focus variation is a very powerful technique for measuring rough surfaces. They also report that it exhibits excellent matching with tactile instruments without causing damage to the measured surface. Townsend *et al.* (2016)reported that the most utilised optical measurement technique for an AM surface metal part is focus variation microscopy, occupying 11% of the reviewed literature.

The focus variation technique can measure a surface with a vertical resolution of 10 nm and 25 mm vertical measurement range. However, the mechanical scanning mechanism has limited the operation of focus variation to offline measurements. Thus, it cannot be used in in-process metrology and is therefore not applicable. It likewise cannot be used to measure super-smooth

surfaces and transparent surfaces because the algorithm cannot sharply distinguish between pixel contrast variation across different focal positions (Kapłonek *et al.*, 2016).

2.5.2.2 Confocal Microscopy

The scheme of laser scanning confocal microscope is illustrated in Figure 2.8. The confocal microscope is equipped with two pinholes at different positions. The first pinhole is located after the illumination source, while the second pinhole is on the detector side and located on the conjugate location of the primary pinhole.

The optimum recorded signal is achieved when the reflected light from the sample is imaged on the confocal aperture and this is obtained when the sampled is located on the focal plane of the microscope lens, as shown in Figure 2.8 (a). A weak signal is recorded when the sample is far from the focal plane of microscope lens, as shown in see Figure 2.8 (b) (R. Leach, 2011a).

The height information is retrieved by processing a sequence of confocal images taken during the head translation along the optical axis. Constructing the intensity distribution for a specific pixel gives a sharp peak at the best focal position; hence, the surface height can be found. The vertical measurement range depends on the scanning range of the translation head and the working distance of the objective.

An areal measurement of the sample is obtained by scanning the beam across the surface point by point in both the X- and Y- directions. Fu *et al.* (2018); Leach (2011a) reported that the confocal microscope can be used in in-situ surface characterisations.

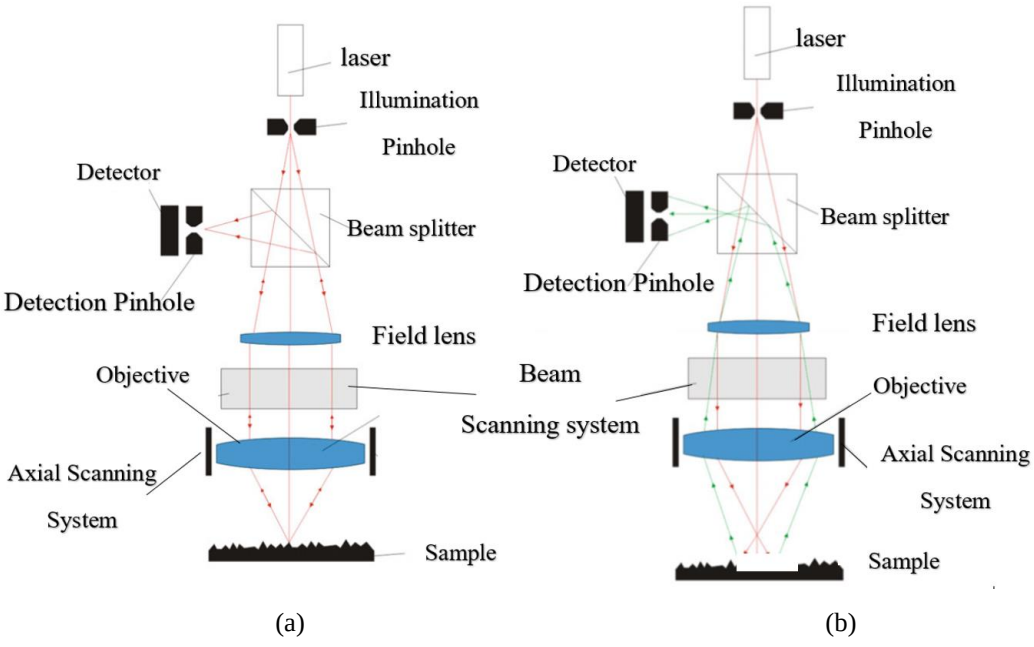

Figure 2.8 Optical setup of a confocal microscope (a) sample in focus (b) sample out of focus [adopted from (Moschetti, 2016)]

2.5.2.3 Chromatic Confocal Microscopy

Chromatic confocal microscopy (CCM) is a measurement process that integrates a chromatic confocal probe and a lateral scanning system in order to perform areal measurement. The CCM extracts the measured surface height information and the related light intensity by sensing each point of the measured surface. The lateral scanning system is dynamic and makes possible the transition from the line profile measurement (with an X-axis stage) to an areal surface (with both the X- and the Y-axis stages). Instead of mechanical vertical scanning, a chromatic confocal microscope is based on the use of an objective with a longitudinal chromatic aberration, which generates different focal positions for each individual wavelength (Daniel, 2007). This feature of the static optical head avoids any additional noise generated by internal mechanical vibrations of the CCM (Leach, 2011a). Figure 2.9 illustrates the chromatic confocal microscope scheme.

The wavelength, which reflects back to the system, should have the same focal position as that of the used objective. The system detector for the surface in focus records the maximum intensity. A spectrometer is used as a detector in CCM. Instantaneous measurement for the best focal position for the object makes the measurement process faster than the conventional confocal microscope.

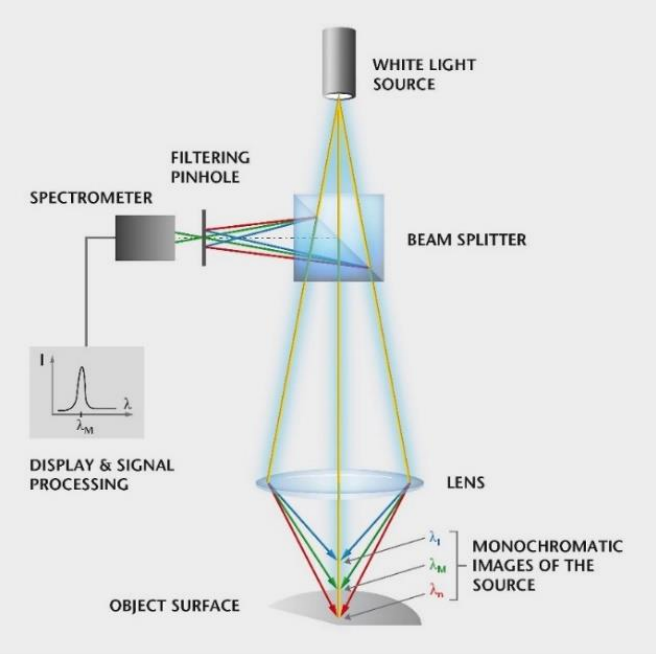

Figure 2.9 Schematic of chromatic confocal microscope [adopted from (Polytec, 2016/07)]

The chromatic confocal measurement range depends on the depth of focus of the microscope objective lens, the wavelength bands (minimum and maximum), the overall optical dispersion, and the confocal pinhole aperture (Kim *et al.*, 2013; Moschetti, 2016).

The vertical resolution of the CCM is controlled by the spectrometer's resolution. Typical vertical resolutions can be change from a micrometres to few nanometres, depending on the selected measurement mode and the optics that used in the setup (Moschetti, 2016; polytec, 2016/07 ; Stilsa, 2016). The CCM's acquisition speed decreases with an increase in the exposure time of the detectors. The reflectivity of the measured surface and the light source intensity are among the parameters that determine the exposure time (Leach, 2011a). CCM is currently sold commercially by several companies (micro-epsilon, 2019; nanovea, 2019; polytec, 2016/07).

Furthermore, Nguyen and Chen (2018) proposed the in-situ one-shot chromatic confocal microscope, which is based on using digital micrometre device (DMD) integrated with the chromatic confocal microscope. The proposed microscope can provide better accuracy than conventional CCM, since it does not require any mechanical movement to obtain areal measurement. The DMD implemented an array of pinholes for the purpose of confocal lateral scanning to substitute the pinholes at the illumination source and conjugate positions in the conventional confocal microscope. The technique used a Mosaic spectral (IMEC) areal scan camera for the single shot purpose. It was equipped with chromatic objective lens for axial wavelength dispersion.

2.5.2.4 Coherence Scanning Interferometry

The operating principles of coherence scanning interferometer (CSI), as shown in Figure 2.10 (a) , are based on fringe localisation using the coherence envelop of a broadband light source (white light). The measured sample is scanned mechanically in the Z-direction to provide an interference fringe along the object. The computer records the intensity value for each consecutive frame captured by the camera. Figure 2.10 (b) shows that the interference fringes change when an interference objective is scanned vertically. The highest fringe visibility is obtained when the measurement arm and the reference arm at the same distance (i.e. at zero optical path difference), while the fringe visibility drops dramatically and quickly when the OPD increases. The surface topography is retrieved after tracking all the coherence peaks collected by the field of view of the microscope lens, as shown in Figure 2.10 (c).

The benefits of using CSI include the ability to measure rough and high-precision surfaces without using any phase unwrapping algorithm (de Groot, 2011). Mainly the scanning range of the translation head and the working distance of the objective lens limit the vertical measurement range.

Claveau *et al.* (2018) employed the CSI technique to measure the thickness and the refractive index for both thin and thick transparent materials. Thus far, several commercial interferometers based on the CSI technique, such as Talysurf CCI 6000 from Taylor Hobson Ltd., which has 0.1

Å vertical resolution (scribd, talysurf-cci-6000). Zaygo Corporation fabricates the NewView 9000, which has a vertical resolution in the sub-nanometre range (zygo, 2019). Gomez *et al.* (2017) used CSI for measuring the additive manufacturing surface topography with the expanded measurement capability of CSI.

The most critical weakness of the CSI technique is the large amount of data that needs to be recorded and processed for each single FOV. The CSI technique is suitable only for offline measurements, and it is not applicable to in-process metrology because the scanning process limits the measurement speed. Some other technical drawbacks, such as bat wings and spiky errors occurring at the edge of the surface feature have to be considered when using CSI (Tang, 2016).

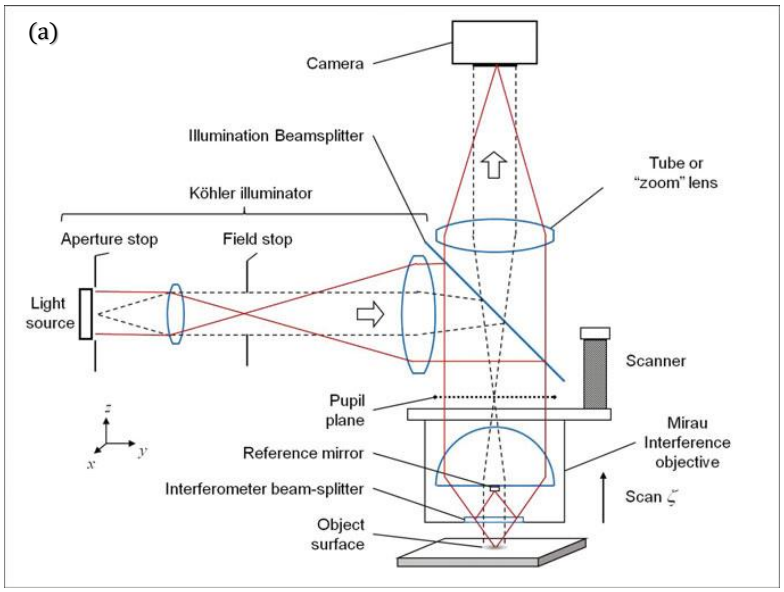

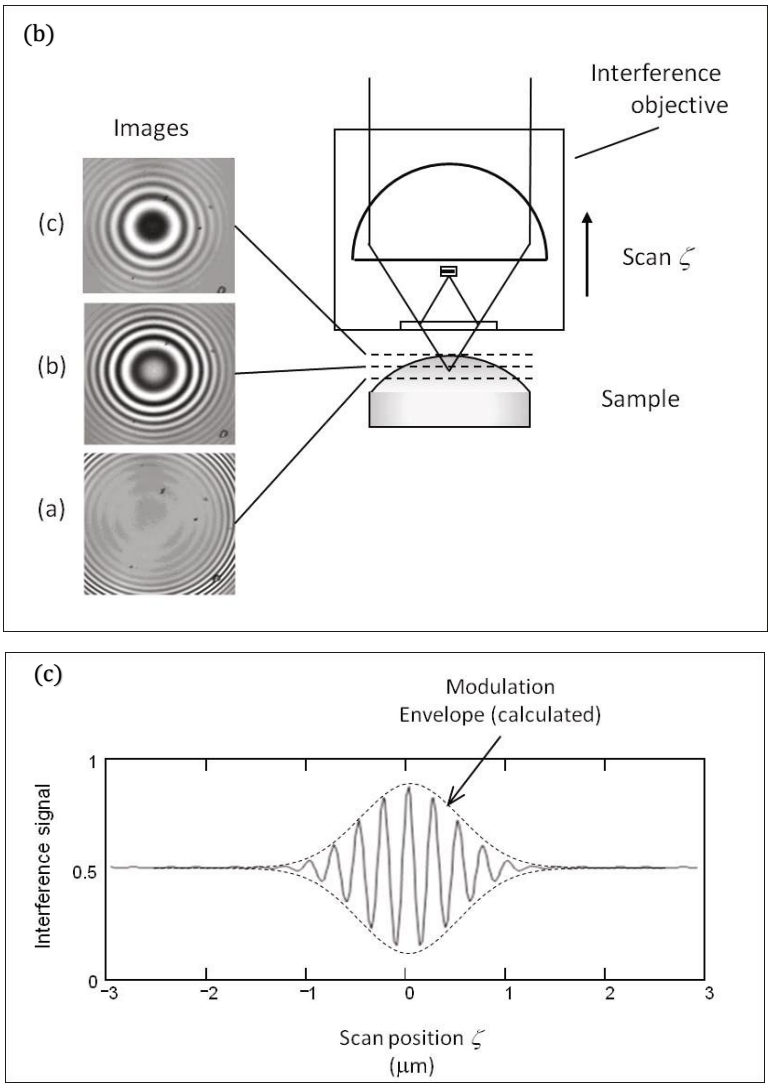

Figure 2.10 (a) Schematic diagram of CSI (b) interference fringe is recorded by CSI at different position. (c) CSI signal for a the modulation envelope of CSI as recorded by single pixel [adopted from (de Groot, 2011)]

Beverage *et al.* (2014) discussed the advantages and disadvantages of using coherence scanning interferometry (CSI) for capturing colour images, and they proposed a new technique for constructing an imaging system. This system would use standard colour detectors, but without a colour filter at the camera.

Moreover, it would include a complex illuminator with RGB LEDs to provide a large range of illumination spectra. Colour information accusation by CSI is divided into two steps, first auguries surface metrology data is acquired in traditional CSI; following that extra data is gathered via a different RGB illumination source - as shown in Figure 2.11. The method can discover discoloration or blemishes that are difficult to recognize by the grey level alone, as a result the true colour information is captured together with areal topography.

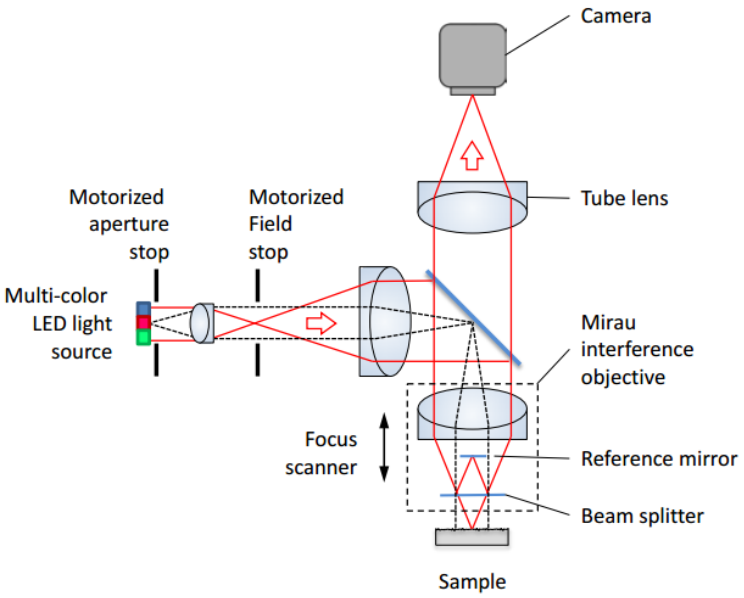

Figure 2.11 Schematic diagram of colour-imaging CSI instrument, equipped with a monochrome camera and a RGB LED illuminator

2.5.2.5 Wavelength Scanning Interferometry

A wavelength scanning interferometer (WSI) is based on the tuning of the wavelength from a broadband illumination source to obtain the required phase shift to calculate the wrapped phase (Suematsu & Takeda, 1991). A sinusoidal intensity variation is obtained for each pixel as a result of the phase shift between the reference and the measurement arm. WSI has an advantage over other interferometers such as CSI in that there is no mechanical scanning during the phase shift operation. Several frames need to be captured sequentially with the wavelength scanning process.

The absence of mechanical scanning makes both the camera frame rate (typically 128 frames or 256 frames are captured) and the algorithm computing time are the main factors that determine the measurement time of WSI. This naturally leads to a large amount of data to be stored for each FOV and allows errors due to external vibrations.

The scanning time was the shortcoming of the technique, which is why it was not found in manufacturer environments as an online measurement tool. This challenge was overcome by (Jiang *et al.*, 2010) by using a second interferometer integrated with the measurement interferometer to actively stabilise the system, as shown in Figure 2.12. The second interferometer works independently as a closed-loop control system, connecting the second mirror to the PZT, which allows the translation mirror in the direction to compensate for the external vibrations without affecting the measurement speed. The system allows the WSI to retrieve the surface with nanometre resolution in the presence of vibrations at 40 Hz × 12.2 dB (Blunt *et al.*, 2013).

An advanced detector was used for WSI; however, the computational time remained close to 31.9 because of the complexity of the algorithms used (Jiang *et al.*, 2010). The integration of technologies such as multiple-core CPUs (Hussam *et al.*, 2011) reduced the computational time to close to 1 s, which allowed the WSI to be used for online defect inspections of the R2R process (Elrawemi *et al.*, 2015). However, as of now, WSI cannot be used to measure moving objects.

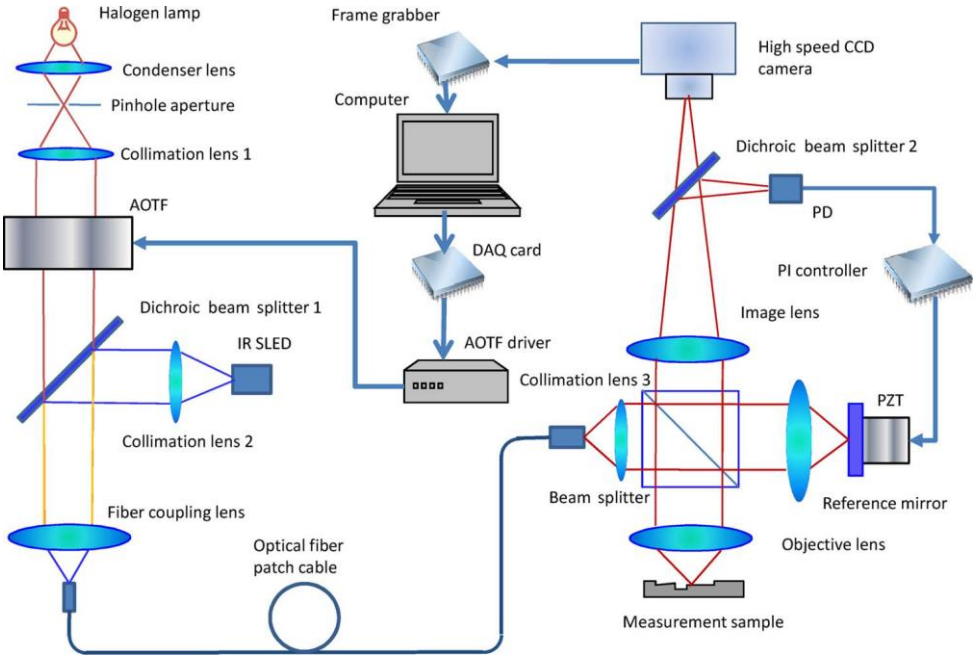

Figure 2.12 WSI System : PD, photodiode; DAQ, data acquisition card [adopted from (Jiang *et al.*, 2010)].

2.5.2.6 Dispersive Interferometry

A dispersive interferometer or spectral resolve white light interferometer (SRWLI) is an interferometer that produces a phase shift through wavelength dispersion without mechanical scanning. It is faster than a coherence scanning interferometer (CSI) or a full field of view wavelength scanning interferometer from the perspective of achieving a surface profile in a single shot. The interference beam is particularly dispersed by prism or diffraction grating and then focused on the interferometer sensor (Daniel, 2007). The phase information is linearly distributed along the chromaticity axis of the camera.

Ruiz *et al.* (2012) investigated a combination of hyper-spectral interferometry with white light interferometry for the single-shot measurement of 3D surface profiles. The surface topography was retrieved by using speckled wave fronts from an optically rough surface. As such, a range of information was obtained from the intensity versus the wave number at each pixel despite a random phase shift. The vertical range of the interferometer was unambiguous. The corresponding optical setup is shown in Figure 2.13. The technique can be used in the measurements of moving substrates such as roll-to-roll measurements.

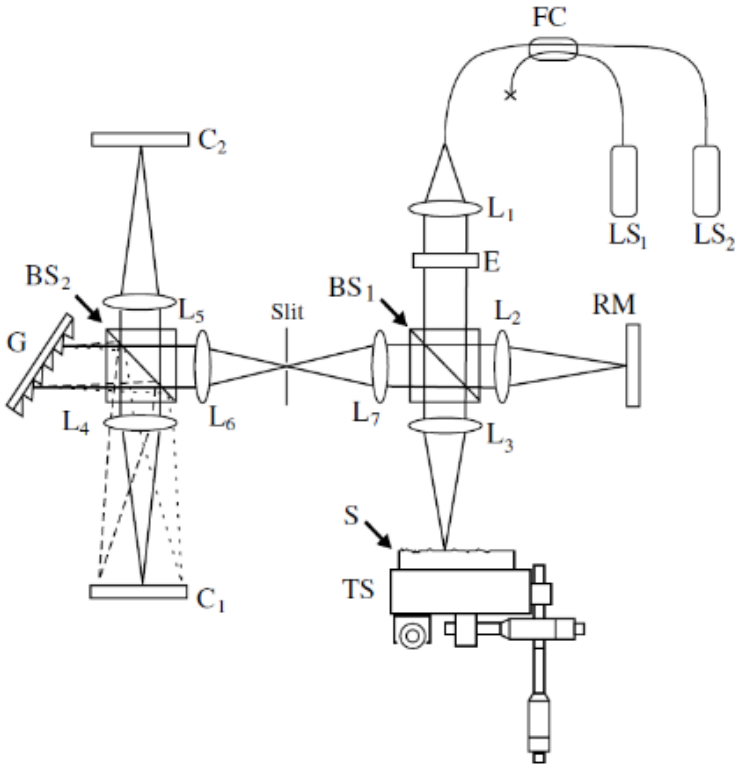

Figure 2.13 Hyperspectral interferometry setup: LS, Laser source; L, Lens; RM, Reference mirror ; S, sample: C, Camera; G, Diffraction grating ; BS, Beam splitter ; E, Beam Expander; TS, Translation stage [adopted from (Ruiz et al., 2012)]

Hassan *et al.* (2018) proposed a spatially dispersed short-coherent interferometer (SDSCI) for in-process profile surface inspections, as shown in Figure 2.14. The operation principle is based on the insertion of a dispersive probe in the measurement arm. The dispersive probe consists of a diffraction grating placed at the focal length distance from the collimating lens. A spatially dispersed beam observes the measured surface and the optical phase calculated simultaneously for each sampled wavelength. The technique can produce a profile of 10 mm with a vertical measurement range limited by$\frac{\lambda}{4}$. This technique can be used for online measurements.

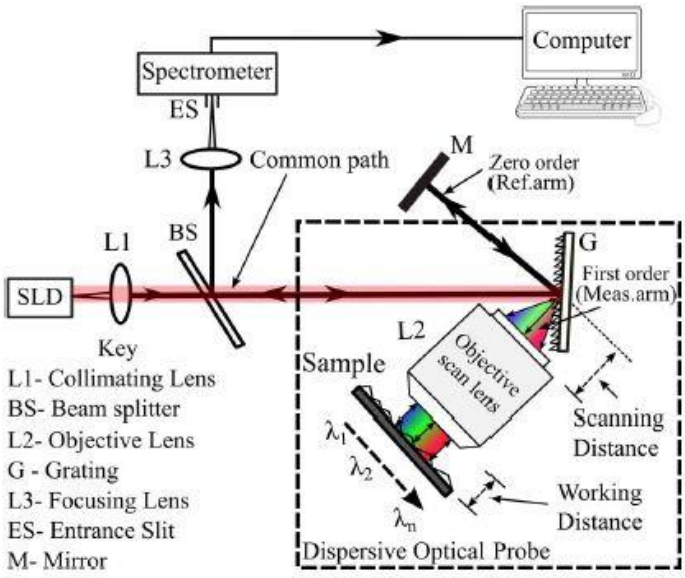

Figure 2.14 New SDSCI sensor configuration arrangement using diffraction order [adopted from (Hassan *et al.*, 2018)]

Tang *et al.* (2018) employed the fringe order method with a single shot line-scan dispersive interferometry (LSDI) for in-process surface inspections. The configuration of the LSDI system is described in Figure 2.15. The operation principle is based on the illumination of the interferometer with a broadband source. Subsequently, the interference beam split into two beams after focusing by the tube lens. One beam is detected by a CCD camera to provide a real-time image, and the second beam is passed to a spectrometer to produce spectral interferograms for the surface profile measurements. The system has no phase ambiguity problem and measurement vertical range is objective depth of focus dependent.

The fringe order method is used to retrieve the phase with nano-scale resolution. A 178.5 + 2.0-nm standard step artefact (from VLSI, USA) was measured using LSDI and compared to the measurement obtained by Talysurf CCI 3000. The measurement results showed a 2.7-nm difference between the two machines. The real surface topography was obtained by scanning the sample mechanically during the measurement, and a lateral sampling resolution of 1.826 μm with a profile length of 876.712 μm was achieved. This technique can be used by measuring moving surfaces produced, for example, by the roll-to-roll process.

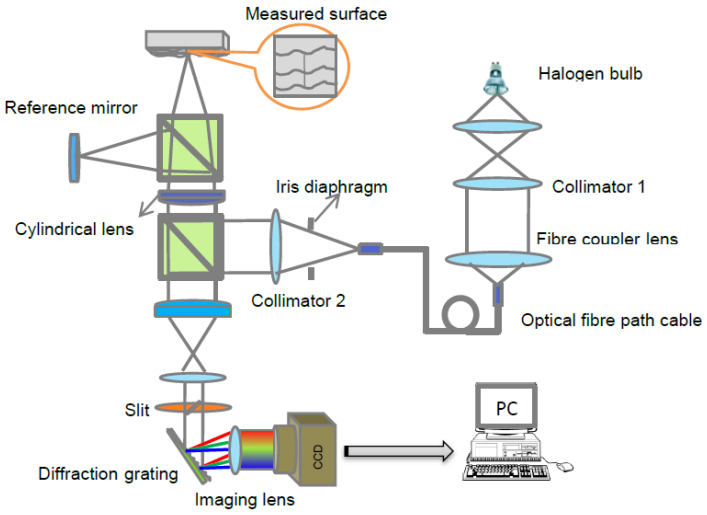

Figure 2.15 Schematic of WLCS [adopted from (Tang *et al.*, 2018)]

2.5.2.7 Phase Shifting Interferometry

Phase shifting interferometry (PSI) is a known method for areal measurements and one of the best techniques for measuring smooth and super-polished surfaces. The vertical measurement resolution in a phase shift interferometer is within 1/1000 of a fringe in optimum measurement environment(Hussam, 2013). The fundamental principle of the phase shift interferometer is to generate the phase difference between the reference wavefront and the measurement wavefront by changing the optical path difference. The conventional phase shift interferometer is based on the physical changes in the length of the optical path between the reference and measurement arms.

A reference mirror with PZT to generate the consecutive step usually carries out this process. The interferometer detector records the intensity at each step. At least three consecutive phase shifts are required to solve the Equation of an interference pattern, which has three variables: the DC intensity I_0, the fringe visibility v, and the phase value (θ), which embeds the measured surface height. The mathematical formula below is used in the case of n phase shifts (Daniel, 2007; Hussam, 2013):

$$\begin{bmatrix} I_1 \\ I_2 \\ . \\ . \\ I_n \end{bmatrix} = \begin{bmatrix} I_0[1 + vcos(\theta + \alpha_1)] \\ I_0[1 + vcos(\theta + \alpha_2)] \\ . \\ . \\ I_0[1 + vcos(\theta + \alpha_3)] \end{bmatrix} \quad (2.1)$$

Where alpha (α) is the induced phase shift.

There are several algorithms can be used later to determine the phase from the collected intensity associated with the number of steps set to shift the phase between the measurement arm and the reference arm. For example, three-step phase shift, Carré, and the four-step phase shift

required four phase shift value and five-step phase shift (Blunt *et al.*, 2013; Carré, 1966; Wyant *et al.*, 1984). Various algorithms have been developed to remove the 2π discontinuities that appear in the raw phase generated from algorithms mentioned above (Herráez *et al.*, 2002; Huntley, 1989; Itoh, 1982). The main limitation of the single wavelength phase shift interferometer is the π phase ambiguity when there is a physical OPD jump greater than $\lambda/4$.

Ngoi *et al.* (2001) proposed new phase shifting interferometry for measuring flat surfaces, which is immune to vibrations. This interferometer is based on quarter-wave plates plus a polariser to obtain the required phase shift. Measurements related to four different phase shifts are performed by using polarisers and quarter-wave plates. Four interferograms are captured instantaneously by using four cameras, as shown in Figure 2.16. This increases the flexibility of this interferometer from the perspective of measuring vibrating objects.

The experiments conducted in this study showed that when an object vibrated at different frequencies from 100 Hz to 1000 Hz with a fixed amplitude, the measurement did not affect by the environmental disturbances, knowing that the data capturing rate is much higher than the vibration frequency. It is important to mention here that the system was operated at a single wavelength, hence the measurement range is limited by $\lambda/4$.

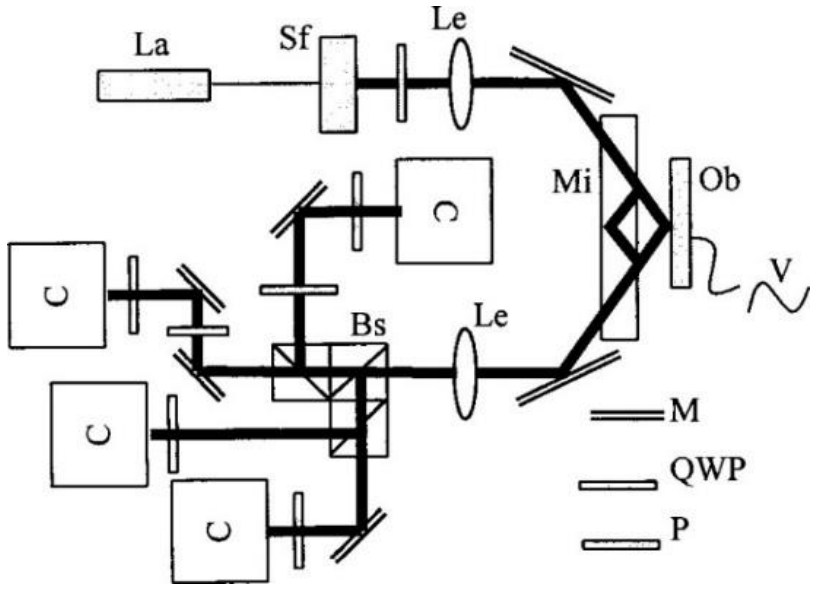

Figure 2.16 Optical setup of phase shifting interferometer based on (Mirau) : La, laser illumination source; Sf, spatial filter; Ob, measurement sample; Mi, Mirau reference objective; Bs, beam splitter; QWP, quarter-wave plate; Le, lens off-focal length; M, mirror; C, camera; Am splitter[adopted from (Ngoi,2001)]

L.-C. Chen *et al.* (2010) introduced a single shot phase shift interferometer based on a single glass plate that used to shift the phase spatially between reference and sample wavefront, as shown in Figure 2.17. They used a three step algorithm, at shifted phase value 90°, 180°, and 270°, to retrieve the original phase information.

System repeatability and accuracy was verified by measuring the flat mirror surface and Mitutoyo gauge blocks. The experimental result shows that the proposed interferometer immunity against environmental disturbances with 10 nm measurement repeatability.

The disadvantage of this system is that it requires a CCD with a high dynamic range (a grey level of 65,536) to instantaneously capture three interferograms. This leads to the reduction of the image acquisition speed. The system also operates at a single wavelength that limits the measurement range to λ/4.

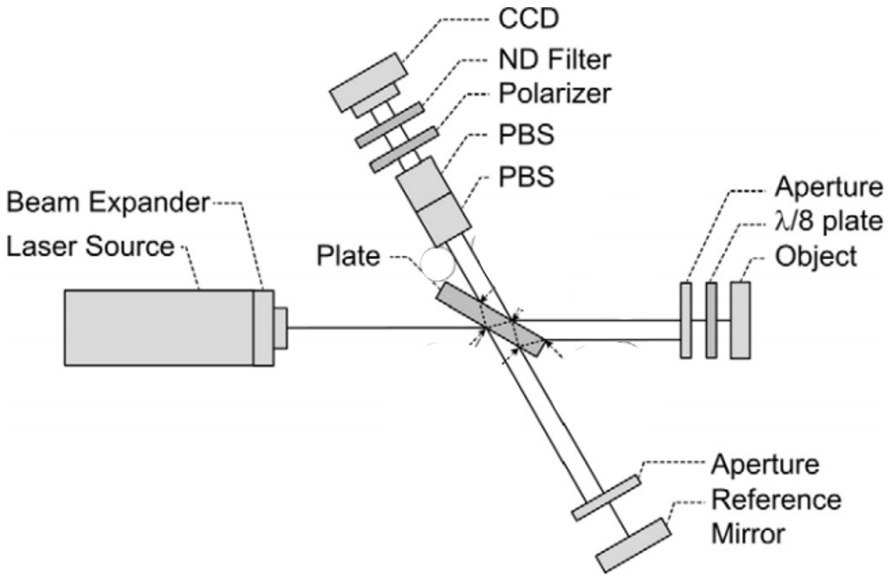

Figure 2.17 Optical configuration of developed simultaneous phase shifting interferometer, ND Filter: Neutral Density Filter; PBS: Polarised beam splitter [adopted from (L.-C. Chen *et al.*, 2010)]

Creath K (2012); Neal *et al.* (2011) introduced a single-shot interferometry apparatus, commercially known as FlexCam from 4D Technology, for dynamic surface measurement. It is currently employed to inspect defects in flexible Photovoltaic (PV) films barrier manufactured using for R2R technology, as shown in Figure 2.18. The pixelated polarised camera is the core of FlexCam technology. This method relies on laser interferometry as the light source to acquire the areal surface data.

It acquires all shifted phases at once; the acquisition time depends the camera exposure time (only one exposure time is required). The goal of FlexCam is to measure the surface topography with milliseconds measurement time and 1.2 µm lateral resolution with 2 nm vertical resolution. The main drawback for this technology is that the vertical range is limited by λ/4, and this may pose a problem to define the surface pattern for characterisation or identifying large vertical defects that exceed λ/4.

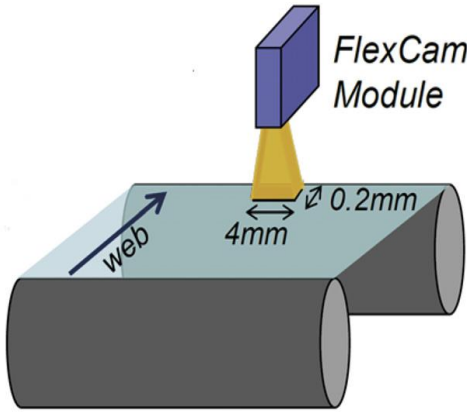

Figure 2.18 FlexCam module [adopted from (Elrawemi *et al.*, 2015)]

All techniques of a single wavelength phase shift interferometer have the common limitation of the vertical measurement range being limited by λ/4. The common solution to extending the measurement range is to use long synthetic wavelength. The synthetic wavelength oscillated at beat frequency $(\omega_1 - \omega_2)$, which is created when combining the optical field of two waves which have different frequencies and are traveling in the same direction, where ω is the angular frequency. In a dual wavelength interferometer, the fringe patterns for the synthetic wavelength result from the addition of the fringe patterns of λ_1 and λ_2 in the image plane. The synthetic wavelength is equal to $\lambda_s = \lambda_1\lambda_2/[\lambda_1 - \lambda_2]$, where λ_1 and λ_2 are the two wavelengths used as shown in the exemplary Figure 2.19. By processing the phase profile for the two wavelengths, an extended synthetic phase profile can be achieved. While the synthetic phase can be calculated from $\varphi_{synth} = \varphi_{short} - \varphi_{long}$, the system noise will be amplified by a factor of $\frac{2\lambda_s}{\lambda_1}$ (Gass et al., 2003). By using the synthetic wavelength the vertical measurement range will be extended from $\frac{\lambda}{4}$ to $\frac{\lambda_s}{4}$

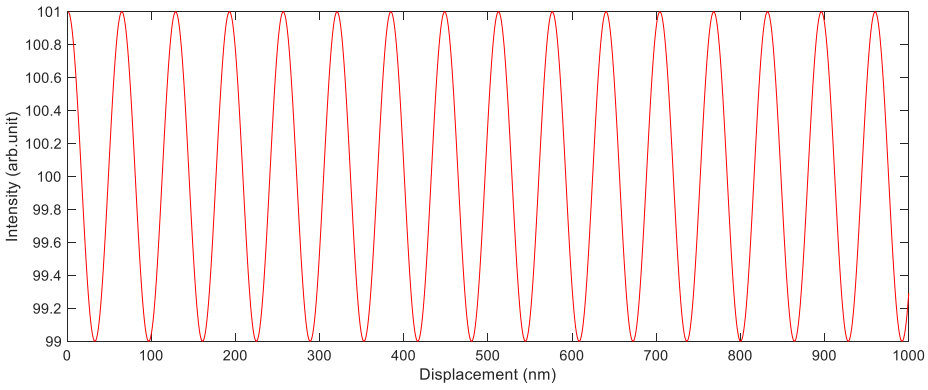

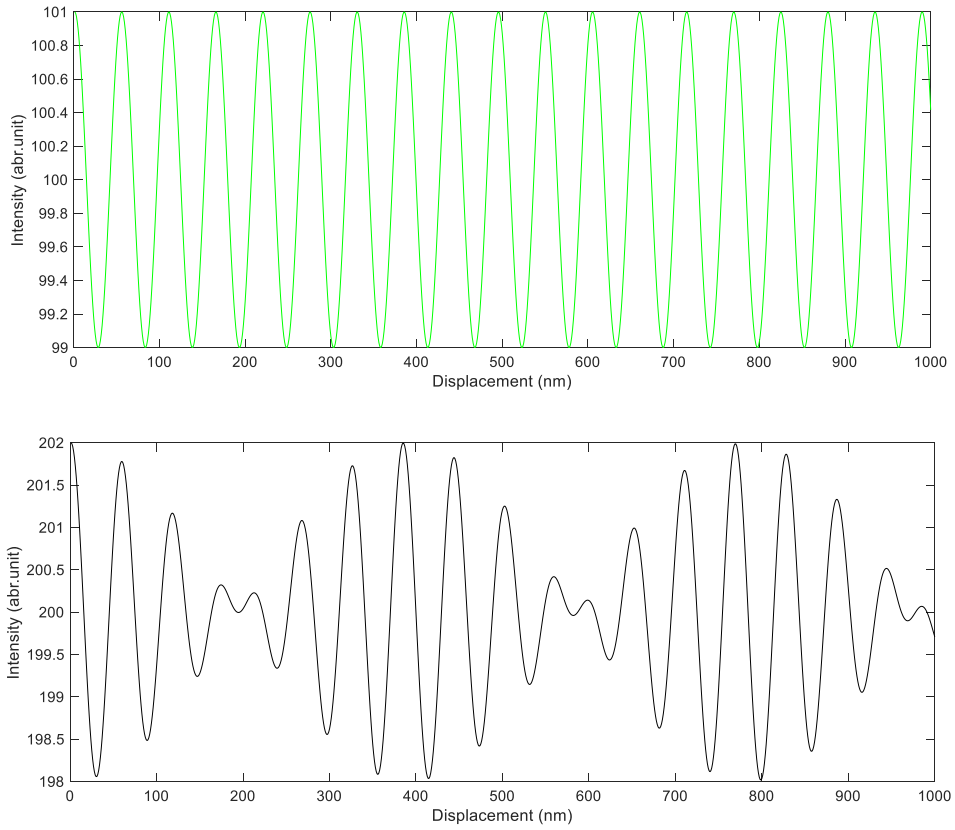

Figure 2.19 Fringe of dual wavelength interferometer: (a) Fringe of λ_a = 640 nm, (b) fringe of λ_b = 540 nm, and (c) Beat pattern

Creath (1987) proposed a two-wavelength phase shift interferometer using the visible bandwidth. The Carré algorithm was used in this study to calculate the wrapped phase value. The phase shift mechanism was mechanically by moving the reference mirror using PZT. Four consecutive frames are captured with a 90° phase shift between the frames. Four different wavelengths (650.9, 631.6, 611.7, and 577.4 nm) with a 10-nm bandwidth are used to produce four respective synthetic wavelengths. However, the mechanical movement is slow for online measurements.

Since then, several studies have proposed different methods to expand the measurement range of the phase shit interferometer using synthetic wavelengths. The data acquisition is usually obtained by several techniques, such as instantaneously using a colour camera equipped with a Bayer filter or after performing phase shift scanning or in a single shot with a tilted surface (Al-Bashir1 *et al.*, 2018; Awatsuji *et al.*, 2015; Kitagawa, 2010; Turko & Shaked, 2017).

Awatsuji *et al.* (2015)proposed a multi-wavelength phase-shift interferometer based on the holography configuration. The surface height of each point on the sample was calculated without depending on the neighbouring pixels. A monochromatic camera equipped a micro-polariser array used to obtain the four-phase shift for the green and blue wavelengths. The measurement of the

1.9 µm step height was successfully demonstrated, however the measurement noise was not reported, and the camera used was too costly for interferometer applications.

Tian *et al.* (2018) proposed a single shot multi-wavelength interference microscope for measuring a large step height and surface roughness, as shown in Figure 2.20. The phase shift was obtained using a linear micro-polariser equipped with a coloured camera sensor to obtain four different wavelengths for RGB wavelengths. The Bayer filter was used to separate the RGB component of the light. A band-pass filter with a 10 nm bandwidth was used to filter the light from LED sources into three colour components: Red, green, and blue.

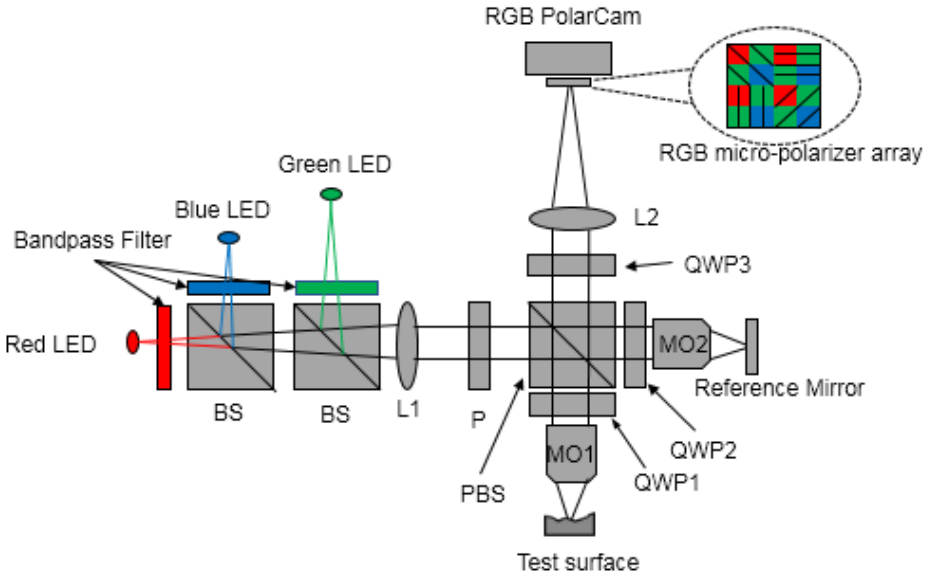

Figure 2.20 System configuration: PBS: Polarised beam splitter; L: lens; P: polariser; BS: 50% beam splitter; MO: microscopy objective; QWP: achromatic quarter-wave plates; RGB PolarCam: a special camera with a wire-grid micro-polariser array on the conventional RGB Bayer filter array [adopted from (Tian *et al.*, 2018)]

To expand the vertical measurement range over the conventional dual wavelength interferometer, the RGB wavelength phase information ($\theta_1, \theta_2, and\ \theta_3$) was used. A long synthetic wavelength $\Lambda_{12-23} = \frac{\Lambda_{12}\Lambda_{23}}{|\Lambda_{12}-\Lambda_{23}|}$ was produced from other two nearly equal synthetic wavelengths $\lambda_{s12} = \frac{\lambda_1\lambda_2}{|\lambda_1-\lambda_2|}$ and $\lambda_{s23} = \frac{\lambda_2\lambda_3}{|\lambda_2-\lambda_3|}$.

The proposed multi-wavelength interference microscope successfully measured a 1.7-µm step height with the resolution of a single wavelength using the fringe order algorithm. The authors suggested an additional fourth wavelength using longer red wavelength laser source to expand the measurement range to 10.5 μm, as shown in Figure 2.21.

However, the use of the fourth wavelength required two shots to retrieve the surface, as the first shot illuminated by RGB and the second shot illuminated by the additional wavelength. The

performance of the system was tested by measurement variety of step heights up to 10 μm. The system was successfully demonstrated excellent few nanometre measurement accuracy compared to Zygo NewView 8300.

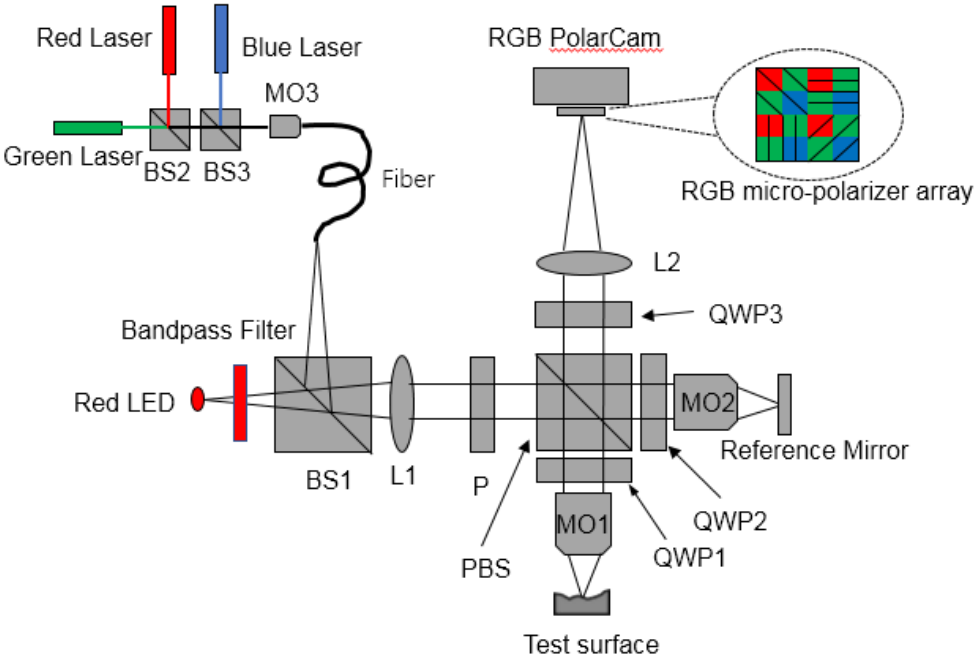

Figure 2.21 Schematic diagram of RGB laser and Red LED as a light source illuminated phase shift interferometer: PBS: Polarised beam splitter; L: lens; P: polariser; BS: 50% beam splitter; RGB PolarCam: special design camera with a wire-grid micro-polariser array on equipped on RGB Bayer filter array ;QWP: achromatic quarter-wave plates; MO: objective lens [adopted from (Tian *et al.*, 2018)]

Kitagawa (2010, 2012) introduced multi-wavelength single shot interferometry for areal surface measurement. The concept is based on using three colours simultaneously to generate colourful fringes and a colour CCD to compose the fringe pattern at the RGB components (see Figure 2.22).

The additional colour information was used to extend the measurement range beyond the single wavelength interferometer, which can potentially overcome the phase ambiguity problem. The vertical resolution is within a few nanometres. The interesting thing about this technique is the crosstalk compensation. The authors demonstrated a sufficient mathematical approach to compensate the crosstalk between colours by calibrating the system offline and calculating the crosstalk parameters. However, the main drawback of this method is that it requires prior knowledge about the surface to estimate the surface height with an accuracy of 95% before calculation. The interference intensity bias, **a**, and the visibility, **b,** are also needed to be estimated to calculate the phase. In order to measure a moving surface, the estimated **a** and **b** should be kept a constant during the surface scanning, which is a condition that might not be satisfied in certain manufacturing applications.

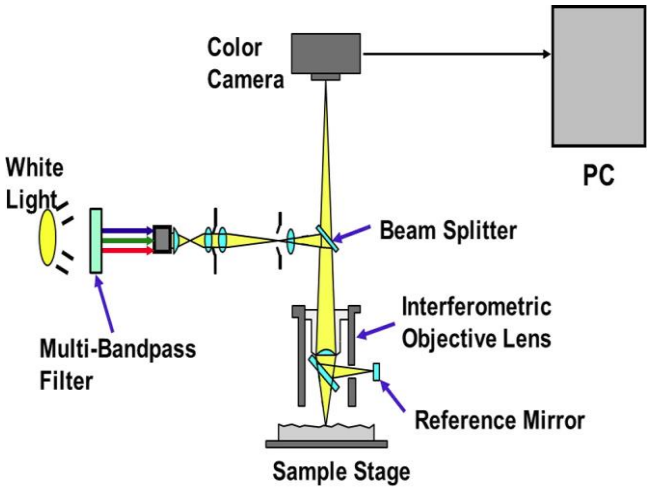

Figure 2.22 Multi-wavelength single shot interferometry [adopted from (K. J. J. o. E. I. Kitagawa, 2012)]

2.6 Summary

Surface geometry consists of roughness, waviness, and form. The surface metrology can investigate the quality of the manufacturing, predict the functional performance of the work pieces, and ultimately control the manufacturing process by reporting the surface parameters to the operator to tune the manufacturing for optimisation.

Machine vision using Cameras provides fast measurement and can be integrated at any point in the production chain. However, camera vision techniques have one common limitation, in that they just offer 2D information that is impossible to reconstruct into 3D surface topography. Hence, surface metric information cannot be obtained. In addition, machine vision can often include unwanted information captured from the reflection of the back-side of a transparent sample (such as thin film barriers of flexible electronics), causing errors in the inspection process (Kimbrough *et al.*, 2015).

Focus variation can be used for determining depth information to measure rough surfaces, depending on the sharpness of the image that is determined by examining the contrast of neighbouring pixels at focal positions. The roughness of micro- and nanostructures can be measured both in profile-mode and as areal, based on true colour information. The slope measurement of focus variation can exceed 80°. However, the method is not suitable for measuring specular surfaces.

A confocal microscope provides a high lateral resolution. The operating principle of the confocal microscope allows for the detection of the strongest signal depth to be measured. Thus, confocal microscope systems are practically suitable for measuring smooth (specular) surfaces. A common drawback of focus variation and confocal microscopy is the considerable amount of data required for each FOV. This makes it not suitable for in-process measurements, nor for the measurement of moving objects.

In general, interferometric techniques provide a high vertical measurement resolution, better than focus variation and confocal methods. These techniques are ideally suited for measuring smooth surfaces such as lenses and glass structures, while rough surfaces are difficult to measure using an interferometer because of the unwanted speckle interference.

A white light interferometer offers a high vertical resolution that can go beyond sun-nanometre with a 100-μm vertical range for areal measurement. However, this requires a large amount of data for each single FOV, which makes it unsuitable for in-process measurements or for the measurement of moving surfaces.

A wavelength-scanning interferometer provides areal measurements with a high vertical resolution. The wavelength scanning interferometer can be integrated with vibration compensation technique, which makes it suitable for applications within a production environment. However, it can only be used to static measurement due to the amount of data required.

Dispersive interferometry offers a single shot long profile measurement with a high vertical resolution, which makes it suitable for applications within the production environment, and it can be used for measuring moving surfaces. However, to construct a full field of view (areal) measurement, a continuous capturing is required during the surface movement.

The current single-shot interferometers are operated by single wavelength and are based on the phase shift technique, which provides high measurement accuracy. The vertical measurement range, however, is limited by $\lambda/4$. To extend the measurement range, multi-wavelength illumination sources are required to implement a synthetic wavelength. The multiple wavelengths information's is used to extend or remove the height ambiguity. The fringe order method is used with synthetic wavelength interferometer to retrieve the measured surface within few nanometres accuracy. The polarised optics is used to obtain the required phase shift without mechanical movements. The summary of surface metrology techniques is illustrated in Table 2.1

Table 2.1 Comparison of surface metrology techniques

Measurement Technique	Arial	Metric Information	Single-shot	Height Ambiguity Limitation
Machine Vision	Yes	No	Yes	Not applicable
Confocal Microscopy	Yes	Yes	No	No (limited by the mechanical scanning range only)
Focus Variation	Yes	Yes	No	No (limited by the mechanical scanning range only)
Phase Shifting Interferometer	Yes	Yes	Yes	Yes (limited by λ/4 for single wavelength)
Wavelength Scanning Interferometer	Yes	Yes	NO (equipped with vibration compensation)	No (limited by objective depth of focus only)
Dispersive Interferometry	No (profile measurement only)	Yes	Yes	No (limited by objective depth of focus only)

Chapter 3: Polarising Interferometer

3.1 Introduction

Phase shifting techniques are common in digital holography, fringe projection, interferometry, and other techniques because they offer sufficient information to retrieve the surface topography with high accuracy. As discussed in chapter 2, the interferometer represents a powerful instrument in surface metrology, especially for in-process measurements. Several methods have been developed over the years to produce instant phase shifts in a single shot interferometer. Two common techniques are used to build a single shot phase interferometer. The first technique is based on using multiple cameras to record several frames at different phases (Koliopoulos, 1992), while the second one is based on using a pixelated phase mask with a single camera (North-Morris *et al.*, 2004). The employment of the polarised optics to produce the required phase shift has the advantage of absent any mechanical scanning during the measurement. A polariser filter and quarter waveplate are the most used in polarised interferometry to achieve the required phase shift. Since a single shot polarising phase shift interferometer is the point of interest of this thesis, this chapter presents the basic concepts of the electromagnetic wave, polarisation, interference principle and polarising interferometer, all of which provide the required knowledge for the following chapters.

3.2 Light and Polarisation

Light is considered as a transverse of the electromagnetic wave, which consists of electrical and magnetic fields that are oscillating perpendicular to the direction of propagation as shown in Figure 3.1. For simplicity's sake, it is convenient to consider the electrical field only in the mathematical expressions. The wave of the electrical field can be described at any point using Equation (3.1) (Hariharan, 2010)

$$\mathrm{E} = \mathrm{E_o} cos(k\mathrm{z} - \omega\mathrm{t}) \qquad (3.1)$$

Where $\mathrm{E_o}$ is the wave amplitude, $\omega = 2\pi f$ is the angular frequency, $k = \frac{2\pi}{\lambda}$ is the wavenumber, λ is the wavelength and z is the direction of propagation. Light field E oscillates at rate 3.4×10^{14} Hz to 7.5×10^{14} making the actual field impossible to detect with any instrument. The irradiance is what can be measured by using optical sensors (e.g. cameras or eye). The irradiance is the amount of light that denoted by the average energy per unit time.

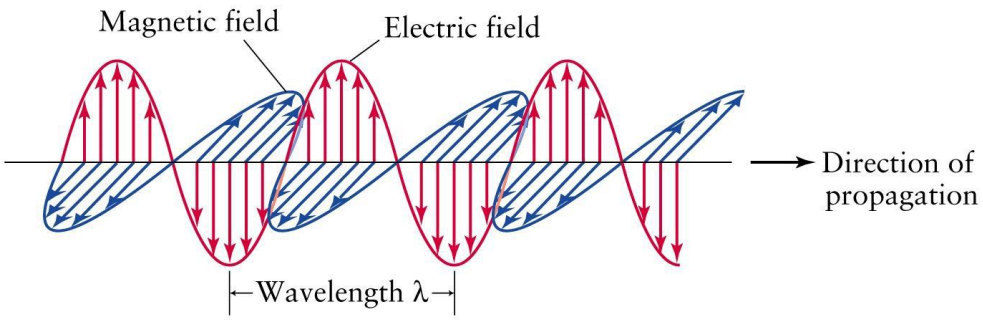

Figure 3.1 Electromagnetic wave [Adopted from (Arashlouzadeh, 2014)]

The direction of oscillation of the electrical field is called the polarisation. Polarised light can be classified into three types, namely linearly polarised, circularly polarised, and elliptically polarised light. However, natural light consists of many waves with different polarisation oscillations, which is called randomly polarised light.

Linearly polarised light, where the electrical field of the wave is kept to a single plane along the direction of propagation, as shown in Figure 3.2 (a). In the linearly polarised light, the decomposition of the electrical wave can be presented by two orthogonal optical disturbance waves (horizontal and vertical upon the direction of propagation) with phase shift equal to zero or odd integer multiple of $\pm \pi$.

Another case of particular interest arises when both orthogonal optical disturbance waves have an equal amplitude but with phase shift equal to $\theta = -\pi/2 + 2m\pi$, where $m = 0, \pm1, \pm2$. The resulting electric field circularly rotates around the direction of propagation as shown in Figure 3.2 (b). When the electrical field rotates counter-clockwise, it is defined as a left-hand circular polarisation (L), while it is defined as a right-hand circular polarisation (R) when it rotates clockwise. The circular polarised light can be transformed to elliptical polarised light, as shown in Figure 3.2 (c), if the orthogonal optical disturbances of the electrical field have different amplitudes. Finally, the state of polarisation can be defined based on the plane in which the electric field of a light is oscillating as the follows:

- Horizontal and vertical polarisation state for linear polarised light.
- L and R states for circular polarised light.
- E state for elliptical polarised light.

The P state can be obtained from the superposition of L or R state, and the same occurs in the E-state (Hecht, 2016).

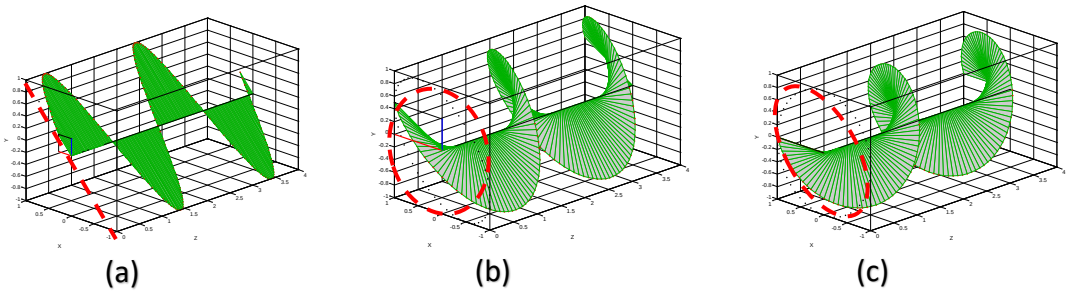

Figure 3.2 Polarisation statues of light (a) linearly Polarised (b) circularly Polarised (c) elliptically Polarised

3.3 Polariser

The polariser represents an essential part in a polarised interferometer. The linear polariser manipulates the polarisation state of the incident light into a form of polarised light. Polarisers are manufactured in several configurations, but the physical mechanisms of these configurations are classified into four groups: scattering; dichroism or selective absorption; reflection; and birefringence or double refraction (Hecht, 2016). The dichroic polariser is of interest in this thesis and is based on transmission and absorption of polarised light for specific wavelengths range (thorlabs, 2019). Dichroic film polarisers provide high absorption of the rejected polarisation, which is ideal for low-power applications.

Polarisers come with a range of performance and specifications. It is important to explore the specifications of the polarisers that used in the proposed interferometer, because the phase shifting mechanism is achieved by the polarisation. It has been reported by (Matt *et al.*, 2005) that error in phase values can occur due to polarisers performance. In general, the performance of polarisers, using any type, can be defined by several parameters such as diattenuation, transmission, and contrast ratio.

The diattenuation (polarisation efficiency) for a perfect polariser is equal to 1.0, where the polariser passes the total radiation that parallels with the polariser degree and prevents whole radiation that has cross polarisation state with the polariser orientation. The diattenuation of the polariser is wavelength-dependent and can be calculated by Equation (3.2).

$$D_\lambda = \frac{T_{max_\lambda} - T_{min_\lambda}}{T_{max_\lambda} + T_{min_\lambda}}, \tag{3.2}$$

where the maximum transmission (T_{max}) occurs when polarisation state of the incident beam is parallel to the degree of polariser , the minimum transmission of polariser (T_{min}) obtained when the axis of the polariser degree is in 90^o with plane of polarisation of the incident beam (Chipman, 1995) as shown in Figure 3.3.

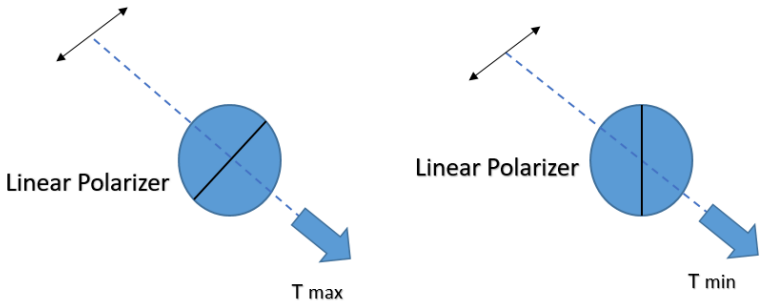

Figure 3.3 Maximum (T max) and minimum (T min) transmitted light from a polariser

The contrast ratio (extinction ratio) is the second property of the polariser that is often used to indicate the polariser quality. The contrast ratio is calculating by dividing the transmittance of light from two polarisers with their transmission axis parallel ($T_{parallel}$) onto the transmittance of the same two polariser having crossed axes ($T_{perpendicular}$), as shown in Equation (3.3) (Crabtree, 2007).

$$C_{R\lambda} = \frac{T_{parallel_{\lambda}}}{T_{perpendicular_{\lambda}}} \tag{3.3}$$

Transmission is the percentage of the transmitted light, which is linearly polarised to the direction of the polarisation axis or the transmission of unpolarised light through the polariser. Transmission can be classified into the parallel transmission and cross-transmission. Parallel transmission is the percentage of randomly polarised light that transmits through two polarisers having the same rotation degree. While the crossed transmission is the transmission of randomly polarised light through two polarisers with a cross axis (Edmund Optics, 2019). Table 3.1 illustrates the comparison between current commercial polarisers

Table 3.1 Different polariser types have different performance characteristics. (*) marks the transmission for light that is aligned with the polarisation axis of the polariser [adopted from (thinklucid, 2019a)]

	CRYSTALLINE	DICHROIC GLASS	DICHROIC POLYMER	DIELECTRIC BEAMSPLITTING	WIRE GRID
Clear Aperture (mm)	5 - 10	1 - 30.4	10 - 50+	10 - 20	1 - 200
Acceptance Angle	± 5°	± 20°	± 10°	± 2°	45°
Part Cost	$500 - $5000	$500 - $5000	$1 - $1000	$100 - $5000	$100 - $5000
Contrast Ratio	10^5	10^6	10^4	10^3	10^4
Damage Resistance (per cm^2)	25 - 30 W	1 W	1 W	500 W	50 KW
Mechanical Thickness (mm)	22.5 - 38.1	0.5 - 6.9	3.3 - 12.7	12.7 - 25.4	0.7 - 1.5
Transmission*	85 - 95%	39 - 98%	45 - 90%	95%	70 - 85%
Wavelength Range (nm)	320 - 2300	325 - 2000	325 - 1800	440 - 1600	400 - 2000+

Malus's law is mainly used to theoretically determine the irradiance/intensity of light transmitted by a polariser. Etienne-Louis Malusin 1809 stated that when a polariser is placed into the path of polarised light, the intensity (I) of emerged light from the polariser is given by Equation (3.4)

$$I = I_o\,(\cos \emptyset)^2 \qquad (3.4)$$

Where I_0 is the intensity of the incident light, and $\emptyset$ is the angle between the incident light's polarisation plane and the axis of the polariser.

This Equation clearly shows that 100% transmission is achieved when $\emptyset = 0$. When cross-polarised, the transmission should be 0% output light. In the real world, 0% is never reached. In the case of unpolarised light with a specific intensity, I_0 passes through the polariser at any degree of polarisation. The intensity of the emerging light will be 50% of I_0. Malus's law was used in thesis, see section 5.7.2, to study the intensity variation in four optical detection arms, where the polarisers are used (Edmund Optics, 2019).

3.4 Quarter Waveplate

The birefringence material is the material which has double refractions with a larger and smaller index of refraction. The double refraction crystal behaviour is due to the anisotropic atomic structure of the lattice that can respond to different polarisation statues of the light waves. This will lead to anisotropic index of refraction at a given frequency range as shown in Figure 3.4.

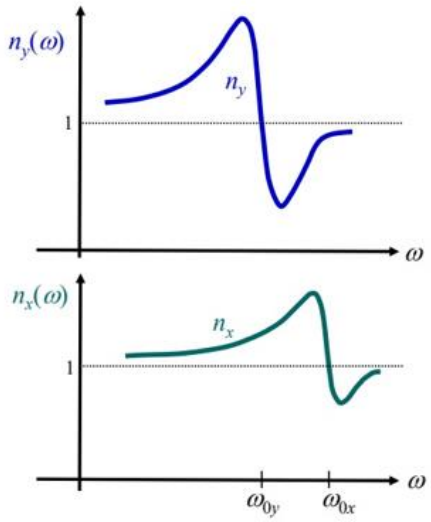

Figure 3.4 Birefringence material: refractive index versus frequency along two axes in a crystal.

Uniaxial crystals have two refractive indexes for light, where the first one (n_e) is polarized along the optic axis where the atoms are arranged symmetrically and the second one (n_o) the light is polarized in either of the two directions perpendicular to it. Calcite is an example for a common birefringent material with n_o= 1.6584 and n_e= 1.486 at 589.3nm (Fang, 2014). The light that is polarised along the optic axis is referred to as the extraordinary ray, and light polarised perpendicular to the optical axis is called the ordinary ray, as shown in Figure 3.5. These polarisation directions represent the principal crystal axes.

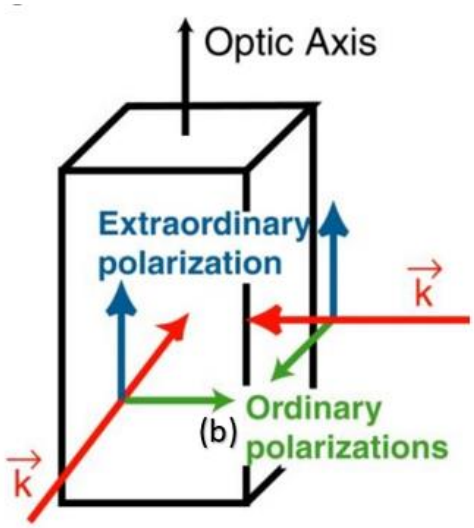

Figure 3.5 Birefringence crystal: extraordinary ray and ordinary ray. Adopted from (Fang, 2014)

For example a quarter-wave plate can be used to convert a linear polarisation light beam to a circularly polarised beam, as shown in Figure 3.6 by using the properties of double refraction. In order to compensate the phase difference, two sliding wedges made of the uniaxial crystal are often used to vary the thickness. The phase shift between the extraordinary and ordinary waves depends

on the properties of the material, the thickness of waveplate and the wavelength of the light as given in Equation (3.5):

$$\Delta\varphi=\frac{2\pi d(n_{e}-n_{o})}{\lambda} \quad (3.5)$$

Where n_e and n_o are the refractive indexes along the extraordinary and ordinary axis, respectively; λ is the wavelength, and d is the thickness of the quarter wave plate. However, studies have reported that error can occur at the phase-shift due to manufacturing constraints (Matt *et al.*, 2005)

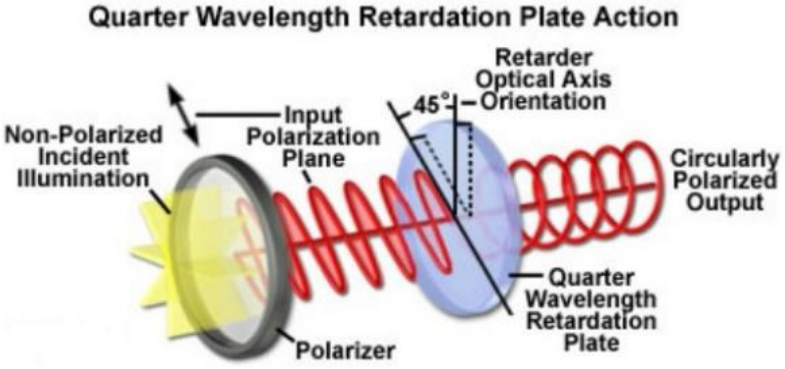

Figure 3.6 QWP (45°) [Adopted from (Crop., 2018)

3.5 Jones Presentation

The interaction between polarisers and a polarised light can be represented mathematically by matrices and arrays invented by R. Clark Jones in 1941. The polarising optical components can be described by 2 × 2 Jones matrices, as shown in Table 3.2, while the polarised light can be described by 2 × 1 Jones vectors, as shown in Table 3.3 (Collett, 2005; Sharma, 2006).

Table 3.2 Jones matrix

Linear Optical Elements	Jones Matrix
Horizontal linear Polariser	$\begin{bmatrix}0 & 0\\0 & 1\end{bmatrix}$
Horizontal Vertical Polariser	$\begin{bmatrix}1 & 0\\0 & 0\end{bmatrix}$
Linear Polariser at +45°	$\begin{bmatrix}1 & 1\\1 & 1\end{bmatrix}$
Quarter waveplate fast axis vertical	$e^{\frac{i\pi}{4}}\begin{bmatrix}0 & 0\\0 & -i\end{bmatrix}$
Quarter waveplate fast axis horizontal	$e^{\frac{i\pi}{4}}\begin{bmatrix}0 & 0\\0 & i\end{bmatrix}$
Quarter waveplate fast axis 45°	$e^{\frac{i\pi}{4}}\begin{bmatrix}i & 0\\0 & i\end{bmatrix}$

Table 3.3 Jones vector

State of Polarisation	Jones vectors
Horizontal P-state	$\begin{bmatrix}1\\0\end{bmatrix}$
Vertical P-state	$\begin{bmatrix}0\\1\end{bmatrix}$
P-state +45°	$\begin{bmatrix}1\\1\end{bmatrix}$
P-state -45°	$\begin{bmatrix}1\\-1\end{bmatrix}$
R-state	$\frac{1}{\sqrt{2}}\begin{bmatrix}1\\-\mathrm{i}\end{bmatrix}$
R-state	$\frac{1}{\sqrt{2}}\begin{bmatrix}1\\-\mathrm{i}\end{bmatrix}$
L-state	$\frac{1}{\sqrt{2}}\begin{bmatrix}1\\\mathrm{i}\end{bmatrix}$

As such, an orthogonally polarised light can be represented by two linearly or circularly polarised waves, which are oscillating in perpendicular plans. The two orthogonal polarised waves can be expressed using horizontally $\begin{bmatrix}1\\0\end{bmatrix}$ and vertically $\begin{bmatrix}0\\1\end{bmatrix}$ polarised vectors, or right and left circularly polarised waves, $(\frac{1}{\sqrt{2}})\begin{bmatrix}1\\j\end{bmatrix}$ and $\left(\frac{1}{\sqrt{2}}\right)\begin{bmatrix}1\\-j\end{bmatrix}$ (Saleh & Teich, 1991)

The exemplar Jones presentation is a summation of orthogonal polarised beams components to produce a linearly polarised light at 45°, as illustrated in Equation (3.6). In the same manner, a linearly polarised light at 45° can be produced with greater amplitude by adding two circularly polarised light rays after passing a linear polariser, as illustrated in Equation (3.7).

$$E=E_H + E_V = \begin{bmatrix}1\\0\end{bmatrix} + \begin{bmatrix}0\\1\end{bmatrix}=\begin{bmatrix}1\\1\end{bmatrix} \tag{3.6}$$

$$E=E_R + E_L = \left(\frac{1}{\sqrt{2}}\right)\begin{bmatrix}1\\j\end{bmatrix} + (\frac{1}{\sqrt{2}})\begin{bmatrix}1\\-j\end{bmatrix}=(\frac{2}{\sqrt{2}})\begin{bmatrix}1\\0\end{bmatrix} \tag{3.7}$$

3.6 Light Interference Principle

Thomas Young is the first one who discovered the interference fringe in 1802 using double slit experiment, while the first interferometer was implemented by Albert A. Michelson in 1882, which base on the superposition of two light beam originating from the same light source.

The principle of superposition is based on the sum of two electrical fields E_1 and E_2 , given in Equation (3.1), at a specific point and frequency. The principle is well documented in many books (Feynman *et al.*, 2011; Hariharan, 2003; Saleh *et al.*, 1991) and can be written as Equation (3.8). The resultant electrical wave E_{sum} has the same frequency, as the frequency of photons corresponding to its energy does not change.

$$\overrightarrow{E_{sum}} = \overrightarrow{E_1} + \overrightarrow{E_2} \tag{3.8}$$

The irradiance can be measured using a photo-detector. As mentioned earlier in this chapter, by considering the time average for the magnitude of the electrical field for the superposed waves, the irradiance is proportional to the square of the amplitude of the electrical field, as given in Equation (3.9).

$$I_{sum} = < \overrightarrow{E_{sum}}^{\,2} > \tag{3.9}$$

where I_{sum} is the light intensity and it is equal to the squared of the time average of the magnitude of the electrical-field as shown in Equation (3.10).

$$I_{sum} = \overrightarrow{E_1}^{\,2} + \overrightarrow{E_2}^{\,2} + 2\overrightarrow{E_1}.\overrightarrow{E_2} \tag{3.10}$$

The result can be rewritten as Equation (3.11)

$$I = I_1 + I_2 + 2I_{12} \tag{3.11}$$

Where I_1 *and* I_2 are constant, and I_{12} is the interference term. The interference term can be represented in Equation (3.12)

$$I_{12} = \overrightarrow{E_1}.\overrightarrow{E_2} = E_{01}cos(\omega t + kz + \varphi_1) \times E_{02}cos(\omega t + kz + \varphi_2) \tag{3.12}$$

Taking the time average for Equation (I_{12}), the result can be simplified in the form of Equation (3.13).

$$I_{12} = \overrightarrow{E_1}\overrightarrow{E_2}\cos(\theta) \tag{3.13}$$

Otherwise, it can be re-written in the form of Equation (3.14)

$$I_{12} = 2\sqrt{I_1.I_2}\ \cos(\theta) \tag{3.14}$$

As such, the resultant of total irradiance can be given as written in Equation (3.15)

$$I_{12} = I_1 + I_2 + 2\sqrt{I_1.I_2}\cos(\theta) \tag{3.15}$$

The superposition of two electrical fields in the interferometer is constructing an interference pattern known as fringe. There are different types of fringe such as such as Brewster, Fizeau, and Newton fringes. The fringe according to Equation (3.15) has a sinusoidal pattern that represents the destructive and constructive interferences fringe. The fringe visibility is defined by Equation (3.16):

$$\nu = \frac{(I_{max} - I_{min})}{(I_{max} + I_{\min})} \tag{3.16}$$

Here, ν is the visibility of the fringe, I_{max} is the maximum fringe intensity, and I_{min} is the minimum fringe intensity. In general, the visibility is a dimensionless number having the value between 0 and 1. In practice, it is difficult to obtain a maximum visibility equal to 1 in the

interferometers, because the reference arm and the measurement arm usually have different reflectivity. Further, the visibility is also related to the coherence between two optical fields.

The word coherence explains the capability of radiant to produce interference phenomena. (Fowles, 1989; Saha, 2011).

$$l_c = \frac{\lambda^2}{\Delta\lambda} \tag{3.17}$$

Where $\lambda$the central wavelength of the light is source, and $\Delta\lambda$ is the bandwidth. According to Equation (3.17). For a broadband light source, the coherence length is short. Table 3.4 demonstrates the relationship between the coherence length and spectral wavelength bandwidth (also known as line-width) based on the Gaussian and Lorentzian spectral form

Table 3.4 The coherence length and spectral linewidth for the filtered light

Spectral profile	Coherence length (*Lc*)	λ=643nm λFWHM=1.7n m	λ = 543 nm λFWHM=1.35 nm	λ = 453 nm λFWHM= 0.88 nm
Gaussian	≈ 0.42 (λ^2/λFWHM)	Lc ≈ 102 μm	Lc ≈ 91.7 μm	Lc ≈ 97.9 μm
Lorentzian	≈ 0.66 (λ^2/ λFWHM)	Lc ≈ 160 μm	Lc ≈ 144 μm	Lc ≈ 153 μm

The temporal coherence time (τ_c) is the maximum transit time difference for excellent visibility. It is directly related to the coherence length as described in Equation (3.18) (Saha, 2011)

$$\tau_c = \frac{l_c}{c} = \frac{\lambda^2}{c\Delta\lambda} \tag{3.18}$$

In a perfectly coherent light, the fringe visibility is supposed to be constant along the optical path. However, for quasi-monochromatic light sources, the visibility is related in direct relation to the complex degree of the coherence length, as shown in Equation (3.19) (Milonni & Eberly, 2010). This is an alternative method for determining the fringe visibility that is defined in Equation (3.16).

$$v = \frac{2\sqrt{I_1 I_2}|\gamma|}{I_1 + I_2} \tag{3.19}$$

where γ is the modulus of the complex degree of coherence. If $I_1 = I_2$, and the visibility is equal to$|\gamma|$.From the definition of visibility, it also holds true that $0 \leq |\gamma| \leq 1$.

Therefore, the fringe sinusoidal mathematical model given Equation (3.15) can be modulated by$|\gamma|$, introducing a coherence envelop function to the pattern as given in Equation (3.20). The coherence length is practically calculated at $1/e^2$ of the coherence envelope.

$$I = I_1 + I_2 + 2\sqrt{I_1 . I_2}\,|\gamma|\cos(\theta) \tag{3.20}$$

3.7 Polarising Interferometer

The light interference in the polarising interferometer is achieved by using polarisation elements such as linear polarisers and quarter waveplate to produce a polarised light in which wavefront propagate on the same plane (i.e. coplanar) and thus can interfere. The first polarising interferometer, which is based on two-beam polarisation interference scheme was introduced by Jamin 1868 (Jamin, 1868).

In 1930, Labeledeff introduced the first interference microscope using the beam-sharing design based on the Jamin interferometer (Bass *et al.*, 2010; Lebedeff, 1930; Wierzba, (2017)).

The polarising interferometers often use polarisation equipment to produce a phase shift between the reference wavefront and measurement wavefront to avoid mechanical or wavelength scanning mechanism. Such systems were described by (Hettwer *et al.*, 2000). The polarising interferometer was subject to intense research as its scope of applications has increased dramatically. The main current research is concentrated on using new states of polarisation and new materials (Wierzba, (2017)).

North-Morris *et al.* (2004) introduced a compact novel polarising phase shift interferometer using a pixelated phase mask polariser. Figure 3.7 illustrates a unit cell consisting of a pixelated polariser oriented at 0º, 45º, 90º, and 135º. Produce an phase-delay between the test and reference wavefront at each pixel and then bring the wavefront on the same propagation plane to interfere. Interferes the transmission light. The test (T) and reference (R) wavefront are originally generated by Michelson interferometer.

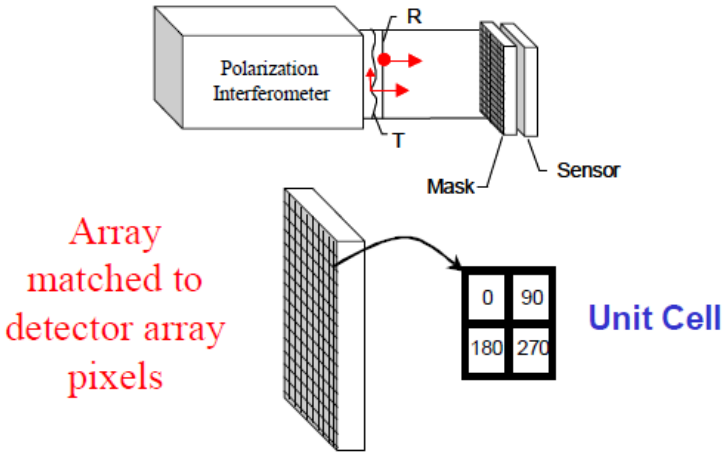

Figure 3.7 Pixelated polarised interferometer: ; R, reference wavefront T, test wavefront [adopted from (North-Morris *et al.*, 2004)]

$$I_{(x,y)} = \frac{1}{2}(I_1 + I_2 + 2\sqrt{I_1 I_2}\,|\gamma|\cos(\Delta\theta_{(x,y)} + 2\alpha_p) \qquad (3.\ 21)$$

Where α_p is the angle of the polariser with respect to the x, y plane.

According to the given unit cell orientation shown in Figure 3.6, the phase shift angles between the wavefront T and R are 0^o, 90^o, 180^o, and 270^o. As such, four intensity values shifted at the given phases can be captured at once for a specific pixel on the sample. Thus, any phase-shifting algorithm to obtain the surface height can process the intensity values.

3.8 Interferometric Configurations

The interferometric configuration can be classified into four types: Michelson, Mirau, Linnik, and Fizeau, as shown in Figure 3.8. Apart from Fizeau, the reference mirror and the test surface are placed at the best focal plane to obtain the largest fringe contrast.

In the Michelson configuration, shown in Figure. 3.8 (a), the collimated beam is focused first by the objective lens, and then it is separated by a beam splitter to the reference and measurement arms. A low-magnification objective with a long working distance and low numerical aperture is only suitable for this setup. As such, it is suitable for applications that require long working distances (Daniel, 2007). Several companies, like Polytec and Nikon, offer a commercial Michelson configuration with 5x magnification and lower.

Mirau has a compact size, as shown in Figure. 3.8 (b). It consists of two small glass plates installed between the test and objective surface. The first plate is equipped with a small reflective piece that represents the reference mirror, and the second plate has one coated side that functions as a beam-splitter. The Mirau interferometer is suitable for mid-range working distance applications with magnifications between 10x and 50x.

A Linnik setup is consist of a beam-splitter and two matching microscope objectives installed in reference and measurement arms, as shown in Figure 3.8 (c). The configuration allows of using high magnification lenses, and achieves higher lateral resolution compared to other configurations. However, balancing the two arms in Linnik requires higher adjustment criteria as more optical surfaces are presented. Furthermore, the configuration can involve dispersion effect when a broadband light source is used (Pförtner & Schwider, 2001). Linnik systems are usually used with a high-magnification objective lenses. They are suitable for applications that require long working distances or high lateral resolution. The three configurations discussed above can be aligned to have equal-path interferometer arms, allowing best fringe contrast at zero optical path (Daniel, 2007).

The Fizeau interferometer shown in Figure 3.8 (d) is an unequal path interferometer and illuminate with long coherence length source. The Fizeau are therefore not suited for white light interferometry, while it is well known for dispersive and monochromatic interferometry. In the Fizeau interferometer, the objective lens produces a collimated beam for the test surface while imaging the surface (Daniel, 2007).

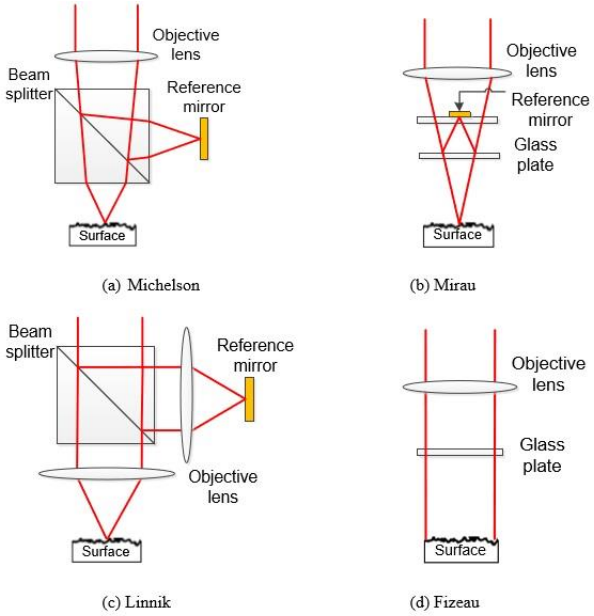

Figure 3.8 Interferometer objective configuration [Adopted from(Hussam, 2013)]

3.9 Summary

The light as an electromagnetic wave with random polarisation can be polarised by using linear polarisers. A quarter waveplate can introduce a 90^o phase-shift between the light components by passing an orthogonal light or polarised light at 45^o into birefringence material that has double refraction. The polarisation can be presented mathematically using Jones vectors and matrices. Moreover, the polarisation can be used to shift the interference fringe phase without using a time-variant conventional phase shifting mechanism.

The interference fringe is a function of phase change. The sinusoidal form of the interference is modulated by the coherence envelope, and the maximum fringe contrast can be achieved at the peak of the coherence envelope, where the optical path difference (OPD) equal to zero. The interferometer can be implemented using different optical configurations, namely the Michelson, Mirau, Linnik, and Fizeau. The information provided in this chapter will be applied in following chapters.

Chapter 4: Methodology and Development Stages of MPI

4.1 Introduction

This chapter briefly describes the methodology and development stages of multi-wavelength single-shot polarized interferometer (MPI) for embedded metrology. The MPI development is divided into two main stages. The first stage describes a proof-of-concept experimental works based on implementing mechanical/non-mechanical phase shifting mechanism and fringe analysis simulations. This stage forms the base to capture initial colour interferograms in order to be analysed by the simulated algorithms, hence paving the way toward the second step, which is developing the final optical setup (MPI). The MPI development is described in detail in chapters five, six and seven respectively.

One of the applications for single shot MPI is measurement of the surface texture of barrier tapes in organic light-emitting diode (OLED) display technology that applied in screens, including TV, smartphone, and tablet. This technology requires protection tapes (or barrier layers) to protect the OLEDs from oxygen and humidity. The tapes, shown in Figure 4.1, are subject to extreme demands as the water vapour transmission rate (WVTR) required for OLED encapsulation should be 100,000 times lower than, for example, milk cartons in the food industry (Geest, 2014). Hence, any defect in the micro-scale or even nano-scale in tape barrier will reduce efficiency of the OLED. The OLED production speed is considered as parallel manufacturing and can reach up to tens of meter square per minute. By using an in-process inspection sensor for this industry, the measurement throughput should not only cope with environmental disturbances but also with the manufacturing speed.

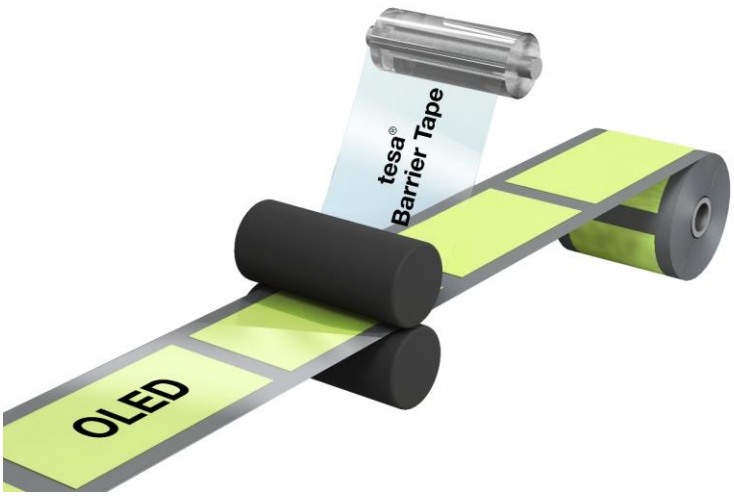

Figure 4.1 Barrier tapes for OLED encapsulation [Adopted from (Geest, 2014)].

4.2 Target Specification

This thesis investigates a novel interferometry system for in-process measurement. The target specification is derived from the literature review based on the industry requirement and the performance of the optical instruments in embedded metrology. Therefore, the target specification shall be: high measurement speed with a fraction of second duration time, large vertical measurement range (greater than few micrometres), and fine resolution better than few nanometres. The interferometry should perform accurate measurement in presence of environmental disturbance without the need for an isolating room, in addition to measurement of moving objects. These specifications can be achieved by designing a multi-wavelength single-shot polarising interferometer (MPI).

4.3 Single-Shot Multi-wavelength Polarising Interferometer (MPI)

The MPI configuration is shown in Figure 4.2. The system optical setup, algorithms, and results are described in detail in chapters five, six and seven respectively.

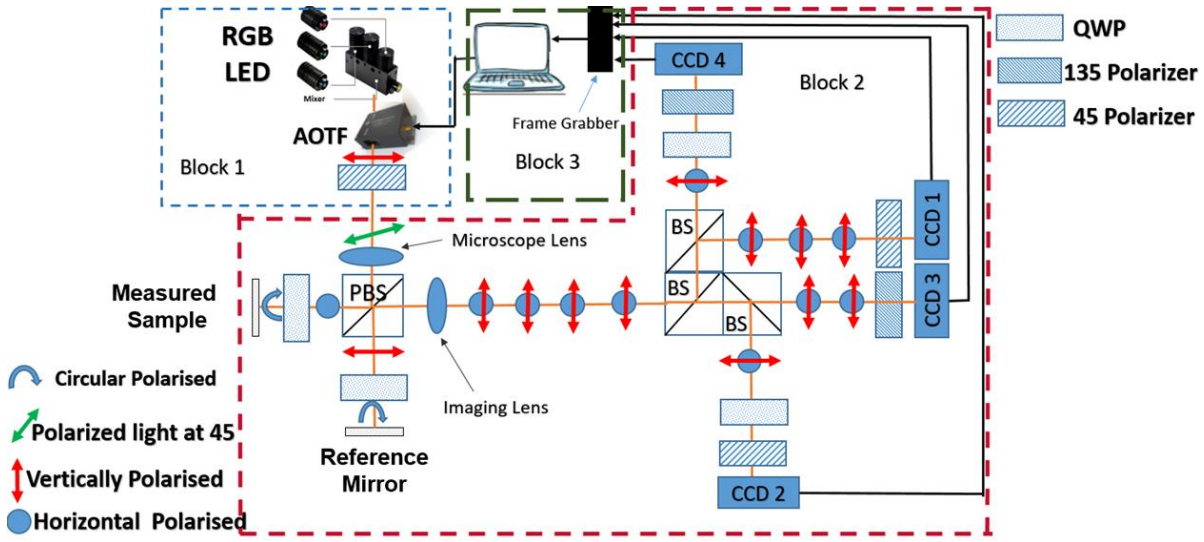

Figure 4.2 Schematic of the MPI Interferometry

The measurement data produced by MPI were captured by identical four-color CMOS cameras. The four cameras were connected to a frame grabber card to trigger them simultaneously. The polarisation optics in front of each camera can shift the phase at a certain degree (e.g. 0^{o}, 90^{o}, 180^{o}, 270^{o}). Table 4.1 can be suggested as a target specification for MPI which is compared to two well-developed interferometers for in-process surface metrology.

Table 4.1 Comparison between commercial instruments and target specification of MPI

Specifications	4D (Creath K, et al. 2012).	WSI (Muhamedsalih, H., 2013)	MPI Target specification
Area (objective dependent)	4 mm^2	0.5–1.8 mm^2	2–4 mm^2
Vertical noise level	Sub-nm	15 nm	≤ 1 nm
Vertical range	< 1 µm	Depth of focus dependent, e.g. 14 µm for 5X	Depth of focus dependent, e.g. 14 µm for 5X
Lateral resolution (objective dependent)	Diffraction limited 2 µm	Diffraction limited 2.98 µm (5X)	Diffraction limited 2.98 µm (5X)
Typical measurement time	120 ms (single exposure time)	3.7 s	Millisecond-scale (single exposure time)
Stabilization bandwidth	Vibration Insensitive (exposure time dependent)	< 300 Hz	Vibration insensitive (exposure time dependent)

4.4 Towards MPI Development: Proof of concept and simulations

The MPI development steps is started by reviewing the literature, simulating colour interference patterns or interferograms, and implementing mechanical (using piezo translation stage) and non-mechanical (using wedge layout) phase shift interferometers to acquire phase shifted colour interferograms. These steps validate the concept of shifting three colour interferograms can extend the measurement range beyond single wavelength λ/4 ambiguity limitation and maintaining the measurement resolution at the same time. This proof-of-concept steps pave the way towards finally implementing multi-wavelength single shot polarising interferometry. These MPI development steps are shown in Figure 4.3.

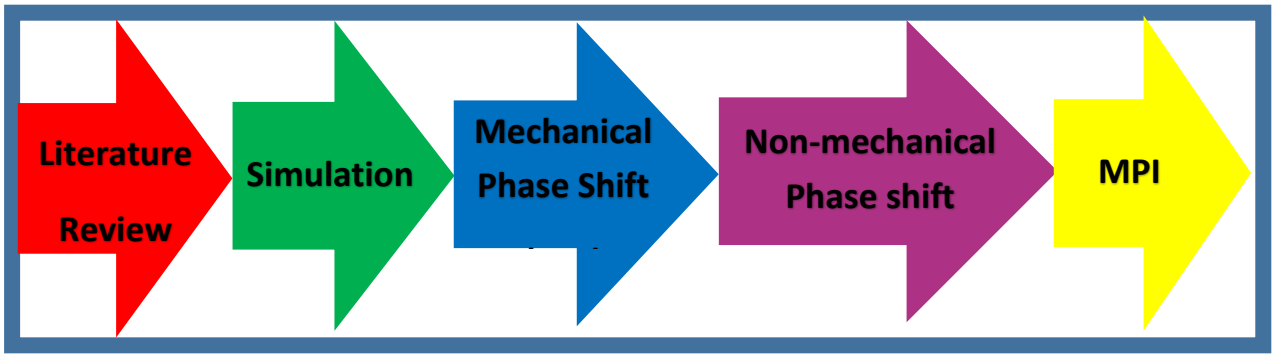

Figure 4.3 MPI development steps

One way to avoid the cost and time-consumption in MPI implementation is to conduct simulations of the system, so as to enable author to understand MPI performance without testing the system in the actual world. In the simulation step, Matlab software is used to build a mathematical model that includes most parameters, such as, measured height, intensity for the three colours, and phase value, upon which it can generate interferograms in virtual form as explained in the Appendix A. The algorithm has succeeded to measure a simulated tilted surface with a maximum height equal to 100 μm. Once the simulation has succeeded in determining the generated surface, a decision is made to proceed to implement the MPI.

The mechanical phase shift interferometer was implemented using simple equipment, such as, a gray camera and a piezoelectric transducer to obtain the required phase shift as explained in details in the appendix B. The purpose of this step is to achieve an initial result with the available equipment in the university laboratory. This step initially indicates the possibility of success or failure in the proposed project from the technical point of view. This step demonstrate that the phase shift interferometer (PSI) can measure surface heights greater than λ/4 without depending on the neighbourhood of pixels, if RGB information is included, however this stage depends on the mechanical translation of the reference mirror, and the required time for measurement means that this will lead to mechanical vibrations convolved into the data. This vibration will lead to a phase error, and that error will translate in retrieving the surface heights as given in the spikes and step jump.

Subsequently, a wedge interferometer step was implemented, based on a colour single camera, Michelson interferometer, and tilted flat surface. The surface height was calculated depending on the neighbour pixel (Takeda *et al.*, 1982). The purpose of this experiment is to obtain a deep understanding of the system performance when using the colour camera and Red-Green-Blue (RGB) light source and explained in details in appendix C. The investigation shows the technique can measure a tilted flat mirror using a single shot technique. The result demonstrates that the wedge interferometer using RGB illumination source can measure 1 μm surface height with nano-scale vertical resolution and without any artefact spikes as compared to mechanical interferometer.

The final step in the MPI development is the implementation of single-shot multi-wavelength polarising interferometer, which was independent of the surface inclination. The phase shifts are achieved by polarization optics and eliminate the need for any mechanical or wavelength scanning mechanism. Four-color cameras were used to capture four frames simultaneously.

4.5 Summary

Current industry demand for low cost photovoltaic power, novel displays has driven advance manufacturing in direction of high-throughput production in roll-to-roll format. The lift time and efficiency of these products depend on many parameters and one of them is the surface quality of the barrier layers (Giusca, 2013). The measurement and inspection technique should measure the defect with high resolution and provide 2D or 3D (i.e. areal) surface information.

This thesis aims to design a single shot polarising interferometer with extended axial measurement range in order to satisfy the industry requirements.

A feasibility study based on simulation and two mechanical/non-mechanical phase shift interferometer experiments are conducted as a proof-of-concept stages to implement the MPI. It has been found that using RGB as an illumination source can extend the vertical measurement range to several micrometres. The vertical measurement resolution can be equivalent to conventional PSI techniques, achieving nano-scale resolution. The mechanical phase shifting mechanism can introduce error to the measurement as the environmental disturbances can be significant and it also limits the measurement speed. Single-shot technique can be used to eliminate the environmental disturbances and also improve the measurement speed to cope with the manufacturing throughput.

Chapter 5: MPI Development and Operation

5.1 Introduction

This chapter introduces the operation principle of the multi-wavelength polarising interferometer (MPI). The operation principle is divided into three blocks as shown in Figure 4.2: block (1) is the Red-Green-Blue (RGB) illumination light source, block (2) is the polarising interferometer, and block (3) is the computing unit including algorithms. Blocks (1) and (2) are explained in detail in this chapter, while block 3 is explained in detail in chapter 6. This chapter also describes polarisation calculation, colour camera specification, experimental setup, intensity calibration, crosstalk compensation, and the SNR of the system.

5.2 MPI Overview

The MPI as a measurement instrument consists of an RGB light source filtered by AOTF, interferometer, and computing parts as detailed in Figure 4.2. The light source shown in block (1) provides the required selected wavelengths combinations. The interferometer, shown in block (2), produces the interference fringe between measurement and reference arms. The computing environment is shown in block (3), and it triggers the cameras to capture the interference fringes and control the driver of the AOTF. The subsequent sections present the basis of operation and data collection in MPI.

5.3 MPI light Source

One of the main MPI features is to extend the measurement range by using a multi-wavelength light source, generating multiple-phase maps at different wavelength for the phase unwrapping process. The primary white light components Red-Green-Blue (RGB) were selected with certain criteria to fulfil the axial range extension. These criteria are to be defined for the light source as most of optical imaging systems (Drexler & Fujimoto, 2008). The criteria are light bandwidth or linewidth, central wavelength and power.

The main features of the light that has been chosen to provide illumination to the MPI are: (a) sufficient output power at the three primary components of RGB; (b) narrow linewidth to increase the coherence length and reduce the crosstalk among the RGB components of the lights in the camera spectrum.

Two possible light sources have been found in the literature (Butler *et al.*, 2016). That can produce RGB light for illumination in the MPI by (a) combining three discrete laser sources (Red-Green-Blue), which is considered as an ideal solution regarding beam linewidth (FWHM); (b) three Gaussian wavelengths with full-width-half-maximum (FWHM) 10 nm are filtered from the LED broadband light source using conventional optical filters. The simulated intensity for three

lasers and filters of the RGB LED illumination, as detected by the interferometer camera at different OPD, are shown in Figure 5.1. It can be seen that visibility of the fringes is directly related to the linewidth. The visibility drops dramatically in the three filtered wavelengths due to short coherence length leading to low SNR at longer OPD, while the visibility whilst using a laser has a constant value over longer OPD with better SNR at longer OPD (linewidth of laser << linewidth of LED). However, the ultra-narrow linewidth given by lasers can produce unwanted interference speckle pattern, limiting the measurement application to only smooth surfaces. The ultra-narrow linewidth can highly increase the coherence length, resulting in the appearance of speckles due to diffusing reflection of laser radiation on optical rough surface.

In this study, a hybrid solution (Figure 4.2 - block 1) was developed by filtering out three discrete wavelengths from the RGB LED with narrow linewidth using an acousto-optic tuneable filter (AOTF). This filtering technique can tune the central wavelength of each RGB component to the best location that minimises cross talk between colours to it is lowest value, and at the same time obtains a maximum measurement range. The average filtered linewidth is 2 nm which avoids the speckle patterns during the measurement.

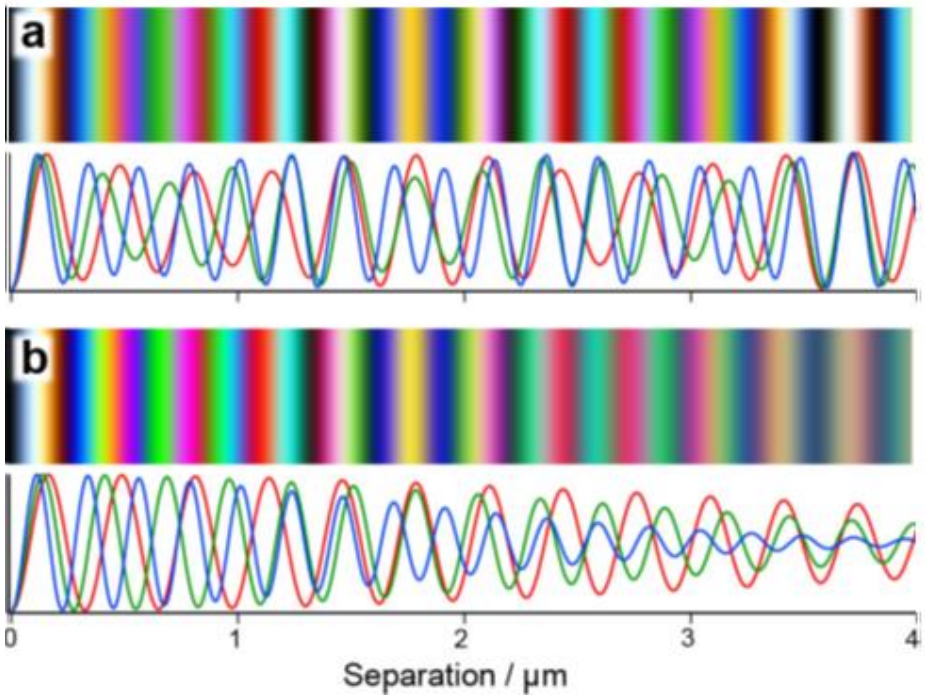

Figure 5.1 Colour intensity of light source for interferometer illumination (a) Three lasers of 450, 550 and 650 nm wavelengths in an idealised interferometer (b) Three filtered wavelengths representing coloured Gaussian peaks centred at same wavelength with FWHM of 10 nm [Adapted from(Butler *et al.*, 2016)]

A high-power light source is necessary because the illumination beam passes through several elements, which dramatically reduces the intensity of the illuminated light, such as, AOTF, polarisation optics, and three non-polarized beam splitters. The drop in light intensity requires an

increase in the camera exposure time, hence a reduction in data acquisition, and noise level amplification. Table 5.1 illustrates the measured light intensity at two different positions and shows the intensity loss. In the first position, the optical power meter (PPM, available from Thorlabs, Inc.) recorded the intensity of the light that emerges from the AOTF directly before the interferometer. In the second position, the power meter records the intensity in front of the cameras for the light bouncing from the reference arm and the measurement arm separately after passing all the optics shown in Figure 4.2.

Table 5.1 Light power recorded by a power meter at entrance and exit of MPI

λ	AOTF Output Power (µW)	Camera 1 Power (µW)	Camera 2 Power (µW)	Camera 3 Power (µW)	Camera 4 Power (µW)
630	1.85	0.0165	0.0107	0.0151	0.0127
535	1.53	0.009	0.0070	0.0080	0.0071
450	2.4	0.008	0.0080	0.0090	0.0067

Therefore, a high power light source (HLV2-3M-RGB) with 3 W output power from (ccs-grp, 2019), as shown in Figure 5.2, is utilised for generating RGB illumination for MPI. The light source consists of three RGB-LEDs and a blending unit. This facilitates mixing of the three light LEDs or dimming of each colour (ccs-grp, 2019) . The spectral distribution of the light was source shown Figure 5.3.

Figure 5.2 RGB LED illuminator [Adopted from (ccs-grp, 2019)]

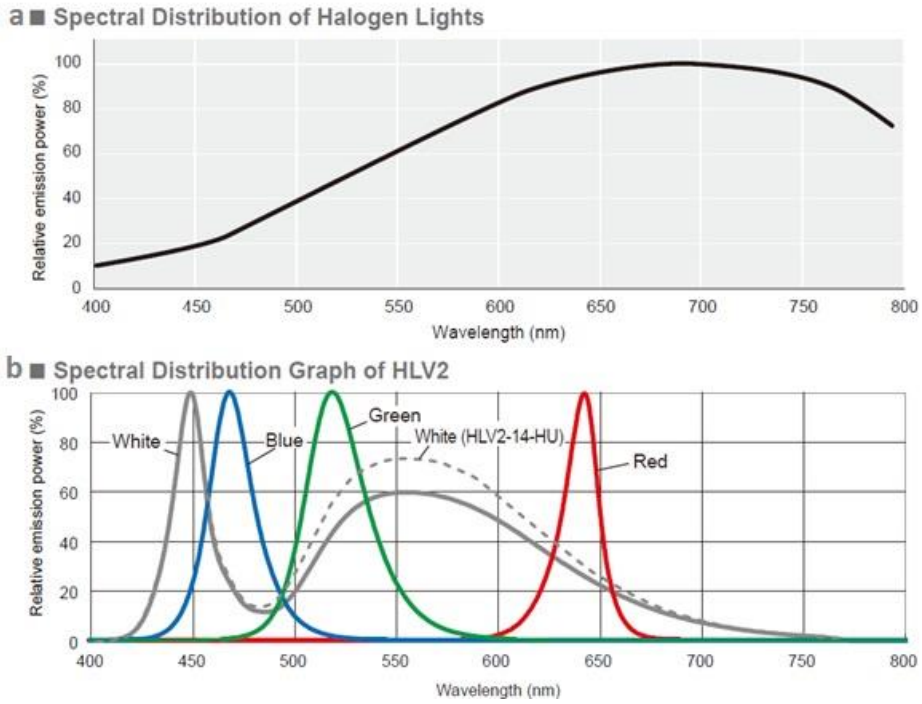

Figure 5.3 Spectral distribution of (a) halogen light (b) HLV2 RGB LED [Adapted from (ccs-grp, 2019)]

Apart from the tuning capability of this light source, another advantage is that the filtered light at each wavelength has a linewidth ranging from 2 nm to 3 nm, which allow sufficient coherence length that covers most of the interferometer applications without producing unwanted speckles of interference that are usually caused by stray reflections when using a laser source because of the long coherence length. The filtration mechanics of AOTF are based on anisotropic diffraction in a birefringent crystal, rotating the polarisation plane of the diffracted wave, as the extraordinary and ordinary light have different refractive indices (Wang, 1992). The polarisation plane of the ordinary diffracted wave is horizontal, while it is vertical for the extraordinary wave as we can see in Figure 5.4.

A single AOTF can be used as a multi-wavelength modulator. Eight excitation wavelengths can be generated simultaneously from a single AOTF. In the MPI setup, the AOTF is used to filter out three RGB channels from RGB LED simultaneously. The AOTF wavelengths operation range with it resolution are shown in Figure 5.5.

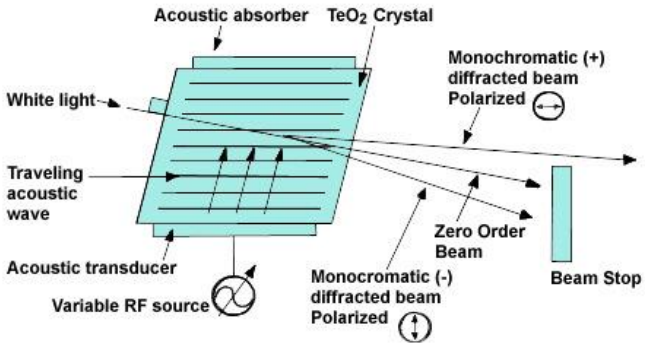

Figure 5.4''Crystalline quartz collinear AOTF produces a beam that is separated from the input with a polariser (top). Tellurium dioxide (TeO2) noncollinear AOTF separates zero-order and diffracted beams without a polariser'' [Adapted from(Wang, 1992)]

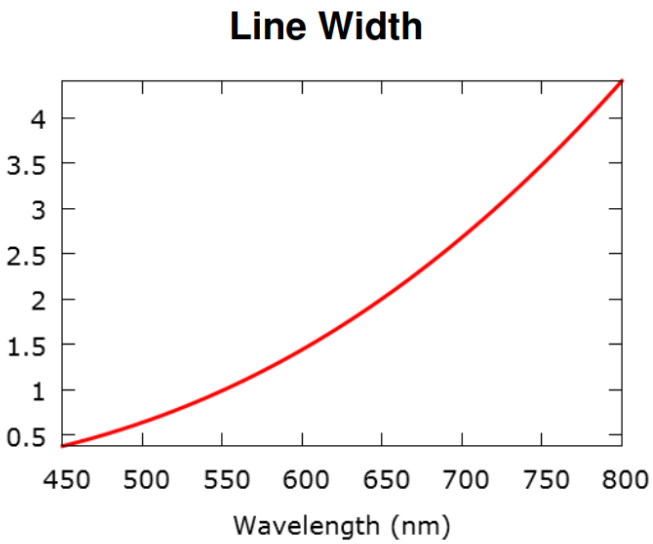

Figure 5.5 The operation range of the AOTF

In practice, the extraordinary channel is used to illuminate the MPI, because the three filtered wavelengths (RGB) are located on the same spot, while in the ordinary channel the RGB are contiguous, as detailed in Figure 5.6.

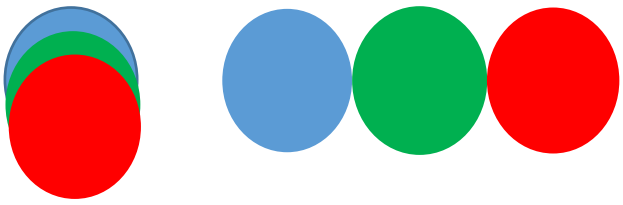

(a) (b)

Figure 5.6 Diffracted wavelength from AOTF (a) Extraordinary component (b) Ordinary component of the filter light

The light source of the MPI consists of RGB LED coupled into fibre bundles (OSL2), then focused by (THORLABS, OSL2FOC Focusing Package) into a pinhole. The pinhole can be considered as the actual source of light positioned at focal length distance equal to 40 mm from the doublets lens (THORLABS, AC254-040-A-ML). The collimated light is coupled to the AOTF(goochandhousego, 2019) as illustrated in Figure 5.7.

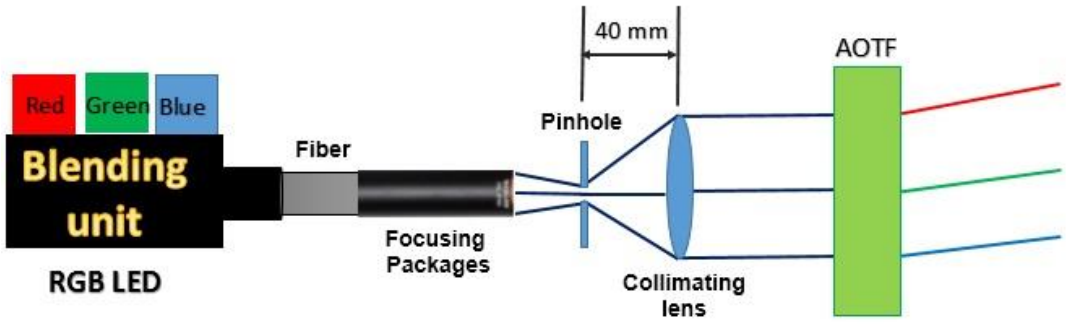

Figure 5.7 MPI light source setup

The filtered beams from AOTF is divided into two beams (zero-order and first order) which are separate by deflection angle. The RGB filter beams is the first order diffracted. In MPI setup, it was practically found that the first order and zero-order beams are physically separated at distant 170 mm. The interferometer was placed at 320 mm.

The filtration relationship between the RGB wavelength and AOTF driving frequency is briefly described in this section. The selected RGB wavelengths are mainly determined by the driving frequency as the other parameters in Equation (5.1) are constants (Jiang *et al.*, 2010).

$$\lambda = \Delta n \alpha \frac{v_a}{f_a} \tag{5.1}$$

where Δn is the birefringence of the crystal used as the diffractive material, α is an abbreviation of many parameters which depend on the design of the AOTF, v_a is the propagation velocity, and f_a is the propagation frequency of the AOTF. In MPI the filtration process was achieved by using a software interface provided by the AOTF manufacturer to select the driving frequencies, hence the RGB wavelengths. This user interface can select up to eight wavelength channels at the same time. The driving radio frequencies are found to be (87.294 MHz for red), (106.071 MHz for green), and (106.071 MHz for blue). The filtered wavelengths are recorded and displayed using a grating spectrometer (Thorlabs, model CCS100) with a spectral resolution less than 1 nm, see Figure 5.8.

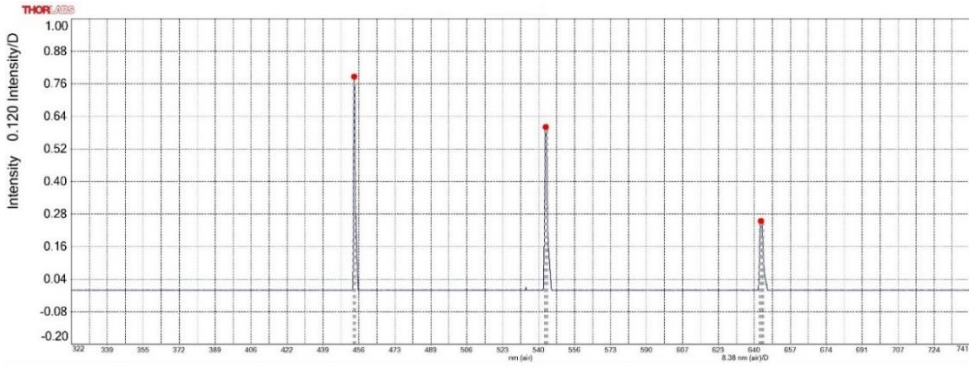

Centroid Wavelength [nm	Peak Wavelength [nm	Peak Level [Intens	FWHM [pm	ΔPeak Position [nm (	Offset Peak Position [nm (
453.7175788	453.6884460	0.7861872	822.848572	0.0000000	0.0000000
543.0688304	543.0944824	0.6001210	1349.05208	89.4060364	89.4060364
643.5231590	643.4246826	0.2542042	1784.96926	100.3302002	189.7362366

Figure 5.8 Wavelength linewidth for (a) Red = 643 nm, (b) Green = 543 nm, and (c) Blue = 453 nm

The RGB filtered wavelengths were chosen by considering the spectrum of the light source, the spectral sensitivity of the camera, and the filtration range of the AOTF. The MPI operation mode can be classified into three different modes (SPI, DPI, and TPI). One example of wavelengths that have been chosen for the TPI mode are ($\lambda_{red} = 643.5$), ($\lambda_{green} = 543$) and ($\lambda_{blue} = 453.7$). It was found that the linewidth of the wavelength at Red ($\lambda_{red} = 643.5$) was equal to 1.78 nm, green ($\lambda_{green} = 543$) was 1.35 nm, and Blue ($\lambda_{blue} = 453.7$) was 0.88 nm. The projection of the selected wavelengths on the LED spectrum as shown in Figure 5.9.

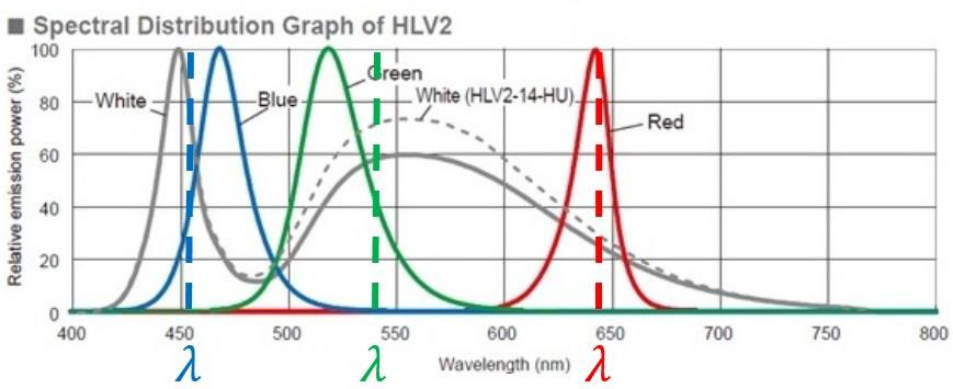

Figure 5.9 RGB LED spectral distribution with the selected wavelength [Adapted from (ccs-grp, 2019)]

5.4 MPI Optical Setup

The MPI experimental setup, see Figure 5.10, shows a LED-RGB light source filtered by AOTF that produces the three RGB channels simultaneously. The filter wavelengths go through a polariser (POL0_45) positioned at 45^{o}, then the light is focused by a 2x microscope objective to the interferometer. The sample was placed in the measurement arm. The reference beam and the measurement beams were combined by the polarised beam splitter (PBS) after passing through quarter waveplate (QWP1 and QWP3) and then focused by an imaging doublet lens, with focal

length equal 100 mm, to the detection unit. The beam is then divided into four beams by three beam splitters (3BS). The beams are passed through a combination of polarisation optics, namely: beam 1 is passed through (POL1_45), beam 2 is passed through (QWP2) and (POL2_45), beam 3 is passed through (POL3_135), and beam 4 is passed through (QWP4) and (POL4_135). Finally, each beam is focused into a colour camera. The four cameras (Cam 1, 2, 3 and 4) can be triggered at once using the electronic box (Norpix). The captured frames are stored in the PC to be processed using fringe analysis algorithms. The alignment procedure of the optics is explained in Appendix D.

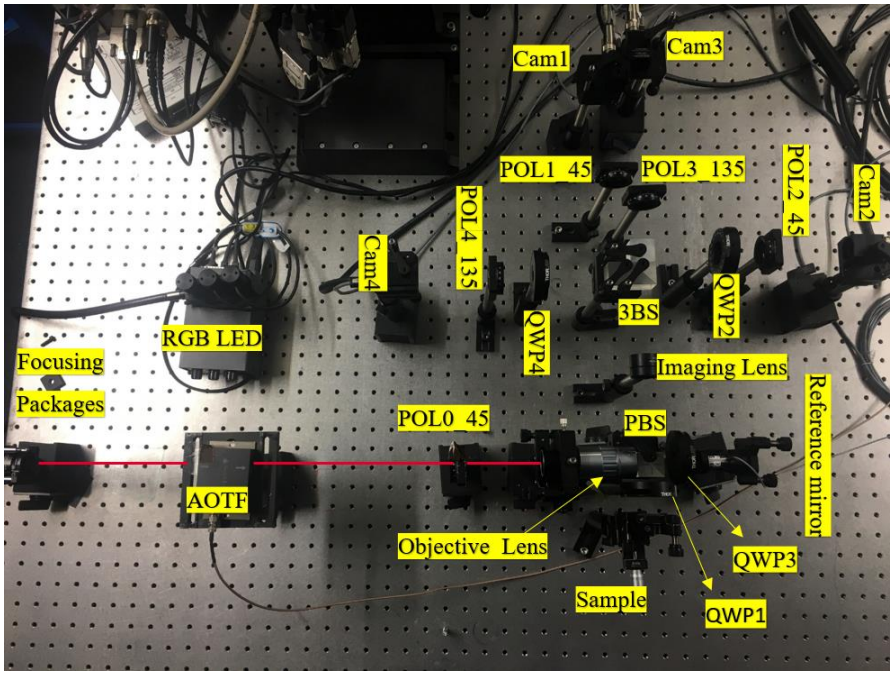

Figure 5.10 MPI optical experimental setup. Abbreviations: QWP is a quarter waveplate, POL_45 is a polariser at 45o, POL_135 is a polariser at 135o, Cam is a camera, PBS is a polarised beam splitter, 3BS is three beam splitters

5.5 Polarisation Setup

The polarisation of light can be manipulated in the interferometer to shift the phases without any scanning mechanism. The PSI usually shifts the phase of the interference over several mechanical steps to measure ultra-precision surfaces with height range limited by λ/4. The wavelength scanning interferometer (WSI) shifts the optical phase over many steps by tuning the scanning wavelength (Hussam, 2013). The coherent correlation interferometer (CCI) scans the envelope of the coherence of a broadband light source by moving the interferometer head in a vertical direction (Kaplonek & Lukianowicz, 2012). In MPI, no time-variant scanning mechanism was used. The phase shift between the reference and measurement wavefront was achieved by splitting the linearly orthogonal beams into four parallel observation arms equipped with linear and quarter wave-plate polarisation optics for simultaneous phase shifting mechanism. The MPI

system, see Figure 4.2, contains a polarising Michelson interferometer that produces a test wave and reference, in which both have an orthogonal polarisation state with respect to each other. The orientation of the polarisers and amount of phase shifts obtained in each detection arm are illustrated in Table-5.2.

Table 5.2 Polarisation and quarter-wave plate's angle used to obtain 90º phase shift increment

Orthogonal Input light	Quarter-Wave Plate (deg.)	Polarisers (deg.)	Phase Shift Achieved (deg.)
Arm 1	None	45^0	0^0
Arm 2	Fast axis at zero	45^0	90^0
Arm 3	None	135^o	180^0
Arm 4	Fast axis at zero	135^0	270^0

In the MPI setup, the achromatic QWP (AQWP05M-600) retardance for the RGB wavelengths are close to each other as provided by the manufacturer (thorlabs.com, 2018), see Figure 5.11. It was found to be equal to 0.24574, 0.27174, and 0.27092 for Blue (460 nm), Green (540 nm) and Red (630 nm), respectively. As such, the phase delay will be considered equal (Tian *et al.*, 2018) . The extinction ratio of the polariser (LPVISE100-A) used in MPI is shown in Figure 5.12, and provided by the manufacturer (thorlabs.com, 2018).

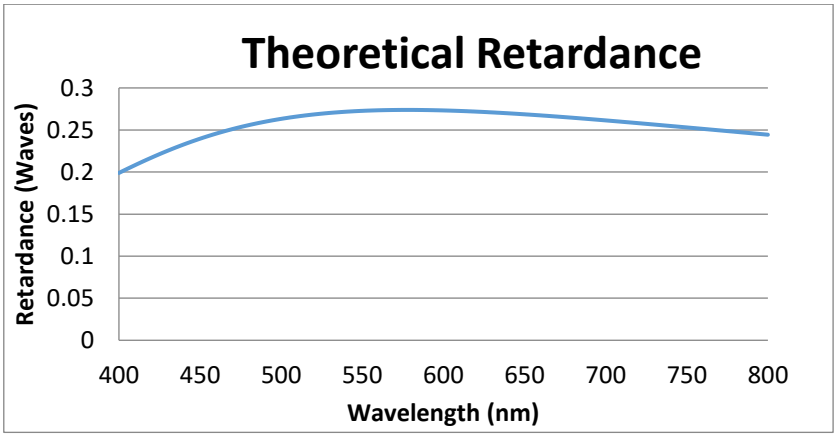

Figure 5.11 Retardance values for quarter wave plate [adapted from (thorlabs.com, 2018)]

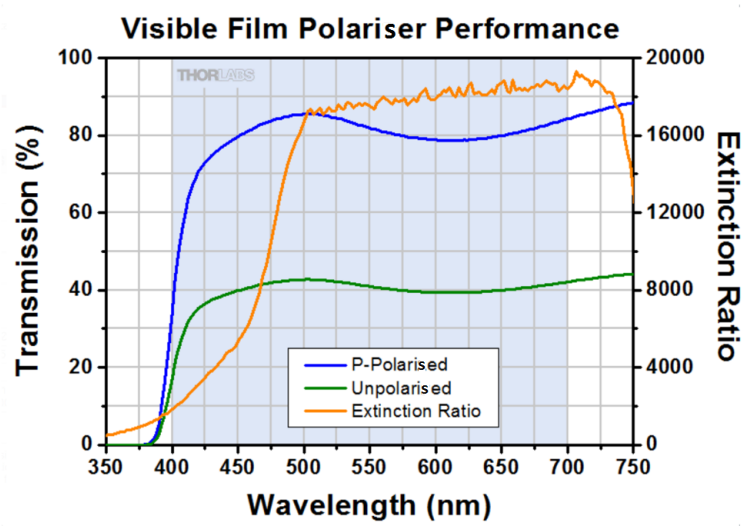

Figure 5.12 Thin film polariser extinction ratio [adapted from (thorlabs, 2019)]

The polarisation efficiency and the diattenuation coefficient illustrate in Table (5.3). Table (5.3-A) shows that the polariser diattenuation at RGB wavelength is almost the same, such that this is not the critical factor when different wavelengths are used in the same setup (Matt *et al.*, 2005).

Table 5.3 A Economy film polarisers, 400 – 700 nm specifications (Thorlabs Ltd, 2018)

Wavelength (nm)	Transmission of S-Polarized Input	Transmission of P-Polarized Input	Extinction Ratio	Diattenuation	Diattenuation Coefficient ($\boldsymbol{\alpha}$)
460	0.02698	81.50208	3020.50	0.999338	0.000662
540	0.0048	82.92752	17262.18	0.999884	0.000116
630	0.00437	78.99960	18069.44	0.999889	0.000111

The polarisation state of the RGB wavelength from the AOTF is vertically polarised. The jones vector of the vertically polarised light is shown in Equation (5.2).

$$E_{rgb} = \begin{bmatrix} 0 \\ 1 \end{bmatrix} \tag{5.2}$$

The light is transmitted through a polariser (P) with a transmission axis positioned at 45° to an optical axis, which is then focused by a 2x objective onto the reference and measurement surfaces of the interferometer. The Jones matrix for the linear polariser has a transmission axis at 45° can be expressed in Equation (5.3) (Hecht, 2016).

$$\mathrm{P}\ (45^{o}) = \frac{1}{2}\begin{bmatrix} 1 & 1 \\ 1 & 1 \end{bmatrix} \tag{5.3}$$

E_i is here the incident Jones vector after passing through the linear polariser at 45° as shown in Equation (5.4).

$$E_i = \frac{1}{2}\begin{bmatrix}1 & 1\\ 1 & 1\end{bmatrix}\begin{bmatrix}0\\ 1\end{bmatrix} = \frac{1}{2}\begin{bmatrix}1\\ 1\end{bmatrix} \tag{5.4}$$

The linear polarised light is separated into horizontal and vertical polarised light after passing through the polarising beam splitter (PBS). The Jones matrix representation of horizontal (p) and vertical (s) components are given in Equation (5.5, 5.6, and 5.7) (T. Y.-F. Chen & Du, 2009).

$$\text{PBS}\left(\frac{\pi}{2}\right) = \begin{bmatrix}1 & 0\\ 0 & 0\end{bmatrix},\ \text{PBS}(0) = \begin{bmatrix}0 & 0\\ 0 & 1\end{bmatrix} \tag{5.5}$$

$$E_p = \begin{bmatrix}1 & 0\\ 0 & 0\end{bmatrix}\frac{1}{\sqrt{2}}\begin{bmatrix}1\\ 1\end{bmatrix} = \frac{1}{\sqrt{2}}\begin{bmatrix}1\\ 0\end{bmatrix} \tag{5.6}$$

$$\begin{bmatrix}0 & 0\\ 0 & 1\end{bmatrix}\frac{1}{\sqrt{2}}\begin{bmatrix}1\\ 1\end{bmatrix} = \frac{1}{\sqrt{2}}\begin{bmatrix}0\\ 1\end{bmatrix} = E_s \tag{5.7}$$

Both horizontal and vertical beams go through the achromatic quarter-wave plate (QWP1 and QWP2), which have a fast axis at 45°. As such, the beams passed twice through the QWPs before returning to the PBS, transforming the p to s state, and vice versa. As such, the Jones matrix of the measurement and reference path including the QWPs can be represented by Q_1 as given in Equation (5.8) (T. Y.-F. Chen *et al.*, 2009; Somers & Bhattacharya, 2005).

$$Q_1 = \begin{bmatrix}0 & 1\\ 1 & 0\end{bmatrix} \tag{5.8}$$

Equations (5.9) and (5.10) can give the transformation of the polarisation state for both beams, see Figure 5.13.

$$E_r = \begin{bmatrix}0 & 1\\ 1 & 0\end{bmatrix}\frac{1}{\sqrt{2}}\begin{bmatrix}1\\ 0\end{bmatrix} = \frac{1}{\sqrt{2}}\begin{bmatrix}0\\ 1\end{bmatrix} \tag{5.9}$$

$$E_m = \begin{bmatrix}0 & 1\\ 1 & 0\end{bmatrix}\frac{1}{\sqrt{2}}\begin{bmatrix}0\\ 1\end{bmatrix} = \frac{1}{\sqrt{2}}\begin{bmatrix}1\\ 0\end{bmatrix} \tag{5.10}$$

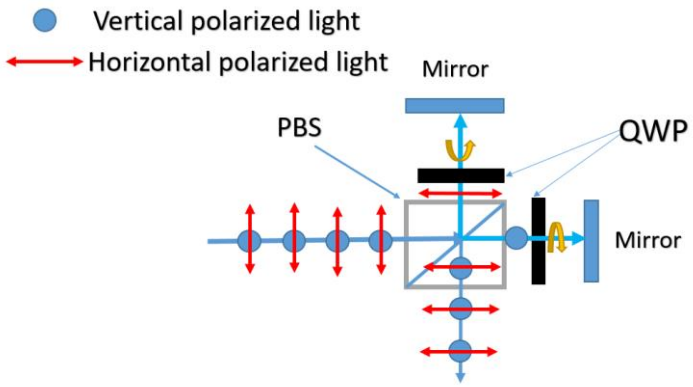

Figure 5.13 Reference and measurement arms

After flipping the polarisation states while retaining their mutually orthogonal polarisation state, the beams are passed towards the four detection arms and focused by an imaging lens with

a focal length of 100 mm. Finally, the focused beams were split by three beam-splitters into four monitoring arms. The combination of the polarisation setup is illustrated in Table 5.2.

Polarisation State of First Observation Arm 1:

In the first observation arm, the two orthogonal plane polarised beams propagate through a linear polariser with a transmission axis positioned at 45°. If the reference beam E_r has a vertical polarisation state, the emerged light from the linear polariser has polarisation state $\mathscr{P}$-stat at + 45°, as given in Equation (5.11).

$$E_{r1} = \frac{1}{2}\begin{bmatrix}1 & 1\\ 1 & 1\end{bmatrix}\frac{1}{\sqrt{2}}\begin{bmatrix}0\\ 1\end{bmatrix} = \frac{1}{2\sqrt{2}}\begin{bmatrix}1\\ 1\end{bmatrix} \tag{5.11}$$

In the same manner, the horizontal polarisation state of the measurement beam E_m transformed to P-state at + 45° as given in (5.12).

$$E_{m1} = \frac{1}{2}\begin{bmatrix}1 & 1\\ 1 & 1\end{bmatrix}\frac{1}{\sqrt{2}}\begin{bmatrix}1\\ 0\end{bmatrix} = \frac{1}{2\sqrt{2}}\begin{bmatrix}1\\ 1\end{bmatrix} \tag{5.12}$$

As such, the 45° orientation of the polariser introduces zero phase shift between the reference and measurement wavefront.

The Polarisation State of the Second Observation Arm 2:

In the second observation arm, the orthogonal light is transmitted through the achromatic quarter wave plate with the fast axis at 0° (i.e. horizontal fast axis) and then goes through a polariser with transmission axis at + 45°. The quarter waveplate is used to delay the vertically polarised light, while the horizontal components pass with less delay, as a result, the phase of vertical polarised light will be lagged by 90 ° compared to the phase of horizontal light. The Jones matrix of the quarter waveplate has a fast horizontal axis, shown in Equations (5.13) (Hecht, 2016).

$$\text{QWP}\ (0) = e^{\frac{i\pi}{4}}\begin{bmatrix}1 & 0\\ 0 & i\end{bmatrix} \tag{5.13}$$

As assumed before, the reference beam E_r has a vertical polarisation state. The emergent beam from the quarter wave plate is described in Equation (5.14).

$$e^{\frac{i\pi}{4}}\begin{bmatrix}1 & 0\\ 0 & i\end{bmatrix}\frac{1}{\sqrt{2}}\begin{bmatrix}0\\ 1\end{bmatrix} = \frac{e^{\frac{i\pi}{4}}}{\sqrt{2}}\begin{bmatrix}0\\ i\end{bmatrix} \tag{5.14}$$

The emerging beam from Equation (5.14) is manipulated again after passing the polariser with a transmission axis at +45° to the optical axis. The last emergent light is described by Equation (5.15).

$$\frac{1}{2}\begin{bmatrix}1 & 1\\ 1 & 1\end{bmatrix}\frac{e^{\frac{i\pi}{4}}}{\sqrt{2}}\begin{bmatrix}0\\ i\end{bmatrix} = \frac{e^{\frac{i\pi}{4}}}{2\sqrt{2}}\begin{bmatrix}1+i\\ 1+i\end{bmatrix} \tag{5.15}$$

The Jones vector of the emerging beam in Equation (5.15) can be modified to Equation (5.16) using the relation below $1 + i = \sqrt{2}e^{i\frac{\pi}{4}}$.

$$E_r = \frac{e^{\frac{i\pi}{4}}}{2\sqrt{2}}\begin{bmatrix}1+i\\1+i\end{bmatrix} = \frac{e^{\frac{i\pi}{4}}}{2\sqrt{2}}\begin{bmatrix}\sqrt{2}e^{+i\frac{\pi}{4}}\\\sqrt{2}e^{+i\frac{\pi}{4}}\end{bmatrix} = \frac{e^{\frac{i\pi}{4}}}{2\sqrt{2}}\sqrt{2}e^{\frac{i\pi}{4}}\begin{bmatrix}1\\1\end{bmatrix} = \frac{1}{2}e^{\frac{i\pi}{2}}\begin{bmatrix}1\\1\end{bmatrix} \quad (5.16\text{-a})$$

$$E_{r2} = \frac{1}{2}i\begin{bmatrix}1\\1\end{bmatrix} \quad (5.16\text{-b})$$

In the same manner, the measurement beam will be manipulated after passing the quarter waveplate. The emergent beam from the quarter waveplate is shown in Equation (5.17).

$$\mathrm{E_{m2}} = \mathrm{e}^{\frac{\mathrm{i}\pi}{4}}\begin{bmatrix}1 & 0\\0 & \mathrm{i}\end{bmatrix}\frac{1}{\sqrt{2}}\begin{bmatrix}1\\0\end{bmatrix} = \frac{\mathrm{e}^{\frac{\mathrm{i}\pi}{4}}}{\sqrt{2}}\begin{bmatrix}1\\0\end{bmatrix} \quad (5.17)$$

After that, the resultant beam given in Equation (5.17) will go through the linear polarizer +45° as described by Equation (5.18).

$$E_{m2} = \frac{1}{2}\begin{bmatrix}1 & 1\\1 & 1\end{bmatrix}\frac{e^{\frac{i\pi}{4}}}{\sqrt{2}}\begin{bmatrix}1\\0\end{bmatrix} = \frac{e^{\frac{i\pi}{4}}}{2\sqrt{2}}\begin{bmatrix}1\\1\end{bmatrix} \quad (5.18\text{-a})$$

$$E_{m2} = \frac{e^{\frac{i\pi}{4}}}{2\sqrt{2}}\begin{bmatrix}1\\1\end{bmatrix} \quad (5.18\text{-b})$$

By comparing Equations (5.16 and 5.18), the Jones vectors show that the quarter waveplate and polariser at 45° cause a 90° phase shift between the reference and measurement wavefront.

Polarization State of the Third Observation Arm 3:

In the third arm, the orthogonal waves for measurements and reference are passed through linear polariser has a transmission axis at 135°. Generally, the Jones matrix for a linear polariser has transmission axis at θ can be given in Equation (5.19) (Bernd, 2012).

$$\mathrm{P}\,(\theta^{\circ}) = \frac{1}{2}\begin{bmatrix}cos^2\theta & sin\theta cos\theta\\sin\theta cos\theta & sin^2\theta\end{bmatrix} \quad (5.19)$$

By substituting the value of $\theta = 135^{\circ}$ in Equation (5.19), we obtain the result in equation (5.20).

$$\mathrm{P}\,(135^{\circ}) = \frac{1}{2}\begin{bmatrix}1 & -1\\-1 & 1\end{bmatrix} \quad (5.20)$$

The reference beam is assumed to have a vertical polarisation state E_r. Then the linear polarised light goes through a polariser with the transmission axis at +135° to the optical axis as given in Equation (5.21). The polarisation state of the emergent reference beam shown in Equation (5.22).

$$\frac{1}{2}\begin{bmatrix}1 & -1\\ -1 & 1\end{bmatrix}\frac{1}{\sqrt{2}}\begin{bmatrix}0\\1\end{bmatrix}=\begin{bmatrix}0\\1\end{bmatrix}=\frac{1}{2\sqrt{2}}\begin{bmatrix}-1\\1\end{bmatrix} \quad (5.21\text{-a})$$

$$E_{r3(135)}=\frac{1}{2\sqrt{2}}\begin{bmatrix}-1\\1\end{bmatrix} \quad (5.21\text{-b})$$

In the same manner, the horizontally polarised beam of the reference arm goes through the polarising beam splitter of the linear polariser at +135°, and the emerging light is described with Equation (5.22).

$$E_{m3(-45)}=\frac{1}{2}\begin{bmatrix}1 & -1\\ -1 & 1\end{bmatrix}\frac{1}{\sqrt{2}}\begin{bmatrix}1\\0\end{bmatrix}=\frac{1}{2\sqrt{2}}\begin{bmatrix}1\\-1\end{bmatrix} \quad (5.22)$$

The Jone vectors given in Equations (5.21-b) and (5.22) show that the phase shift in the third observation arm is 180° between the reference and measurement wavefront.

Polarization State of the Fourth Observation Arm 4:

In the fourth arm, the orthogonal polarised light from reference and measurement arms were passed through quarter waveplate with a fast axis at 0° (i.e. horizontal fast axis), then they go through a linear polariser at 135°. As explained with the second arm, the quarter waveplate delayed the vertical polarized light, which produced a 90° phase delay corresponding the horizontal component.

As we assumed before, the reference beam E_r has vertical polarisation state. The polarization state of the beam that emerges from the quarter waveplate shown in Equation (5.23).

$$E_{r4}=e^{\frac{i\pi}{4}}\begin{bmatrix}1 & 0\\ 0 & i\end{bmatrix}\frac{1}{\sqrt{2}}\begin{bmatrix}0\\1\end{bmatrix}=\frac{e^{\frac{i\pi}{4}}}{\sqrt{2}}\begin{bmatrix}0\\i\end{bmatrix} \quad (5.23)$$

The emergent beam given in Equation (5.24) goes through the polariser with transmission axis positioned at +135°. The polariser will manipulate the beam to the form given in Equation (5.24).

$$E_{r4}=\frac{1}{2}\begin{bmatrix}1 & -1\\ -1 & 1\end{bmatrix}\frac{e^{\frac{i\pi}{4}}}{\sqrt{2}}\begin{bmatrix}0\\i\end{bmatrix}=\frac{e^{\frac{i\pi}{4}}}{2\sqrt{2}}\begin{bmatrix}-i\\+i\end{bmatrix}=\frac{e^{\frac{i\pi}{4}}}{2\sqrt{2}}i\begin{bmatrix}-1\\1\end{bmatrix} \quad (5.24)$$

In the same manner, the measurement beam E_m has horizontal polarised state, and it will go through the quarter waveplate first. The polarisation state of the emerging light is given in equation (5.25)

$$E_{m4}=e^{\frac{i\pi}{4}}\begin{bmatrix}1 & 0\\ 0 & i\end{bmatrix}\frac{1}{\sqrt{2}}\begin{bmatrix}1\\0\end{bmatrix}=\frac{e^{\frac{i\pi}{4}}}{\sqrt{2}}\begin{bmatrix}1\\0\end{bmatrix} \quad (5.25)$$

After that, emergent light from the quarter waveplate, as given in Equation (5.25), will pass through the linear polariser +135°, and the result will be described in Equation (5.26)

$$E_{m4}=\frac{1}{2}\begin{bmatrix}1 & -1\\ -1 & 1\end{bmatrix}\frac{e^{\frac{i\pi}{4}}}{\sqrt{2}}\begin{bmatrix}1\\0\end{bmatrix}=\frac{e^{\frac{i\pi}{4}}}{2\sqrt{2}}\begin{bmatrix}1\\-1\end{bmatrix} \quad (5.26)$$

The Jone vectors given in Equations (5.25) and (5.27) show that the quarter waveplate and polariser at 135^{o} cause a 270^{o} phase shift between the reference and measurement wavefront.

5.6 Matching Field of Views

The MPI uses four cameras to measure a specific spot on the sample. As such, it is crucial that all captured frames must view the same spot. Any misalignment should be corrected by matching the pixels of the cameras. An optical test target (Thorlabs, 1951 USAF Resolution Test Targets, 3" x 3") was placed on the measurement path in the interferometer to match the four cameras pixels to each other and crop the images accordingly. To avoid any error that may occur if there is a significant tilt in the USAF target, the target has been placed at equal distance from the reference mirror in order to obtain a high contrast fringe that used to level the sample by getting a single fringe across the field of view.

After that, the reference arm was covered, and four cameras, shown in Figure 5.14 (a), captured four images. A specific point defined by the feature edge was chosen as a reference to shift pixels in X-Y directions to obtain the same field of view for the cropped images with exact and matched locations for the feature edges as shown in Figure 5.14 (b).

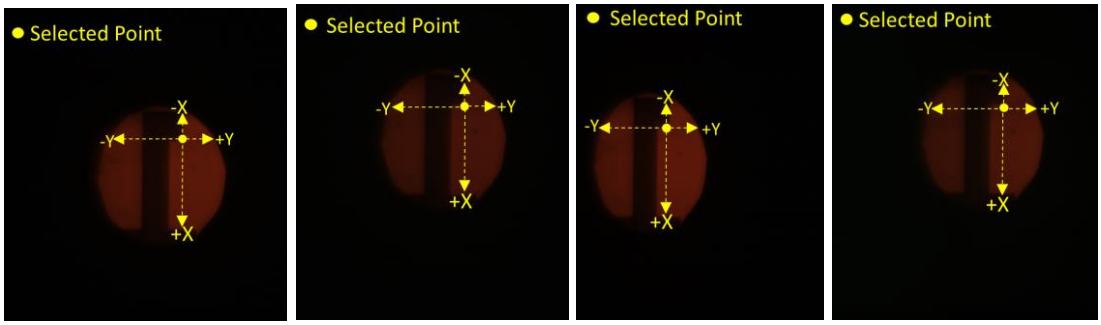

(a)

(b)

Figure 5.14 (a) Original image capture by four cameras and (b) cropped images

5.7 Intensity Calibration of Interference Fringes

The MPI detection unit is based on four colour cameras that simultaneously gather four intensity values for each measurement point. However, the intensity that detected by the four cameras were not equal because the ratio of reflected and transmitted beam through the three non-polarised beam splitters were not equal, as shown in the Table 5.4. This non ideal splitting can cause significant intensity variation between the cameras, generating errors in phase shifting interferometer (Daniel, 2007)

Thus, the captured frames need to be calibrated to cancel any intensity variation in the fringe bias and visibility.

Table 5.4 Transmission and reflection light ratio for non-polarised beam splitter

	% Transmission		% Reflection	
Wavelength (nm)	P-Polarized	S-Polarized	P-Polarized	S-Polarized
460 (blue)	54.29	51.24	39.73	42.26
540 (green)	56.26	51.20	39.78	45.75
630 (red)	53.49	50.47	42.36	46.49

Chapter 3 describes the interference of light and illustrates that the interference/fringe intensity (I) can be written as:

$$I = A_{bias} + B_{vis}\, cos(\theta) \qquad (5.27)$$

Where $A_{bias} = I_{ref} + I_{meas}$ represents the fringe bias and $B_{vis} = 2\sqrt{I_{ref} I_{meas}}$ represents the fringe visibility and θ is the phase of the interference. The fringe intensity I_{ref} and I_{meas} are the beam intensities in the reference and measurement paths respectively. The Equation shows that the intensity values only exist in A_{bias} and B_{vis} terms, while the phase is independent of I_{ref} and I_{meas}. Thus, by removing A_{bias} and B_{vis} from the interference signals, the fringes can have the same contrast, achieving the cameras calibration.

The following procedure has been developed for the intensity calibration by measuring the intensity values I_{ref} and I_{meas} in each detection arm to determine A_{bias}andB_{vis}. The MPI is illuminated by RGB filtered wavelengths. The RGB intensity of the reference beam I_{ref} was captured by the cameras after blocking the measurement beam of the interferometer in order to determine a single I_{ref} value for each camera. Similarly, the intensity of the measurement beam was captured. The RGB components were extracted using a Matlab code, see Appendix E, to determine I_{ref} and I_{meas} for each colour and their corresponding A_{bias} and B_{vis} parameters. The

fringe intensity (I) was determined for each camera at each colour using captured interferograms shown in Figure 5.15 (a). The fringe bias and visibility were removed by subtracting the calculated A_{bias} from the captured I values and dividing the result over B_{vis} as given in the following Equation:

$$\frac{I-A_{bias}}{B_{vis}} = cos(\Delta\theta) \tag{5.28}$$

In order to add a constant bias and fringe visibility to all RGB interferograms, the minimum calculated values for A_{bias} and B_{vis} were selected among others to replace the cancelled as given in Equations (5.29-5.32), producing calibrated interferograms for MPI.

$$I_1(\lambda) = A_{min} + B_{min}\, cos(\Delta\emptyset + 0) \tag{5.29}$$

$$I_2(\lambda) = A_{min} + B_{min}\, cos(\Delta\emptyset + 90) \tag{5.30}$$

$$I_3(\lambda) = A_{min} + B_{min} cos(\Delta\emptyset + 180) \tag{5.31}$$

$$I_4(\lambda) = A_{min} + B_{min}\, cos(\Delta\emptyset + 270) \tag{5.32}$$

The four frames that were captured by the cameras before calibration are shown in Figure 5.15(a). Meanwhile, the effect of the intensity calibration is shown in Figure 5.15 (b). The same profile was plotted on all frames before and after the calibration, as shown in Figure 5.16. It can be seen that the calibrated interference signal has better intensity distribution over the field of view.

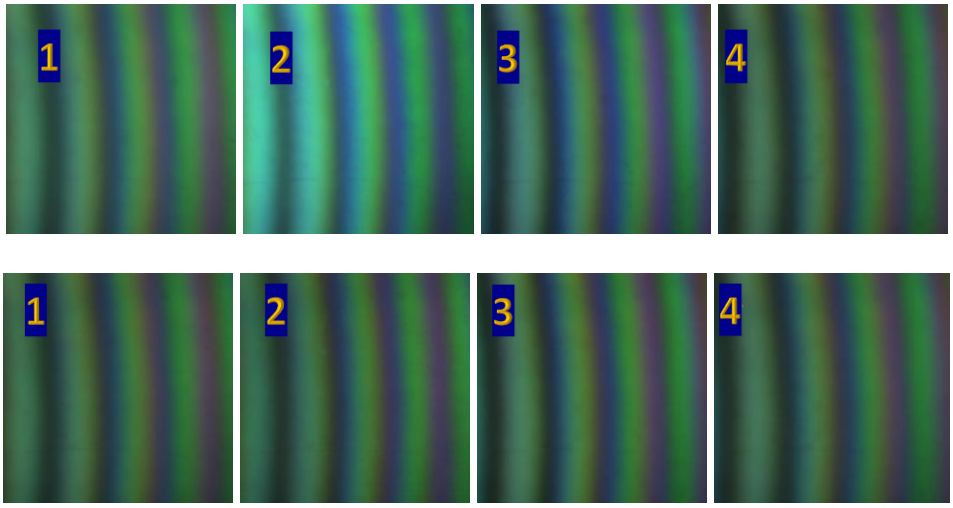

Figure 5.15 Four images captured by MPI (a) before calibration (b) after calibration

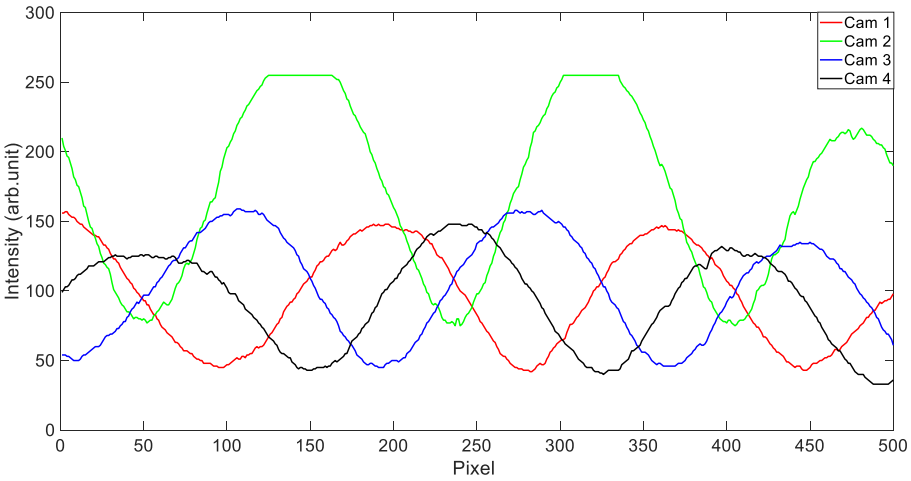

(a)

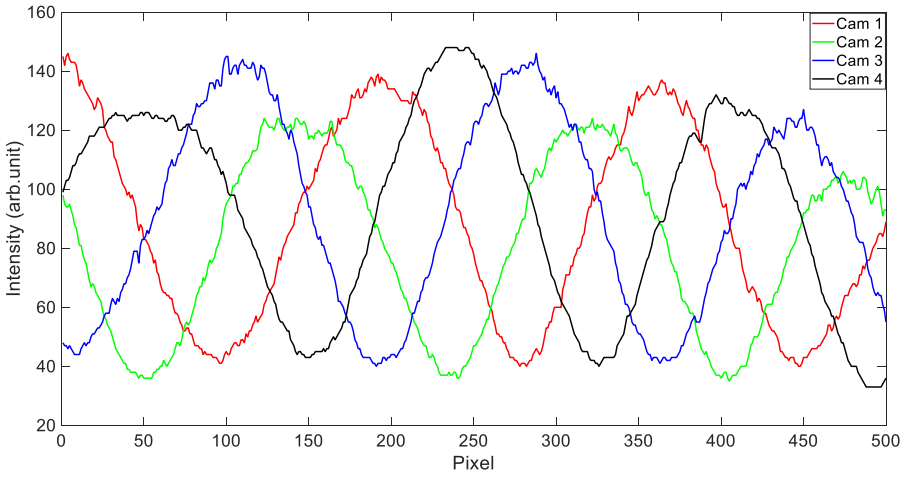

(b)

Figure 5.16 Four camera intensity after (a) before calibration (b) after calibration

5.8 Colour Camera

The MPI uses colour cameras to capture multi-wavelength (i.e. RGB) interferograms instantaneously. One of the drawbacks of using colour cameras is the colour crosstalk occurs between adjacent pixels and that cause error in the phase of the interference fringes. Here is a description about the colour cameras types, suggesting the best type for the MPI.

The camera's sensors, which are dedicated to visible light, are classified into two main types, namely mono and colour. Mono sensors consists of pixels that are sensitive to all visible wavelengths. Colour sensors have an additional layer that is installed below the microlens, called (mosaic of colour filters), which is used to absorb undesired colour wavelengths, as each resultant pixel is sensitive to a specific colour wavelength. Currently the most widely used colour filter

among the other types is from Bayer (1976). It consists of a repetition of 2x2 blocks in which the green component has double the area of the blue and red, as illustrated in Figure 5.17.

Then the colour interpolation algorithm, which reconstructs the missing values, works to provide a full image. This is called “de-mosaicing” interpolation algorithms, which used to produce colour data by converting the sub-sampled information at the image location (Beverage *et al.*, 2014; S. Andriani & H. Brendel, 2013).

In the last years, the trend of camera companies was to increase the spatial resolution of the sensor while at the same time keeping the same sensor size. As a result, the pixels gets smaller and closer to each other, but the drawback of reducing the pixel size is the increase the noise level and crosstalk value because of the interactions among adjacent pixels (S. Andriani and H. Brendel, 2013).

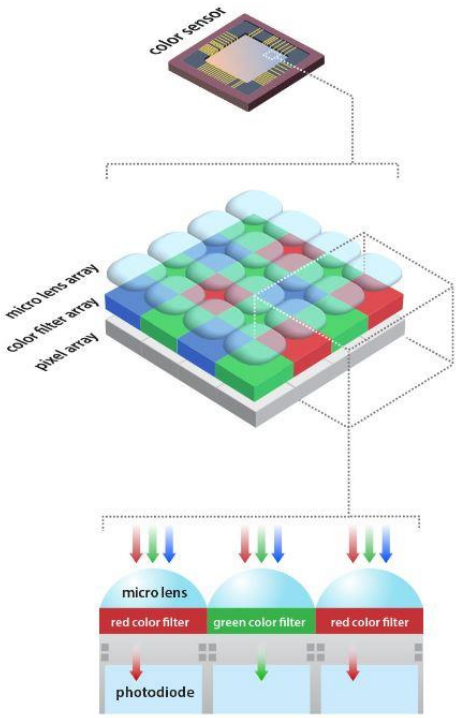

Figure 5.17 Colour sensor using Bayer pattern [Adapted from (thinklucid, 2019b)]

One of the drawbacks of using the colour camera with a single sensor that the sampling in colour filter will reduce the resolution of the detector array compared to a monochromatic one (Hubel *et al.*, 2004). As such, to compensate for the loss of sampling resolution, the system magnification should be increased, hence reduction in the field of view (Beverage *et al.*, 2014).

Most of the limitation of using a single sensor (Bayer) colour camera disappears when using three- sensors colour camera, which can simultaneously capture colour information at each pixel location. The basic concept of the camera to split the incoming light into the three primary

component RGB, so each component has distinct optical path ended with and each monochromatic detector for capturing, as shown in Figure 5.18 (Picart *et al.*, 2015; Upputuri *et al.*, 2016). The drawback of these devices is a limited detector size choices, slower than single sensor camera and high cost.

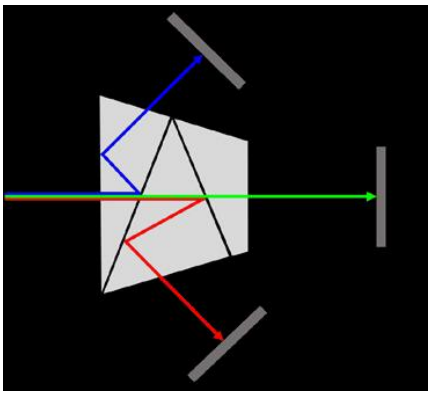

Figure 5.18 Three sensors camera equipped with RGB prism to detect the three primary colour of light separately

An alternative method to avoid using the Bayer filter for the colour sensor is to use the Foveon X3 image sensor using of the ability of silicon to separate the RGB within each pixel by absorbing a different wavelength of light to varying depths in silicon (Hubel *et al.*, 2004). The shorter wavelength detected closer to the entrance of the sensor interface, while the red photon propagates deep within the based pixel structure this type of technology based on the stack the red, green, and blue pixel vertically as shown in Figure 5.19. The limitation of this solution is limited options for total pixel count and pixel size and slow frame rate.

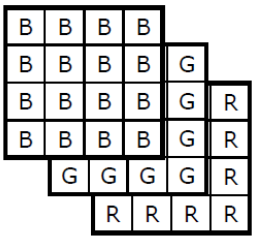

Figure 5.19 ''Schematic depiction of Foveon X3 image sensor showing stacks of colour pixels, which record colour depth-wise in silicon'' [Adapted from (Hubel *et al.*, 2004)]

The most practical and cost effective solution to adding colour imaging to the MPI is to use a colour camera equipped with a mosaic colour filter lined up with its pixels. The CMOS cameras equipped with a Sony sensor were used in the MPI. The cameras spectral response and the three RGB filtered wavelengths can be found in Figure 5.20.

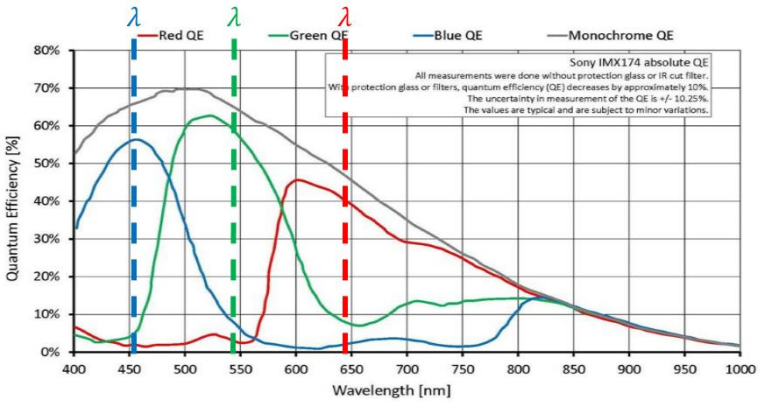

Figure 5.20 RGB selected wavelengths projected on camera spectrum

5.8.1 Cross Talk Calculation

In MPI, the CMOS cameras employed Bayer filters placed in front of the sensors to filter the three RGB primary components. The spectral response of the sensor (Sony IMX174 sensor) used in these cameras shows that the crosstalk between the colours is non-negligible, as shown in Figure 5.21. However, the MPI utilised the AOTF to tune the filtered wavelength to the positions where the crosstalk is minimum. The colour crosstalk changes fringe envelope for Red, Green and Blue components.

The operation principle of MPI allowed capturing the interferograms based on three different modes, namely: single wavelength interferometer (SPI) or dual wavelength interferometer (DPI), or triple wavelength interferometer (TPI), which were also presented as RGB interferometer. The specification of these modes will be discussed in detail in chapters 6 and 7. This section discusses the illumination of the TPI mode, because it includes all crosstalk probability.

In the TPI mode, the MPI was illuminated by (λ_{red} = 643.5 nm, λ_{green} = 543 nm, and λ_{blue} = 453.7 nm) simultaneously. An initial crosstalk ratio was checked by turning off the blue and green channels from the light source, while capturing the interferograms. Then RGB components were extracted as shown in Figure 5.21. The figure shows that there is existing values for the blue and green components that is extracted from the red fringe, evidencing that there is red light passing the green and blue Bayer filters.

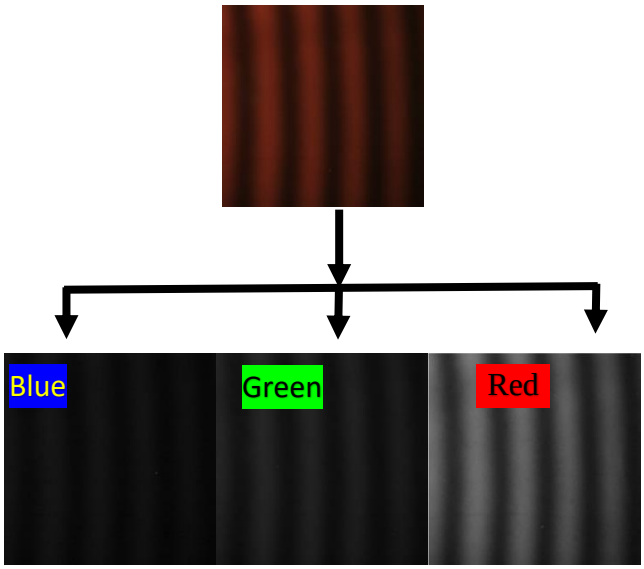

Figure 5.21 RGB components, when the green component is off

The crosstalk value was investigated by illuminating the MPI by RGB wavelengths sequentially, first red, then green, and finally blue light. Single frames captured respectively.

The crosstalk value in the red, green and blue Bayer filter were calculated by the following procedure. Firstly, the red component was extracted from the red fringe, the green component was extracted from the green fringe, and the blue component was extracted from blue fringe, and all were registered as reference values. The green and blue components that were extracted from red fringe were registered as crosstalk values. Similarly, the red and blue components that extracted from green fringe were registered as crosstalk values. Finally, the red and green components that extracted from the blue fringe were registered as crosstalk values. The reference and crosstalk values are shown in Figure 5.22.

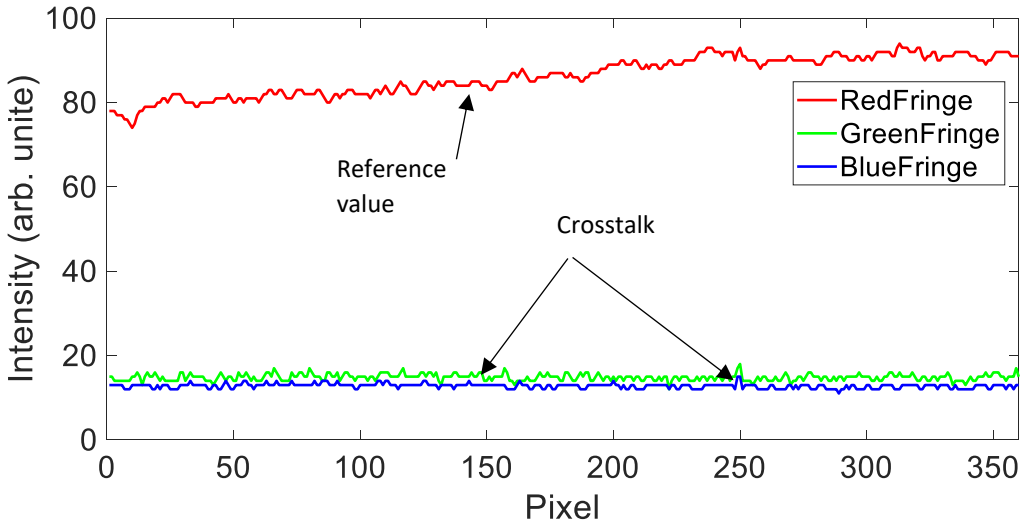

(a)

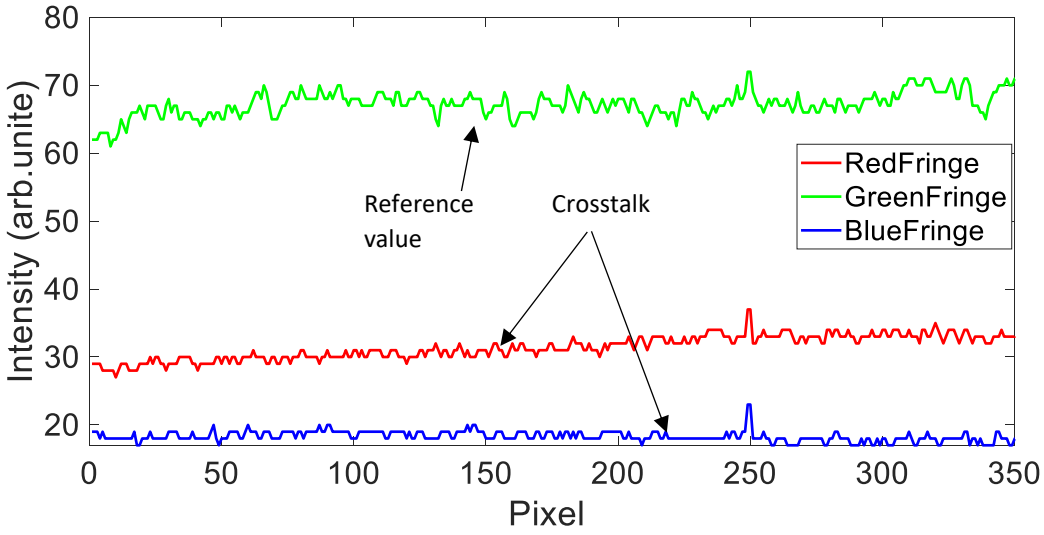

(b)

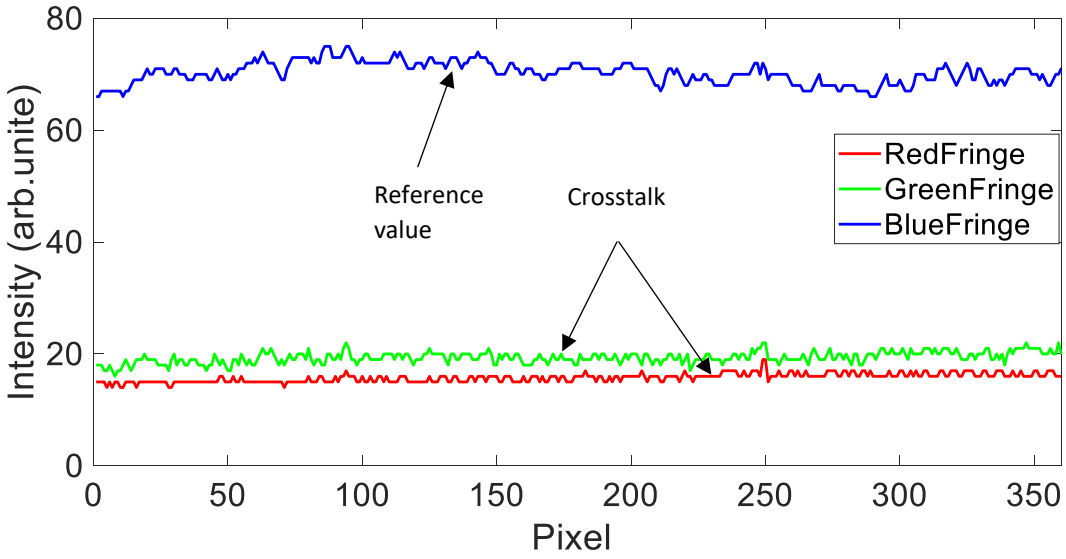

(c)

Figure 5.22 Bayer filters intensity record along one profile (a) Red (b) Green (c) Blue

The crosstalk percentage is calculated using Equation (5.33).

$$crosstalk\ \% = \frac{Crosstalk\ value}{Reference\ value} * 100 \tag{5.33}$$

The crosstalk of red was found to be 35% in the green Bayer filter and 17% in blue Bayer filter. The crosstalk percentage of red, green and blue in the other Bayer filters were illustrated in Table (5.5). This test shows that there is significant crosstalk for all colours, especially for the red in the green Bayer filter. Therefore, a crosstalk compensation has been carried out as demonstrated in the next section.

Table 5.5 Cross talk Value recorder by the RGB Bayer filters

Bayer Filters	**Blue** crosstalk %	**Green** crosstalk %	**Red crosstalk %**
Blue Bayer filter	Reference Value	29%	17%
Green Bayer filter	25%	Reference Value	35%
Red Bayer filter	18%	24%	Reference Value

5.8.2 Cross Talk Compensation

The colour crosstalk compensation has been carried out to obtain true colour to enhance the fringe distribution, hence improving the measurement accuracy. The MPI was illuminated by RGB wavelengths and a colour interferograms was captured. The RGB components including the crosstalk can be given in the form of Equation (5.34, 5.35, and 5.36) (Kitagawa, 2010).

$$B' = B + aG + bR \tag{5.34}$$

$$G' = cB + G + dR \tag{5.35}$$

$$R' = eB + fG + R \tag{5.36}$$

Where B‘, G‘, R’ are the observed values for blue, green and red components that extracted from colour fringe. The R, G and B are the true colour values to be calculated, and the b, c, d, e, and f are the crosstalk coefficients given in Table 5.7. These Equations can be rewritten in a matrices form as given in Equation (5.37).

$$\begin{pmatrix} B' \\ G' \\ R' \end{pmatrix} = \begin{bmatrix} 1 & a & b \\ c & 1 & d \\ e & f & 1 \end{bmatrix} * \begin{pmatrix} B \\ G \\ R \end{pmatrix} \tag{5.37}$$

Finally, the true colour values of B, G, and R were calculated using Equation (5.38).

$$\begin{pmatrix} B \\ G \\ R \end{pmatrix} = inverse \begin{bmatrix} 1 & a & b \\ c & 1 & d \\ e & f & 1 \end{bmatrix} * \begin{pmatrix} B' \\ G' \\ R' \end{pmatrix} \tag{5.38}$$

An example of frame before and after crosstalk compensation was shown in Figure 5.23. It can be seen that the fringe contrast is improved after the compensation.

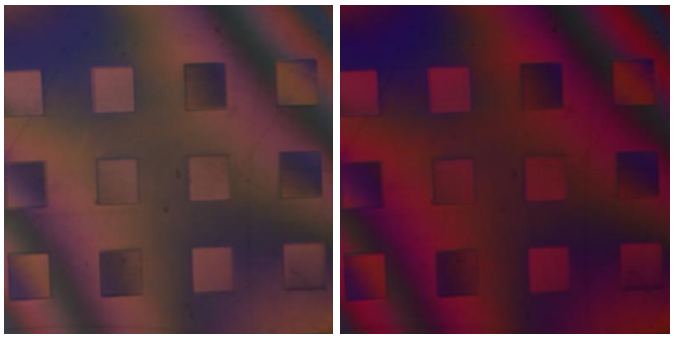

(a) (b)

Figure 5.23 Frame image (a) before crosstalk compensation (b) after crosstalk compensation

5.9 Coherence Length of MPI

The interference fringe of any interferometry method can only be obtained within the coherence length of the deployed light source. The coherence length of MPI was theoretically calculated in chapter three, section 3.8, and it was found to be equal to 96 μm ,which is exceeding the measurement range target of MPI, by considering a Gaussian spectral profile with linewidth equal to 2 nm. The coherence length of MPI was practically measured by monitoring the fringe visibility along range of optical path differences (OPD).

The OPD was scanned 60 μm away from zero OPD by moving the reference mirror using a high-resolution stepper motor for 5 μm for each step. A 2x microscope objective lens was implemented in this experiment, where the depth of focus (DoF) is greater than the scanning distance (DoF = 92 μm).

A tilt angle was introduced to the reference mirror to generate several fringes across the captured field of view where the measurement sample was also a flat mirror. The sinusoidal distribution of the fringes is used to determine the maximum and minimum intensities (I_{ref} and I_{meas}) of constructive and destructive interference to calculate the fringe visibility as given by:

$$\text{visibility} = \frac{I_{\max} - I_{\min}}{I_{\max} + I_{\min}} \tag{5.39}$$

During OPD scanning, a colour interferograms were captured at every 5 μm and decomposed into it is primary RGB colours. The fringe visibility for each colour was calculated as shown in Figure 5.24. The results show that the fringe visibility decreases with increases in the OPD distance.

The visibility of the blue component has the lowest values compared to other components. As such, the coherence length of MPI is limited by the blue component. The fringe visibility of blue almost vanishes at 60 μm. The fringe amplitude for each RGB component and it is corresponding phase are demonstrated at three OPDs positions as shown in Figures 5.25-5.27. It can be seen that the phase retrieval fails at 60 μm for the blue component.

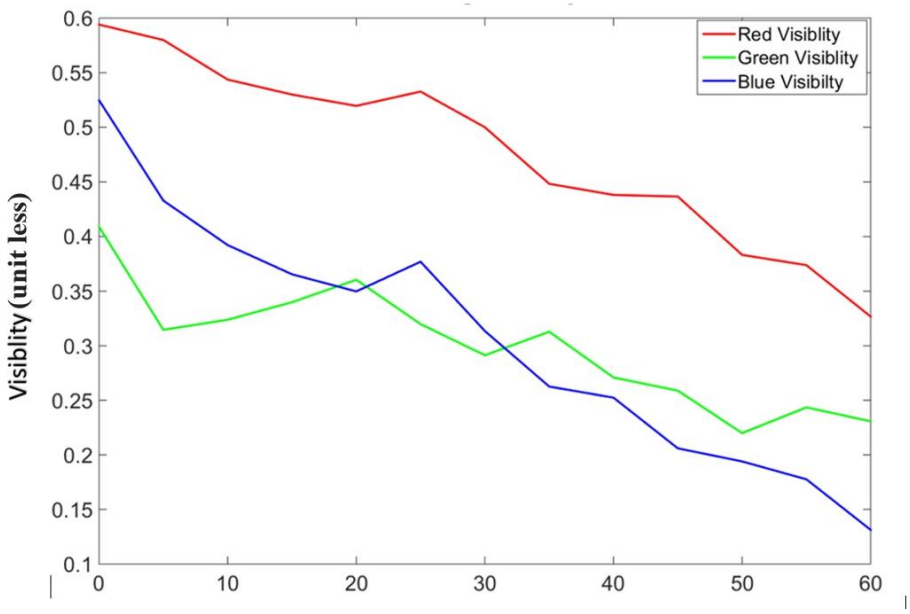

Figure 5.24 RGB fringe visibility along 60 μm OPD

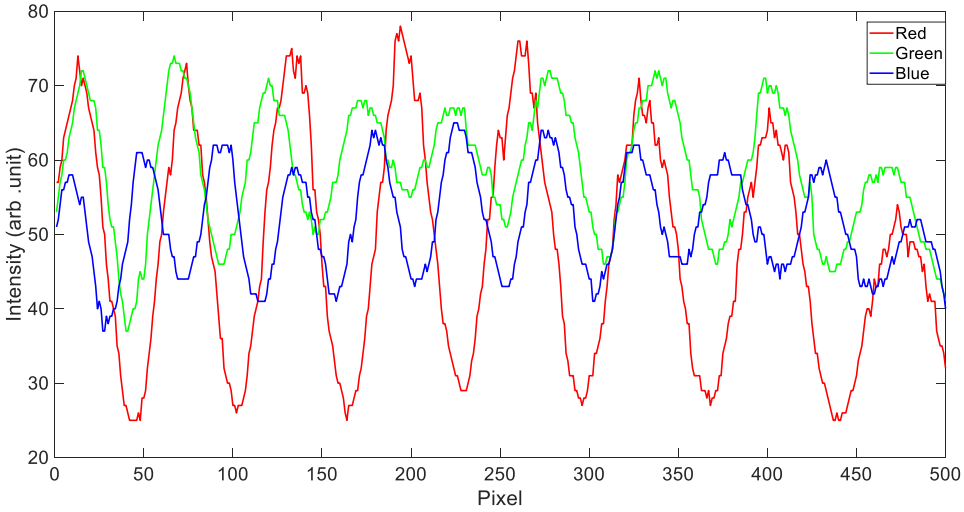

(a)

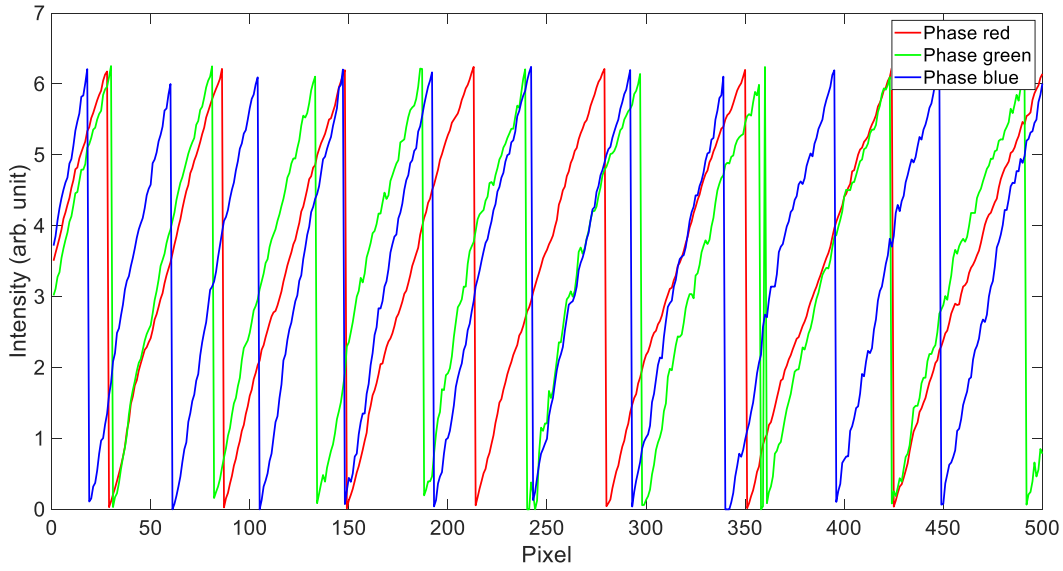

(b)

Figure 5.25 Fringe visibility and warped phase at zero µm OPD (a) RGB fringe (b) RGB phase

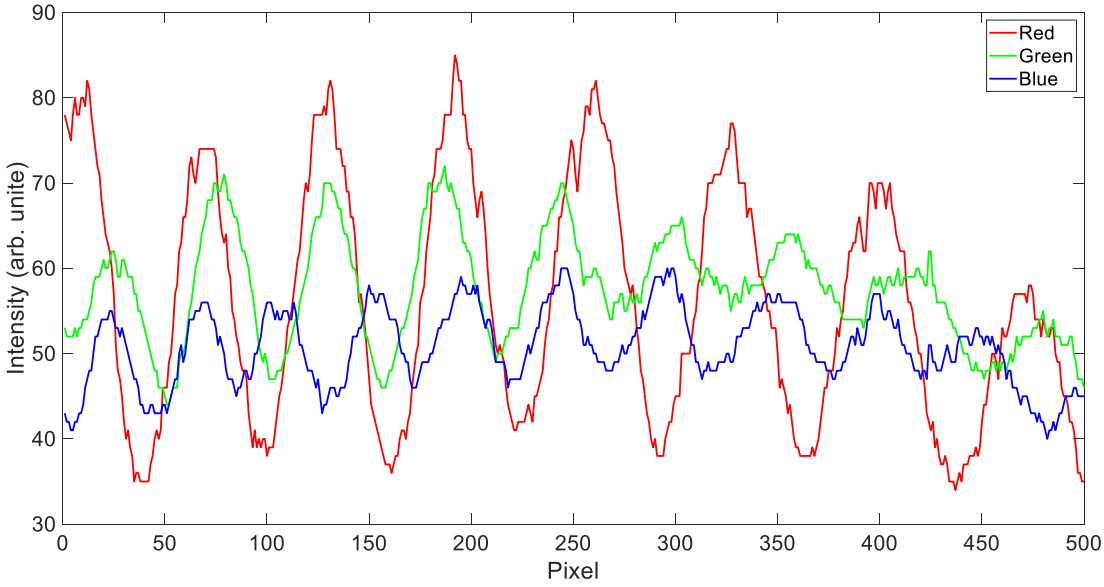

(a)

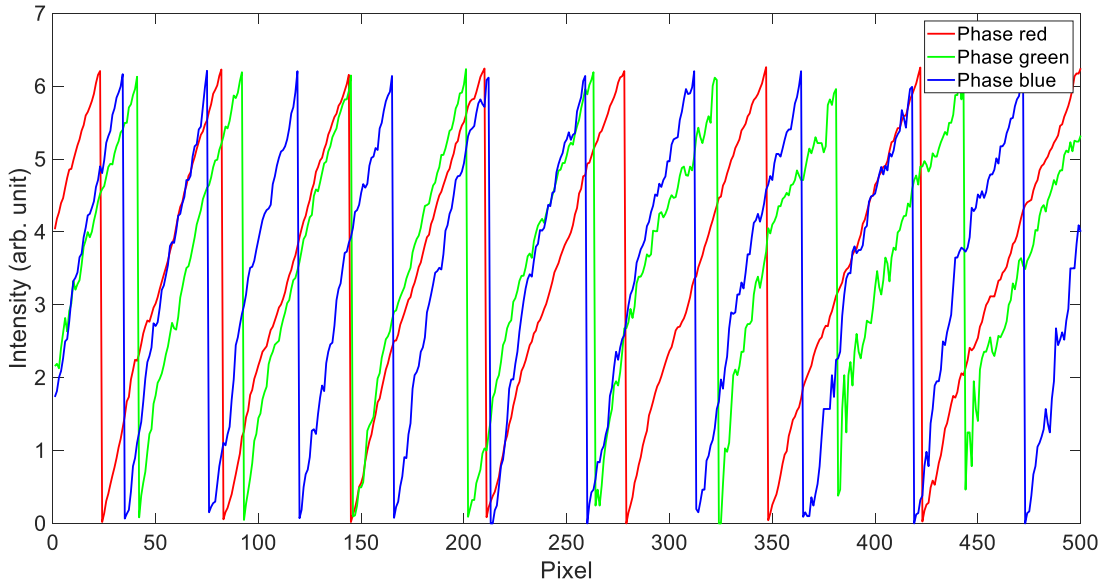

(b)

Figure 5.26 Fringe visibility and warped phase at 30 µm OPD (a) RGB fringe (b) RGB phase

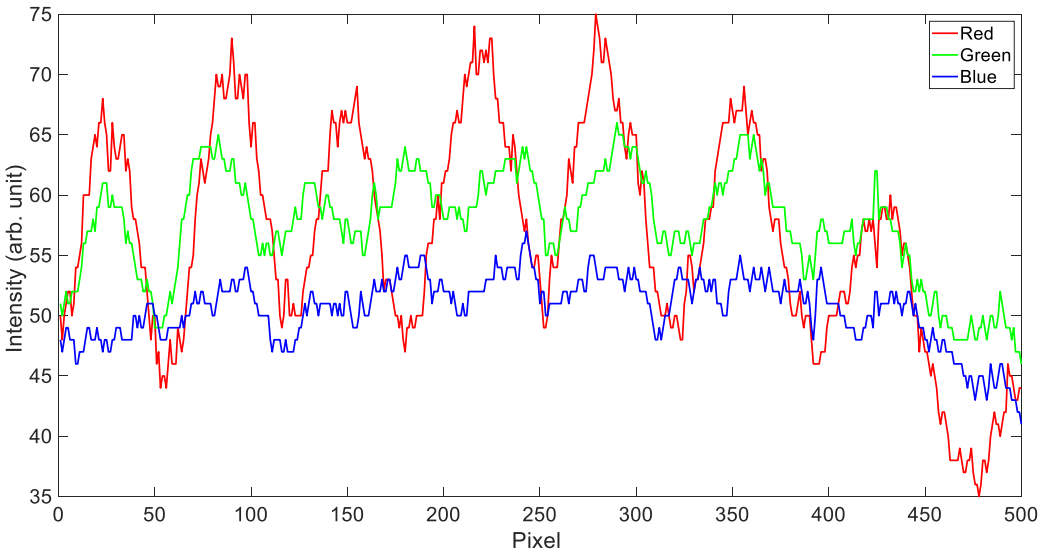

(a)

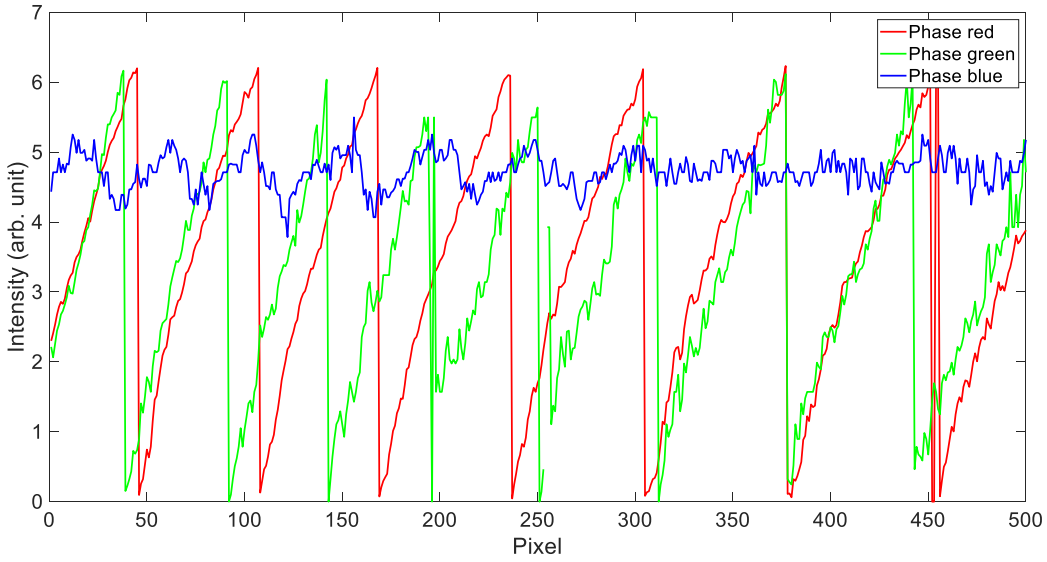

(b)

Figure 5.27 Fringe visibility and warped phase at 60 µm OPD (a) RGB fringe (b) RGB phase

5.10 Summary

This chapter was introduced the MPI optical setup and operation principles as a single shot multi-wavelength polarising interferometer. The AOTF was utilised to filter three primary colour wavelengths (λ_{red}= 643.5 nm, λ_{green}= 543 nm, and λ_{blue}= 453.7 nm) with narrow linewidth equal to 1.784 nm, 1.349 nm, and 0.822 nm respectively. Since the filtration Process is dynamic, this enable the MPI to work at different operation modes: Single wavelength (SPI), Dual wavelength (DPI) and Triple wavelength (MPI). The coherence length was vanished at 60 µm for the blue colour. It was found that the blue has the lowest visibility across different OPD distances.

The polarization optics were used to produce instantaneous phase shift without any mechanical movement. The four MPI observation arms were equipped with different polarization optics to shift the phase 90º sequentially between the colour cameras. A linear polarisers were positioned at angles 45º and 135º in arm one and arm three respectively. A quarter wave-plate was placed in arms two and four followed by linear polarisers positioned at 45º and 135º respectively.

Four Colour Cameras were used at end of monitoring arms. The Colour Cameras were equipped commercial Bayer filter. The colour crosstalk in the Bayer filter is not negligible. The cross talk coefficient was calculated and colour compensation procedure was implement.

Chapter 6: Fringe Analysis and Algorithm

6.1 Introduction

This chapter describes the fringe pattern obtained from the MPI and gives a detailed fringe analysis process. Because the wavelength switchable filtration feature in the AOTF, three experiments/operation modes have emerged from single-shot MPI, which were single wavelength polarising phase shift interferometer (SPI), dual wavelengths polarising phase shift interferometer (DPI), and three wavelengths (RGB) polarising phase shift interferometer (TPI). Each mode required accurate algorithms to extract a wrapped phase information and then unwrapping the phase to determine the surface heights. In general, there is a number of different algorithms have been developed over the last decades to extract the phase, such as, FFT(Takeda *et al.*, 1982), Hilbert transform (Debnath & Kothiyal, 2006), and phase shift interferometer algorithms including four-step and Carre algorithms. In this research, four-step algorithm was used to extract the wrapped phase which then processed by either two-dimensional spatial phase unwrapping method for SPI or best-match method for MPI. The synthetic wavelength was also used to avoid the wrapping phase by constructing longer equivalent wavelength. The surface height was calculated by using fringe order method to enhance the measurement resolution to nano-scale level.

6.2 MPI Operation Modes

The MPI measurement system, as described in chapter 5, was used to measure a precision surface by capturing four colour interferograms in a single shot. The system was operated instantaneously at three separate wavelengths, RGB. The polarisation arrangement, as described in section 5.5 chapter 5, is used to consecutively shift the interferograms 90°, as shown in Figure 6.1. The MPI allowed captured interferograms to be analysed based on the operation mode (SPI, or DPI or TPI). These three modes share the same algorithm for calculating the wrapped phases using four-step method. However, the phase unwrapping is processed by different methods to retrieve the surface heights.

The SPI mode illuminated by single filtered light, either λ_{red} = 630 nm or λ_{green} = 543.7 nm or λ_{blue} = 454 nm. The wavelengths were selected based on compromising between the spectral distribution of the light source and camera's spectral response in order to obtain minimum colours crosstalk.

In DPI mode, three combinations of dual wavelengths were filtered to generate three synthetic wavelengths. However, only one synthetic can be used at a time to measure the surface. The three combinations were (λ_{red}= 630 nm and λ_{green}= 560 nm), (λ_{green}= 560 nm and λ_{blue}= 450 nm) and (λ_{red} = 625 nm - λ_{blue} = 485 nm), the combination of dual wavelengths was chosen based on

compromising between the longest synthetic and less colour crosstalk as discussed in details in chapter 7.

The TPI mode is similar to DPI mode but two synthetic wavelengths are used at the same time to generate even longer third synthetic wavelength to extend the measurement range. The selected RGB illumination wavelengths in this mode were (λred = 630 nm, λgreen = 540 nm, and λblue = 460 nm). The longest synthetic wavelength ($\Lambda_{\text{redgreen}-\text{Greenblue}}$) was obtained from two subs synthetic wavelength ($\Lambda_{\text{red}-\text{green}}\ and\ \Lambda_{\text{green}-\text{blue}}$) to achieve ($\Lambda_{\text{redgreen}-\text{Greenblue}}$= 17.388) μm and expand measurement range to ($\frac{\Lambda_{\text{redgreen}-\text{Greenblue}}}{4}$ =4.347μm) in the same time maintain the minimum colour crosstalk as much as possible.

The TPI mode can also use best-match algorithm to extend the measurement range without even constructing synthetic wavelengths. The MPI illuminated simultaneously by (λ_{red}=643.5 nm, λ_{green} =543 nm, and λ_{blue} = 453.7 nm).

The filtered RGB wavelengths and their spectral linewidths are described in section 5.4 chapter 5. The four colour cameras were triggered at once to capture four colour interferograms, as shown in Figure 6.1. The capturing rate was one frame per second. The CCD colour cameras, type 'MC023CG-SY' with sensor (Sony IMX174, size 1936 * 1216) with a mosaic of colour filters lined up with its pixels.

Equation (6.1) shows the mathematical representation of the (Red-Green-Blue) intensity distribution (Hariharan, 2003).

$$I_{xy(rgb)} = A_{xy(rgb)} + B_{xy(rgb)} \cos(\theta_{xy(rgb)} + \Delta\theta) \qquad (6.1)$$

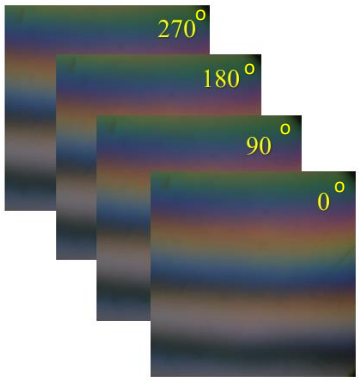

Figure 6.1 Four frames captured simultaneously using four CMOS cameras with a 90° phase shift between each consecutive frame

By considering all pixels in a vertical direction across first RGB frame shown in Figure 6.1, a periodic sinusoidal intensity distribution for red, green, and blue components was obtained as

shown in Figure 6.2 The red, green, and blue components of the colour interferograms were extracted, as shown in Figure 6.3.

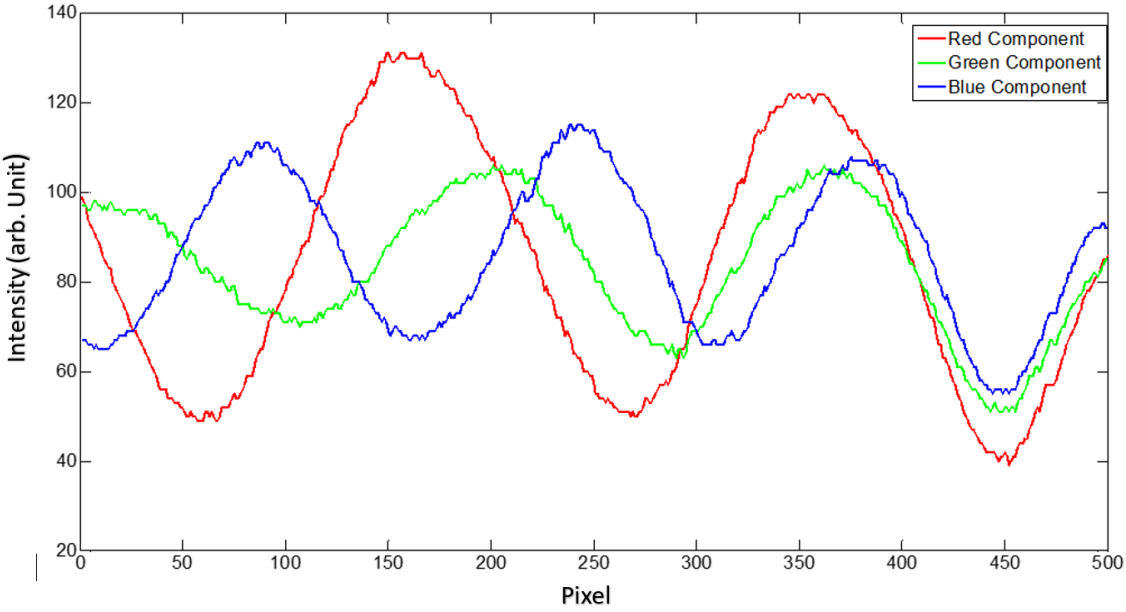

Figure 6.2 Red, green, and blue interference fringe along one profile on the sample

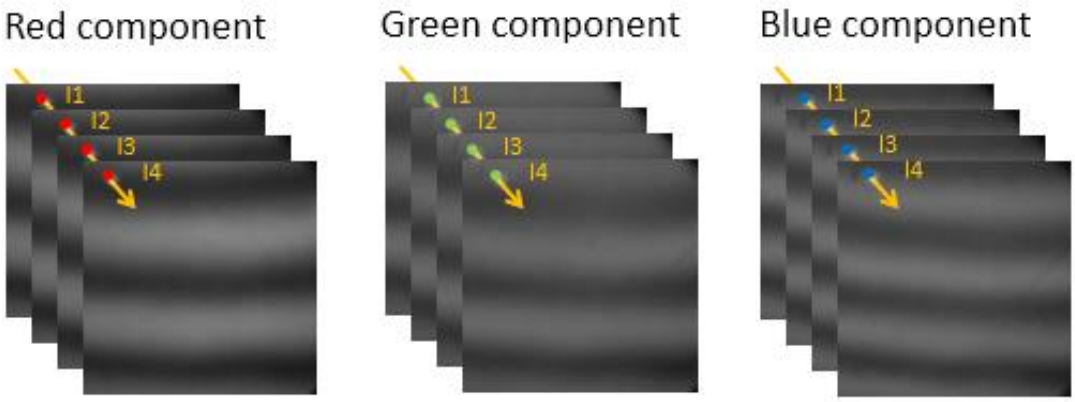

Figure 6.3 Red, green and blue components of each colour interferograms

Each pixel on the tested sample is represented by four intensity values for each colour, as described in Table 6.1

Table 6.1 Intensity values for red, green and blue components extracted from RGB fringe recorded by four colour CMOS cameras

λ = **Red**	λ = **Green**	λ = **Blue**
$I1_{(r)} = A_{(r)} + B_{(r)}\cos(\theta_r + 0)]$	$I1_{(g)} = A_{(g)} + B_{(g)}\cos(\theta_g + 0)]$	$I1(b) = A_{(b)} + B_{(b)}\cos(\theta_b + 0)]$
$I2_{(r)} = A_{(r)} + B_{(r)}\cos(\theta_r + \pi/2)]$	$I2_{(g)} = A_{(g)} + B_{(g)}\cos(\theta_g + \pi/2)]$	$I2(b) = A_{(b)} + B_{(b)}\cos(\theta_b + \pi/2)]$
$I3_{(r)} = A_{(r)} + B_{(r)}\cos(\theta_r + \pi)]$	$I3_{(g)} = A_{(g)} + B_{(g)}\cos(\theta_g + \pi)]$	$I3(b) = A_{(b)} + B_{(b)}\cos(\theta_b + \pi)]$
$I4_{(r)} = A_{(r)} + B_{(r)}\cos(\theta_r + 3\pi/2)]$	$I4_{(g)} = A_{(g)} + B_{(g)}\cos(\theta_g + 3\pi/2)]$	$I4(b) = A_{(b)} + B_{(b)}\cos(\theta_b + 3\pi/2)]$

6.3 MPI Wrapped Phase Calculation

A four-step phase shift algorithm was chosen to determine the wrapped phase for the collected intensity values from RGB interferograms in SPI, DPI, and TPI because it is required four intensity values that phase shifted by $\boldsymbol{\pi}/2$ at each step. This requirement is fulfilled by the MPI. The shifted phase values in MPI using polarisation technique are θ_{rgb}=0, π/2, π, 3π/2:

Table 6.1 can be obtained by substituting each of the four phases into Equation (6.1). Re-arranging these Equations using trigonometry, as given in Appendix F, the original phase value can be obtained as given in Equation (6.2).

$$\theta_{(RGB)} = \tan^{-1}\left[\frac{I_{4-} I_2}{I_1 - I_3}\right] \qquad (6.2)$$

However, the phase here is wrapped and having the limited range between $(-\frac{\pi}{2})$ to $(\frac{\pi}{2})$ because it is inherited in arctangent function. This phase values should be corrected before proceeding with phase unwrapping process because the desired wrapped phase values for the red, green and blue should be within the range from 0 to 2π. By correcting the phase value, the maximum measurement range will be $\frac{\lambda}{4}$. The process of extended the arctangent ambiguity could be done using Table 6.2. Figure 6.4 shows the corrected wrapped phase value of (red, green and blue) within a value between 0 to 2π.

Table 6.2 Modulo 2π phase correction[adapted from (Daniel, 2007)]

Sine	Cosine	Corrected phase $\theta(x,y)$	Phase range
0	+	0	0
+	+	$\theta(x,y)$	0 to $\pi/2$
+	0	$\pi/2$	$\pi/2$
+	−	$\theta(x,y)+\pi$	$\pi/2$ to π
0	−	π	π
−	−	$\theta(x,y)+\pi$	π to $3\pi/2$
−	0	$3\pi/2$	$3\pi/2$
−	+	$\theta(x,y)+2\pi$	$3\pi/2$ to 2π

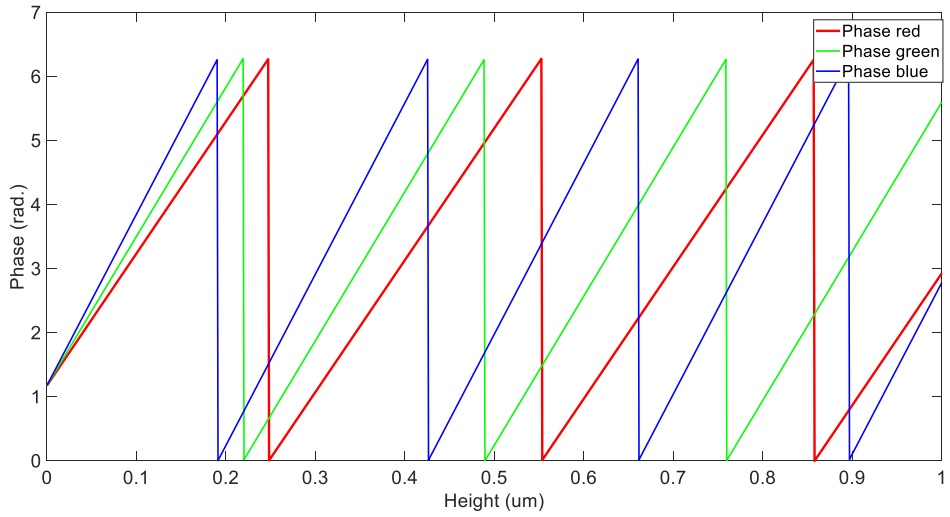

Figure 6.4 RGB wrapped phase determined by four-step algorithm

6.4 Phase Unwrapping in MPI (SPI, DPI, and TPI)

In order to reconstruct the surface topography, a phase unwrapping process is required to remove any 2π discontinuity. The following sections describe phase unwrapping methods that were used in SPI, DPI, and TPI operation modes.

6.4.1 Single Wavelength Interferometer (SPI) Phase Unwrapping

Phase shift interferometry can provide a high accuracy level of measurement that can reach up to $\frac{\lambda}{1000}$ (Ai & Wyant, 1987) when using a single wavelength. However, the vertical measurement range is limited by $\frac{\lambda}{4}$ (Neal *et al.*, 2011), where λ is the wavelength of the light source. For example, when operating the MPI with a single wavelength λ_{red} = 630 nm, the measurement range

is 157.5 nm only. The surface height information is embedded within the phase (θ) as given in Equation (6.3).

$$\theta = \frac{4\pi}{\lambda} h \tag{6.3}$$

Where h is the height of the measured surface at each pixel, which can be calculated by re-arranging the above Equation (6.3) as the following:

$$h = \frac{\theta\lambda}{4\pi} \tag{6.3}$$

Herráez *et al.* (2002) suggested a novel technique for two-dimensional phase unwrapping, which is dependent on 3x3 neighbouring pixels to determine the reliability function for every pixel. Furthermore, the algorithm does not follow a continuous path to perform the unwrapping operation, avoiding unwrapping errors caused by bad data across the measured area. This algorithm, as presented in Appendix G, was employed in MPI for phase unwrapping that can be used for smooth and flat surfaces. Flow chart of the algorithm is introduced in Appendix H. Figure 6.5 shows the simulated interference fringe for titled flat surface profile with maximum height equal to 5 µm and it is corresponding wrapped phase, see Figure 6.5. The algorithm was successfully unwrapped the phase at the discontinuities and retrieved the surface, see Figure 6.6. This algorithm can be used with MPI setup but for single wavelength only.

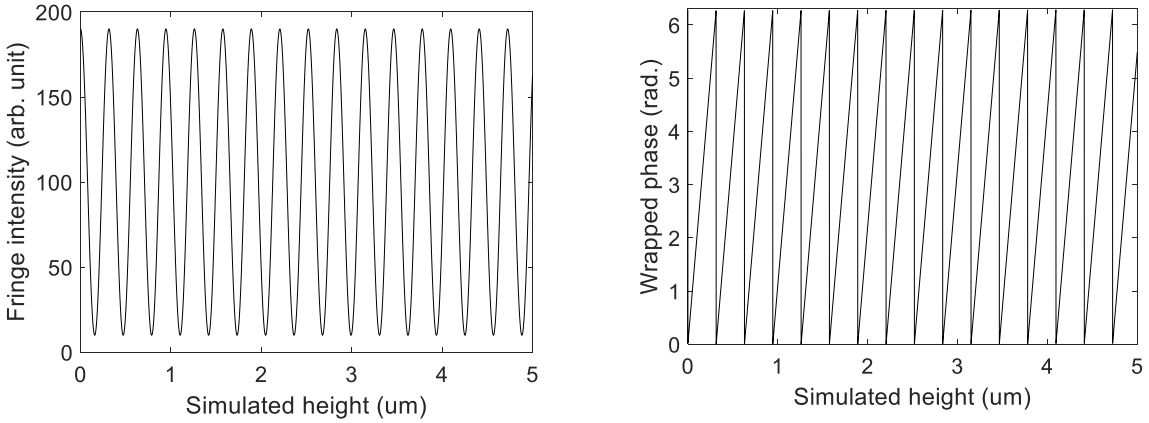

Figure 6.5 SPI simulation a) simulated interference fringe b) calculated wrapped phase

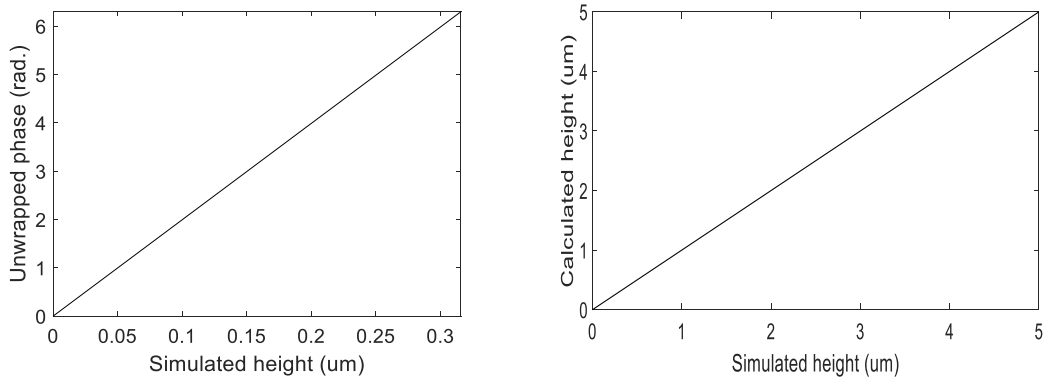

Figure 6.6 Simulation result a) calculated unwrapped phase b) retrieved surface profile

6.4.2 Dual Wavelengths Interferometer (DPI) Phase Unwrapping

The spatial phase unwarping technique that usually used for single wavelength interferometer is not suitable for measuring surfaces with large discontinues exceeding λ/4, as it depends on neighbouring pixels.

Dual wavelength interferometry represents a straightforward technique, which is used to extend the vertical measurement range to $\left(\frac{\lambda_s}{4}\right)$, where $\lambda_s = \frac{\lambda_1 \lambda_2}{|\lambda_1 - \lambda_2|}$ enables the 2π phase ambiguity to expand (Awatsuji *et al.*, 2015; L.-C. Chen *et al.*; North-Morris *et al.*, 2004) the aim of DPI is to extend the measurement range by constructing a synthetic wavelength and synthetic phase generated from two wavelength interferograms.

The synthetic phase is calculated by subtraction the phase value of the shorter wavelength from the longer one at each pixel, as given in Equation (6.4).

$$\theta_{\text{syn}} = \theta_{\text{short}} - \theta_{\text{long}} \tag{6.4}$$

The synthetic wrapped phase θ_{syn} has a slower phase change as compared to the single wavelength phase map. As a result of this subtraction, the phase jumps could appear because of a spatial mismatch between the two wrapped phases' maps (Turko *et al.*, 2017). However, the resultant wrapped phase for synthetic wavelength should be within $0 \leq \theta_{\text{syn}} \leq 2\pi$, so the phase jumps could be corrected by adding 2π to the synthetic phase when it is value is negative, or subtracting 2π from the synthetic phase when their value is higher than 2π, as described below.Finally, the surface height is calculated using Equation (6.5).

$$\theta_{\text{syn}} = \begin{cases} \theta_{\text{syn}} < 0 \rightarrow \theta_{\text{syn}} + 2 * \pi \\ \theta_{\text{syn}} > 2\pi \rightarrow \theta_{\text{syn}} - 2 * \pi \end{cases} \tag{6.5}$$

$$h_{sub} = \frac{1}{2}\left[\frac{\theta \text{syn}\, \lambda_s}{2\pi}\right] \tag{6.6}$$

The dual wavelength technique DPI has been tested by writing a simulation Matlab code, presented in Appendix I, to construct a linear height profile with a range from (0 μm to 2 μm) with a 1 nm step change. The interference signals for each step height have been constructed for RGB wavelengths. Each interference signal was shifted four steps to generate a wrapped phase profile for each colour, see Figure 6.7, using the four-step algorithm described in section 6.3.

The three combinations of dual wavelengths were simulated (λ_{red} = 630 nm - λ_{green} = 540 nm), (λ_{green} = 540 nm - λ_{blue} = 460 nm), and (λ_{red} = 630 nm- λ_{blue} = 460 nm) producing synthetics (3.7 μm, 3.1 μm, and 1.7 μm) sequentially. The simulation result of the synthetic phase map for the three combinations of wavelengths is illustrated in Figure 6.7. The figure clearly shows that

the wrapped phase for synthetic wavelengths had extended 2π interval range compared to the single wavelength phase map. The simulated height result for a single wavelength and the three synthetic wavelengths is shown in Figure 6.8. It shows that the synthetic height is expanded as a result of synthetic phase and wavelength.

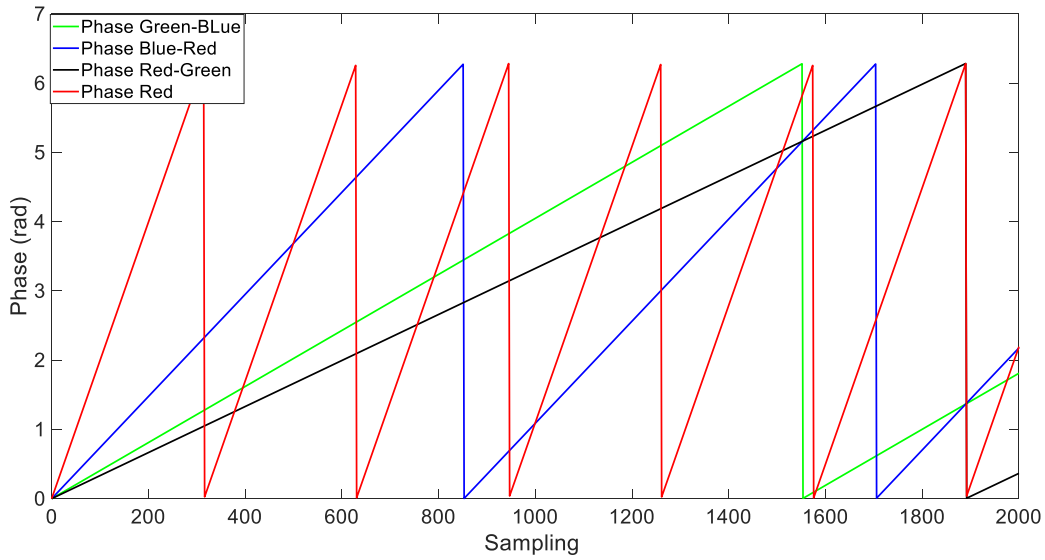

Figure 6.7 Simulated phase for a single wavelength (λ_{red}) and synthetic unwrapped phase for ($\lambda_{red-Green}$, $\lambda_{Green-Blue}$ and $\lambda_{red\ -Blue}$)

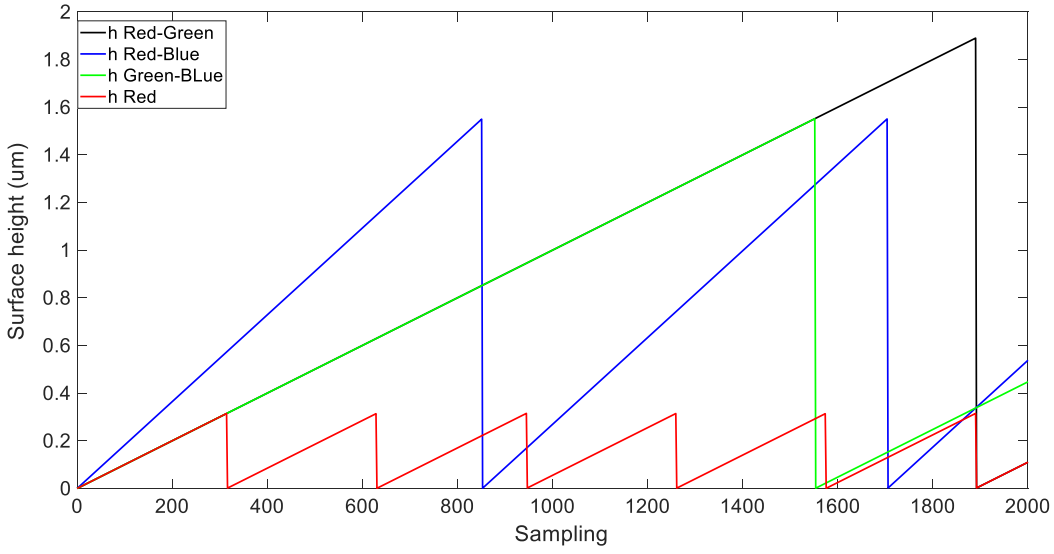

Figure 6.8 Simulation result for the height (h_{red}) and synthetic height ($h_{red-Green,}h_{Green-Blue\ and\ h_{Red-Blue}}$)

The dual wavelength is a simple technique to extend the vertical measurement range; however, the synthetic phase error will be amplified by a factor of $2\frac{\lambda_s}{\lambda_1}$ (Gass *et al.*, 2003). To investigate the noise amplification in dual wavelength, a comparison study was performed between the surface

roughness parameters (R_{pv}) obtained by single wavelength (λ_{red} = 630 nm) and R_{pv} obtained by dual wavelengths (λ_{red} = 630 nm - λ_{green} = 540 nm).

The noise amplification in DPI was tested by simulating interference fringes contaminated by a specific noise level using 'additive white Gaussian noise' Matlab function (Zhang *et al.*, 2018), see Appendix J. The SNR represents the main parameter to control the quality of the generated signal, and it was set at 35 dB. A simulated 900 nm step height surface profile was re-calculated as shown in Figure 6.9, based on the contaminated interference fringes, as given in section 6.4.2. The R_{pv} was calculated, using a SurfStand commercial software package, for a single wavelength (λ_{red} = 630 nm) and dual wavelength (λ_{red} = 630 nm - λ_{green} = 540 nm). The R_{pv} for a single wavelength was 1.2912 nm, while the R_{pv} for the dual wavelength was 11.1623 nm. As such, the surface noise is amplified at least 8 times when the dual wavelength is used.

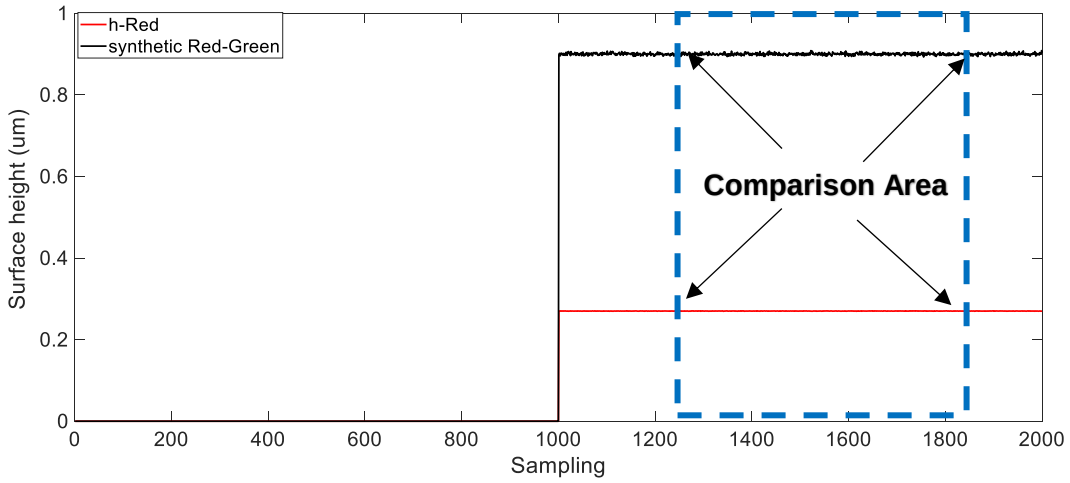

Figure 6.9 Simulation result of 900 nm step-height at 35 dB SNR, using single wavelength and synthetic wavelength

6.4.3 Fringe Order Method: Algorithm Improvement for DPI

As mentioned in section (6.4.2), the phase noise will be amplified by a factor of two to the wavelength magnification in DPI, such that the resultant synthetic phase noise is equal to $\theta_{syn} = 2\pi(\epsilon_1 + \epsilon_2)$, when considering that the single wavelength noise equal to $\theta_1 = 2\pi\epsilon_1$. According to the noise amplification, the measured surface height will be of the actual sample height, and the amplification noise, as illustrated in Equation (6.7). As result of the noise amplification, the system accuracy will be reduced.

$$h_{sub} = h_{\lambda} + \Delta \qquad (6.7)$$

Where the h_{sub} is the synthetic height, the h_{λ} is the surface height was calculated based on single wavelength and Δ noise amplification. A fringe order methods were suggested by (Muhamedsalih

et al., 2018; Xiong *et al.*, 2017) and used to retrain the measurement result of synthetic height to a single wavelength resolution.

The single wavelength phase and the fringe order that calculated from synthetic wavelength can be combined to determine the surface height without noise amplification, yet extended the measurement range provided by the synthetic wavelength, as described in Equation (6.8).

$$h_{\lambda 1} = \frac{\lambda_1}{2}\left[N_{\lambda 1} + \frac{\theta_1}{2\pi}\right] \tag{6.8}$$

Where $N_{\lambda 1}$ is an integer number related to a fringe order that will be added to the single wavelength phase.

The traditional technique to calculate the fringe order is to round the synthetic height to the nearest integer by using Equation (6.9).

$$N_1 = round\left(\frac{2h_{\text{sub}}}{\lambda_1}\right) \tag{6.9}$$

Meanwhile (Muhamedsalih *et al.*, 2018) technique is based on using Equation (6.10),

$$N_{\lambda 1} = round\left(\frac{\lambda_s - \frac{\lambda_1}{2}}{h_1}\right) \tag{6.10}$$

However, several spike jumps can appear due to a wrong estimation of the fringe order number. These jumps can be reduced by employing a correction factor suggested by (Gass *et al.*, 2003) using Equation (6.11).

$$c_1 = round\left(\frac{h_{sub} - h_{\lambda 1}}{\lambda_1}\right) \tag{6.11}$$

Finally, the surface height can be rewritten in the form of Equation (6.12).

$$h_{\lambda 1} = \frac{\lambda_1}{2}\left[N_{\lambda 1} + c_1 + \frac{\theta_1}{2\pi}\right] \tag{6.12}$$

This method can accurately retrieve the surface height by with extended measurement range in the same time cancelling the noise amplification problem, maintaining the resolution of the single wavelength measurement.

In order to study the noise amplification in fringe order method in DPI mode, the noise amplification study of the dual wavelength that described in section 6.4.3 was repeated with the same conditions to check the noise amplification for surface height that is retrieved using DPI and the fringe order method. The simulation result of 900 nm step height is illustrated in Figure 6.10. The R_{pv} for single wavelength Red was (1.6486) while the R_{pv} of Red-Green (3.2973). The

experiment clearly shows that the fringe order method succeeded to expand the vertical range while keeping the resolution closed to single wavelength resolution.

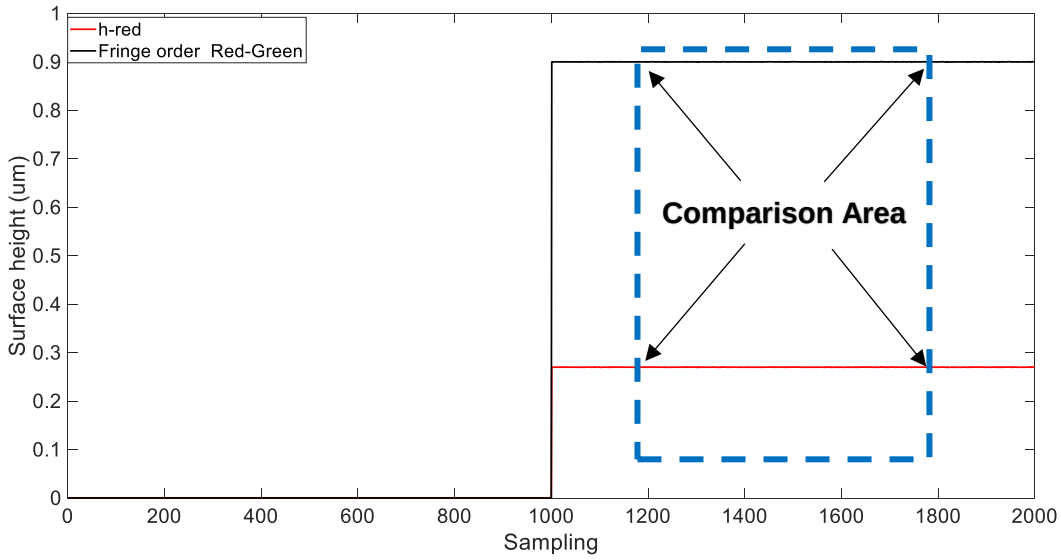

Figure 6.10 Simulation result of 900 nm step height at 35 dB SNR using the fringe order method, for a single wavelength and synthetic wavelength

6.4.4 Triple Wavelength RGB Interferometer (TPI) Synthetic Mode Phase Unwrapping

The concept of the fringe order method combined with synthetic wavelength as discussed in section (6.4.3) was expanded by integrating it with RGB illumination. The technique is a modified version of (Tian *et al.*, 2018). The goal of this experiment is to produce tens of micrometres of synthetic wavelength from two sub-synthetic wavelengths.

The RGB wavelengths were chosen as (λ_{red} = 630 nm, λ_{green} = 540 nm, and λ_{blue} = 460 nm) to make $\lambda_{s_{12}}$ and $\lambda_{s_{23}}$ nearly equal to generate the longest possible synthetic wavelength $\Lambda_{12-23} = \frac{\lambda_{s12}\lambda_{s23}}{|\lambda_{s12}-\lambda_{s23}|}$, which is equal Λ_{12-23} = 17.388 µm. As such the measurement range can be extended to $\Lambda_{12-23}/4$ =4.347 µm.

The single wavelength wrapped phases θ_{red}, θ_{green}, θ_{blue} were calculated using the four-step phase algorithm. The process of unwrapping and correcting the synthetics phases was done according to section 6.4. The surface height H_{12-23} with extended measurement range is computed using Equation (6.13).

$$H_{12-23} = \frac{\Lambda_{12-23}}{2} \frac{\left(\theta_{\text{green}} - \theta_{\text{red}}\right) - \left(\theta_{\text{blue}} - \theta_{\text{green}}\right)}{2\pi} \tag{6.13}$$

As mentioned earlier that the measurement range increase from $\frac{\lambda_1}{4}$ to $\frac{\Lambda_{12-23}}{4}$. This, however, will amplify the phase noise by a factor equal to $2\frac{\Lambda_{12-23}}{\lambda_1}$, which means the phase noise will be magnified 27 times compared to the error of single wavelength when using H_{12-23} directly.
To improve the accuracy of the system fringe, the fringe order method described in Equation (6.12) was used.

$$h_{\lambda 1} = \frac{\lambda_1}{2}\left[N_{\lambda 1} + c_1 + \frac{\theta_1}{2\pi}\right] \tag{6.12}$$

Because the noise amplification is very high, the consequences is that the algorithm fails to estimate the fringe order and jumps appear on the surface. In order increase, the system noise limit when using fringe order method, (Tian et al., 2018) suggested to calculate the fringe order method for H_{12} based on H_{12-23} and then calculate the $h_{\lambda 1}$ based on H_{12}. The maximum noise limit is increased from $\frac{\lambda_1}{4\Lambda_{12-23}}$ to $\frac{\lambda_1}{4\lambda_{s_{12}}}$, because the algorithm was calculate the resolution of single wavelength based on the resolution $\lambda_{s_{12}}$ which is have low noise comparing to the noise of Λ_{12-23}.

In order to investigate the noise amplification in TPI mode with fringe order method, the TPI using RGB (λ_{red} = 630 nm, λ_{green} = 540 nm, and λ_{blue} = 460 nm) were simulated using Matlab code presented in Appendix K. The wrapped phases for red, green, and blue were calculated using the four-step algorithm. The synthetic wavelengths and synthetic phases for (red-green) and (green-blue) were calculated using the same procedure described in section 6.3. The longest synthetic wavelengths were derived from the two sub synthetic wavelengths, and the most extended synthetic height (H_{12-23}) height was calculated using Equation (6.13).

First transition (h_{rg}) height was calculated using Equation (6.*12-a*) based on synthetic height H_{12-23} using the fringe order method, which is described in section 6.4.3. Next, the final transition $h_{\lambda 1}$, which is based on transition h_{rg}, was calculated using Equation (6.12-b) and the same fringe order method.

$$h_{rg} = \frac{\lambda_{rg}}{2}\left[N_{rg} + c_{rg} + \frac{\theta_{rg}}{2\pi}\right] \tag{*6.12-a*}$$

$$h_{\lambda 1} = \frac{\lambda_r}{2}\left[N_{\lambda 1} + c_{\lambda 1} + \frac{\theta_{\lambda 1}}{2\pi}\right] \tag{6.12-b}$$

The simulation result shows that fringe order retrieves a surface height of 4000 nm with the resolution of a single wavelength (less than few nanometer). Figure 6.11 shows the simulation result of surface height H_{12_23}, which is calculated using Equation (6.13), including the noise amplification. Figure 6.12 shows the simulation result of surface height $h_{\lambda 1}$ calculated by Equation (6.12-b), which is overcome the noise amplification problem.

The R_{pv} surface parameter for $H_{12\text{-}23}$ was 146.1582 nm, while the R_{pv} for the second transition height h_r was 0.88 nm. The experiment clearly shows that the fringe order method succeeded to expand the vertical range and measure 4000 nm while keeping the resolution close to single wavelength resolution.

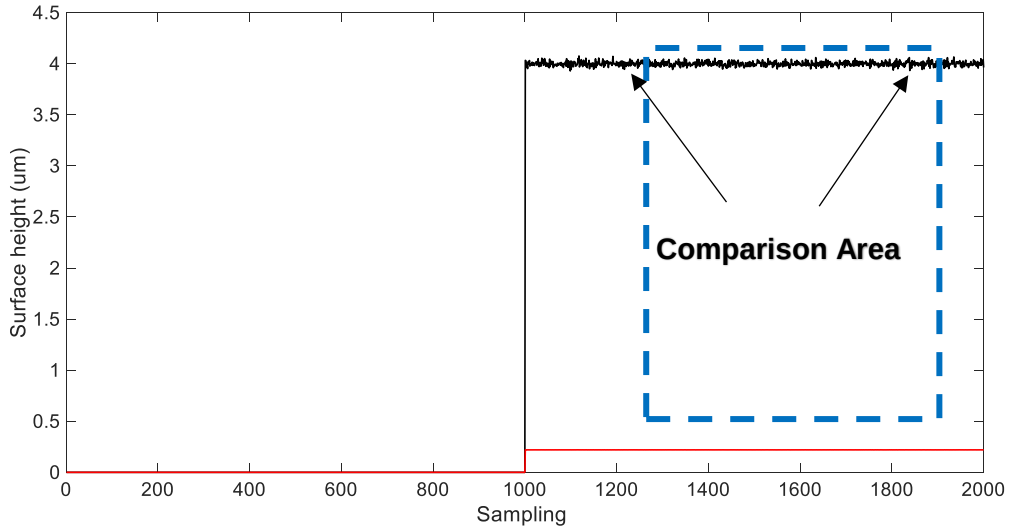

Figure 6.11 Simulation result of 4000 nm step height at 35 dB using standard synthetic wavelength phase unwrapping method

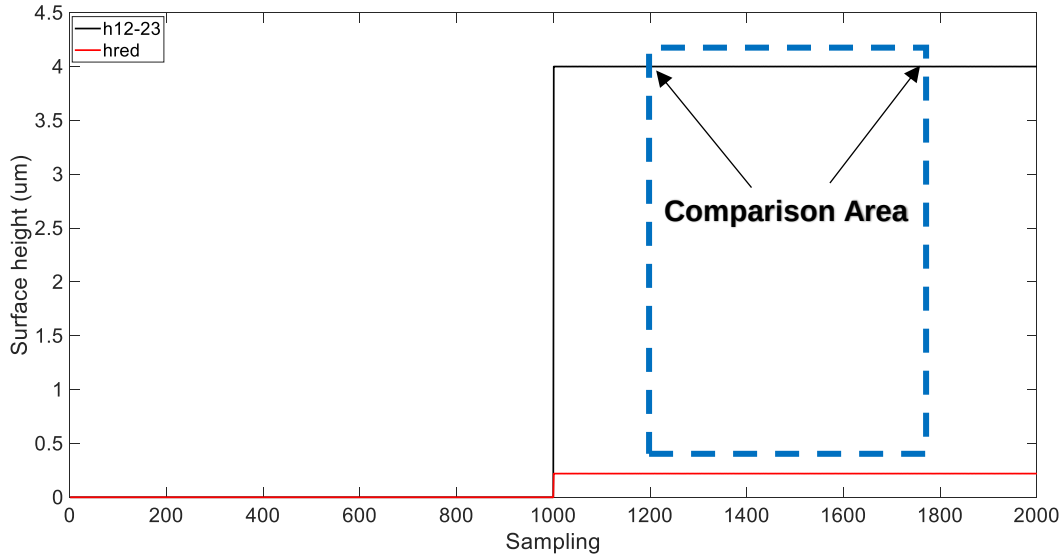

Figure 6.12 Simulation result of 4000 nm step height at 35 dB SNR using fringe order method

6.4.5 TPI Phase Unwrapping Using Non-Synthetic Wavelength

As mentioned earlier in chapter 4, target specification will investigate methods to extend the measurement range to optimally cover depth of focus of the objective lens. This means that the interferometer is 2π phase ambiguity free or has a vertical measurement range of tens of

micrometres. This was the motivation to investigate a technique that is able to remove or extend the height ambiguity that is present in all single shot single wavelength phase shift interferometer. A phase unwrapping method (Kitagawa, 2010) based on finding a certain fringe order that makes the surface height at the three colours was employed in MPI, noted as "best match" method. The fringe order can be determined by best matching the height values for three colours, given in Equations (6.14, 6.15, and 6.16), at different fringe order ni.

$$h_{red} = (\frac{\lambda_{red}}{2})(\frac{\theta_{red}}{2\pi} + N_r) \quad (6.14)$$

$$h_{green} = (\frac{\lambda_{green}}{2})(\frac{\theta_{green}}{2\pi} + \mathrm{N}_g) \quad (6.15)$$

$$h_{blue} = (\frac{\lambda_{blue}}{2})(\frac{\theta_{blue}}{2\pi} + \mathrm{N}_b) \quad (6.16)$$

Where θ the phase, and λ is is the wavelength.

The unknown fringe order n was examined at a wide integer range (e.g. n > 100) so that the three candidate heights (h_{red},h_{green}, and h_{blue}) matched the best using the following condition:

$$h_{red} = h_{green} = h_{blue}$$

By solving the Equations (6.14-6.16) using trial and error to find the best-match heights, the interference order for each colour can be determined using Equation (6.17). Thus the 2π phase ambiguity problem can be overcome.

$$N = (\frac{h2}{\lambda}) - (\frac{\theta}{2\pi}) \quad (6.17)$$

Finally, the surface height can be calculated, using Equation (6.18), with the resolution of the single wavelength, but with measurement range can cover the depth of focus of objective lenses.

$$h = (\frac{\lambda}{2})\left(\frac{\theta}{2\pi} + N\right) \quad (6.18)$$

The best match technique was used to unwrap the phase produced by the four-step algorithm for λ_{red} =643.5 nm, λ_{green} =543 nm, and λ_{blue} = 453.7 nm . A surface height range (0-5 μm) was simulated to produce the interference colour fringes, see Figure 6.13, using a Maltab code as given in Appendix A.

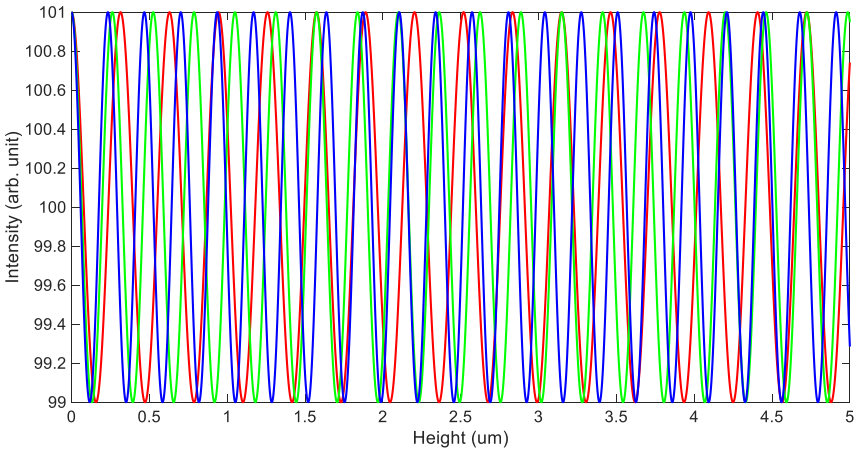

Figure 6.13 Simulated RGB interference fringes at different heights

Although, the RGB wrapped phase maps can be found, see Figure 6.14.

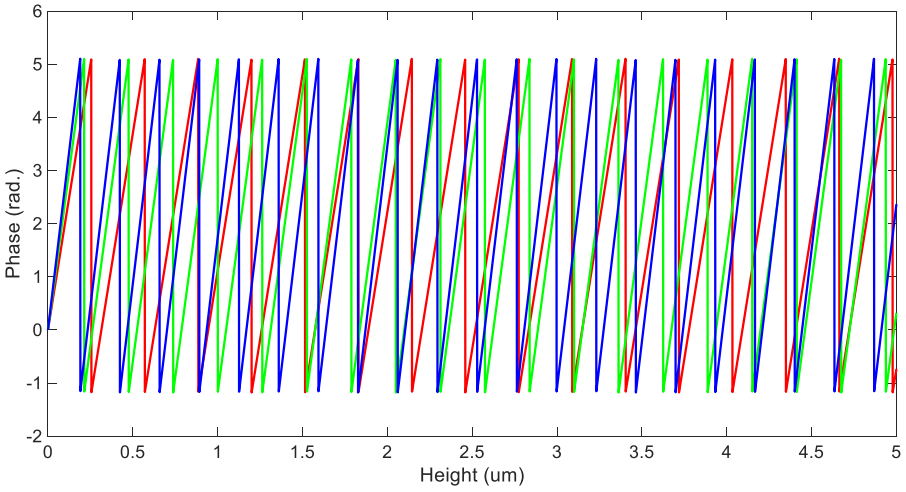

Figure 6.14 Calculated wrapped phase for each colour

Although, the Fringe order number of the three colour can be found, see Figure 6.15.

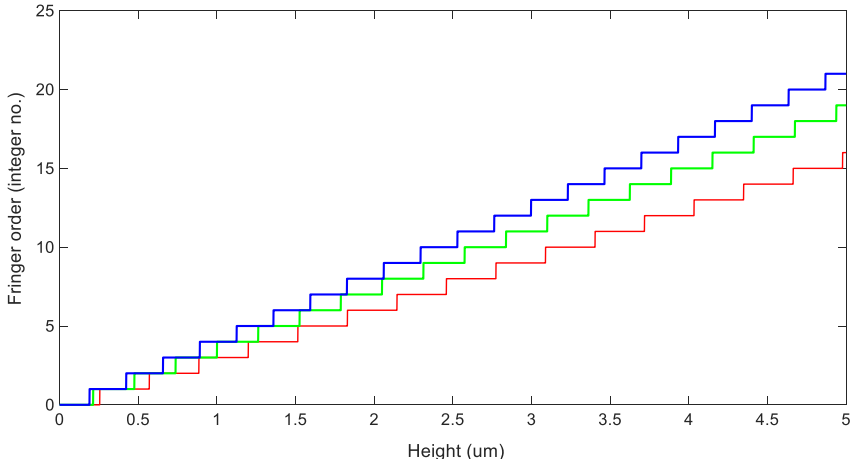

Figure 6.15 Calculated fringe order for RGB at height (0 to 5 µm)

The algorithm succeeded to determine the simulated surface height up to 5-µm height with nanometre resolution as shown in Figure 6.16. This algorithm has been successfully tested by much greater height up to 100 µm as explained in appendix (A).

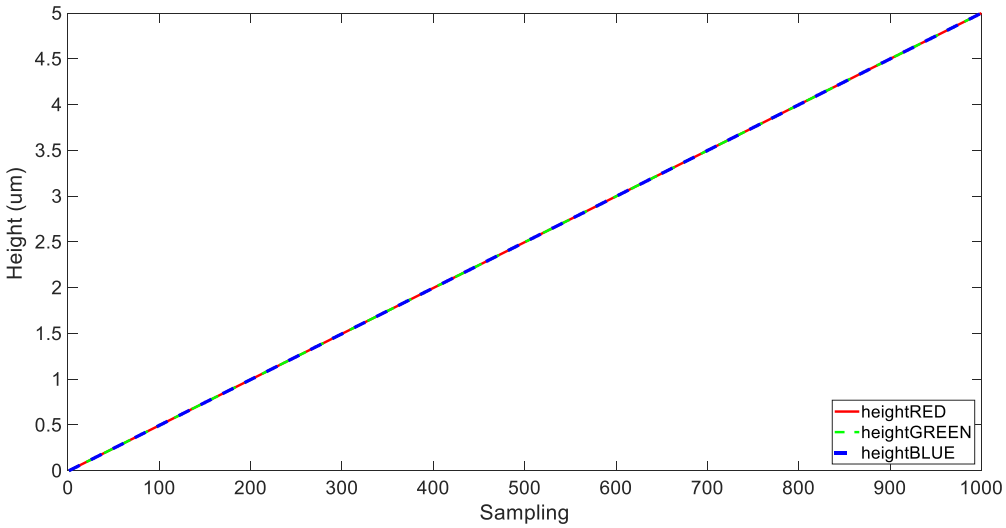

Figure 6.16 Simulation result using best match method

Numerous sources of error are expected to be convolved with the operation of MPI in the actual world. This error could reduce the signal-to-noise ratio (SNR) of the MPI system. A study was done to evaluate the robustness of the best match method to the additive noise. A range of noise level (from 10 dB to 100dB) was generated using Matlab additive white Gaussian noise function (awgn) and added to the simulated signal, as given in Appendix L. Figure 6.17 shows the error in the retrieved surface height when originally fixed at 5 µm within SNR range. The result demonstrates that when the SNR≤ 51 dB in the colour interference fringes, the algorithm fails to retrieve the generated surface.

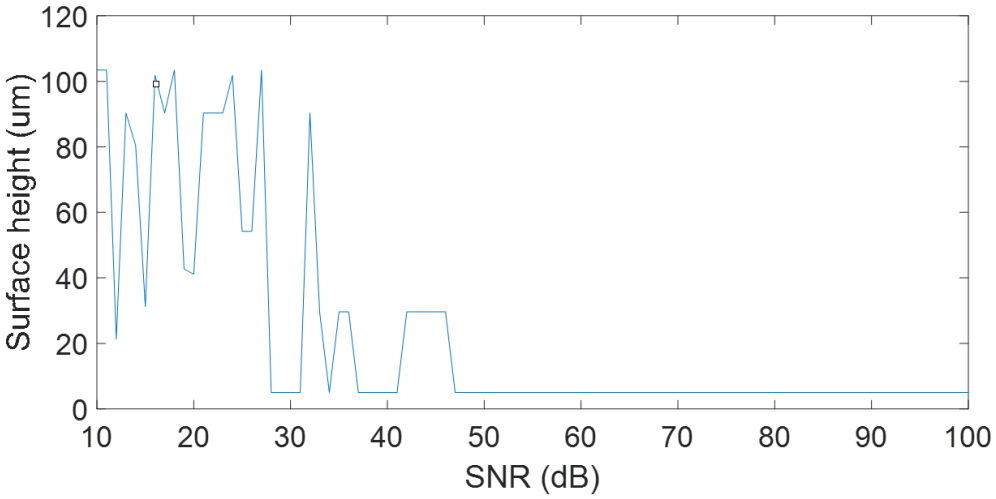

Figure 6.17 One alterations: Best match performance at different SNR when height = 5 µm

A study was done to evaluate the probability of success the algorithm to retrieve 5 um surface height after added different value white Gaussian noise function (awgn) and run the algorithms for one thousand of iteration attempts. Table 6.3 illustrate the ratio of successful retrieve the surface height at specific SNR.

Table 6.3 The ratio of successfully retrieve service height at specific SNR for thousands of iteration

SNR dB	Ratio of Correct Surface Height (1000 iteration)
53	100 %
52	100 %
51	99.9 %
50	98 %
49	97.9 %

6.5 Summary

This chapter introduces the algorithms were used in single shot multi-wavelength phase shift interferometer MPI, with three operation modes namely (SPI, DPI, and TPI). The three modes were sharing the same algorithm for calculating the wrapped phase while it has different phase unwrapping techniques.

The SPI mode is dedicated for measuring flat surfaces, spherical surface and step height (having vertical range $< \lambda/4$) with very high vertical resolution up to the fraction of nanometer. Dedicated phase unwrapping algorithm which depends on neighbour pixel was employed to correct this limitation when measuring a tilted flat surface or concave surface.

The DPI mode was simulated to increase the measurement range in MPI. The DPI was capable the MPI to measure structure surface with an extended measurement range up to $\frac{\Lambda_{\text{synth}}}{4}$; however, the measurement noise will be increased by a factor equal to the twice of wavelength amplification. The fringe order method was used in DPI to extend the measurement range while keeping the resolution closed of the single wavelength. The vertical resolution in DPI can be improved from 10^{th} of nanometres to few nanometre when using a fringe order method.

The concept of DPI was expanded using the information of three wavelengths (RGB) to generate the longest synthetic from two sub-synthetics wavelengths. The vertical measurement range was expanded to $\approx 4\mu$. The fringe order method was employed again to retrieve the area measurement with a resolution of the single wavelength.

TPI RGB (Non-Synthetic modes) were simulated based on two techniques (Best-Fit) and (Best-Match) technique. The two techniques were based on the phase information of the three wavelengths (RGB) to calculate the fringe order. The simulation result shows that the two methods

can remove the height ambiguity with keeping the resolution closed of the single wavelength. The capability of each technique to retrieve the surface at different SNR was checked. The study shows that the (Best-match) technique give a better result than (Best-Fit) at low SNR.

Chapter 7: MPI Measurement Result

7.1 Introduction.

This chapter verifies the performance of the MPI system proposed in Chapter 5, by measuring precision standard samples. Interferograms algorithms described in Chapter 6 are used to analyse the interference signal and determine the surface topography. The system operation is based on combining RGB interferometer and polarising interferometer in one optical setup. Four shifted colour interferograms are obtained at a single exposure. The MPI has three operation modes; it can operate as a single wavelength polarising interferometer (SPI), dual wavelength polarising interferometer (DPI), and triple/RGB polarising interferometer (TPI). Measurement results at each operation mode are presented and discussed in this chapter. The system noise is also evaluated and quantified.

Three types of sample, namely cross grating, flat surface and step height were measured using the MPI. The same samples were measured using a commercial Coherent Correlation Interferometer (CCI) manufactured by Taylor Hobson Ltd with a 5X microscope objective lens.

7.2 Measurement Results

The measurement results of the three-operation mode of MPI (SPI, DPI and MPI) were illustrated in this chapter in order to investigate the performance of each mode in terms of areal measurement. Different precisions standard sampled were measured and registered in this chapter.

7.2.1 Measurement Result of SPI

A standard step height sample from VLSI Inc., having 43.7nm ± 1.4nm step height at single wavelength operation (SPI) mode, was measured and evaluated according to ISO 5436, using commercial software (SurfStand) which is developed by university of Huddersfield. The aim of using single wavelength measurement is to investigate the performance of the Polarising interferometer only, without any potential error that may occur due to multiplexing more wavelengths, which could cause colour crosstalk in the RGB camera. Three primary wavelengths, Red: 643.7 nm, Green: 543.7 nm and Blue: 454 nm, were operated separately for measuring the same spot at each wavelength.

The measurement was done using 2X objective lens, allowing long depth of focus up to 96 μm. Figure 7.1 illustrates the SPI areal measurement result with cross section profile when it is illuminated by Red wavelength. The wrapped phase determination was done using the four-step algorithm. The measurement step height was found to be 42.29 nm for Red giving a step error equal to 1.4 nm, while it shows step height values equal to 40.70 nm using Green and 42.39 nm using Blue, giving error values equal to 3 nm and 1.3 nm respectively as compared to the value

the that provided by the sample manufacturer. All MPI measurement result were evaluated using (SurfStand) software based on ISO 5436-1. The detailed procedure is shown in Appendix M.

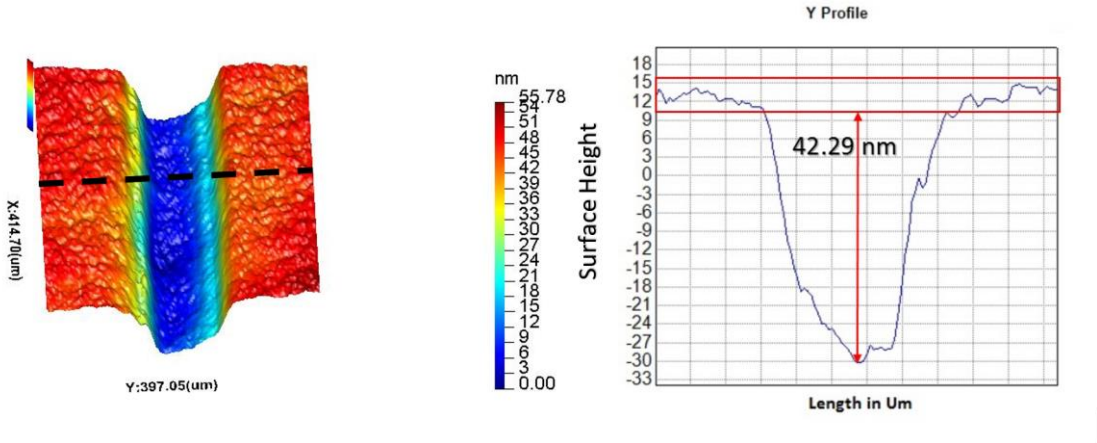

Figure 7.1 SPI mode measurement results for 40nm standard VLSI step height sample using Red-643.7nm and four-step algorithm (a) areal measurement (b) cross-sectional profile

The same sample was measured by CCI and evaluated using the same ISO 5436 that build in (SurfStand) software. The step height measurement was found to be 42.55 nm, as shown in Table 7.1. The results show good agreement by comparing the measurements of CCI and MPI. The maximum error is less than 5 nm, proving that the polarising interferometer works precisely for the primary wavelengths.

Table 7.1 Measurement result step comparison between SPSI (Red-G7.4reen-Blue) and CCI for 40nm step height

ST	Red- (λ643.7)nm	Green- (λ 543.7) nm	Blue- (λ 454)nm	CCI	ST-RED	ST-Green	ST-Blue
43.7 ±1.4nm	42.29nm	40.7nm	42.399nm	42.55 nm	1.4 ±1.4nm	3 ±1.4nm	1.3 ±1.4nm

ST: Step height values (nm) ±0expanded uncertainty.

CCI: Coherent Correlation Interferometer.

ST-RED: Abs error |ST-RED| Red (nm).

ST-Green: Abs error | ST-GREEN| Green (nm).

ST-Blue: Abs error |ST-BLUE| BLUE (nm).

In order to demonstrate the SPI capability to measure a continuous surface (i.e. no height jump > λ/4), a concave mirror was measured using the SPI. A fast two-dimensional phase-unwrapping algorithm as described in section (6.4.1) was successfully used to unwrap the phase and determine the surface height. The areal surface topography and a corresponding surface profile are demonstrated in Figure 7.2.

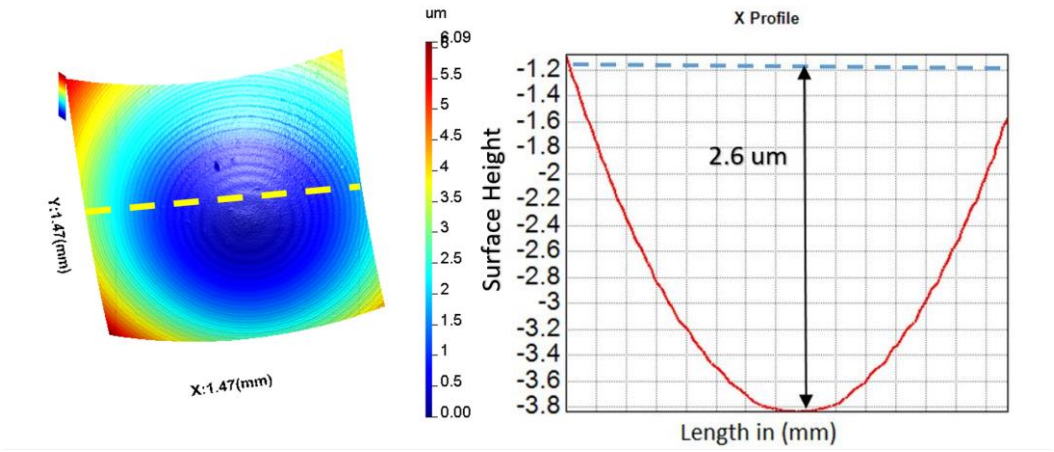

Figure 7.2 SPI mode measurement result for concave mirror using single wavelength (λ =630nm) and dedicated phase unwrapping algorithm (a) areal measurement (b) cross-sectional profile

7.2.2 Measurement Result of DPI

As was mentioned earlier, the MPI system was operated at dual wavelength operation mode (DPI) in order to extend the 2π ambiguity range without any mechanical movement (Al-Bashir1 *et al.*, 2018). A three combination of dual wavelengths have been filtered out by AOTF, the first one (Red 630 nm, Green 560 nm) in order to produce synthetic wavelength equal 5.04 μm, extending the measurement range to ≃1.26 μm. The second combination is (Green 560 nm, Blue 450nm) which produces a shorter synthetic wavelength equal 2.29 μm, but with less crosstalk and system noise, extending the measurement range to ≃ 0.57 μm. The final combination of dual wavelengths was (Red 625nm, Blue 485 nm) which produces the shorter synthetic wavelength equal 1.714 μm to extend the measurement range to ≃ 0.42 μm.

Three sample grating sample with step heights equal to 1264 ±4nm, 502.0 ±4nm and 185.9±2.3 nm have been measured using the dual wavelength combinations. The measurement has been done using 2X objective lens and evaluated using ISO 5436. The results demonstrate that the Red-Green combination has a measurement error of 86 nm, while with the Green-Blue combination, the average error reduces to 27.1 nm and finally the Red-Blue gives an error of 18.9 nm.

The measurement results of 185.9 nm step height illuminated by Red-Green, Green-Blue and Red-Blue are shown in Figures 7.3, 7.4 and 7.5 respectively. The measurement topographies of 1264 ±4nm and 502.0 ±4nm step height samples are presented in Appendix N. The samples have also been measured by CCI to generate more reference measurements to verify DPI performance.

The measurement results are illustrated in Tables 7.2. The errors are presented for different height value. It can be seen that the error for Red-Green light combinations is the highest among the combinations. The degradation in signal-noise-ratio, due to crosstalk between colours and synthetic wavelength phase noise amplification, as described in Chapters 5 and 6, can be

contributors to the measurement error. It has been found that the red crosstalk is maximum (35%) in the Green Bayer filter, also the noise amplification factor for Red-Green was found to be 32 compared to the single red colour. All measurement result shown in Figures 7.3-7.6, shows a batwing around at the edge of step height, this common in multi wavelengths interferometers. The batwings were filtered out before calculate the surface height using (SurfStand) software, after that the surface is levelled to remove the variation in the surface using the (SurfStand) software; finally the step height was measured according to ISO 5436-1.

The fringe order method described in section (6.4.3) has also been used to retrieve the surfaces measured using dual wavelengths. The results demonstrate that error was significantly improved to be less than 10 nm and even beyond few nanometre at Green-Blue illumination as shown in Figure 7.6 and illustrated in Table 7.3. This is mainly because the system vertical measurement resolution is limited by a single wavelength resolution only, avoiding any noise amplification factors.

Table 7.2Measurement results of DPI (Red-Green, Green-Blue, Red-Blue) and CCI for NPL cross grating using standard synthetic phase unwrapping method

ST	DPI RG (nm)	DPI GB (nm)	DPI RB (nm)	CCI (nm)	ABS DPIRG– NPL	ABS DPIGB – NPL	ABS DPIRB – NPL	ABS DPIRG – CCI
185.9 ±2.3nm	257.0	217.3	167	192.1	71.1 ±2.3 nm	20.9 ±2.3 nm	18.9 ±2.3 nm	64.9 nm
502.0 ±4.1nm	588.3	475.4	Failed	516.4	86.3 ± 4.1nm	27 ± 4.1 nm	Not applicable	41.9 nm
1264 ±4nm	1213.2	Failed	Failed	1268	50.8 ± 4 nm	Not applicable	Not applicable	54.8 nm

Table 7.3 Measurement results of DPI (Red-Green, Green-Blue, Red-Blue) and CCI for NPL cross grating using fringe order method

ST	DPIRG (nm)	DPIGB (nm)	DPIRB (nm)	ABS DPIRG– NPL	ABS DPIGB – NPL	ABS DPIRB – NPL
185.9 ±2.3 nm	189.5	187.7	192.0	3.6 ±2.3 nm	1.8 ±2.3nm	6.1 ±2.3 nm
502.0 ±4.1nm	511.8	498.0	Failed	9.8 ±4.nm	4 ± 4.1nm	Not applicable
1264 ±4nm	Fail	Fail	Fail			

ST: Step height value (nm) ±0 expanded uncertainty.

DPIRG: DPI using Red-Green illumination.

DPIGB: DPI Green-Blue illumination.

DPIRB: DPI Red-Blue illumination.

CCI: Measurements result of Coherence Correlation Interferometer (CCI).

ABS DPIRG – NPL: Abs error |DPI – ST | at Green-Blue.

ABS DPIGB – NPL: Abs error |DPI – ST| at Red-Green.

ABS DPIRB – NPL: Abs error |DPI – ST| at Red-Blue.

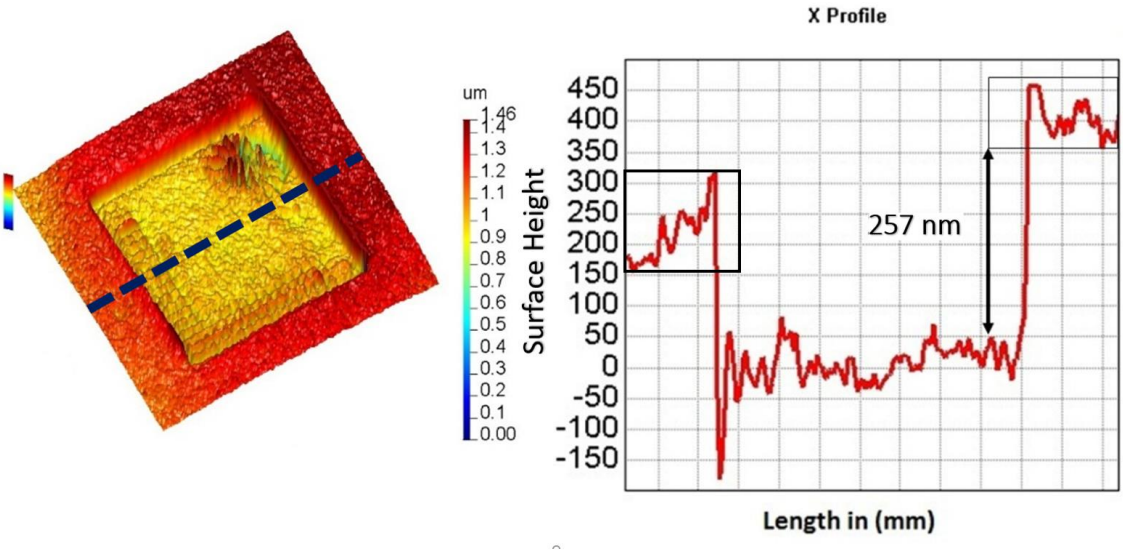

Figure 7.3 DPI measurement for cross grating depth 185.9 nm standard sample, illuminated by red and green sources. (a) areal measurement (b) cross-sectional profile

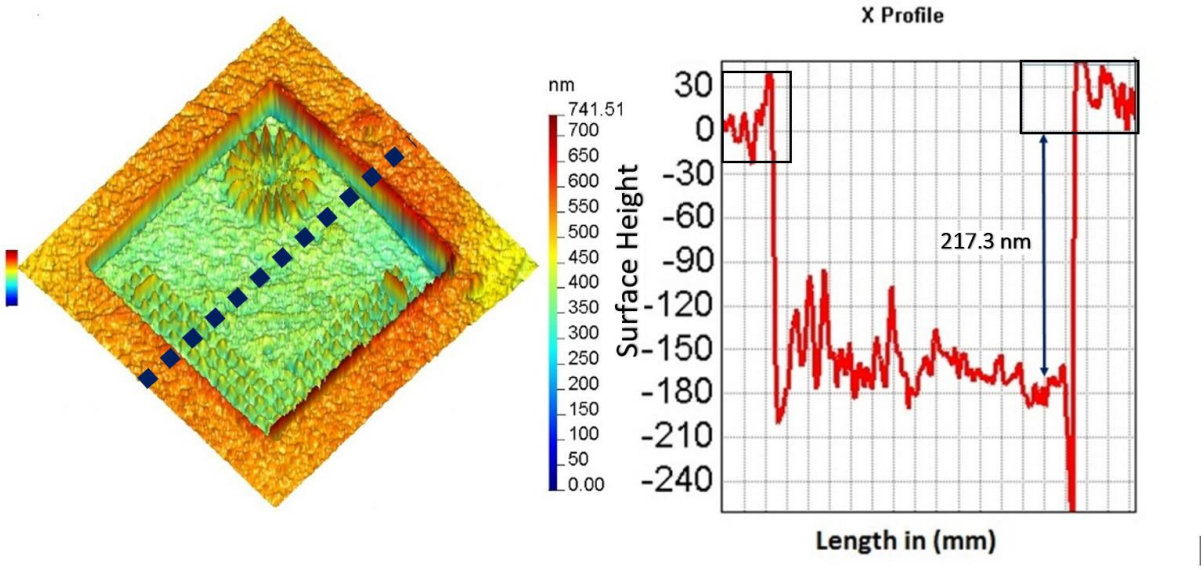

Figure 7.4 DPI measurement for cross grating depth 185.9 nm standard sample, illuminated by Green and Blue sources. (a) areal measurement (b) cross-sectional profile

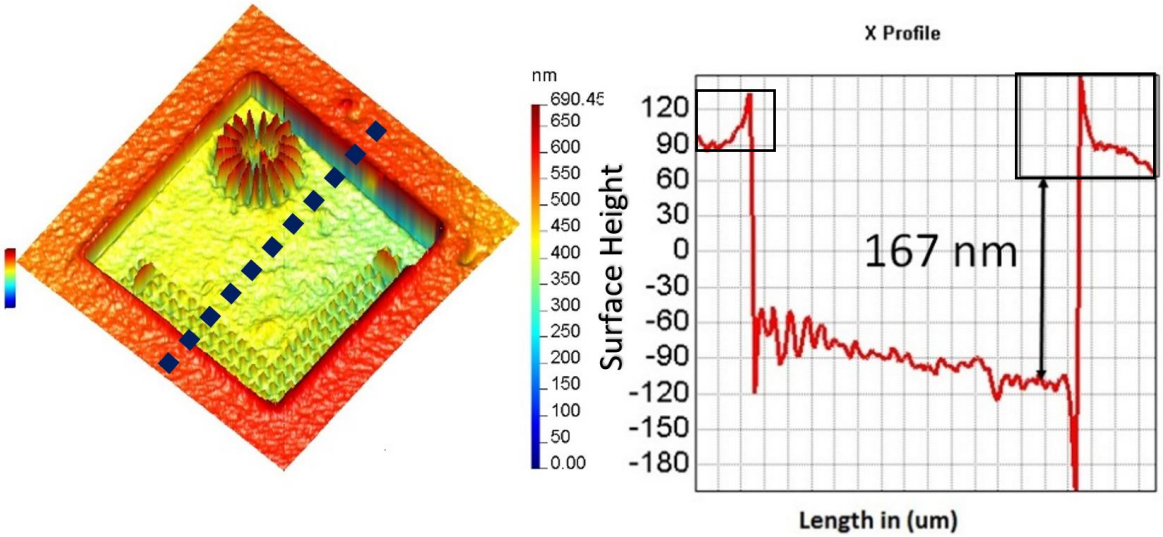

Figure 7.5 DPI measurement result for cross grating depth 185.9 nm standard sample, illuminated by Red and Blue sources (a) areal measurement. (b) cross-sectional profile

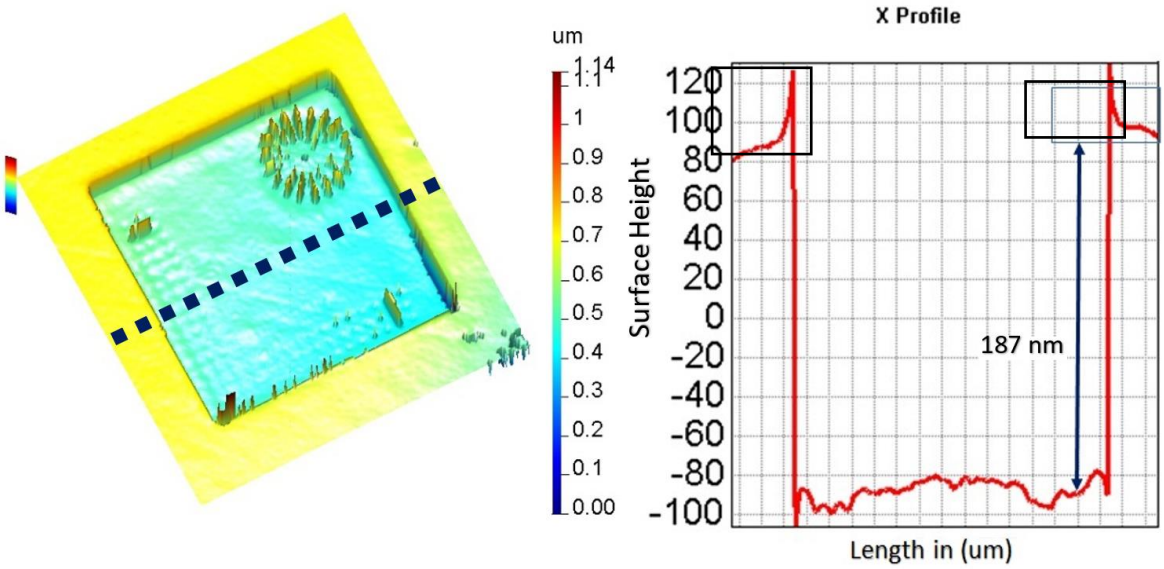

Figure 7.6 DPI measurement result for cross grating depth 185.9 nm standard sample Using the fringe order method, illuminated by Green and Blue sources (a) areal measurement (b) cross-sectional profile

7.2.3 Measurement of TPI (RGB) using Long Synthetic Wavelength

Two samples, one is a standard cross grating sample, with step height equal to 2050.9 +4.1 nm, from National Physical Laboratory (NPL), and the other is a non-standard sample made by diamond-turning machine, with 4100 nm step height, were measured and evaluated according to ISO 5436. The TPI synthetic operation mode as described in section (6.4.4) was used in the measurement. The aim of using three wavelengths (R-630, G-540 and B-460) is to expand the measurement range up to 4.347 μm using a single shot. The measurement was carried out using 2X objective lens, allowing a long depth of focus 96 μm.

The measurement of the standard sample was found to be 1998.2 nm. While measurement of the non-standard sample was found to be 3962 nm, see Figures 7.7 and 7.8. As such, the measurement range has been successfully expanded to measure larger step heights. The error in this technique is less than 20 nm. The difference in measurement between CCI and TPI is increased as the step height is increased as illustrated in Table 7.4. It can be seen that the algorithm create fake jumps and spikes in the surface, leading to error in calculating the fringe order. Low fringe visibility and colour crosstalk can contribute to this error.

Table 7.4 Measurement result of TPI using long synthetic wavelength

Nominal height of Step	TPI (nm)	CCI (nm)	TPI - ST	TPI - CCI
2050.9nm ±4.1nm	1998.2	2018.6	52.7 nm	20.4 nm
4000 nm	3962	3909	Not a standard sample	53 nm

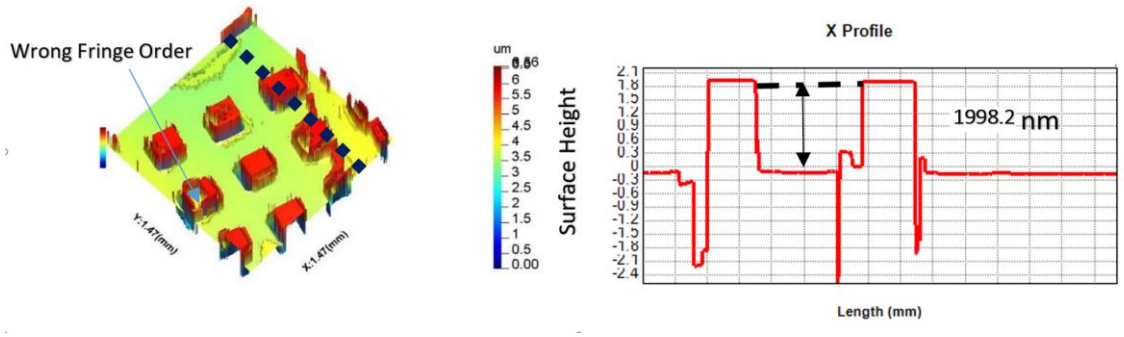

Figure 7.7 TPI synthetic mode measurement result for cross grating depth 2000_nm standard sample (a) areal measurement (b) cross-sectional profile

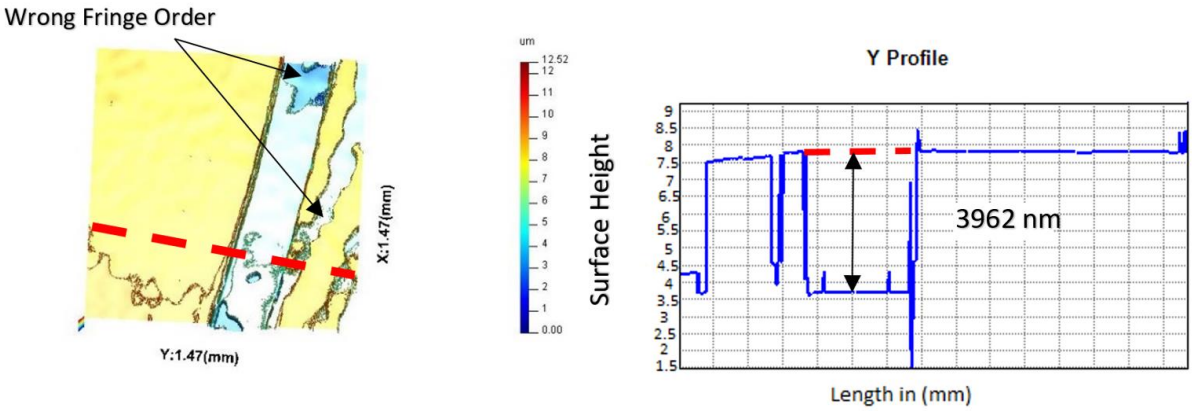

Figure 7.8 TPI synthetic mode measurement result for step height depth 4000_nm step height sample (a) areal measurement (b) cross-sectional profile

7.2.4 Measurement Results of TPI (RGB) using Best Match Method

The measurement range for MPI described above is always limited by 2π phase ambiguity, although ambiguity range can be extended by using a synthetic wavelength. However, if the fringe order can be determined by a trial and error method using the phase information obtained at three wavelengths, the measurement range can be significantly increased. The best match algorithm has been discussed in section (6.4.5) and can be viewed as a way forward to determine the fringe order and remove phase ambiguity problem.

The performance of MPI using best match algorithm was tested by measuring three standard sample, two from NPL and one from VLSI, with step height equal two 43.7 ±1.4 nm, 185.9 ±4.1 nm, and 2050.9 ±4.1 nm. And samples supplied by NPL. The measurement was carried out with 2X objective lenses. The measurement results were found to be 2024 nm with average error 26 nm, 189 nm with average error 4 nm and 44.7 nm with an average error 1 nm sequentially as shown in Table 7.5. All the measurements were done close to zero OPD to obtain the best fringe visibility. The areal measurement result with the cross section profile is shown in Figures 7.9-7.11.

Table 7.5 Measurement result comparison between MPI and CCI

ST	MPI_{RGB} (nm)	CCI (nm)	ABS MPI_{RGB} - CCI	ABS MPI_{RGB} - ST
43.7±1.4nm	44.7	42.551	2.149 nm	1±1.4nm
185.9 ±2.3nm	189	192.1	3.1	3.1±2.3
2050.9_nm ± 4.1	2024	2018	6	26

ST: Step height value (nm) ±0expanded uncertainty.

MPI_{RGB}: MPI using RGB illumination.

ABS MPI_{RGB} - CCI: Absolute error $|MPI_{RGB} – CCI|$.

ABS MPI_{RGB} - ST: Absolute error $| MPI_{RGB} – ST|$.

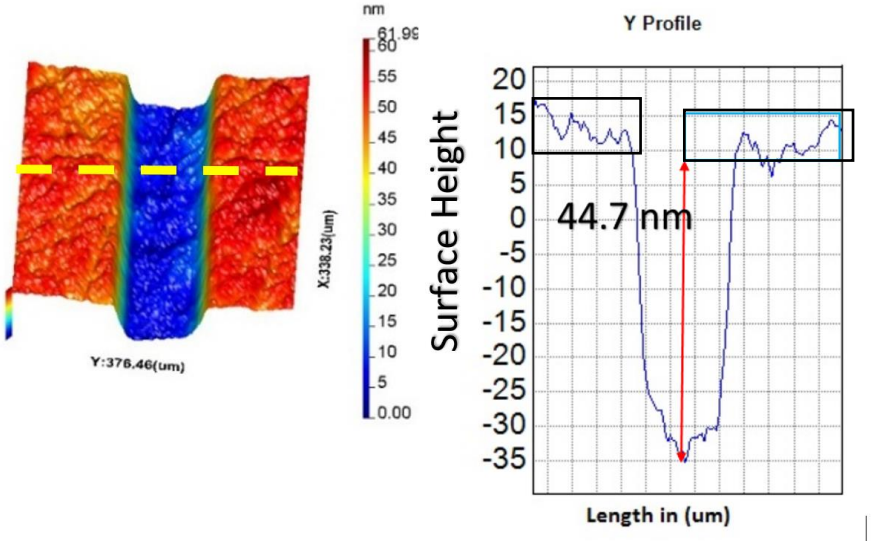

Figure 7.9 TPI measurement using Best match algorithm for 43.7 nm step height (a) areal measurement (b) cross-sectional profile

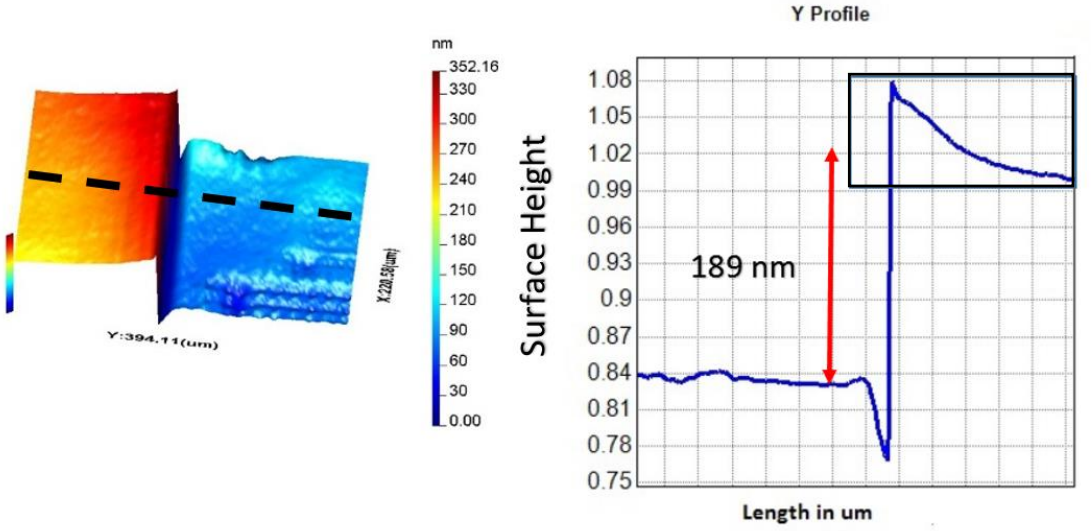

Figure 7.10 TPI measurement using Best match algorithm for 185 nm step height (a) areal measurement (b) cross-sectional profile

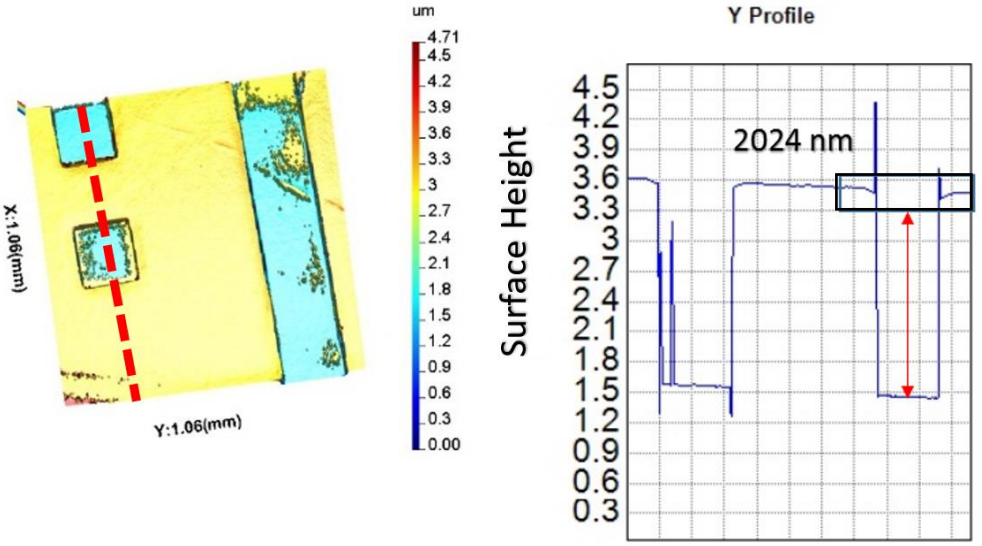

Figure 7.11 TPI measurement using Best match algorithm for 2050 nm step height (a) areal measurement result (b) cross-sectional profile

It can be seen that there are surface jumps and spikes in the third sample. In order to investigate this further, the second sample (ST=185.9 nm) was placed at approximately 1 μm distance away from zero OPD. The expected fringe order at the red wavelength is 3, calculated using Equation 6.25. In the best match algorithm, two range sets were tested from (0 to 10) and (3 to 20) respectively. In the first N-order range, the best match has only found one fringe order candidate value that satisfies the condition (hr=hg=hb) as described in chapter six, while two N-order candidate values were found in the second range, see Figures 7.12 and 7.13. As such, searching N

order over wider range can increase the error probability. This is mainly because the fringe colour is almost repeated itself at every 3.6 μm, as shown in Figure 7.14 (Butler *et al.*, 2016).

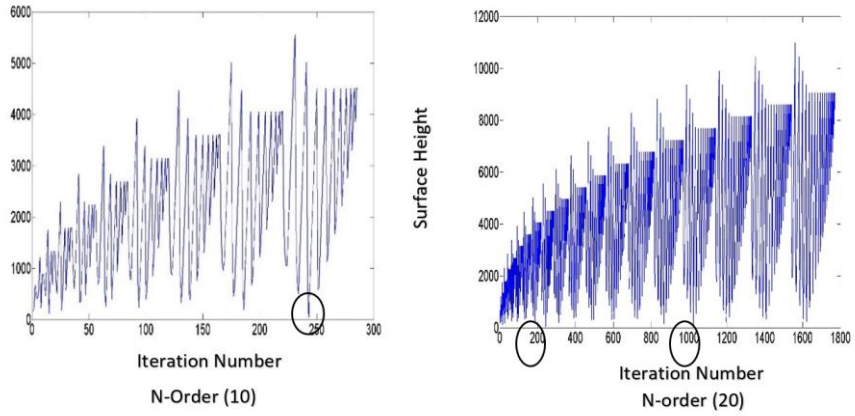

Figure 7.12 Minimum height difference between (hred-hgreen-hblue) calculated by the algorithm at specific N-order

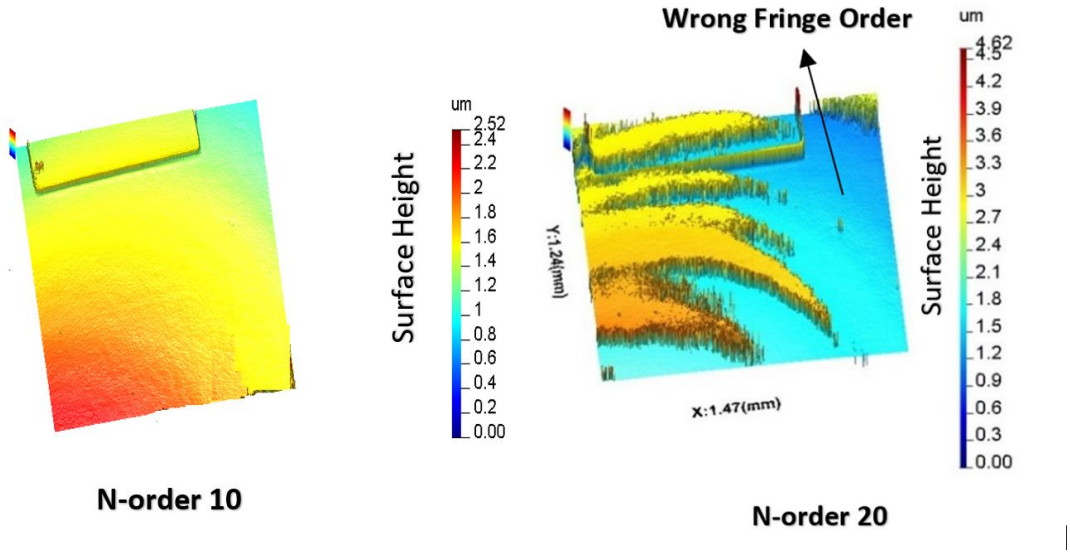

Figure 7.13 TPI non-synthetic mode measurement result for 185 nm step height (a) when fringe order is 10 (b) when fringe order is 20

In order to observe the colour repetition in the existing MPI setup, a reference mirror was moved four steps, 5 μm for each step, using an accurate stepper, and a colour interferograms was captured at each step, see Figure 7.15. The repetition of (pink-green-pink-green) combination is an exemplar. If the MPI cannot sense the slight change in colours, a fringe jump errors can be occurred.

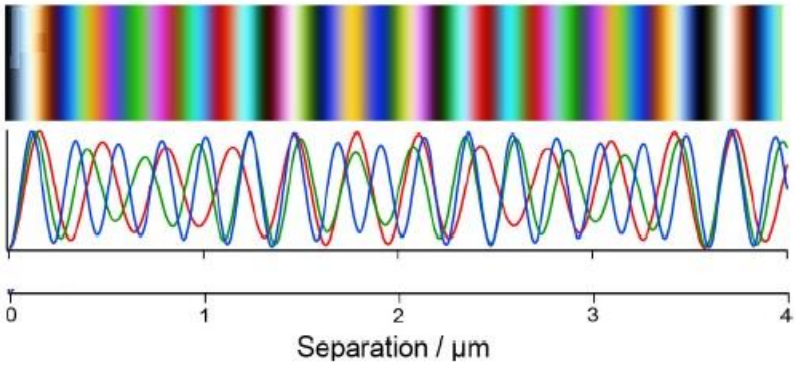

Figure 7.14 Colour fringes at different OPDs. Adopted from (Butler *et al.*, 2016)

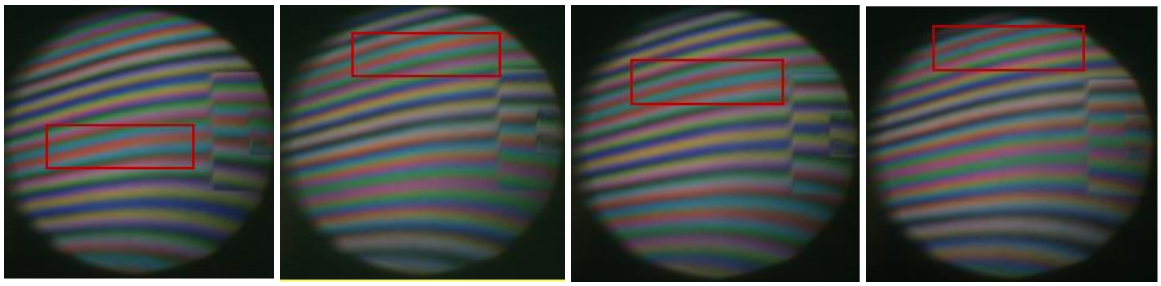

[a] **[b]** **[c]** **[d]**

Figure 7.15 RGB interference fringe captured at (a) 0 um, (b) 5 um, (c) 10 um and (d) 15 um

7.3. Comparison Study between Carré and Four-Step Algorithms

Four-step algorithm was used to determine the wrapped phase in MPI as described in Chapter 6. The algorithm performance was investigated by comparing it with Carré algorithm. Both algorithms can be used for calculating the wrapped phase in phase shifting interferometers. The standard VLSI sample (having 43.7 nm ± 1.4 step) was measured using SPI, while NPL standards having depth values of (1264_nm ± 4 nm), (502 nm ± 4 nm) and (185 nm ± 2 nm) were measured using DPI. The captured interferograms were analysed by the two algorithms separately.

For SPI, the results demonstrate that the absolute error is 1.14 nm using the four-step algorithm and 2.8 nm using Carré algorithm as illustrated in Table 7.6. For DPI using (Red-Green), the results demonstrate that the absolute error is 71.1 nm using the four-step algorithm and 82.1 nm using the Carré algorithm as illustrated in Table 7.7. The Carré results also show more spike errors across the surface as shown in Figure 7.16 .The error difference between the two algorithms can be caused by the 90^0 phase shift, as this value is not the optimum for the Carré algorithm in the presence of noise (Al-Bashir1 *et al.*, 2018; Qian *et al.*, 2000).

Table 7.6 Four step and Carre comparison using SPI

ST (**nm)**	Red _Four Step (nm)	Red Carré (nm)	ABS- four step (nm)	ABS-Carré (nm)
43.7 ±1.4	42.29	46.5	1.41	2.8

Table 7.7 Four step and Carre comparison using DPI

ST (nm)	DPI-Four Step (nm)	DPI–Carré (nm)	ABS-Four Step (nm)	ABS-Carré (nm)
185.9 ±2.3nm	257.0	268	71.1	82.1
502.0 ±4.1nm	588.3	645	86.3	143
1264 ±4 nm	1213	1116	51	148

ST: Step height value (nm) ± expanded uncertainty.

Red _Four-Step: Four-step measurement using Red.

Red Carré: Carré measurement using Red.

DPI- Four: DPI (nm) using Four-step Algorithm (Red-Green).

DPI-Carré: DPI (nm) using Carré Algorithm (Red-Green).

ABS-Four: Abs error |DPI–ST| using Four-step algorithm.

ABS-Carré: Abs error |DPI–ST| using Carré Algorithm

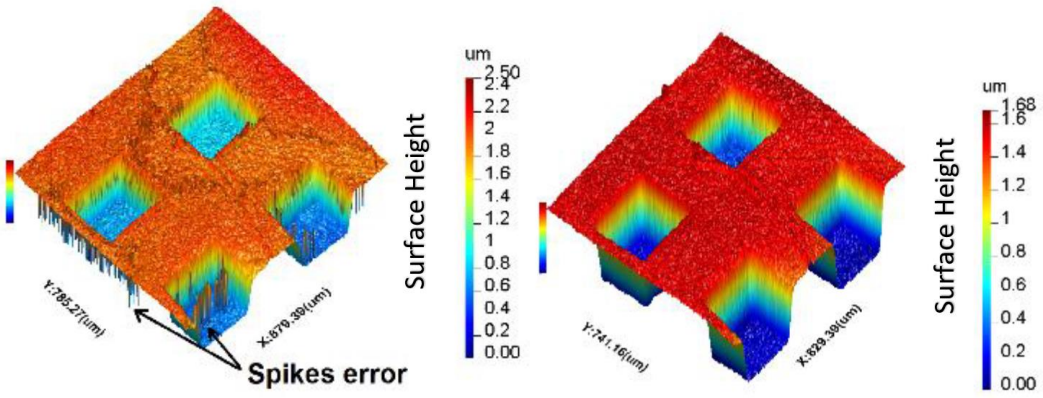

Figure 7.16 Measurement of 1264 nm standard sample, illuminated by red and green light (a) carré algorithm (b) Four-step algorithm

7.4 Measurement Noise of MPI

The measurement noise of any metrology instrument combines the internal noise produced by the instrument, external noise and the noise produced from the mechanical scanning

process(Giusca, 2013). There are two techniques capable of isolating the measurement noise from the surface roughness.

The first technique is to isolate the noise by subtracting two measurement results for the same spot, and the second technique is to average several measurement results, so that the effect of noise is decreased by the square root of the number of measurement (Giusca, 2013).

In this chapter, the subtraction technique is considered. A standard flat artefact was measured using a 2X Mitutoyo microscope lens at the same position three times for each MPI mode (SPI, DPI and TPI)(Muhamedsalih1 *et al.*, 2018). The subtraction of the first measurement from the second and second one from the third have generated to two maps of the measurement's noise. The commercial software package SurfStand was used to calculate the root mean square height (Sq). The final system noise can be obtained by using Equation (7.1).

$$M_{noise} = \frac{Sq}{\sqrt{2}} \tag{7.1}$$

7.4.1 Measurement Noise of SPI

The noise of MPI was first investigated using the single wavelength operation mode. The primary wavelengths were operated separately in order to avoid the effect of crosstalk which is inherited in most colour cameras equipped with Bayer filters. A standard silver mirror provided by Thorlabs was measured. The MPI average noise at single wavelength operation mode is found to be 0.711 nm for Red, 2.3 nm for Green, and 1.65 nm for Blue as illustrated in Table 7.8. The noise amount is mainly produced by the polarising interferometer components.

Table 7.8 Measurement noise estimation of SPIS using the single wavelength

Mnoise (nm) (Red)		Average Mnoise (nm) (Red)
0.711	0.711	0.711
Mnoise (nm) (Green)		Average Mnoise (nm) (Green)
2.37	2.29	2.33
Mnoise (nm) (Blue)		Average Mnoise (nm) (Blue)
1.6	1.7	1.65

7.4.2Measurement Noise of DPI

The noise of the MPI was investigated using the dual wavelength operation mode (DPI). Three combinations of dual wavelengths were operated separately in order to have three different synthetic wavelengths. The phase unwrapping was calculated first using the straightforward technique explained in section (6.4.2)

Table 7.9 shows that the DPI has an average measurement noise of 42.175 nm when using (Red 630 nm, Green 560nm) combination, 19.8 for (Green 560 nm, Blue 450 nm) combination

and 4.9 for (Red 625 nm, Blue 485nm) combination, which is expected for two reasons: the first is the camera spectrum response which is discussed in Chapter 5, the potential for crosstalk between Red and Green combination is higher than (Green-Blue) and (Red-Blue), while (Red-Blue) combination has the lowest crosstalk, the second reason reflects the fact that it is known from the literature that phase noise for single wavelength is amplified by a factor equal to the twice magnification of wavelengths (Gass *et al.*, 2003)

Table 7.9 Measurement noise estimation of DPI using three different combinations of dual wavelengths

M_{noise} (nm)	M_{noise}(nm)		Average M_{noise}(nm)
Red 630 nm, Green 560 nm	41.38	35.35	42.175
Green 560 nm, Blue 450 nm	22.87	16.9	19.8
Red 625 nm, Blue 485 nm	4.9	4.9	4.9

7.4.3 TPI RGB Non-Synthetic Mode System Noise

The noise of MPI was quantified by measuring the standard flat surface at TPI/RGB operation mode. Four colour interferograms were captured at once and analysed using four step and best-match algorithms together. The system noise of MPI is reported in Table 7.10.

Table 7.10 Measurement noise estimation of MPI using RGB wavelengths

M_{noise}(nm) RGB	M_{noise}(nm) RGB	Average M_{noise} (nm)
2.7nm	2.21nm	2.45nm

7.5 System Repeatability

The VLSI standard sample, having 43.7 nm ± 1.4 step height, was placed approximately at zero OPD and measured 10 times using 2x microscope lenses as stated in Table 7.11. The time separation between each measurement was approximately 1 second. The standard deviation was calculated according to Equation (7.2).

$$S_n = \sqrt{\frac{1}{N-1}\sum_{i=1}^{N}(x_i - \bar{x})^2} \qquad (7.2)$$

Where x_i is the measurement of i^{th} sample, N is the number of observations, and $\bar{x}$ is the mean value of the total measurement sets where it is found 44.57 nm. The calculated standard deviation value is equal to 1.78 nm. As such, the MPI system has nano-scale repeatability.

Table 7.11 Step height repeatability using SPSI

Measurement Number	40 step height
1	41.31
2	42.26
3	45.19
4	45.54
5	44.42
6	46.56
7	47.16
8	43.87
9	44.79
10	44.60
Mean	44.57 nm
Std. Dev.	1.78 nm

7.6 Image Enhancement

The fringe order, which was used in section (7.2.3) to retrieve the 3D surface in synthetic wavelength, is very sensitive to the phase noise. There are several expected reasons to produce noise such as low fringe visibility or external vibration. Image smoothing is a useful technique to eliminate the noise affect, however, if it is made on the wrapped phase for the three colour (Red, Green and Blue) this will be smeared the discontinuity of the tan function. The solution is to use the filter before the calculated wrapped phase, so the filter could be used on numerator and denominator of the tan function as shown in Equation (7.3) (Daniel, 2007).

$$\tan\theta = \frac{sin\theta}{cos\theta} \approx \frac{filter\,(\sin\theta)}{filter\,(\sin\theta)} \qquad (7.3)$$

Gaussian filter has been used in the MPI to smooth the image in order to eliminate the spike error and retrieve the surface, see Figure 7.17. It has been found that Gaussian filtering shows the best result among other filters such as averaging filters.

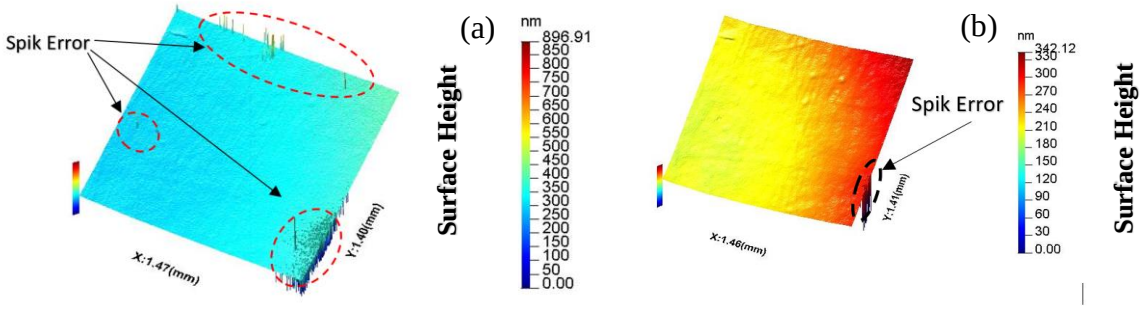

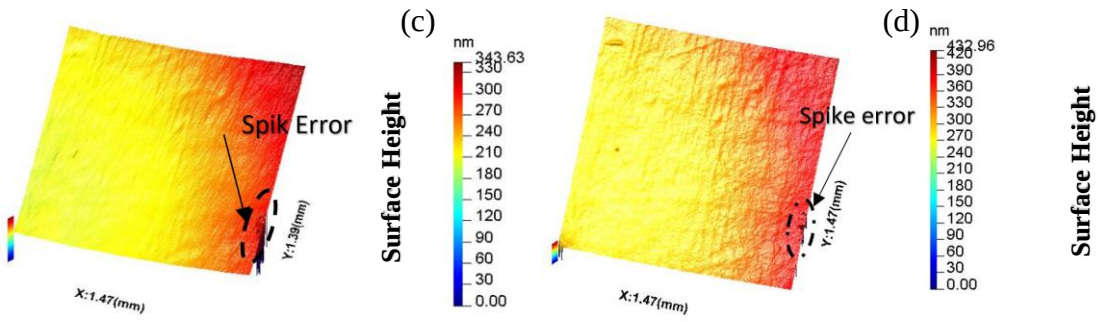

Figure 7.17 Shows the retrieve surface using fringe order method (a) without filter (b) using 2-D special average filter with (9*9 mask) (c) using 2-D special motion filter ('motion',20,15) (d) using 2-D Gaussian ($\sigma = 2$)

7.7 Lateral Range and Lateral Resolution of the MPI

In general the resolution is to break up into constituent parts (Webster, 1989). The lateral resolution in the interferometer is the ability to separate individual features from each other. The most popular form to represent the lateral resolution in the interferometer is a single number, expressing the small separation between features that can be distinguished in an interferometer image (de Groot *et al.*, 2012).

When the optical instrument is illuminated by a very small point source, in addition to it having a finite numerical aperture (NA) and finite wavelength, as a result of all that, the image will be a finite size (Hussam, 2013). The image spot is represent as the Point Spread function (PSF) of an optical apparatus. The Rayleigh criterion illustrates that if there are two incoherent sources like stars, they can be resolved into '' two point sources when the maximum of PSF of the first point source falls on the first minimum of the PSF produced by the second source'' (de Groot *et al.*, 2012), as detailed in Figure 7.18 . Equation (7.4) describe Rayleigh the mathematic relation that describe the resolution of optical system.

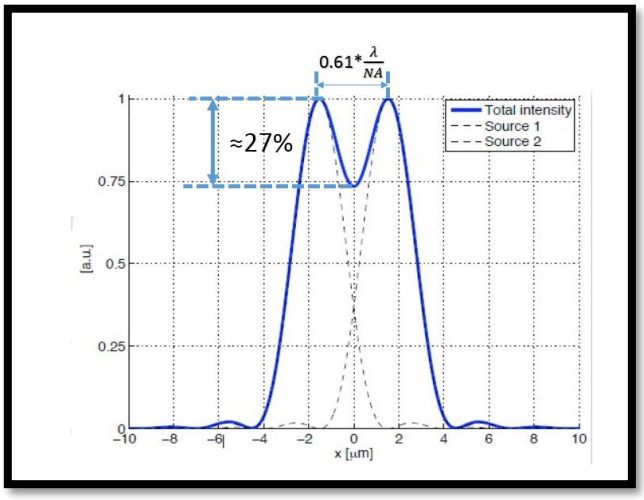

Figure 7.18 Adjacent PSF separated by a distance equal to the Rayleigh

$$R=0.61\frac{\lambda}{(NA)} \quad (7.4)$$

Where R is the lateral resolution, NA is the numerical aperture, λ is the wavelength of the light source of the lens. Since the MPI is illuminated by a RGB wavelength, the lateral resolution in not constant. The lateral resolution is estimated at Red light (worst case) which is 630 nm as illustrated in Table 7.12. Using Equation (7.4).

Table 7.12 The lateral resolution based on Rayleigh criterion

Wavelength	Objective lens	Numerical aperture (NA)	Lateral resolution (μm)
630	2X	0.055	7.58
540	2X	0.055	5.99
460	2X	0.055	5.101

The lateral range, or field of view (FOV) is defined as the sample's area that can be observed by the interferometer sensor. The lateral range or affective sampling area on the specimen is dependent on a number of factors such as NA microscope lens, the diameter of iris diagram, the size of the instrument's sensor and the total magnification of the optical system (Tang, 2016).

One of the approaches to determine the CMOS pixilation presentation on the measured sample is to employ a VLSI standard sample, which consists of a precisely etched positive step. The step is 750 micrometres in length and 100 micrometres wide and it is clearly marked with arrows below.

The VLSI step height was captured with 2X objective lens and a 350×350 pixel used from CMOS array as shown in Figure 7.19. The contrast of the two-headed red arrow shown in Figure L.2 was analysed using Matlab and the result shown in Figure 7.20.

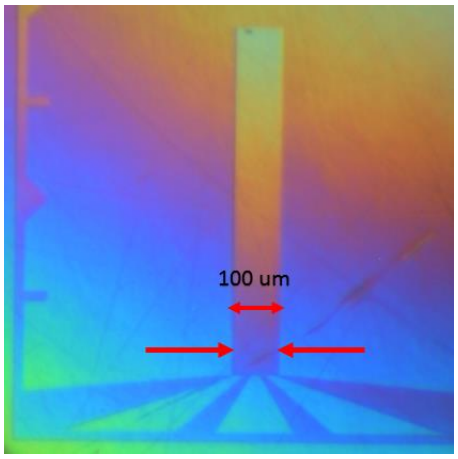

Figure 7.19 Captured frame for VLSI standard step height with 100μm width using a 2X lens

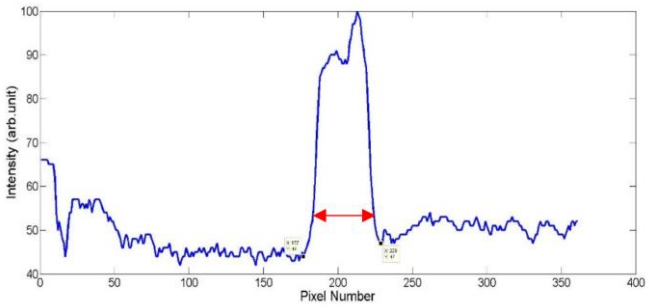

Figure 7.20 Relationship between step height, width and pixilation for 2X lens

It is found that 40 pixels cover 100 um of image surface. As a result, each pixel division represents 2.5um on a sample. Since the objective lens has cylindrical symmetry shape, the vertical pixel division is assumed to be equal to the pixel number in the horizontal direction. Therefore the lateral range in both y and x direction (Lr_x,Lr_y) can be calculated using:

$$Lr=P_d*P_n$$

$$Lr_x=2.5*501=1.252 \text{ mm}$$

$$Lr_y=2.5*501=1.252 \text{ mm}$$

7.8 Summary

This chapter introduces a single shot multi-wavelength polarising phase shift interferometer with three single shot operation modes, namely, a single wavelength phase shift interferometer (SPI), a dual wavelength interferometer (DPI), and a triple wavelength polarising interferometer (TPI). Changing the operation mode of the MPI can change the measurement range and accuracy from micrometre to nanometre scale.

The SPI measurement range is limited by $\lambda/4$ with an average absolute error 4 nm. The average error in SPI mode suggests that the polarisation technique shifts the phase precisely 90^0 degrees.

It is also found that the measurement range of DPI mode changes with the wavelength combination that have been used. The maximum measurement range of (Red-Green) was 1.2 um with an average absolute error of 71.1 nm due to crosstalk affect.

The fringe order method was used to improve the measurement resolution in DPI mode, the measurement error of the DPI mode is found to be (1.8-9.8 nm). However the maximum measurement range was limited to 500 nm. The measurement result also show excellent matching with the CSI measurement with an average error of 7.5 nm.

The TPI using long synthetic wavelength is a modified version of fringe order used in DPI and it is used to extend the measurement to 4 µm. The TPI was used to measure the 4 µm diamond-turned step height sample, and 2 µm cross grating step height sample. The maximum measurement error of TPI is found to be 20 nm compared to CCI result.

It is found that the vertical measurement range of the TPI using best match algorithm is 3.6 μm. The maximum measurement error in TPI is found to be 26 nm. The measurement result also shows good matching with CSI.

A performance comparison between four-step and Carré algorithms were checked in DPI operation mode. It is found that the four step algorithm is more robust against spikes error that appeared in Carre algorithm. A Gaussian spatial filter was successfully used to illuminate the spike error further in the fringe order.

Chapter 8: Discussion, Conclusions and Future Work

8.1 Discussion and conclusions

Interferometers are commonly used for measuring precision surfaces with nano/mico-scale structures such as optics, thin film substrates and silicon wafers. A coherence scanning interferometer is commonly used for measuring samples with a fraction of nanometres vertical resolution and hundreds of micrometre vertical range. Phase shift interferometer is another technique, which offers high measurement accuracy with limitation that the phase different between two adjacent point on the sample should be less than$\lambda/2$. However, both techniques have a common limitation in that they are slow and not suitable for in-process measurement. We presented a single shot polarisation based phase shift Interferometer combined with multiple wavelengths illumination source system (MPI) for measuring micro/nano-scale surface topographies without the need for environmental disturbances compensation such as mechanical vibrations. The speed of measurement should be much faster than common manufacturing environmental disturbances.

The MPI consists of five parts, namely light source, interferometer, polarised optics, four coloured CMOS cameras and the computing unit, including algorithms. There are several light sources capable to provide multi-wavelength illumination such as a multiple laser source or RGB LED with a commercial optical dichroic filter. Although the laser source offers a very narrow linewidth wavelength spectral, it causes unwanted speckles, while the LED plus dichroic filter offers short coherence length because of the broad linewidth. In MPI, the wavelength filtration with 2 nm linewidth using AOTF can increase the coherence length up to 60 µm for worst case (blue) wavelength. The AOTF drivers have the ability to filter multiple channels simultaneously, which enables the MPI to work at three operation modes namely: SPI, DPI and TPI.

The Michelson interferometric configuration was used in MPI. It is easy to align and has low probability of RGB dispersion as compared to a Linnik interferometer (Pförtner *et al.*, 2001). In Linnik setup, any small asymmetry in interferometer means that the light rays pass through different geometrical path lengths in dispersive elements such as glass, which is different in two interferometer arms, and this situation is highly likely. There are two possible reasons for asymmetrical rays paths, the first one is that the two microscope objectives may be not be identical in there glass and the second one that cube beam splitter may be not perfectly cubic. The- polarised Michelson was equipped with a 2X objective lens in the MPI bench setup. The orthogonal beam produced by the polarised interferometer is focused onto four monitoring arms. An incremental

phase-shift of 90^o has been achieved between the four monitoring arms using linear polarisers and a quarter-wave plate without any mechanical scanning.

The main advantage of using four Cameras in MPI is to achieve instantaneous phase shift. Another advantage of using multiple cameras is not to sacrifice the lateral resolution as compared to the pixelated phase mask single camera. The interference fringes are recorded by four two-dimensional colour CMOS cameras, which were equipped with sensor models Sony IMX174. The data acquisition of the three operation modes of MPI (SPI, DPI and TPI) were obtained by capturing interferograms instantaneously by using a Bayer filter in front of the camera. The crosstalk between colours was found to be significant in this sensor. The crosstalk of red in the green filter, green in the red filter, green in the blue filter and blue in the green filter is 30.8%, 15.5%, 23.1% and 18.7% respectively.

As discuss in chapter 6, the vertical range and resolution can be changed by changing the operation mode and algorithm used. MPI dedicates an accurate algorithm to extract a wrapped phase information and then unwrapping the phase to determine the surface heights. In this research, a four-step algorithm was used to extract the wrapped phase, which was then processed by either two-dimensional spatial phase unwrapping method for SPI or best-match method for MPI. The synthetic wavelength was also used to extend the ambiguity range by constructing a longer equivalent wavelength. The surface height was calculated by using the fringe order method to enhance the measurement resolution to nanoscale level.

The SPI is dedicated for measuring a flat surfaces such as plane and concave mirrors, and step height less than $\frac{\lambda}{4}$. The average measurement error is 3.292 nm and measurement noise is approximately equal to 0.7 nm, which indicates that the polarisation technique shifts the phase at 90^0 precisely.

In DPI mode, the three combination of dual wavelengths have been tested using the AOTF capabilities. The maximum measurement range using Red-Green combination was 1.6 μm. The measurement error was found to be significant and approximately 72 nm when compared to the CCI measurement. The crosstalk and noise amplification factor in dual wavelengths are the main contributor to the error. The measurement accuracy of DPI significantly was improved by using the fringe order method; the measurement error was reduce to 9.8 nm and shows a good agreement with CCI with average error equal 7.5 nm.

The TPI using longer synthetic wavelength is a modified version of fringe order used in DPI and it is used to extend the measurement to 4.347 μm. The measurement error is found to be 18 nm. However, the algorithms fail to calculate the correct fringe order in some part of the measured surface. The performance of TPI using best match algorithm was used to remove the 2π phase

ambiguity and extended the measurement range. The measurement result of using MPI showed excellent matching with CCI with 6 nm measurement difference. All the measurements were done close to zero OPD. However best match fails when the OPD increases because of fringe order jumps. This fringe order jumps is mainly because is that the colour fringes repeated itself every 3.6 μm. Therefore, the maximum height can only be determined to a multiple of 3.6 μm.

The absence of mechanical scanning in this research can advance the MPI for not only single shot capability but also to eliminate regular calibration procedures, hence improving the system repeatability. As illustrated in chapter seven, the root mean square deviation of 10 measurements was 1.78 nm in SPI mode.

In roll-to-roll industry the production speed is in more than 50m/min, the current measurement speed of MPI is 5 meter/27min and it is slow due to the dramatically drop in light intensity. So in the current development step , the MPI is can be used for On-machine metrology only because it is single shot it can do the measurement in present of external vibration but the system have the potential to be used for in process metrology as will be discussed in future work.

To conclude, we proposed single shot multi-wavelength polarising phase shift interferometer with three operation modes SPI, DPI and TPI, with extended measurement range greater than $\frac{\lambda}{4}$ and nano-scale vertical resolution. As such, MPI has the potential to be used for measuring moving surfaces with micro-scale structure and features. The achieved MPI specification is stated in Table 8.1

Table 8.1MPI specification

Performance		**Value**
Field of view (objective dependent)		1.2×1.2 mm
Vertical measurement accuracy	Step height ≤ 185.9 nm	3.1 nm
	Step height = 2050.9 nm	26 nm
Vertical range	SPI	157 nm
	DPI	1.2 μm
	TPI	4.3 μm
Lateral resolution (objective dependent)		7.5 μm (2X)
System noise	SPI	0.711 (nm)
	DPI (conventional synthetic wavelength phase unwrapping)	42.175 (nm)
	DPI (Fringe order synthetic wavelength phase unwrapping)	1.65 (nm)
	TPI	1.65 (nm)
Measurement repeatability		1.78 nm
Measurement time	Capturing time	0.39 sec
	Analysis time	2.71 sec

8.2 Major contribution

The summary of contributions in this research is:

- A novel single shot MPI was successfully developed and operated. Integrating three wavelength Red-Green-Blue (RGB) and polarising interferometer was also successfully achieved to offer fast measurement as data acquisition limited only by a single exposure, robustness against environmental disturbances and high accuracy measurement better than 10 nm with extended measurement range exceeding $\lambda/4$. The developed MPI has overcome the height ambiguity and the speed limitation that exists in commercial phase shift interferometry using polarising and three colour light source.
- Advance algorithms were investigated and successfully employed to analyse colour interferograms. These algorithms can be used for the three MPI operation modes (SPI, DPI and TPI). The four step algorithm was successfully employed to extract the wrapped phase. Short and long synthetic was investigated to retrieve the surface topography with larger measurement range. The fringe order algorithm was successfully employed in DPI and TPI to improve the measurement accuracy down to 2 nm.
- The colour crosstalk in MPI was successfully justified and compensated using a calibration routine. The tuning process of AOTF and a mathematical model was used to minimise the crosstalk.
- The performance of MPI was evaluated by measuring range of precision and standard samples. As such, the MPI measurement capability, measurement accuracy and measurement noise were verified in this thesis.
- Furthermore, this work was presented in three conferences (EUSPEN, IEEE and SPIE) and in a keynote session in Euspen. This work was awarded a prise for best presentation in Early Career Researcher Symposium organised by EPSRC Future Metrology Hub at the University of Huddersfield.

8.3 Future work

Future work can be carried out to overcome the current challenges and limitations in MPI and enhance the metrology system in terms of accuracy, data accusation rate and analysis time.

8.3.1 Accelerate the capturing time and computing time

Although the MPI is a single shot interferometer, the period of single exposure was found to be three frame/second due to a dramatic drop in the beam intensity. One possible solution to enhance the capturing time is to investigate a new light source with high power such as a laser source in order to decrease the exposure time of the camera and increase the frame rate. However, the potential of speckles due to long coherence will be increased.

8.3.2 Reduce the colour crosstalk

The colour camera crosstalk is found to be significant. As discussed in chapter five, three possible solutions have been presented to compensate for the colour cross talk.

- Study the potential to change the colour cameras by monochromatic cameras, however, the drawback of this option is that the DPI mode and TPI mode cannot be operated at single shot.
- Study the potential of using three separate monochrome sensors on a single camera that simultaneously splits the incoming light into three separate optical paths. The crosstalk can potentially be reduced if not be completely removed using this cameras. However, the drawback of this option is the camera price is expensive.
- Study the potential of using RGB Prism to separate the RGB component into three beams and use three monochromatic pixelated cameras to record four phases for each colour components.

8.3.3 Improve vertical measurement accuracy

Investigate the current error in the fringe order method used in TPI mode and correct it in order to increase the measurement range to 4.3 μm using single shot with accuracy of single wavelength interferometer.

8.3.4 Increase the lateral resolution

The current development step of the MPI is equipped with 2X microscope objective lens, which limits the lateral resolution to 7.58 μm and the consequences of that cannot be used in thin film inspections especially of small defects. The lateral range and resolution of MPI was determined using optical target and Rayleigh criteria as described in in section 7.7. To make the MPI versatile across various applications especially for thin film inspection, MPI have to be equipped with high magnification lens such as 5X. By equipping the MPI with a 5X objective lens, the lateral resolution will be improved to 2.98 μm.

9. References

Ai, C., & Wyant, J. C. (1987). Effect of piezoelectric transducer nonlinearity on phase shift interferometry. *Applied optics, 26*(6), 1112-1116.

Al-Bashir1, S., Hussam Muhamedsalih1, Feng Gao1, & Jiang1, X. (2018). An Investigation of a Single Shot Dual Wavelength Polarised Interferometer which uses Carre and Four Step Phase Shift Algorithms. *euspen's 18th International Conference & Exhibition, Venice, IT, 2018*, 113-114.

alliedvision.(2017).Seeing Through the Cracks.[Online].Available: https://www.alliedvision.com/en/news/detail/news/seeing-through-the-cracks.html

Arashlouzadeh, A. (2014). Surface Roughness Measurment: Multi-bandFrequency Shift Interferometer based onPolarization Measurement. In.

Awatsuji, Y., Lee, Y., Ito, Y., Tahara, T., Xia, P., Nishio, K., & Matoba, O. (2015, 1-5 June 2015). *Single-shot 3D measurement by multi-wavelength parallel phase-shifting digital holography.* Paper presented at the 2015 14th Workshop on Information Optics (WIO).

Bass, M., DeCusatis, C., Enoch, J., Lakshminarayanan, V., Li, G., Macdonald, C., . . . Van Stryland, E. (2010). Handbook of Optics, Volume I: Geometrical and Physical Optics. *Polarized Light, Components and Instruments (set), 3*.

Bernd, D. (2012). polarimetry. In *Handbook of Optical Systems, Volume 5: Metrology of Optical Components and Systems* (Vol. 5, pp. 594): John Wiley & Sons.

Beverage, J. L., Colonna de Lega, X., & Fay, M. F. (2014). *Interferometric microscope with true color imaging*.

Blunt, L., Fleming, L., Elrawemi, M., Robbins, D., & Muhamedsalih, H. (2013). In-line metrology of functional surfaces with a focus on defect assessment on large area Roll to Roll substrates. In: EUSPEN.

Blunt, L., & Jiang, X. (2003). *Advanced techniques for assessment surface topography: development of a basis for 3D surface texture standards" surfstand"*: Elsevier.

Brock, N. J., Crandall, C., & Millerd, J. E. (2014). *Snap-shot imaging polarimeter: performance and applications.* Paper presented at the Polarization: Measurement, Analysis, and Remote Sensing XI.

Brock, N. J., Millerd, J. E., Wyant, J. C., & Hayes, J. B. (2007). Pixelated phase-mask interferometer. In: Google Patents.

Butler, S. C., Seeger, L. E. Z., Bell, D. M. T., Bishop, I. A., & Tabor, F. R. (2016). Local determination of thin liquid film profiles using colour interferometry. *The European Physical Journal E, 39*(2), 1-7. doi:10.1140/epje/i2016-16014-9

Carré, P. (1966). Installation et utilisation du comparateur photoélectrique et interférentiel du Bureau International des Poids et Mesures. *Metrologia, 2*(1), 13.

ccs-grp.(2019).HLV2-3M-RGB-3W.[Online]. Available: https://www.ccs-grp.com/products/model/1676

Chen, L.-C., Yeh, S.-L., Tapilouw, A. M., & Chang, J.-C. (2010). 3-D surface profilometry using simultaneous phase-shifting interferometry. *Optics Communications, 283*(18), 3376-3382.

Chen, T. Y.-F., & Du, Y.-L. (2009). *Instantaneous surface profile measurement using polarized phase-shifting.* Paper presented at the International Conference on Experimental Mechanics 2008 and Seventh Asian Conference on Experimental Mechanics.

Chipman, R. A. J. P., 2nd ed. M. Bass ed. McGraw Hill, New York. (1995). Handbook of optics. *2*.

Claveau, R., Montgomery, P., & Flury, M. (2018). *Application of coherence scanning interferometry for local spectral characterization of transparent layers.* Paper presented at the Optical Micro-and Nanometrology VII.

Collett, E. (2005). *Field guide to polarization* (Vol. 15): SPIE press Bellingham.

Crabtree, K. (2007). Polarization Critical Optical Systems: Important Effects and Design Techniques. *Tutorial_Paper-Crabtree*.

Creath, K. (1987). Step height measurement using two-wavelength phase-shifting interferometry. *Applied optics, 26*(14), 2810-2816. doi:10.1364/AO.26.002810

Creath K, e. A. (2012). Dynamic Phase-Shifting Microscopy Tracks Living Cells. *Biomedical Optics Express, 3(11)*, 2866-2880

Crop., O. S. S. A. (2018). The Quarter Wavelength Retardation Plate.

Daniel, M. (2007). Surface Profilers, Multiple Wavelength. In *Optical shop testing, third edition* (pp. 667-717). Hoboken, N.J: Wiley-Interscience.

Danzl, R., Helmli, F., & Scherer, S. (2009). *Focus variation–a new technology for high resolution optical 3D surface metrology.* Paper presented at the The 10th International Conference of the Slovenian Society for Non-Destructive Testing.

de Groot, P. (2011). Coherence scanning interferometry. In *Optical measurement of surface topography* (pp. 187-208): Springer.

de Groot, P. (2015). Principles of interference microscopy for the measurement of surface topography. *Advances in Optics and Photonics, 7*(1), 1-65.

de Groot, P., de Lega, X. C., Sykora, D., & Deck, L. (2012). The meaning and measure of lateral resolution for surface profiling interferometers. *Optics and photonics news, 23*(4), 10-13.

Debnath, S. K., & Kothiyal, M. P. (2006). *Analysis of spectrally resolved white light interferometry by Hilbert transform method.* Paper presented at the SPIE Optics + Photonics.

Drexler, W., & Fujimoto, J. G. (2008). *Optical coherence tomography: technology and applications*: Springer Science & Business Media.

Edmund Optics. (2019). Polarizer Selection Guide. [Online]. Available: https://www.edmundoptics.com/resources/application-notes/optics/polarizer-selection-guide/

Elrawemi, M., Blunt, L., Muhamedsalih, H., Gao, F., & Fleming, L. J. I. J. o. A. T. (2015). Implementation of in process surface metrology for R2R flexible PV barrier films. *9*(3), 312-321.

Fahlteich, J., Steiner, C., Top, M., Wynands, D., Wanski, T., Mogck, S., . . . Schiller, N. (2015). *10.1: Invited Paper: Roll-to-Roll Manufacturing of Functional Substrates and Encapsulation Films for Organic Electronics: Technologies and Challenges.* Paper presented at the SID Symposium Digest of Technical Papers.

Fang, N. (2014). Polarization-Lecture Notes-Introduction to Optics -2.71/2.710-MIT OpenCourseWare.

Feynman, R. P., Leighton, R. B., & Sands, M. (2011). *The Feynman lectures on physics, Vol. I: The new millennium edition: mainly mechanics, radiation, and heat* (Vol. 1): Basic books.

Fowles, G. R. (1989). *Introduction to modern optics*: Courier Corporation.

Fu, S., Cheng, F., Tjahjowidodo, T., Zhou, Y., & Butler, D. J. S. (2018). A non-contact measuring system for in-situ surface characterization based on laser confocal microscopy. *18*(8), 2657.

gardasoft. (2018). Application example of different Pulse intensities for individual lights.

Gass, J., Dakoff, A., & Kim, M. K. (2003). Phase imaging without 2π ambiguity by multiwavelength digital holography. *Optics letters, 28*(13), 1141-1143. doi:10.1364/OL.28.001141

Geest, G. v. d. (2014). OLED encapsulation with unique barrier tapes from tesa. *Annual Press Conference: Consumer electronics*.

Giusca, C., & L, Leach, R K. (2013). Calibration of the metrological characteristics of coherence scanning interferometers (CSI) and phase shifting interferometers (PSI). *National Physical Laboratory, Measurement Good Practice Guide No. 127*.

Gomez, C., Thompson, A., DiSciacca, J., Lawes, S., & Leach, R. (2017). Coherence scanning interferometry for additive manufacture.

goochandhousego. (2019). Acousto-Optic Tunable Filter Retrieved from https://goochandhousego.com/wp-content/uploads/2013/12/IWDS013-V1.1-TF625-350-2-11-BR1A-data-sheet1.pdf

Harding, K. (2013). *Handbook of optical dimensional metrology*: CRC Press.

Hariharan, P. (2003). Two-Beam Interference In *Optical Interferometry, 2e* (pp. 11): Elsevier.

Hariharan, P. (2010). Interference. In *Basics of interferometry* (pp. 3): Elsevier.

Hassan, M. A., Martin, H., & Jiang, X. J. A. o. (2018). Development of a spatially dispersed short-coherence interferometry sensor using diffraction grating orders: publisher's note. *57*(1), 5-5.

Hecht, E. (2016). Polarization In *Optics* (pp. 8-327): Pearson Education.

Herráez, M. A., Burton, D. R., Lalor, M. J., & Gdeisat, M. A. (2002). Fast two-dimensional phase-unwrapping algorithm based on sorting by reliability following a noncontinuous path. *Applied optics, 41*(35), 7437-7444.

Hettwer, A., Kranz, J., & Schwider, J. (2000). Three channel phase-shifting interferometer using polarization-optics and a diffraction grating. *Optical Engineering, 39*(4), 960-967.

Hiersemenzel, F., Petzing, J. N., Leach, R. K., Helmli, F., & Singh, J. (2012). Areal texture and angle measurements of tilted surfaces using focus variation methods.

Hubel, P. M., Liu, J., & Guttosch, R. J. (2004). *Spatial frequency response of color image sensors: Bayer color filters and Foveon X3.* Paper presented at the Sensors and Camera Systems for Scientific, Industrial, and Digital Photography Applications V.

Huemer, F., Jamalieh, M., Bammer, F., & Hönig, D. J. t.-T. M. (2016). Inline imaging-ellipsometer for printed electronics. *83*(10), 549-556.

Huntley, J. J. A. o. (1989). Noise-immune phase unwrapping algorithm. *28*(16), 3268-3270.

Hussam, M. (2013). *Investigation of wavelength scanning interferometry for embedded metrology.* University of Huddersfield,

Hussam, M., Blunt, L., Martin, H., Jiang, X., & Elrawemi, M. (2014). An interferometric auto-focusing method for on-line defect assessment on a roll-to-roll process using wavelength scanning interferometry. In: EUSPEN.

Hussam, M., Jiang, X., & Gao, F. (2011). Acceleration computing process in wavelength scanning interferometry.

Itoh, K. (1982). Analysis of the phase unwrapping algorithm. *21*(14), 2470-2470.

Jamin, J. (1868). Sur un refracteur différentiel pour la lumière polarisée. *CR Acad. Sci.(Paris), 67*, 814.

Jaturunruangsri, S. (2015). *Evaluation of material surface profiling methods: contact versus non-contact.* Brunel University London,

Jiang, X., Scott, P. J., Whitehouse, D., Blunt, L. J. P. o. t. R. S. A. M., Physical,, & Engineering Sciences. (2007). Paradigm shifts in surface metrology. Part II. The current shift. *463*(2085), 2071-2099.

Jiang, X., Wang, K., Gao, F., & Muhamedsalih, H. (2010). Fast surface measurement using wavelength scanning interferometry with compensation of environmental noise. *Applied optics, 49*(15), 2903-2909. doi:10.1364/AO.49.002903

Kaplonek, W., & Lukianowicz, C. (2012). Coherence correlation interferometry in surface topography measurements. In *Recent Interferometry Applications in Topography and Astronomy*: InTech.

Kapłonek, W., Nadolny, K., & Królczyk, G. M. J. M. S. R. (2016). The use of focus-variation microscopy for the assessment of active surfaces of a new generation of coated abrasive tools. *16*(2), 42-53.

Kim, T., Kim, S. H., Do, D., Yoo, H., & Gweon, D. (2013). Chromatic confocal microscopy with a novel wavelength detection method using transmittance. *Optics Express, 21*(5), 6286-6294.

Kimbrough, B., & Novak, E. (2015). *In-line roll-to-roll metrology for flexible electronics.* Paper presented at the SPIE Optical Engineering + Applications.

Kitagawa, K. (2010). Fast surface profiling by multi-wavelength single-shot interferometry. *International Journal of Optomechatronics, 4*(2), 136-156.

Kitagawa, K. (2012). Single-shot interferometry without carrier fringe introduction. *SPIE*.

Koliopoulos, C. L. (1992). *Simultaneous phase-shift interferometer.* Paper presented at the Advanced Optical Manufacturing and Testing II.

Leach, R. (2011a). Chromatic Confocal Microscopy. In *Optical measurement of surface topography* (Vol. 14, pp. 71-105): Springer.

Leach, R. (2011b). Focus Variation Instruments. In *Optical measurement of surface topography* (Vol. 14, pp. 132-166): Springer.

Leach, R. (2018). *Information-rich manufacturing metrology.* Paper presented at the International Precision Assembly Seminar.

Lebedeff, A. (1930). L'interféromètre à polarisation et ses applications. *Rev. d'Opt, 9*, 385-413.

Mathia, T., Pawlus, P., & Wieczorowski, M. J. W. (2011). Recent trends in surface metrology. *271*(3-4), 494-508.

Matt, N., Millerd, J., Brock, N., North-Morris, M., Hayes, J., & Wyant, J. J. A. O. (2005). Analysis of a micropolarizer array-based simultaneous phase-shifting interferometer. *44*(32), 6861-6868.

micro-epsilon. (2019). Confocal chromatic sensors. [Online]. Available: https://www.micro-epsilon.co.uk/displacement-position-sensors/confocal-sensor/confocal-chromatic-sensors/

Milonni, P. W., & Eberly, J. H. (2010). *Laser Physics*: Wiley.

Moschetti, G. (2016). Development and calibration of wavelength scanning interferometry for surface topography measurement. *University of Huddersfield*.

Muhamedsalih1, H., Al-Bashir1, S., Gao1, F., & Jiang1, X. (2018). Single Shot Dual Wavelength Polarised Interferometer. *IEEE International Instrumentation and Measurement Technology Conference (I2MTC)*, 353-358.

Muhamedsalih, H., Al-Bashir, S., Gao, F., & Jiang, X. (2018). *Single-shot RGB polarising interferometer.* Paper presented at the Interferometry XIX.

nanovea. (2019). CHROMATIC CONFOCAL TECHNIQUE. Retrieved from https://nanovea.com/chromatic-confocal/

NDC.(2018).IN-LINE WEB SURFACE INSPECTION SYSTEMS. [Online]. Available: https://www.ndc.com/~/media/Documents/Web-Gauging/Brochures/FECBRSENSWeb-Surface-InspectionEN2018MAR14.ashx?la=en

Neal, B., Kimbrough, B. T., & Millerd, J. E. (2011). *A pixelated micropolarizer-based camera for instantaneous interferometric measurements.* Paper presented at the Polarization Science and Remote Sensing V.

Ngoi, B., Venkatakrishnan, K., & Sivakumar, N. (2001). Phase-shifting interferometry immune to vibration. *Applied optics, 40*(19), 3211-3214.

Nguyen, D. T., & Chen, L.-C. J. a. p. a. (2018). Development of novel one-shot full-field surface profilometer using chromatic confocal microscopy.

North-Morris, M. B., Millerd, J. E., Brock, N. J., & Hayes, J. B. (2004). *Phase-shifting multiwavelength dynamic interferometer.* Paper presented at the Interferometry XII: Techniques and Analysis.

Novak, E. (2014). *Advanced defect and metrology solutions* (Vol. 9110): SPIE.

Pförtner, A., & Schwider, J. J. A. o. (2001). Dispersion error in white-light Linnik interferometers and its implications for evaluation procedures. *40*(34), 6223-6228.

Picart, P., Malek, M., Garcia-Sucerquia, J., Edely, M., Moalla, R., Delorme, N., & Bardeau, J.-F. (2015). *Topography of nanometric thin films with three-wavelength digital interferometry*.

polytec. (2016/07). Configurable Chromatic Confocal Point Sensors [Online]. Available: https://www.polytec.com/fileadmin/d/Oberfl%C3%A4chenmesstechnik/OM_DS_TopSens-Series_E_42364.pdf

Qian, K., Shu, F., & Wu, X. (2000). Determination of the best phase step of the Carré algorithm in phase shifting interferometry. *Measurement Science and Technology, 11*(8), 1220.

R; Danzl, T. Lankmair, Helmli:, F., & Alicona, D. A.-S. a., 8074 Raaba. (2019). Fully automatic inline measurement using collaborative robot systems equipped with fast high resolution 3D sensor. [Online].Available:https://www.emva-forum.org/files/emva/pdf/abstract_emvaf02_danzl.pdf

Ruiz, P. D., Huntley, J. M., & Widjanarko, T. (2012). *Single-shot profilometry of rough surfaces using hyperspectral interferometry* (Vol. 8413): SPIE.

S. Andriani, & H. Brendel. (2013). Crosstalk correction technique for single sensor camera provided with Bayer color filter array. *IEEE International Conference on Image Processing*, pp. 2252-2255.

Saha, S. K. (2011). Principles of Interference. In *Aperture Synthesis* (pp. 31-49): Springer.

Saleh, B., & Teich, M. (1991). Polarization And Crystal Optics. In W. Series & J. W. Goodman (Eds.), *Fundamental of photonics* (pp. 6-199): John Wiley & Sons, New York.

scribd.(talysurf-cci-6000).[Online]. Available: https://www.scribd.com/document/154706596/talysurf-cci-6000

Sharma, K. K. (2006). *Optics: principles and applications*: Elsevier.

Somers, P. A., & Bhattacharya, N. (2005). *Polarization plane rotator used as a phase stepping device in a 2-channel shearing speckle interferometer.* Paper presented at the Optical Measurement Systems for Industrial Inspection IV.

Stilsa. (2016). Optical Sensors , Distance and thickness measurment Retrieved from http://ecatalog.stil-sensors.com/STIL-catalog.pdf

Stout, K., Blunt, L. J. I. J. o. M. T., & Manufacture. (2001). A contribution to the debate on surface classifications—random, systematic, unstructured, structured and engineered. *41*(13-14), 2039-2044.

Suematsu, M., & Takeda, M. J. A. o. (1991). Wavelength-shift interferometry for distance measurements using the Fourier transform technique for fringe analysis. *30*(28), 4046-4055.

Takeda, M., Ina, H., & Kobayashi, S. (1982). Fourier-transform method of fringe-pattern analysis for computer-based topography and interferometry. *JosA, 72*(1), 156-160.

Tang, D. (2016). Investigation of Line-Scan Dispersive Interferometry for In-Line Surface Metrology. *University of Huddersfield*.

Tang, D., Kumar, P., Gao, F., & Jiang, X. (2018). *Phase retrieval algorithm for line-scan dispersive interferometry.* Paper presented at the Sixth International Conference on Optical and Photonic Engineering (icOPEN 2018).

thinklucid. (2019a). Beyond Conventional Imaging: Sony's Polarized sensor Retrieved from https://thinklucid.com/tech-briefs/polarization-explained-sony-polarized-sensor/

thinklucid. (2019b). Understanding The Digital Image Sensor. Retrieved from https://thinklucid.com/tech-briefs/understanding-image-sensors/

thorlabs. (2019). Economy Film Polarizers, 400 - 700 nm. [Online]. Available: https://www.thorlabs.com/newgrouppage9.cfm?objectgroup_id=4984&pn=LPVISE100-A#7210

thorlabs.com. (2018). AQWP05M-600 - Ø1/2" Mounted Achromatic Quarter-Wave Plate, Ø1" Mount, 400 - 800 nm [Online]. Available: https://www.thorlabs.com/login.cfm?lc=create

Tian, X., Tu, X., Zhang, J., Spires, O., Brock, N., Pau, S., & Liang, R. J. O. e. (2018). Snapshot multi-wavelength interference microscope. *26*(14), 18279-18291.

Townsend, A., Senin, N., Blunt, L., Leach, R., & Taylor, J. J. P. E. (2016). Surface texture metrology for metal additive manufacturing: a review. *46*, 34-47.

Tsai, D.-M., Wu, S.-C., & Li, W.-C. (2012). Defect detection of solar cells in electroluminescence images using Fourier image reconstruction. *Solar Energy Materials and Solar Cells, 99*, 250-262.

Turko, N. A., & Shaked, N. T. (2017). Simultaneous two-wavelength phase unwrapping using an external module for multiplexing off-axis holography. *Optics letters, 42*(1), 73-76. doi:10.1364/OL.42.000073

Upputuri, P. K., Pramanik, M., Nandigana, K. M., & Kothiyal, M. P. (2016). Multi-colour microscopic interferometry for optical metrology and imaging applications. *Optics and Lasers in Engineering, 84*, 10-25.

Wang, X. (1992). Acousto-optic tunable filters spectrally modulate light. *Laser Focus World, 28*(5), 178-180.

Webster, M. (1989). *The New Merriam-Webster Dictionary for Large Print Users*: Merriam Webster.

Whitehouse, D. J. (2011). Characterization In *Handbook of surface and nanometrology* (pp. 5). Boca Raton, Fla; London: CRC.

Wierzba, P. ((2017)). Selected applications of polarization interferometry,[Pdf.Document].

Williamson, J. (2016). *Dispersed reference interferometry for on-machine metrology.* University of Huddersfield,

Wyant, J. C., Koliopoulos, C. L., Bhushan, B., & George, O. E. J. A. t. (1984). An optical profilometer for surface characterization of magnetic media. *27*(2), 101-113.

Xiong, J., Zhong, L., Liu, S., Qiu, X., Zhou, Y., Tian, J., & Lu, X. (2017). Improved phase retrieval method of dual-wavelength interferometry based on a shorter synthetic-wavelength. *Optics Express, 25*(7), 7181-7191.

Yoneyama, S., Arikawa, S. J. T., & Letters, A. M. (2016). Instantaneous phase-stepping interferometry based on a pixelated micro-polarizer array. *6*(4), 162-166.

Zhang, T., Gao, F., Muhamedsalih, H., Lou, S., Martin, H., & Jiang, X. (2018). Improvement of the fringe analysis algorithm for wavelength scanning interferometry based on filter parameter optimization. *Applied optics, 57*(9), 2227-2234. doi:10.1364/AO.57.002227

zygo.(2019). NewView™9000 .[Online]. Available: https://www.zygo.com/?/met/profilers/newview9000/

10. Appendix

10. Appendix A. MPI Simulation

The MPI design is based on using three filtered RGB wavelengths instantaneously to generate colour fringes (or interferograms) shifted by equal phase steps. The MPI proposal that described in Figure 4.2 is based on using four different arms of polarising optics to simultaneously produce a 90^{o} phase shift between each arm. Every arm is equipped by a colour CMOS camera that can detect the primary colours at the same time. A Matlab code, given in Appendix A.1, was written to simulate Red-Green-Blue (RGB) colour fringes that mimicked to the MPI design. The simulation flow chart is illustrated in Figure A.1.

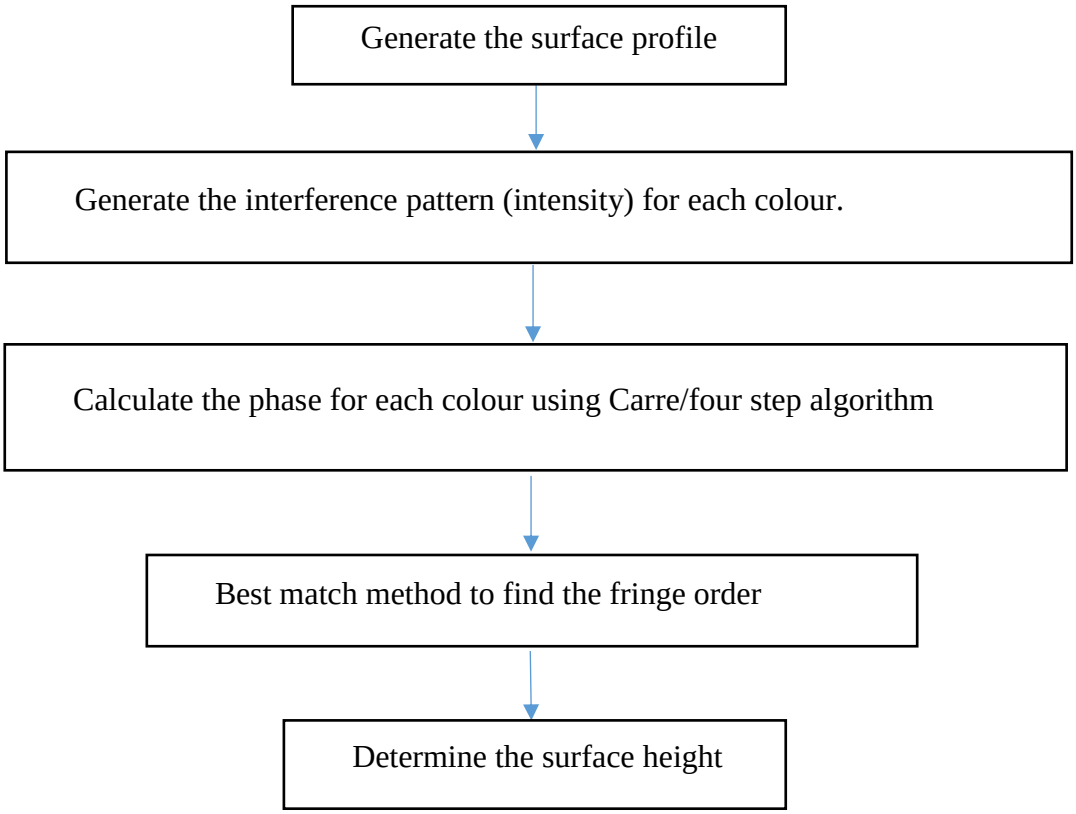

Figure A.1 Simulation flow chart

The simulated surface height was 100 μm of a flat-sloped surface. The RGB wavelengths were simulated to be similar to the real filtered wavelengths ($\lambda_{red} = 643.5$ nm, $\lambda_{green} = 543$ nm, $\lambda_{blue} = 453.7$ nm respectively). The consecutive simulated phase shifts were chosen to be 0^0, 90^0, 180^0 and 270^0. The Carré algorithm (Carré, 1966) was used to calculate the phase information using four shifted intensity values gathered from the from the simulated fringe intensity patterns. Carre algorithm was used in the early steps of MPI development (simulations, Mechanical and Wedge calculation, because it does not require a 90^0 increment in the phase shift between each step. The reference phase shift between two consecutive measurements is considered

as known in order to provide a solution during analysis. The original phase value can be obtained as given in Equation (A.1).

$$\theta(x,y) = tan^{-1}\left\{\frac{\{[3(I_2-I_3)-(I_1-I_4)][(I_1-I_4)+(I_2-I_2)]\}^{\frac{1}{2}}}{(I_2+I_3)-(I_1-I_4)}\right\} \quad \text{(A.1)}$$

Where I_1, I_2, I_3 and I_4 are the first, second, third and fourth intensity consequently were collected as each phase shift steps. As such, wrapped phase maps for three colours can be produced.

To unwrap the phase and retrieve the surface height, three-wavelength information is used. As suggested by (Kitagawa, 2010) the fringe order can be determined by matching the height values of Red, Green and Blue, at different fringe order number. The algorithm are described in detail in section 6.4.5. The algorithm has succeeded to measure a simulated tilted surface with a maximum height equal to 100 μm, as shown in Figure A.2. This range can actually cover the depth of focus for most commercial objective lenses.

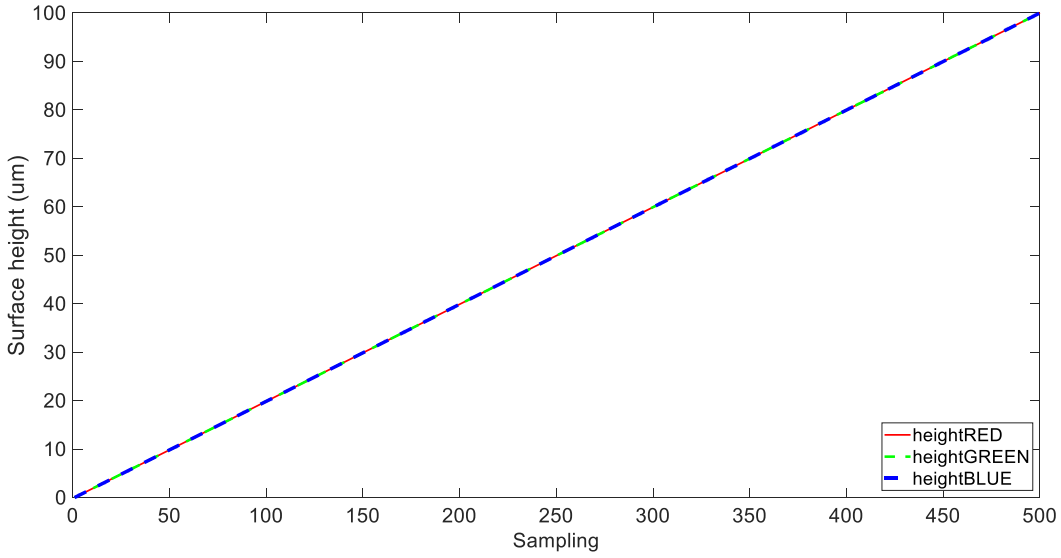

Figure A.2 Simulation result of a tilted surface with a 100 μm maximum height

10. Appendix A.1 TPI Mode Simulation in Three Colour with Best-Match Method (Matlab code)

```
Clear
clc
close all;
a=100;  % interference biase
b=1;    % fringe contrast
TotalSampling=1000; % number of measurement point
hTrueRange=1000;    %nm Upper limit of the measurement range
hStart=0;          %nm Lower limit of the measurement range
hTrue=linspace(hStart,hTrueRange,TotalSampling);
RED=610;    %RED will be shifted by 70 nm to get green color
GREEN=540;  %GREEN will be shifted by 70 nm to get blue color
BLUE=470;   %See above

% In this simulation 4 shifts are used to retrieve the phase information using Carre method.
% However, for experimental setup three phase shifts are requird.
for i=1:TotalSampling
%-- Simulated phases to get intensities
% (1) RED colour
PhaseRED=(4*pi*hTrue(i))/RED;              % first phase information
PhaseRED_45=((4*pi*hTrue(i))/RED+(pi/4));   % second phase information shifted by 45 degree
PhaseRED_90=((4*pi*hTrue(i))/RED+(pi/2));   % third phase information shifted by 90 degree
PhaseRED_135=((4*pi*hTrue(i))/RED+(3*pi/4));% four phase information shifted by 135 degree
%-- From the practical setup, only intensities will be obtained
I_RED_1=a+b*cos(PhaseRED);                % Intensity of the first phase
I_RED_2=a+b*cos(PhaseRED_45);              % Intensity of the second phase
I_RED_3=a+b*cos(PhaseRED_90);              % Intensity of the third phase
I_RED_4=a+b*cos(PhaseRED_135);             % Intensity of the fourth phase
%-- Determine the phase using Carre method
phaseRED(i)=Carre(I_RED_1,I_RED_2,I_RED_3,I_RED_4);
Ired(i)=I_RED_1;       % Just for plot purpose (nothing to do with the algorithm at this stage of research)

%----Repeat the above setups for (2) Green and blue colours
PhaseGREEN=(4*pi*hTrue(i))/GREEN;
PhaseGREEN_45=((4*pi*hTrue(i))/GREEN+(pi/4));
PhaseGREEN_90=((4*pi*hTrue(i))/GREEN+(pi/2));
PhaseGREEN_135=((4*pi*hTrue(i))/GREEN+(3*pi/4));
I_GREEN_1=a+b*cos(PhaseGREEN);
I_GREEN_2=a+b*cos(PhaseGREEN_45);
I_GREEN_3=a+b*cos(PhaseGREEN_90);
I_GREEN_4=a+b*cos(PhaseGREEN_135);
phaseGREEN(i)=Carre(I_GREEN_1,I_GREEN_2,I_GREEN_3,I_GREEN_4);
Igreen(i)=I_GREEN_1;    % Just for plot purpose (nothing to do with the algorithm at this stage of research)
PhaseBLUE=(4*pi*hTrue(i))/BLUE;
PhaseBLUE_45=((4*pi*hTrue(i))/BLUE+(pi/4));
```

```
PhaseBLUE_90=((4*pi*hTrue(i))/BLUE+(pi/2));
PhaseBLUE_135=((4*pi*hTrue(i))/BLUE+(3*pi/4));
I_BLUE_1=a+b*cos(PhaseBLUE);
I_BLUE_2=a+b*cos(PhaseBLUE_45);
I_BLUE_3=a+b*cos(PhaseBLUE_90);
I_BLUE_4=a+b*cos(PhaseBLUE_135);
phaseBLUE(i)=Carre(I_BLUE_1,I_BLUE_2,I_BLUE_3,I_BLUE_4);
Iblue(i)=I_BLUE_1;      % Just for plot purpose (nothing to do with the algorithm at this stage of research
%----Best matching method to determine the fringe order for colour ------
%----Start----
nRED=0;     % initial estimate for the Fringe order of RED colour
nGREEN=0;   % initial estimate for the Fringe order of GREEN colour
nBLUE=0;    % initial estimate for the Fringe order of BLUE colour
for j=1:6   % Investigate the height at 6 fringe order and then find best match
   hRED(j)=(phaseRED(i)/(2*pi)+nRED)*(RED/2);          % surface height using red
   hGREEN(j)=(phaseGREEN(i)/(2*pi)+nGREEN)*(GREEN/2);  % surface height using green
   hBLUE(j)=(phaseBLUE(i)/(2*pi)+nBLUE)*(BLUE/2);      % surface height using blue
   nRED=nRED+1;        % incrementing the red fringe order
   nGREEN=nGREEN+1;    % incrementing the green fringe order
   nBLUE=nBLUE+1;      % incrementing the blue fringe order
end

% if(i==220)
% figure;plot(hRED,'r');hold on;plot(hGREEN,'g'); plot(hBLUE,'b')
% end
% Find best match and calculate the fringe order
j=1;
nRED=0;
nGREEN=0;
nBLUE=0;
min=abs((abs(hRED(j))- abs(hGREEN(j))))+abs((abs(hRED(j))-
abs(hBLUE(j))))+abs((abs(hGREEN(j))- abs(hBLUE(j)))); % Best match should give least magnitude
for j=2:6
   %- To understand the if condition statment, run the program and check the wrap phase figure
if (phaseBLUE(i) > phaseGREEN(i)) && (phaseBLUE(i) > phaseRED(i)) % condition where the blue above the green, and the green above the red
   newValue=abs((abs(hRED(j))- abs(hGREEN(j))))+abs((abs(hRED(j))-
abs(hBLUE(j))))+abs((abs(hGREEN(j))- abs(hBLUE(j))));
   if newValue < min
   min=newValue;
   nBLUE=nBLUE+1;      % All the colours have the same fringe order
   nGREEN=nBLUE;       % All the colours have the same fringe order
   nRED=nBLUE;         % All the colours have the same fringe order
   end
elseif (phaseBLUE(i) < phaseGREEN(i)) && (phaseBLUE(i) < phaseRED(i)) % condition where the blue below the green, and the green below the red
   newValue=abs((abs(hRED(j-1))- abs(hGREEN(j-1))))+abs((abs(hRED(j-1))-
abs(hBLUE(j))))+abs((abs(hGREEN(j-1))- abs(hBLUE(j))));
   if newValue < min
```

```
   min=newValue;
   nBLUE=nBLUE+1;      % The fringe order of the blue is > green and red by 1
   nGREEN=nBLUE-1;     % The green and red have the same fringe order
   nRED=nBLUE-1;       %  The green and red have the same fringe order
   end
elseif (phaseBLUE(i) > phaseGREEN(i)) && (phaseBLUE(i) < phaseRED(i)) % condition
where the blue above the green, but the blue below the red
   newValue=abs((abs(hRED(j-1))- abs(hGREEN(j))))+abs((abs(hRED(j-1))-
abs(hBLUE(j))))+abs((abs(hGREEN(j))- abs(hBLUE(j))));
   if newValue < min
   min=newValue;
   nBLUE=nBLUE+1;      % The blue and green have the same fringe order
   nGREEN=nBLUE;       % The blue and green have the same fringe order
   nRED=nBLUE-1;       % The red fringe order is < red and Green by 1
   end
end
end
FringeOrderRED(i)=nRED;     % Update the fringe order for the red
FringeOrderGREEN(i)=nGREEN; % Update the fringe order for the green
FringeOrderBLUE(i)=nBLUE;   % Update the fringe order for the blue
%----End of best matching algorithm----
end

%%%
function [phase]=Carre(I1,I2,I3,I4)% Carre Function

a=(3*(I2-I3))-(I1-I4);
b=(I2-I3)+(I1-I4);
c=(I2+I3)-(I1+I4);
num1=(a*b);
den=c;
phase=atan((sqrt(abs(num1)/den^2)));
num=(I2-I3);
phase=PhaseWraping(num,den,phase);

%%%%%%%

function [phase]=PhaseWraping(num,den,phase); % Wrapped Phase function

if ((num > 0) && (den > 0))
   phase=phase;

elseif ((num > 0) && (den < 0))
   phase=pi-phase;

elseif ((num < 0) && (den < 0))
   phase=pi+phase;

elseif ((num < 0) && (den > 0))
   phase=(2*pi)-phase;
```

```
elseif (num == 0)
   phase=pi;

elseif ((num > 0) && (den==0))
   phase =0.5*pi;

elseif ((num < 0) && (den==0))
   phase =1*pi;

end
```

10. Appendix B. Mechanical Phase Shift Interferometer

Michelson interferometer configuration was implemented, as shown in Figure B.1, to generate the interference signal (i.e. fringes). The interferometer illuminated by RGB filtered wavelengths using an acousto-optic tuneable filter (AOTF) as described in section 5.3. The interferometer consisted of two equal arms split by a beam splitter. The two optical arms are a measurement arm ended by a sample surface and reference arm ended by a reference mirror. The reflected beams from the reference mirror and measured sample are added together by B.S to produce the interference fringes. Two lenses was used in this experiment; one to focus the light on the reference and sample surfaces and other to focus the interference fringes on a gray-level CCD using 250 mm and 100 mm focal lengths respectively.

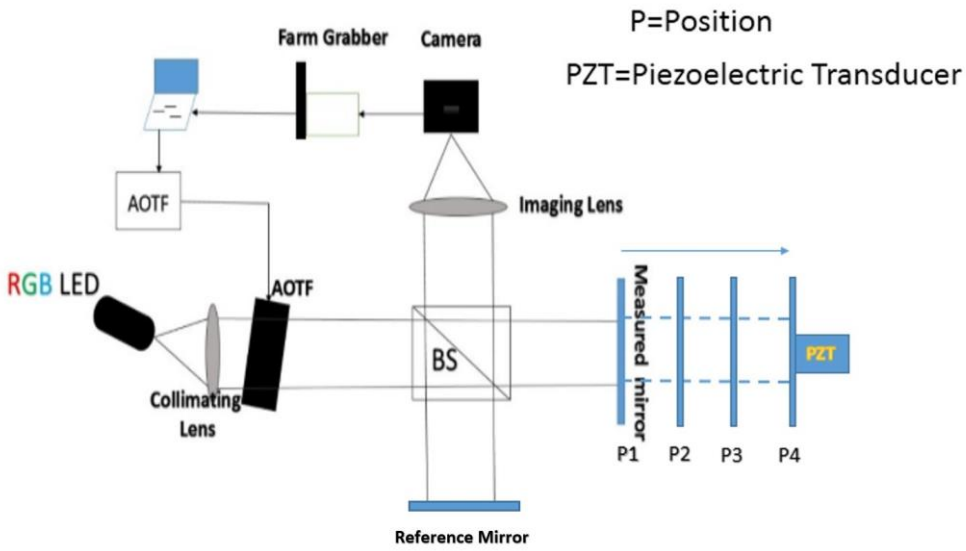

Figure B.1 Schematic of the mechanical RGB phase shift interferometry

The required phase shift was obtained mechanically using a piezoelectric translation stage (PZT), which was attached to the reference arm and controlled by a voltage-set power supply, which was providing the voltage set (0 v, 1.05 v, 2.10 v, and 3.15 v) to obtain four phase shift 45^0 phase shift for each wavelength individually and sequentially as shown in Figure B.1. The 45^0 was chosen at early stages of MPI developments because it was expected that the Carre algorithm just required any four equally steps of phase shift values.

The phase was calculated using Carré algorithm by processing four shifted intensity values using Equation (A.1). Meanwhile the best match technique as described in section 6.4.5, was used to unwrap the phase and retrieve the surface height. This routine is repeated in a successive manner to process all measured pixels to determine the entire surface. The algorithms are described in detail in chapter 6.

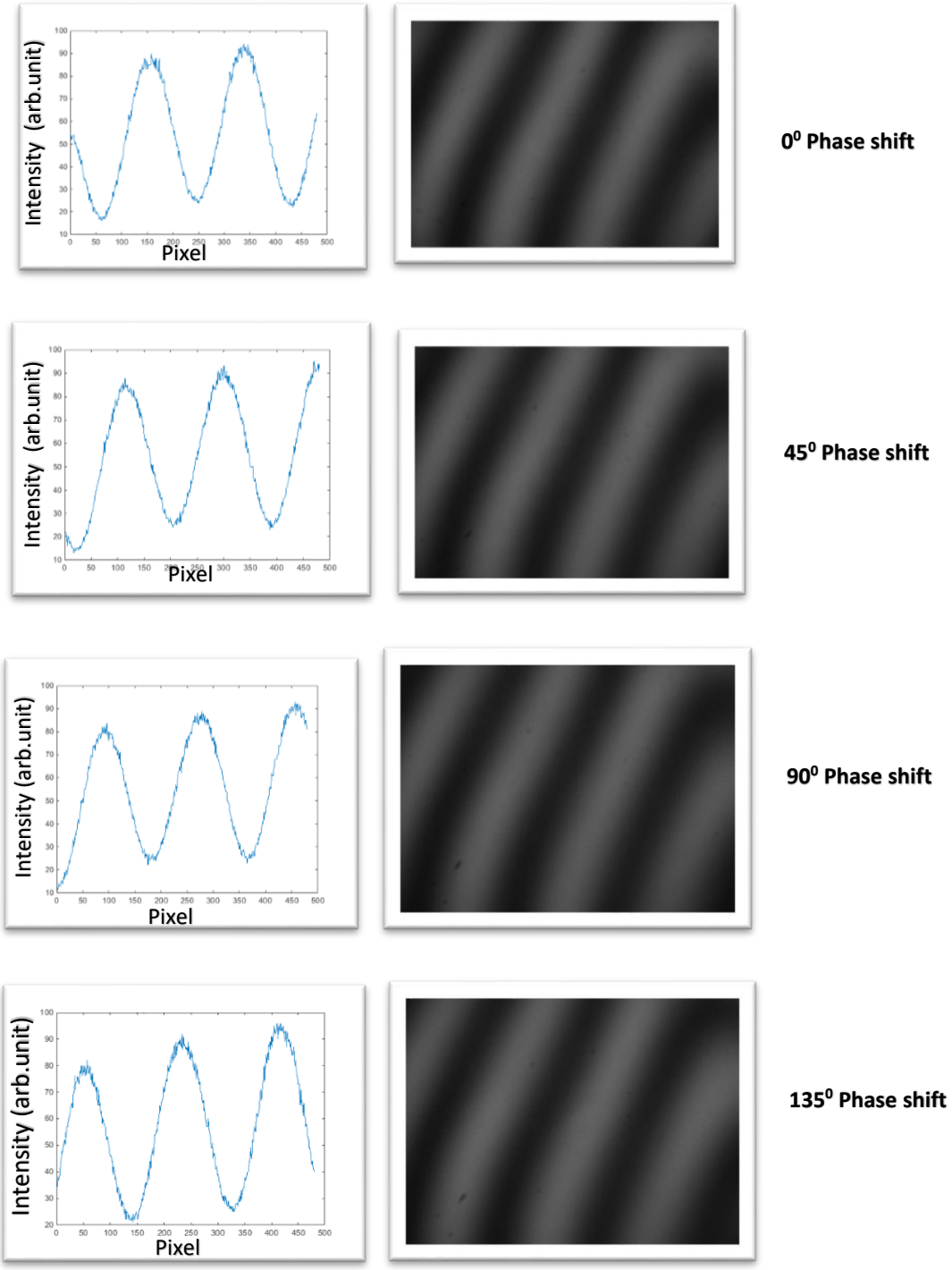

Figure B.2 Four interferograms recorded at a specific wavelength with 45º phase shift incremental step

The experiment was performed at two different timings (day and night time). The external disturbance of such vibrations causes an unwanted change in the OPD of the interferometers, which cause an error in the measurement result. It is important to mention that the optics laboratory was located in the third floor. The third floor acting as a membrane, producing low-frequency movement occurs in the region of 20–200 Hz (Blunt *et al.*, 2013). The building vibration value changing between day and night times led to a difference in the measurement error value. The

night measurement shows the better result, especially in the wrapped phase. The Day and Night wrapped phase for flat mirror were illustrated in Figure B.2 and B.3 respectively. The mechanical phase shift interferometer experiment night result is shown in Figure B.4. Measurement results demonstrate that the phase shift interferometer (PSI) can measure surface heights greater than λ/4 without depending on the neighbourhood of pixels, if RGB information is included. The overall surface inclination in this experiment exceeds 1 μm.

Since this stage depends on the mechanical translation of the reference mirror, and the required time for measurement means that this will lead to mechanical vibrations convolved into the data. This vibration will lead to a phase error, and that error will translate in retrieving the surface heights as given in the spikes and step jump errors in Figure B.5.

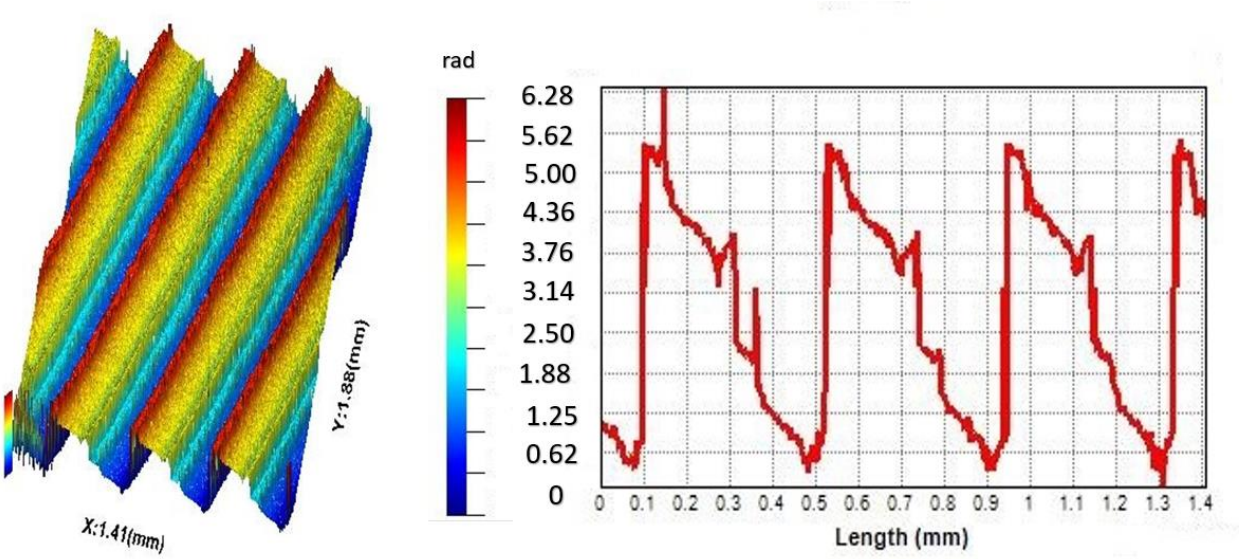

Figure B.3 Flat mirror Day measurement result using a mechanical phase shift measurement (a) Wrapped phase (b) Cross-sectional profile

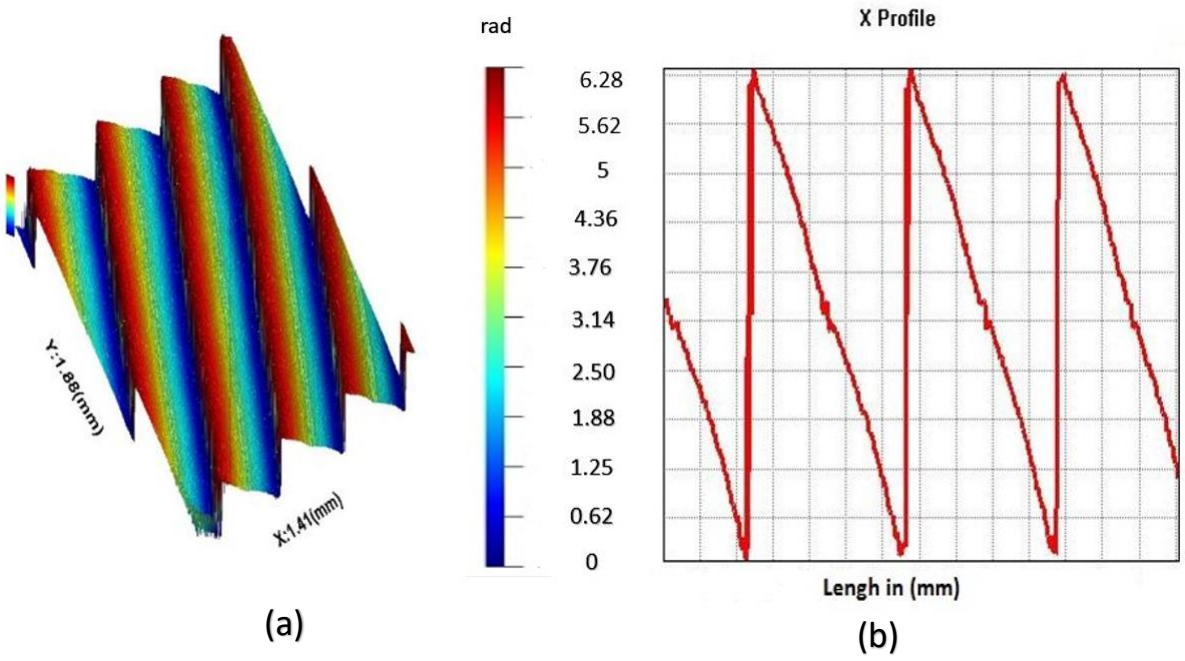

Figure B.4 Mechanical PSI at a specific wavelength (a) wrapped phase (b) cross-sectional profile

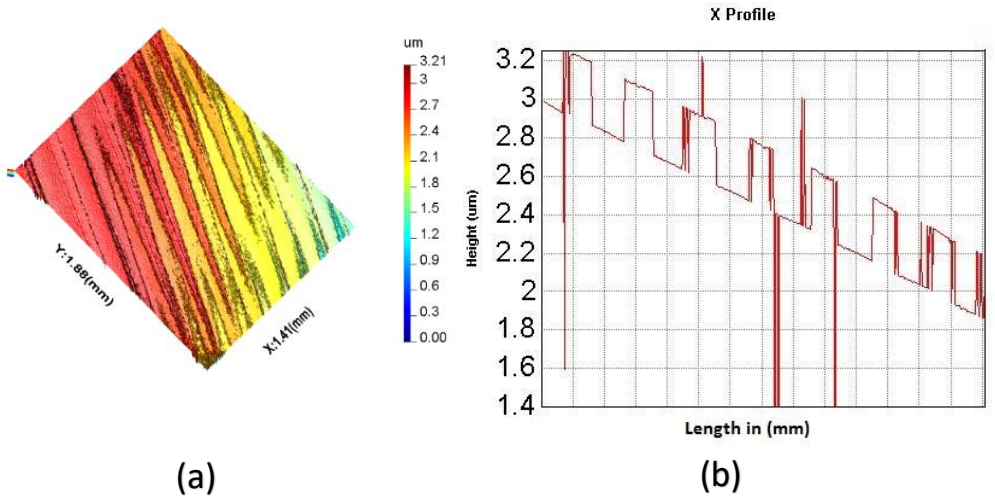

Figure B.5 RGB mechanical PSI measurement (a) areal surface (b) cross-sectional profile

10. Appendix C. Non-Mechanical (Wedge) Interferometer

The wedge interferometer experiment can provide a valid feasibility study about integrating multi-wavelength (RGB) and phase shift interferometer in a single optical setup. While the phase sift is achieved by tilting the reference mirror, the setup is simple and has colour camera that can capture all the information in a single shot. The advantage of this setup is that it can overcome any external vibration that causes measurement error. This is, however, dependent on the neighbour pixels to unwrap the phase.

The optical configuration of the RGB wedge interferometer is similar to the above setup but with replacing the CCD by a colour one (type 'evo1050CFLGEC', from svs-vistek ltd) and removing the PZT, as shown in Figure C.1. The reference mirror was tilted in order to introduce several fringes across the field-of-view.

The Carré algorithm was used to determine the wrapped phase using four intensity values gathered from neighbour pixels with separation approximately equal to one quarter of a full fringe period. The phase unwrapping is achieved by compensating for any 2π phase jump (Takeda *et al.*, 1982). Measurement of a mirror surface is shown in Figure C.1. The result demonstrates that the wedge interferometer using RGB illumination source can measure 1 μm surface height and nano-scale vertical resolution with a single shot approach.

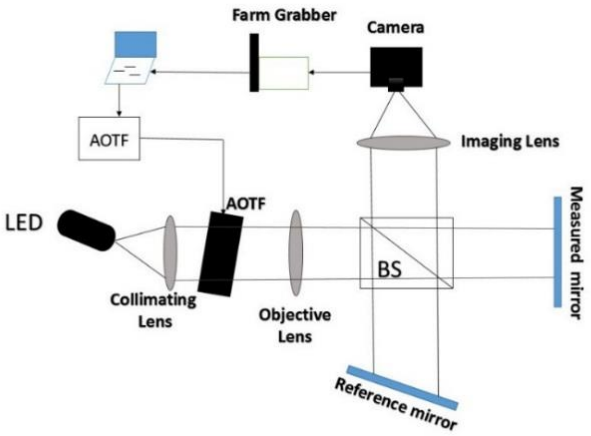

Figure C.1 Schematic of RGB wedge interferometry system

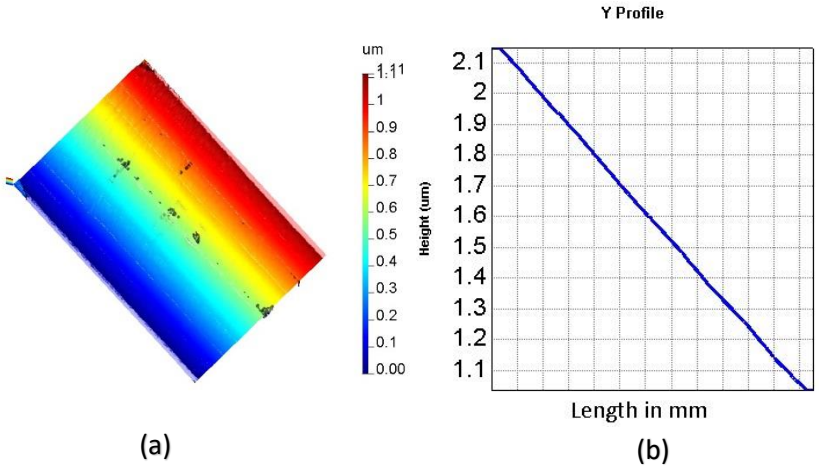

Figure C.2 RGB wedge measurement for flat mirror (a) areal measurement (b) Cross-sectional profile

10. Appendix D. MPI Setup Alignment Procedure

The alignment of the microscope objective is essential for the overall performance of interferometer (Tang, 2016). As mentioned earlier, the Michelson interferometer was used in MPI. The alignment procedure is as follows: at the beginning, mount the objective on a kinematic platform (Thorlabs, KM100B/M) to adjust the angular positions, ensuring the objective is levelled and centred with respect to the optical axis of the MPI setup. A collimated laser beam with small aperture is used for the alignment step. The polarised beam splitter (Thorlabs, PBS251) was also mounted on a kinematic base (Thorlabs, KM100B/M) in order to guarantee that the two separated beams have the same height by adjusting the angular positions of the base.

Subsequently, the objective and the polarised beam splitter were aligned together. Then, the standard step height surface was placed in the measurement arm at the focus of the objective lenses. After that, the reference arms were placed at the focus of the objective lens and translated until obtained the fringe.

The fast axis of the quarter waveplate (QWP1 or QWP2) were set to obtain high intensity measured by power meter for the reference and measurement arm separately. The power meter was installed before the imaging lens and after the beams were combined by polarised beam splitter. The combined beams were focused by a doublet lens (Thorlabs, AC254-100-A1-f=100.0mm). The doublet lens focus the beam to three Non-polarized beam splitter.

The three non-polarized beam splitter (Thorlabs, BS013) are placed on a single kinematic base (Thorlabs, KM100B/M) to ensure that they have same tilt and height. The angular adjustments of all kinematic mounts and bases were made by targeting the level of a single collimated laser diode beam.

The four observation arms, which generated by the three beam splitter are equipped with polarisation equipment as listed in Table 5.1. The four arms end with four colour cameras. The reference arm was blocked, and cameras were translated until the sample is observed on the cameras. Afterwards, the reference mirror is brought to focus and adjusted until zero fringes were obtained, indicating that there is no tilt between the two arms, and the best fringe is obtained at zero OPD.

10. Appendix E. Four Cameras Intensity Calibration (Matlab code)

```
Ref1=imread('R1.bmp'); % read the reference camera 1
Refer1=Ref1(200:700,153:653,1:3);
ReferRed1=double(Refer1(:,:,1));
ReferGreen1=double(Refer1(:,:,2));
ReferBlue1=double(Refer1(:,:,3));
S1=imread('S1.bmp'); %read the sample camera 1
Sample1=S1(200:700,153:653,1:3);
SamplRed1=double(Sample1(:,:,1));
SamplGreen1=double(Sample1(:,:,2));
SamplBlue1=double(Sample1(:,:,3));
Ref2=imread('R2.bmp'); % read the reference camera 2
Refer2=Ref2(176:676,127:627,1:3);
ReferRed2=double(Refer2(:,:,1));
ReferGreen2=double(Refer2(:,:,2));
ReferBlue2=double(Refer2(:,:,3));
S2=imread('S2.bmp'); % read the sample camera 2
Sample2=S2(176:676,127:627,1:3);
SamplRed2=double(Sample2(:,:,1));
SamplGreen2=double(Sample2(:,:,2));
SamplBlue2=double(Sample2(:,:,3));
Ref3=imread('R3.bmp'); % read the reference camera 3
Refer3=Ref3(134:634,159:659,1:3);
ReferRed3=double(Refer3(:,:,1));
ReferGreen3=double(Refer3(:,:,2));
ReferBlue3=double(Refer3(:,:,3));
S3=imread('S3.bmp'); % read the sample camera 3
Sample3=S3(134:634,159:659,1:3);
SamplRed3=double(Sample3(:,:,1));
SamplGreen3=double(Sample3(:,:,2));
SamplBlue3=double(Sample3(:,:,3))
```

```
Ref4=imread('R4.bmp'); % read the reference camera 4
Refer4=Ref4(94:594,113:613,1:3);
ReferRed4=double(Refer4(:,:,1));
ReferGreen4=double(Refer4(:,:,2));
ReferBlue4=double(Refer4(:,:,3));
S4=imread('S4.bmp'); % read the sample camera 4
Sample4=S4(94:594,113:613,1:3);% i have to add it o O2
SamplRed4=double(Sample4(:,:,1));
SamplGreen4=double(Sample4(:,:,2));
SamplBlue4=double(Sample4(:,:,3));
AR1=ReferRed1+SamplRed1;% A for Red color (reference + sample)
AR2=ReferRed2+SamplRed2;% A for Red color (reference + sample)
AR3=ReferRed3+SamplRed3;% A for Red color (reference + sample)
AR4=ReferRed4+SamplRed4;% A for Red color (reference + sample)
A1Rm=mean(AR1(:)); % mean for Red component (reference + sample)
A2Rm=mean(AR2(:));  % mean for Red component (reference + sample)
A3Rm=mean(AR3(:)); % mean for Red component (reference + sample)
A4Rm=mean(AR4(:)); % mean for Red component (reference + sample)
ArrayMeanR=[A1Rm A2Rm A3Rm A4Rm];
[MinMean1 index1]=min(ArrayMeanR);% index for red component (reference+sample)
VBR1=ReferRed1.*SamplRed1; % multiblication of A*B for red componet (referenc*sample)
VBR2=ReferRed2.*SamplRed2; % multiblication of A*B for red componet (referenc*sample)
VBR3=ReferRed3.*SamplRed3; % multiblication of A*B for red componet (referenc*sample)
VBR4=ReferRed4.*SamplRed4; % multiblication of A*B for red componet (referenc*sample)
BR1=2*(VBR1.^0.5); % fringe contrast(B) for red component (2 * sqrt(reference+sample).
BR2=2*(VBR2.^0.5); % fringe contrast(B) for red component (2 * sqrt(reference+sample).
BR3=2*(VBR3.^0.5); % fringe contrast(B) for red component (2 * sqrt(reference+sample).
BR4=2*(VBR4.^0.5); % fringe contrast(B) for red component (2 * sqrt(reference+sample).
%%%%%% start now with green
AG1=ReferGreen1+SamplGreen1; % A1 for Green color (reference and sample)
AG2=ReferGreen2+SamplGreen2; %A2 for Green color (reference and sample)
AG3=ReferGreen3+SamplGreen3; %A3 for Green color (reference and sample)
```

```
AG4=ReferGreen4+SamplGreen4; %A4 for Green color (reference and sample)

A1Gm=mean(AG1(:)); % mean for Green component (reference and sample)

A2Gm=mean(AG2(:)); % mean for Green component (reference and sample)

A3Gm=mean(AG3(:)); % mean for Green component (reference and sample)

A4Gm=mean(AG4(:)); % mean for Green component (reference and sample)

ArrayMeanG=[A1Gm A2Gm A3Gm A4Gm];

[MinMean2 index2]=min(ArrayMeanG); % index for Green component (reference+sample)

VBG1=ReferGreen1.*SamplGreen1; % multiblication of A*B for Green componet
(referenc*sample)

VBG2=ReferGreen2.*SamplGreen2; % multiblication of A*B for Green componet
(referenc*sample)

VBG3=ReferGreen3.*SamplGreen3; % multiblication of A*B for Green componet
(referenc*sample)

VBG4=ReferGreen4.*SamplGreen4; % multiblication of A*B for Green componet
(referenc*sample)

BG1=2*(VBG1.^0.5); % fringe contrast(B) for Green component (2 * sqrt(reference+sample).

BG2=2*(VBG2.^0.5);

BG3=2*(VBG3.^0.5);

BG4=2*(VBG4.^0.5);

%%%%%% start now with Blue

AB1=ReferBlue1+SamplBlue1; %A1 for Blue color (reference and sample)

AB2=ReferBlue2+SamplBlue2; %A2 for Blue color (reference and sample)

AB3=ReferBlue3+SamplBlue3; %A3 for Blue color (reference and sample)

AB4=ReferBlue4+SamplBlue4; %A4 for Blue color (reference and sample)

A1Bm=mean(AB1(:)); % mean for Blue component (reference and sample)

A2Bm=mean(AB2(:)); % mean for Blue component (reference and sample)

A3Bm=mean(AB3(:)); % mean for Blue component (reference and sample)

A4Bm=mean(AB4(:)); % mean for Blue component (reference and sample)

ArrayMeanB=[A1Bm A2Bm A3Bm A4Bm];

[MinMean3 index3]=min(ArrayMeanB); % index for Blue component (reference+sample)

VBB1=ReferBlue1.*SamplBlue1; % multiblication of A*B for Blue componet
(referenc*sample)

VBB2=ReferBlue2.*SamplBlue2; % multiblication of A*B for Blue componet
(referenc*sample)
```

```
VBB3=ReferBlue3.*SamplBlue3; % multiblication of A*B for Blue componet (referenc*sample)
VBB4=ReferBlue4.*SamplBlue4; % multiblication of A*B for Blue componet (referenc*sample)
BB1=2*(VBB1.^0.5); % fringe contrast(B) for Blue component (2 * sqrt(reference+sample).
BB2=2*(VBB2.^0.5);
BB3=2*(VBB3.^0.5);
BB4=2*(VBB4.^0.5);
%%%%%%%
O1=imread('O1.bmp');
colorfring1=O1(200:700,153:653,1:3); % read fringe camera 1
imwrite(colorfring1,'OO1.bmp')
ColorRed1=double(colorfring1(:,:,1)); % extract the red components of camera 1
SubtractionR1=ColorRed1-AR1;
CosPhaseRed1=SubtractionR1./BR1; % extract the red phase value of Camera 1.
colorfringGreen1=double(colorfring1(:,:,2)); % extract the green components of camera 1
SubtractionG1=colorfringGreen1-AG1;
CosPhaseGreen1=SubtractionG1./BG1;%extract the Green phase value of Camera 1.
colorfringeblue1=double(colorfring1(:,:,3)); % extract the blue components of camera 1
SubtractionB1=colorfringeblue1-AB1;
CosPhaseBlue1=SubtractionB1./BB1; % extract the Blue phase value of Camera 1.
O2=imread('O2.bmp'); % read fringe camera 2
colorfring2=O2(176:676,127:627,1:3);
ColorRed2=double(colorfring2(:,:,1)); %extract the red components of camera 2
SubtractionR2=ColorRed2-AR2;
CosPhaseRed2=SubtractionR2./BR2; % extract the Red phase value of Camera 2.
colorfringGreen2=double(colorfring2(:,:,2)); % extract the green components of camera 2
SubtractionG2=colorfringGreen2-AG2;
CosPhaseGreen2=SubtractionG2./BG2;% extract the Green phase value ofCamera 2.
colorfringeblue2=double(colorfring2(:,:,3)); % extract the blue components of camera 2
SubtractionB2=colorfringeblue2-AB2;
CosPhaseBlue2=SubtractionB2./BB2; % extract the blue phase value of Camera 2.
O3=imread('O3.bmp'); % read fringe camera 3
```

```
colorfring3=O3(134:634,159:659,1:3);
ColorRed3=double(colorfring3(:,:,1));% extract the red components of camera 3
SubtractionR3=ColorRed3-AR3;
CosPhaseRed3=SubtractionR3./BR3;% extract the Red phase value of Camera 3.
colorfringGreen3=double(colorfring3(:,:,2));% extract the green components of camera 3
SubtractionG3=colorfringGreen3-AG3;
CosPhaseGreen3=SubtractionG3./BG3;% extract the Green phase value of Camera 3
colorfringeblue3=double(colorfring3(:,:,3)); % extract the blue components of camera 3
SubtractionB3=colorfringeblue3-AB3;
CosPhaseBlue3=SubtractionB3./BB3;%extract the blue phase value of Camera 3.
O4=imread('O4.bmp'); % read fringe camera 4
colorfring4=O4(94:594,113:613,1:3);
ColorRed4=double(colorfring4(:,:,1));% extract the red components of camera 4
SubtractionR4=ColorRed4-AR4;
CosPhaseRed4=SubtractionR4./BR4; %extract red phase value of Camera 4
colorfringGreen4=double(colorfring4(:,:,2));% extract the green components of camera 4
SubtractionG4=colorfringGreen4-AG4;
CosPhaseGreen4=SubtractionG4./BG4;%  extract Green phase value of Camera 4.
colorfringeblue4=double(colorfring4(:,:,3)); % extract the blue components of camera 4
SubtractionB4=colorfringeblue4-AB4;
CosPhaseBlue4=SubtractionB4./BB4;%extract Blue phase value of Camera 4.
if index1==1 % set the bias and visibility value for minimum index for red componente
    CosPhaseRed1=CosPhaseRed1.*BR1;
    CosPhaseRed2=CosPhaseRed2.*BR1;
    CosPhaseRed3=CosPhaseRed3.*BR1;
    CosPhaseRed4=CosPhaseRed4.*BR1;
    Redfringebuild1=CosPhaseRed1+AR1;
    Redfringebuild2=CosPhaseRed2+AR1;
    Redfringebuild3=CosPhaseRed3+AR1;
    Redfringebuild4=CosPhaseRed4+AR1;
   Redbalance1=uint8(Redfringebuild1);
   Redbalance2=uint8(Redfringebuild2);
```

```
    Redbalance3=uint8(Redfringebuild3);
    Redbalance4=uint8(Redfringebuild4);
elseif index1==2 % set the bias and visibility value for minimum index for red componente
    CosPhaseRed1=CosPhaseRed1.*BR2;
    CosPhaseRed2=CosPhaseRed2.*BR2;
    CosPhaseRed3=CosPhaseRed3.*BR2;
    CosPhaseRed4=CosPhaseRed4.*BR2;
    Redfringebuild1=CosPhaseRed1+AR2;
    Redfringebuild2=CosPhaseRed2+AR2;
    Redfringebuild3=CosPhaseRed3+AR2;
    Redfringebuild4=CosPhaseRed4+AR2;
    Redbalance1= uint8(Redfringebuild1);
    Redbalance2= uint8(Redfringebuild2);
    Redbalance3= uint8(Redfringebuild3);
    Redbalance4= uint8(Redfringebuild4);
elseif index1==3 % set the bias and visibility value for minimum index for red componente
    CosPhaseRed1=CosPhaseRed1.*BR3;
    CosPhaseRed2=CosPhaseRed2.*BR3;
    CosPhaseRed3=CosPhaseRed3.*BR3;
    CosPhaseRed4=CosPhaseRed4.*BR3;
    Redfringebuild1=CosPhaseRed1+AR3;
    Redfringebuild2=CosPhaseRed2+AR3;
    Redfringebuild3=CosPhaseRed3+AR3;
    Redfringebuild4=CosPhaseRed4+AR3;
    Redbalance1=uint8(Redfringebuild1);
    Redbalance2=uint8(Redfringebuild2);
    Redbalance3=uint8(Redfringebuild3);
    Redbalance4=uint8(Redfringebuild4);
else % set the bias and visibility value for minimum index for red componente
    CosPhaseRed1=CosPhaseRed1.*BR4;
    CosPhaseRed2=CosPhaseRed2.*BR4;
    CosPhaseRed3=CosPhaseRed3.*BR4;
```

```
    CosPhaseRed4=CosPhaseRed4.*BR4;
    Redfringebuild1=CosPhaseRed1+AR4;
    Redfringebuild2=CosPhaseRed2+AR4;
    Redfringebuild3=CosPhaseRed3+AR4;
    Redfringebuild4=CosPhaseRed4+AR4;
    Redbalance1=uint8(Redfringebuild1);
    Redbalance2=uint8(Redfringebuild2);
    Redbalance3=uint8(Redfringebuild3);
    Redbalance4=uint8(Redfringebuild4);
end
if index2==1 % set the bias and visibility value for minimum index for green componente
    CosPhaseGreen1=CosPhaseGreen1.*BG1;
    CosPhaseGreen2=CosPhaseGreen2.*BG1;
    CosPhaseGreen3=CosPhaseGreen3.*BG1;
    CosPhaseGreen4=CosPhaseGreen4.*BG1
    Greenfringebuild1=CosPhaseGreen1+AG1;
    Greenfringebuild2=CosPhaseGreen2+AG1;
    Greenfringebuild3=CosPhaseGreen3+AG1;
    Greenfringebuild4=CosPhaseGreen4+AG1;
    greanbalance1=uint8(Greenfringebuild1);
    greanbalance2=uint8(Greenfringebuild2);
    greanbalance3=uint8(Greenfringebuild3);
    greanbalance4=uint8(Greenfringebuild4);
elseif index2==2 % set the bias and visibility value for minimum index for green componente
    CosPhaseGreen1=CosPhaseGreen1.*BG2;
    CosPhaseGreen2=CosPhaseGreen2.*BG2;
    CosPhaseGreen3=CosPhaseGreen3.*BG2;
    CosPhaseGreen4=CosPhaseGreen4.*BG2;
    Greenfringebuild1=CosPhaseGreen1+AG2;
    Greenfringebuild2=CosPhaseGreen2+AG2;
    Greenfringebuild3=CosPhaseGreen3+AG2;
    Greenfringebuild4=CosPhaseGreen4+AG2;
```

```
    greanbalance1=uint8(Greenfringebuild1);
    greanbalance2=uint8(Greenfringebuild2);
    greanbalance3=uint8(Greenfringebuild3);
    greanbalance4=uint8(Greenfringebuild4);
%
elseif index2==3 % set the bias and visibility value for minimum index for green componente
    CosPhaseGreen1=CosPhaseGreen1.*BG3;
    CosPhaseGreen2=CosPhaseGreen2.*BG3;
    CosPhaseGreen3=CosPhaseGreen3.*BG3;
    CosPhaseGreen4=CosPhaseGreen4.*BG3;
    Greenfringebuild1=CosPhaseGreen1+AG3;
    Greenfringebuild2=CosPhaseGreen2+AG3;
    Greenfringebuild3=CosPhaseGreen3+AG3;
    Greenfringebuild4=CosPhaseGreen4+AG3;
    greanbalance1=uint8(Greenfringebuild1);
    greanbalance2=uint8(Greenfringebuild2);
    greanbalance3=uint8(Greenfringebuild3);
    greanbalance4=uint8(Greenfringebuild4);
%
else % set the bias and visibility value for minimum index for green componente
    CosPhaseGreen1=CosPhaseGreen1.*BG4;
    CosPhaseGreen2=CosPhaseGreen2.*BG4;
    CosPhaseGreen3=CosPhaseGreen3.*BG4;
    CosPhaseGreen4=CosPhaseGreen4.*BG4;
    Greenfringebuild1=CosPhaseGreen1+AG4;
    Greenfringebuild2=CosPhaseGreen2+AG4;
    Greenfringebuild3=CosPhaseGreen3+AG4;
    Greenfringebuild4=CosPhaseGreen4+AG4;
    greanbalance1=uint8(Greenfringebuild1);
    greanbalance2=uint8(Greenfringebuild2);
    greanbalance3=uint8(Greenfringebuild3);
    greanbalance4=uint8(Greenfringebuild4);
```

```
end
if index3==1 % set the bias and visibility value for minimum index for blue componente
    CosPhaseBlue1=CosPhaseBlue1.*BB1;
    CosPhaseBlue2=CosPhaseBlue2.*BB1;
    CosPhaseBlue3=CosPhaseBlue3.*BB1;
    CosPhaseBlue4=CosPhaseBlue4.*BB1;
    Bluefringebuild1=CosPhaseBlue1+AB1;
    Bluefringebuild2=CosPhaseBlue2+AB1;
    Bluefringebuild3=CosPhaseBlue3+AB1;
    Bluefringebuild4=CosPhaseBlue4+AB1;
    Bluebalance1=uint8(Bluefringebuild1);
    Bluebalance2=uint8(Bluefringebuild2);
    Bluebalance3=uint8(Bluefringebuild3);
    Bluebalance4=uint8(Bluefringebuild4);
elseif index3==2 % set the bias and visibility value for minimum index for blue componente
    CosPhaseBlue1=CosPhaseBlue1.*BB2;
    CosPhaseBlue2=CosPhaseBlue2.*BB2;
    CosPhaseBlue3=CosPhaseBlue3.*BB2;
    CosPhaseBlue4=CosPhaseBlue4.*BB2;
    Bluefringebuild1=CosPhaseBlue1+AB2;
    Bluefringebuild2=CosPhaseBlue2+AB2;
    Bluefringebuild3=CosPhaseBlue3+AB2;
    Bluefringebuild4=CosPhaseBlue4+AB2;
    Bluebalance1=uint8(Bluefringebuild1);
    Bluebalance2=uint8(Bluefringebuild2);
    Bluebalance3=uint8(Bluefringebuild3);
    Bluebalance4=uint8(Bluefringebuild4);
elseif index3==3 % set the bias and visibility value for minimum index for blue componente
    CosPhaseBlue1=CosPhaseBlue1.*BB3;
    CosPhaseBlue2=CosPhaseBlue2.*BB3;
    CosPhaseBlue3=CosPhaseBlue3.*BB3;
    CosPhaseBlue4=CosPhaseBlue4.*BB3;
```

```
    Bluefringebuild1=CosPhaseBlue1+AB3;
    Bluefringebuild2=CosPhaseBlue2+AB3;
    Bluefringebuild3=CosPhaseBlue3+AB3;
    Bluefringebuild4=CosPhaseBlue4+AB3;
    Bluebalance1=uint8(Bluefringebuild1);
    Bluebalance2=uint8(Bluefringebuild2);
    Bluebalance3=uint8(Bluefringebuild3);
    Bluebalance4=uint8(Bluefringebuild4);

else % set the bias and visibility value for minimum index for blue componente
    CosPhaseBlue1=CosPhaseBlue1.*BB4;
    CosPhaseBlue2=CosPhaseBlue2.*BB4;
    CosPhaseBlue3=CosPhaseBlue3.*BB4;
    CosPhaseBlue4=CosPhaseBlue4.*BB4;
    Bluefringebuild1= CosPhaseBlue1+AB4;
    Bluefringebuild2= CosPhaseBlue2+AB4;
    Bluefringebuild3= CosPhaseBlue3+AB4;
    Bluefringebuild4= CosPhaseBlue4+AB4;
    Bluebalance1=uint8(Bluefringebuild1);
    Bluebalance2=uint8(Bluefringebuild2);
    Bluebalance3=uint8(Bluefringebuild3);
    Bluebalance4=uint8(Bluefringebuild4);
end
RGB1 = cat(3, Redbalance1, greanbalance1,Bluebalance1 ); % c RGB components for camera 1
RGB2= cat(3, Redbalance2, greanbalance2,Bluebalance2 ); % combined the RGB components
for camera 2
RGB3= cat(3, Redbalance3, greanbalance3,Bluebalance3 );  % combined the RGB components
for camera 3
RGB4= cat(3, Redbalance4, greanbalance4,Bluebalance4 ); % RGB components for camera 4
 imwrite(RGB1,'1.bmp') % rewrite the colour fringe for camera 1
 imwrite(RGB2,'2.bmp') % rewrite the colour fringe for camera 2
 imwrite(RGB3,'3.bmp') % rewrite the colour fringe for camera 3
 imwrite(RGB4,'4.bmp') % rewrite the colour fringe for camera 4
```

10. Appendix F. Trigonometry Equations for Calculating the Wrapped Phased in Four-Step Phase Shift Algorithm.

$$I_{rgb} = a_{rgb} + b_{rgb}\cos(\theta_{rgb}) \quad \text{(F.1)}$$

$$I_{rgb} = a_{rgb} + b_{rgb}\cos(\theta_{rgb} + \frac{\pi}{2}) \quad \text{(F.2)}$$

$$I_{rgb} = a_{rgb} + b_{rgb}\cos(\theta_{rgb} + \pi) \quad \text{(F.3)}$$

$$I_{rgb} = a_{rgb} + b_{rgb}\cos(\theta_{rgb} + \frac{3 * \pi}{2}) \quad \text{(F.4)}$$

Using trigonometric identity yields

$$I_{1rgb} = a_{rgb} + b_{rgb}\cos(\theta_{rgb}) \quad \text{(F.5)}$$

$$I_{2rgb} = a_{rgb} - b_{rgb}\sin(\theta_{rgb}) \quad \text{(F.6)}$$

$$I_{3rgb} = a_{rgb} - b_{rgb}\cos(\theta_{rgb}) \quad \text{(F.7)}$$

$$I_{4rgb} = a_{rgb} + b_{rgb}\sin(\theta_{rgb}) \quad \text{(F.8)}$$

The intensity bias term is eliminated by subtraction the Equations:

$$I_{4rgb} - I_{2rgb} = 2b_{rgb}\sin(\theta_{rgb}) \quad \text{(F.9)}$$

$$I_{1rgb} - I_{3rgb} = 2b_{rgb}\cos(\theta_{rgb}) \quad \text{(F.10)}$$

Taking the ratio of Equation (F.9) and (F.10) to eliminate the fringe visibility as illustrated in equation (F.11).

$$\frac{I_{4rgb} - I_{2rgb}}{I_{1rgb} - I_{3rgb}} = \frac{\sin \emptyset_{rgb}}{\cos \emptyset_{rgb}} = tan_{rgb}\,[\,\theta_{rgb}] \quad \text{(F.11)}$$

10. Appendix G. Single Wavelength Phase Unwrapping Algorithm in SPI Mode (Matlab code)

```
%-----Initial Matlab simulation code for phase shift interferometer and three
colour interferometer
%----- Date 6th of Nov 2015
clear
clc
close all;

a=100;  % interference biase
b=90;    % fringe contrast
TotalSampling=5000;  % number of measurement point
hTrueRange=5000;   % nm Upper limit of the measurement range
hStart=0;          % nm Lower limit of the measurement range
hTrue=linspace(hStart,hTrueRange,TotalSampling);
RED=630;        %610;    %RED will be shifted by 70 nm to get green color
GREEN=540;      %540;    %GREEN will be shifted by 70 nm to get blue color
BLUE=460;       %470;    %See above
% In this simulation 4 shifts are used to retrieve the phase information using Carre method.
% However, for experimental setup will use three phase shifts.
for i=1:TotalSampling
%-- Simulated phases to get intensities
% (1) RED colour
PhaseRED_0=(4*pi*hTrue(i))/RED+(0*(pi/180));    % first phase information
PhaseRED_90=(4*pi*hTrue(i))/RED+(90*(pi/180));  % second phase information shifted by 45
degree
PhaseRED_180=(4*pi*hTrue(i))/RED+(180*(pi/180));  % third phase information shifted by 90
degree
PhaseRED_270=(4*pi*hTrue(i))/RED+(270*(pi/180));% four phase information shifted by 135
degree
%-- From the practical setup, only intensities will be obtained
I_RED_1=a+b*cos(PhaseRED_0);              % Intensity of the first phase
I_RED_2=a+b*cos(PhaseRED_90);             % Intensity of the second phase
I_RED_3=a+b*cos(PhaseRED_180);            % Intensity of the third phase
I_RED_4=a+b*cos(PhaseRED_270);            % Intensity of the fourth phase
%-- Determine the phase using Carre method
phaseRED(i)=FourStepARIZONA(I_RED_1,I_RED_2,I_RED_3,I_RED_4);
Ired(i)=I_RED_1;       % Just for plot purpose (nothing to do with the algorithm at this stage of
research)
i
end
phi_R=unwrap_phase(phaseRED);
hREDCal=(phi_R./(2*pi))*(RED/2);         % surface height using red
%%%%%%%%%%%%%%%%%%%%%%%%%%%%%%%%%%%%%%%%%%%%%%%%%%%%%%%%%%%%%%%%%%%%%%%%%%%%%%%%
% Fast unwrapping 2D phase image using the algorithm given in:                %
%     M. A. HerrÃ¡ez, D. R. Burton, M. J. Lalor, and M. A. Gdeisat,           %
%     "Fast two-dimensional phase-unwrapping algorithm based on sorting by    %
%     reliability following a noncontinuous path", Applied Optics, Vol. 41,   %
%     Issue 35, pp. 7437-7444 (2002).                                         %
```

```
%                                                                       %
% If using this code for publication, please kindly cite the following:       %
% * M. A. Herraez, D. R. Burton, M. J. Lalor, and M. A. Gdeisat, "Fast        %
%   two-dimensional phase-unwrapping algorithm based on sorting by reliability %
%   following a noncontinuous path", Applied Optics, Vol. 41, Issue 35,       %
%   pp. 7437-7444 (2002).                                                     %
% * M. F. Kasim, "Fast 2D phase unwrapping implementation in MATLAB",         %
%   https://github.com/mfkasim91/unwrap_phase/ (2017).                        %
%                                                                       %
% Input:                                                                %
% * img: The wrapped phase image either from -pi to pi or from 0 to 2*pi.     %
%       If there are unwanted regions, it should be filled with NaNs.         %
%                                                                       %
% Output:                                                               %
% * res_img: The unwrapped phase with arbitrary offset.                       %
%                                                                       %
% Author:                                                               %
%     Muhammad F. Kasim, University of Oxford (2017)                        %
%     Email: firman.kasim@gmail.com                                         %
%%%%%%%%%%%%%%%%%%%%%%%%%%%%%%%%%%%%%%%%%%%%%%%%%%%%%%%%%%%%%%%%%%%%%%%%%%%
%%%%%%%%%%%%%%%%%%%%%%%%%%%%%%%%%%%%%%%%%%%%%%%%%%%%%%%%%%%%%%%%%%%%%%%%%%%

function res_img = unwrap_phase(img)
    [Ny, Nx] = size(img);

    % get the reliability
    reliability = get_reliability(img); % (Ny,Nx)

    % get the edges
    [h_edges, v_edges] = get_edges(reliability); % (Ny,Nx) and (Ny,Nx)

    % combine all edges and sort it
    edges = [h_edges(:); v_edges(:)];
    edge_bound_idx = Ny * Nx; % if i <= edge_bound_idx, it is h_edges
    [~, edge_sort_idx] = sort(edges, 'descend');

    % get the indices of pixels adjacent to the edges
    idxs1 = mod(edge_sort_idx - 1, edge_bound_idx) + 1;
    idxs2 = idxs1 + 1 + (Ny - 1) .* (edge_sort_idx <= edge_bound_idx);

    % label the group
    group = reshape([1:numel(img)], Ny*Nx, 1);
    is_grouped = zeros(Ny*Nx,1);
    group_members = cell(Ny*Nx,1);
    for i = 1:size(is_grouped,1)
        group_members{,  #90} = i;
    end

    % propagate the unwrapping
    res_img = img;
    num_nan = sum(isnan(edges)); % count how many nan-s and skip them
```

```
    for i = num_nan+1 : length(edge_sort_idx)
        % get the indices of the adjacent pixels
        idx1 = idxs1(i);
        idx2 = idxs2(i);

        % skip if they belong to the same group
        if (group(idx1) == group(idx2)) continue; end

        % idx1 should be ungrouped (swap if idx2 ungrouped and idx1 grouped)
        % otherwise, activate the flag all_grouped
        all_grouped = 0;
        if is_grouped(idx1)
            if ~is_grouped(idx2)
                idxt = idx1;
                idx1 = idx2;
                idx2 = idxt;
            else
                all_grouped = 1;
            end
        end

        % calculate how much we should add to the idx1 and group
        dval = floor((res_img(idx2) - res_img(idx1) + pi) / (2*pi)) * 2*pi;

        % which pixel should be changed
        if all_grouped
            pix_idxs = group_members{group(idx1)};
        else
            pix_idxs = idx1;
        end

        % add the pixel value
        if dval ~= 0
            res_img(pix_idxs) = res_img(pix_idxs) + dval;
        end

        % change the group
% change the group
        g1 = group(idx1);
        g2 = group(idx2);
        len_g1 = length(group_members{g1});
        group_members(Daniel)(end+1:end+len_g1) = group_members{g1};
        group_members{g1} = [];
        group(pix_idxs) = g2;

        % mark idx1 and idx2 as already being grouped
        is_grouped(idx1) = 1;
        is_grouped(idx2) = 1;
    end
end
```

```
function rel = get_reliability(img)
    rel = zeros(size(img));

    % get the shifted images (N-2, N-2)
    img_im1_jm1 = img(1:end-2, 1:end-2);
    img_i_jm1   = img(2:end-1, 1:end-2);
    img_ip1_jm1 = img(3:end  , 1:end-2);
    img_im1_j   = img(1:end-2, 2:end-1);
    img_i_j     = img(2:end-1, 2:end-1);
    img_ip1_j   = img(3:end  , 2:end-1);
    img_im1_jp1 = img(1:end-2, 3:end  );
    img_i_jp1   = img(2:end-1, 3:end  );
    img_ip1_jp1 = img(3:end  , 3:end  );

    % calculate the difference
    gamma = @(x) sign(x) .* mod(abs(x), pi);
    H  = gamma(img_im1_j   - img_i_j) - gamma(img_i_j - img_ip1_j  );
    V  = gamma(img_i_jm1   - img_i_j) - gamma(img_i_j - img_i_jp1  );
    D1 = gamma(img_im1_jm1 - img_i_j) - gamma(img_i_j - img_ip1_jp1);
    D2 = gamma(img_im1_jp1 - img_i_j) - gamma(img_i_j - img_ip1_jm1);

    % calculate the second derivative
    D = sqrt(H.*H + V.*V + D1.*D1 + D2.*D2);

    % assign the reliability as 1 / D
    rel(2:end-1, 2:end-1) = 1./D;

    % assign all nan's in rel with non-nan in img to 0
    % also assign the nan's in img to nan
    rel(isnan(rel) & ~isnan(img)) = 0;
    rel(isnan(img)) = nan;
end

function [h_edges, v_edges] = get_edges(rel)
    [Ny, Nx] = size(rel);
    h_edges = [rel(1:end, 2:end) + rel(1:end, 1:end-1), nan(Ny, 1)];
    v_edges = [rel(2:end, 1:end) + rel(1:end-1, 1:end); nan(1, Nx)];
end
```

10. Appendix H. Single Wavelength Phase Unwrapping Flow Chart

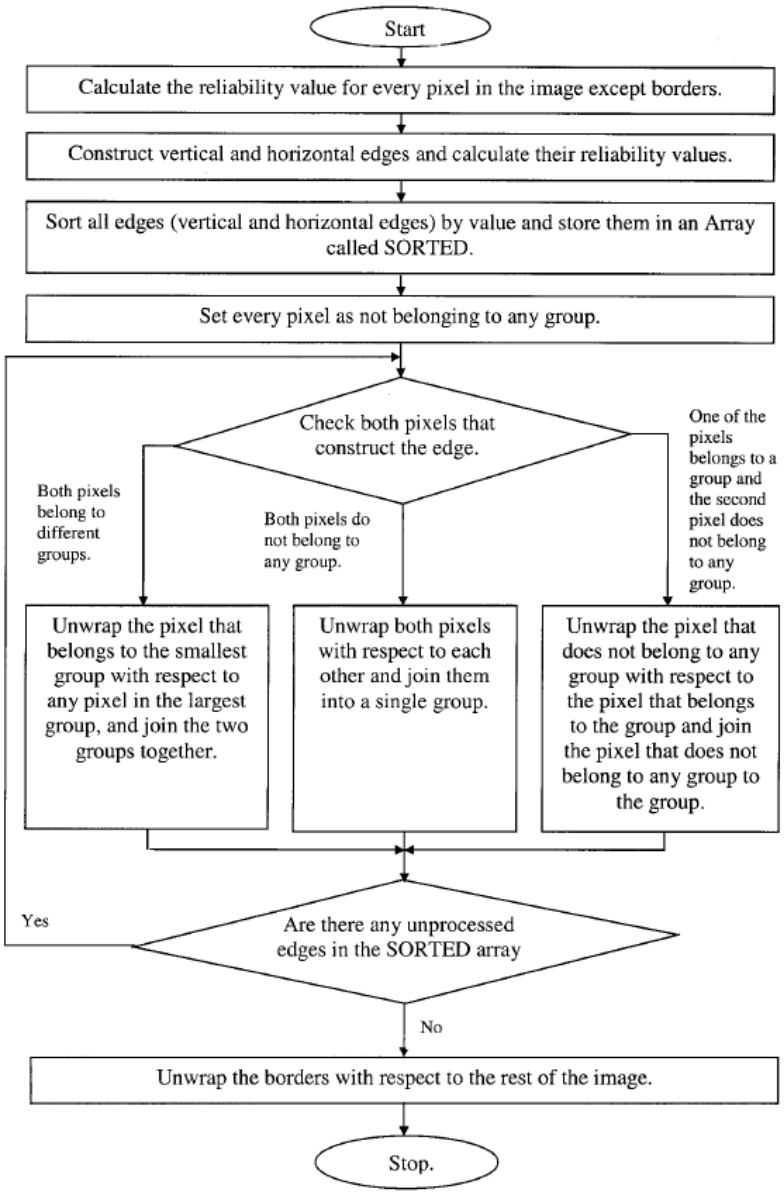

Figure H.1 Flow chart for the Phase unwrapping algorithm base on sorting by reliability following a non-continuous path, Adapted from

10. Appendix I. Simulation of Straight Forward Dual Wavelength Technique DPI Mode (Matlab code)

```
clear
clc
close all;

pxs=1;
pys=1;
FrameNumber=4;
N=FrameNumber;
%RED=642.7;       %610;    %RED will be shifted by 70 nm to get green color
GREEN=640.7;
BLUE=550.7;
A=BLUE*GREEN;
B=abs(GREEN-BLUE);
Leq=A/B;
nRange=15;
f1=('D:\4 Cameras single shot\October 27th 1.2um-200nm-concave\200nm\Red(640)-
Green(550)\SDF');

FolderName='D:\4 Cameras single shot\October 27th 1.2um-200nm-concave\200nm\Red(640)-
Green(550)\';

for cam=1:FrameNumber
   if (cam==1)
   Path=strcat(FolderName,int2str(cam),'.bmp')
   C1=imread(Path);
   CC1=C1;
   elseif (cam==2)
   Path=strcat(FolderName,int2str(cam),'.bmp')
   C1=imread(Path);
   CC1=C1;
   elseif (cam==3)
   Path=strcat(FolderName,int2str(cam),'.bmp')
   C1=imread(Path);
   CC1=C1;
   else
   Path=strcat(FolderName,int2str(cam),'.bmp')
   C1=imread(Path);
   CC1=C1;
   end
   CC1size=size(CC1);
   pxl=CC1size(1);
   pyl=CC1size(2);

   aoriginalGreen=CC1(:,:,1);
   aoriginalBlue=CC1(:,:,2);

   FringeGreen(cam,pxs:pxl,pys:pyl)=aoriginalGreen(pxs:pxl,pys:pyl);
   FringeBlue(cam,pxs:pxl,pys:pyl)=aoriginalBlue(pxs:pxl,pys:pyl);
```

```
    clear CC1
end

tic
for px=1:pxl
for py=1:pyl

IntGreen=double(FringeGreen(1:cam,px,py)); % (1) gathering the pixel values; once at a time
IntBlue=double(FringeBlue(1:cam,px,py)); % (1) gathering the pixel values; once at a time
I_GREEN_1=IntGreen(1);
I_GREEN_2=IntGreen(2);
I_GREEN_3=IntGreen(3);
I_GREEN_4=IntGreen(4);
phaseGREEN=fourstep(I_GREEN_1,I_GREEN_2,I_GREEN_3,I_GREEN_4);%-
(67.5*(pi/180));
%hGREENWrapped(px,py)=(phaseGREEN/(2*pi))*(GREEN/2);          % surface height using
red
phaseG(px,py)=phaseGREEN;
I_BLUE_1=IntBlue(1);
I_BLUE_2=IntBlue(2);
I_BLUE_3=IntBlue(3);
I_BLUE_4=IntBlue(4);
phaseBLUE=fourstep(I_BLUE_1,I_BLUE_2,I_BLUE_3,I_BLUE_4);%-(67.5*(pi/180));
%hBLUEWrapped(px,py)=(phaseBLUE/(2*pi))*(BLUE/2);          % surface height using red
phaseB(px,py)=phaseBLUE;

eqPhase=phaseB(px,py)-phaseG(px,py);

if (eqPhase < 0)
    eqPhase=(eqPhase+2*pi);
end

if (eqPhase > 2*pi)
    eqPhase=(eqPhase-2*pi);
end

hTwoWavelength(px,py)=(eqPhase/(2*pi))*(Leq/2);

end
px
end
```

10. Appendix J. Investigation the Noise Amplification in Straight Forward Dual Wavelength in DPI (Matlab code)

```
%-----Initial Matlab simulation code for phase shift interferometer and three colour interferometer
%----- Date 6th of Nov 13515
clear
clc
close all;

a=100;  % interference biase
b=1;    % fringe contrast
TotalSampling=900; % number of measurement point
hTrueRange=2000;    %nm Upper limit of the measurement range
hStart=0;          %nm Lower limit of the measurement range

hTrue=linspace(hStart,hTrueRange,TotalSampling);
StairStep=linspace(0,0,TotalSampling);

RED=630;       %610;    %RED will be shifted by 70 nm to get green color
GREEN=540;
BLUE=460;
AA=RED*GREEN;
BB=abs(GREEN-RED);
Leq12=AA/BB;
%nRange=15;
AAs=RED*GREEN;% short
BBs=abs(GREEN+RED);% short
Leq12s=AAs/BBs;% short
%nRange=15;
A=BLUE*GREEN;
B=abs(GREEN-BLUE);
Leq23=A/B;
%Leq2nge=15
Fn=Leq12*Leq23;
FD=abs(Leq12-Leq23);
LeQ_12_23=Fn/FD;
for i=1:TotalSampling;
PhaseRED_0=(4*pi*hTrue(i))/RED+(0*(pi/180));    % first phase information
PhaseRED_45=(4*pi*hTrue(i))/RED+(90*(pi/180));  % second phase information shifted by 45 degree
PhaseRED_90=(4*pi*hTrue(i))/RED+(180*(pi/180));  % third phase information shifted by 90 degree
PhaseRED_135=(4*pi*hTrue(i))/RED+(270*(pi/180));% four phase information shifted by 135 degree
%-- From the practical setup, only intensities will be obtained
I_R_0=b*cos(PhaseRED_0);
I_R_45=b*cos(PhaseRED_45);
I_R_90=b*cos(PhaseRED_90);
I_R_135=b*cos(PhaseRED_135);
```

```
I_RED_1=a+awgn(I_R_0,35,'measured');      % Intensity of the first phase plus add white guisen noise.
I_RED_2=a+awgn(I_R_45,35,'measured');     % Intensity of the second phase plus add white guisen noise.
I_RED_3=a+awgn(I_R_90,35,'measured');     % Intensity of the third phase plus add white guisen noise.
I_RED_4=a+awgn(I_R_135,35,'measured');    % Intensity of the fourth phase plus add white guisen noise.
%-- Determine the phase using Carre method

phaseR=fourstep(I_RED_1,I_RED_2,I_RED_3,I_RED_4);%-(67.5*(pi/180));
phaseRED(i)=phaseR;
Ired(i)=I_RED_1;        % Just for plot purpose (nothing to do with the algorithm at this stage of research)
%----Repeat the above setups for (2) Green and blue colours
PhaseGREEN_0=(4*pi*hTrue(i))/GREEN+(0*(pi/180));
PhaseGREEN_45=(4*pi*hTrue(i))/GREEN+(90*(pi/180));
PhaseGREEN_90=(4*pi*hTrue(i))/GREEN+(180*(pi/180));
PhaseGREEN_135=(4*pi*hTrue(i))/GREEN+(270*(pi/180));
I_G_0=b*cos(PhaseGREEN_0);
I_G_45=b*cos(PhaseGREEN_45);
I_G_90=b*cos(PhaseGREEN_90);
I_G_135=b*cos(PhaseGREEN_135);
I_GREEN_1=a+awgn(I_G_0,35,'measured');
I_GREEN_2=a+awgn(I_G_45,35,'measured');
I_GREEN_3=a+awgn(I_G_90,35,'measured');
I_GREEN_4=a+awgn(I_G_135,35,'measured');
%
phaseG=fourstep(I_GREEN_1,I_GREEN_2,I_GREEN_3,I_GREEN_4);%-(67.5*(pi/180));
phaseGREEN(i)=phaseG;
Igreen(i)=I_GREEN_1;    % Just for plot purpose (nothing to do with the algorithm at this stage of research)
PhaseBLUE_0=(4*pi*hTrue(i))/BLUE+(0*(pi/180));
PhaseBLUE_45=(4*pi*hTrue(i))/BLUE+(90*(pi/180));
PhaseBLUE_90=(4*pi*hTrue(i))/BLUE+(180*(pi/180));
PhaseBLUE_135=(4*pi*hTrue(i))/BLUE+(270*(pi/180));
I_B_0=b*cos(PhaseBLUE_0);
I_B_45=b*cos(PhaseBLUE_45);
I_B_90=b*cos(PhaseBLUE_90);
I_B_135=b*cos(PhaseBLUE_135);
I_BLUE_1=a+awgn(I_B_0,35,'measured');
I_BLUE_2=a+awgn(I_B_45,35,'measured');
I_BLUE_3=a+awgn(I_B_90,35,'measured');
I_BLUE_4=a+awgn(I_B_135,35,'measured');
%
phaseB=fourstep(I_BLUE_1,I_BLUE_2,I_BLUE_3,I_BLUE_4);%-(67.5*(pi/180));
phaseBLUE(i)=phaseB;
Iblue(i)=I_BLUE_1;      % Just for plot purpose (nothing to do with the algorithm at this stage of research)
```

```
eqPhaseBG=phaseB-phaseG; % Phase green Blue

if (eqPhaseBG < 0)
   eqPhaseBG=(eqPhaseBG+2*pi);
end

if (eqPhaseBG > 2*pi)
   eqPhaseBG=(eqPhaseBG-2*pi);
end

PHQBG(i)=eqPhaseBG;  % Blue min Green corrected

eqPhaseGR=phaseG-phaseR; % Phase Red Green

if (eqPhaseGR < 0)
   eqPhaseGR=(eqPhaseGR+2*pi);
end

if (eqPhaseGR > 2*pi)
   eqPhaseGR=(eqPhaseGR-2*pi);
end

 PHQGR(i)= eqPhaseGR; %
% phase Red Blue

eqPhaseBR=phaseB-phaseR; % Phase Red Green

if (eqPhaseBR < 0)
   eqPhaseBR=(eqPhaseBR+2*pi);
end

if (eqPhaseBR > 2*pi)
   eqPhaseBR=(eqPhaseBR-2*pi);
end

 PHQBR(i)= eqPhaseBR; %


h12(i)=(eqPhaseGR/(2*pi))*(Leq12/2); % h sythetic hrg

hgb(i)=(eqPhaseBG/(2*pi))*(Leq23/2); % h sythetic hgb

hrb(i)=(eqPhaseBR/(2*pi))*(Leq23/2); % h sythetic rb

hr(i)=(phaseR/(2*pi))*(RED/2); % h sythetic rb

i
end
```

10. Appendix K. Investigation of the Noise Amplification in Fringe Order Method with Synthetic Wavelength (Matlab code.)

```
clear
clc
close all;
a=100;  % interference biase
b=1;    % fringe contrast
% fringe contrast
TotalSampling1=1000; % number of measurement point
hTrueRange1=0;    %nm Upper limit of the measurement range
hStart1=0;          %nm Lower limit of the measurement range
hTrue1=linspace(hStart1,hTrueRange1,TotalSampling1);
hTrue1=hTrue1*1;
TotalSampling2=1000; % number of measurement point
hTrueRange2=4000;    %nm Upper limit of the measurement range
hStart2=4000;          %nm Lower limit of the measurement range
hTrue2=linspace(hStart2,hTrueRange2,TotalSampling2);
hTrue=[hTrue1,hTrue2];
RED=630;       %610;    %RED will be shifted by 70 nm to get green color
GREEN=540;
BLUE=460;
AA=RED*GREEN;
BB=abs(GREEN-RED);
Leq12=AA/BB;
A=BLUE*GREEN;
B=abs(GREEN-BLUE);
Leq23=A/B;
DD=BLUE*RED;
CC=abs(RED-BLUE);
Leq13=DD/CC;
Fn=Leq12*Leq23;
FD=abs(Leq12-Leq23);
```

```
LeQ_12_23=Fn/FD;

for i=1:2000

%-- Simulated phases to get intensities

% (1) RED colour

%%%%%%%%%%%%%%%%%%%%%%%%%%%%%%%%%%%%%%%%%%%%%%%%%%%%

%Phase with noise

PhaseRED_0=((4*pi*hTrue(i))/RED)+(0*(pi/180));    % first phase information

PhaseRED_45=((4*pi*hTrue(i))/RED)+(90*(pi/180));  % second phase information shifted by 45 degree

PhaseRED_90=((4*pi*hTrue(i))/RED)+(180*(pi/180));  % third phase information shifted by 90 degree

PhaseRED_135=((4*pi*hTrue(i))/RED)+(270*(pi/180));% four phase information shifted by 135 degree

%-- From the practical setup, only intensities will be obtained

I_R_0=b*cos(PhaseRED_0);

I_R_45=b*cos(PhaseRED_45);

I_R_90=b*cos(PhaseRED_90);

I_R_135=b*cos(PhaseRED_135);

I_RED_1=a+I_R_0+ awgn(I_R_0,35,'measured');      % Intensity of the first phase plus add white guisen noise.

I_RED_2=a+I_R_45+ awgn(I_R_45,35,'measured');     % Intensity of the second phase plus add white guisen noise.

I_RED_3=a+I_R_90+ awgn(I_R_90,35,'measured');     % Intensity of the third phase plus add white guisen noise.

I_RED_4=a+I_R_135+ awgn(I_R_135,35,'measured');    % Intensity of the fourth phase plus add white guisen noise.

%-- Determine the phase using Carre method

phaseR=fourstep(I_RED_1,I_RED_2,I_RED_3,I_RED_4);%-(67.5*(pi/180));

phaseRED(i)=phaseR;

Ired(i)=I_RED_1;        % Just for plot purpose (nothing to do with the algorithm at this stage of research)

%----Repeat the above setups for (2) Green and blue colours

PhaseGREEN_0=((4*pi*hTrue(i))/GREEN)+(0*(pi/180));

PhaseGREEN_45=((4*pi*hTrue(i))/GREEN)+(90*(pi/180));

PhaseGREEN_90=((4*pi*hTrue(i))/GREEN)+(180*(pi/180));
```

```
PhaseGREEN_135=((4*pi*hTrue(i))/GREEN)+(270*(pi/180));
I_G_0=b*cos(PhaseGREEN_0);
I_G_45=b*cos(PhaseGREEN_45);
I_G_90=b*cos(PhaseGREEN_90);
I_G_135=b*cos(PhaseGREEN_135);
I_GREEN_1=a+awgn(I_G_0,35,'measured');
I_GREEN_2=a+awgn(I_G_45,35,'measured');
I_GREEN_3=a+awgn(I_G_90,35,'measured');
I_GREEN_4=a+awgn(I_G_135,35,'measured');
%
phaseG=fourstep(I_GREEN_1,I_GREEN_2,I_GREEN_3,I_GREEN_4);%-(67.5*(pi/180));
phaseGREEN(i)=phaseG;
Igreen(i)=I_GREEN_1;    % Just for plot purpose (nothing to do with the algorithm at this stage of research)
PhaseBLUE_0=((4*pi*hTrue(i))/BLUE)+(0*(pi/180));
PhaseBLUE_45=((4*pi*hTrue(i))/BLUE)+(90*(pi/180));
PhaseBLUE_90=((4*pi*hTrue(i))/BLUE)+(180*(pi/180));
PhaseBLUE_135=((4*pi*hTrue(i))/BLUE)+(270*(pi/180));
I_B_0=b*cos(PhaseBLUE_0);
I_B_45=b*cos(PhaseBLUE_45);
I_B_90=b*cos(PhaseBLUE_90);
I_B_135=b*cos(PhaseBLUE_135);
I_BLUE_1=a+awgn(I_B_0,35,'measured');
I_BLUE_2=a+awgn(I_B_45,35,'measured');
I_BLUE_3=a+awgn(I_B_90,35,'measured');
I_BLUE_4=a+awgn(I_B_135,35,'measured');
phaseB=fourstep(I_BLUE_1,I_BLUE_2,I_BLUE_3,I_BLUE_4);%-(67.5*(pi/180));
phaseBLUE(i)=phaseB;
Iblue(i)=I_BLUE_1;      % Just for plot purpose (nothing to do with the algorithm at this stage of research)
%%%%%%%%%%%%%%%%%%%%%%%%%%%%%%%%%%%%%%%%%%%%%%%%%%%%%%%%%%%%%
eqPhaseBG=phaseB-phaseG; % Phase green Blue
```

```
if (eqPhaseBG < 0)
    eqPhaseBG=(eqPhaseBG+2*pi);
end
if (eqPhaseBG > 2*pi)
    eqPhaseBG=(eqPhaseBG-2*pi);
end
PHQBG(i)=eqPhaseBG;  % Blue min Green corrected
%%%%%%%%%%%%%%%%%%%%%%%%%%%%%%%%%%%%%%%%%%%%%%
%%%%%%
eqPhaseGR=phaseG-phaseR; % Phase Red Green
if (eqPhaseGR < 0)
    eqPhaseGR=(eqPhaseGR+2*pi);
end
if (eqPhaseGR > 2*pi)
    eqPhaseGR=(eqPhaseGR-2*pi);
end
 PHQGR(i)= eqPhaseGR; %
 %%%%%%%%%%%
 % phase Red Blue
eqPhaseBR=phaseB-phaseR; % Phase Red Green
if (eqPhaseBR < 0)
    eqPhaseBR=(eqPhaseBR+2*pi);
end
if (eqPhaseBR > 2*pi)
    eqPhaseBR=(eqPhaseBR-2*pi);
end
 PHQBR(i)= eqPhaseBR; %
 %%%%%%%%%%%%%%%%%%%%%%%
% longest syntheic wavelength
 eqPhase12_23=eqPhaseBG-eqPhaseGR;
if (eqPhase12_23< 0)
    eqPhase12_23=(eqPhase12_23+2*pi);
end
```

```
if (eqPhase12_23 > 2*pi)
   eqPhase12_23=(eqPhase12_23-2*pi);
end
PHQ12_23(i)=eqPhase12_23;  % synthetic (12-34)  corrected
%%%%%%%%%%%%%%%%%%%%%
h12_23(i)=(eqPhase12_23/(2*pi))*(LeQ_12_23);  % sythetic h12-23
h12_23_1(i)=h12_23(i)/2; % for drawing
h12(i)=(eqPhaseGR/(2*pi))*(Leq12/2); % h sythetic hrg
hgb(i)=(eqPhaseBG/(2*pi))*(Leq23/2); % h sythetic hgb
hrb(i)=(eqPhaseBR/(2*pi))*(Leq13/2); % h sythetic rb
hred(i)=(phaseR/(2*pi))*(RED/2); % h sythetic rb
%%%%%%%%%%%%%%%%%%%%%
h_roundGR(i)=(2*h12_23(i)-(Leq12/2))/Leq12; %h_roundGR(i)=(h12_23(i)-(Leq12/2))/Leq12
r1GR(i)=round(h_roundGR(i)); % Arizona method
h_burringGR=((eqPhaseGR/(2*pi))+r1GR(i))*(Leq12);
DGR(i)=(h12_23(i)-h_burringGR); % difference parameter
c1GR(i)=round(DGR(i)/Leq12); % correcting factor (1, 0, -1)
transition_heightGR(i)=((eqPhaseGR/(2*pi))+r1GR(i)+c1GR(i))*(Leq12);
%%%%%%%%%%%%
h_roundR(i)=(2*transition_heightGR(i)-(RED/2))/RED;
r1(i)=round(h_roundR(i)); % Arizona method
h_burring(i)=((phaseRED(i)/(2*pi))+r1(i))*RED;
D(i)=(transition_heightGR(i)-h_burring(i)); % difference parameter
c1(i)=round(D(i)/RED); % correcting factor (1, 0, -1)
transition_heightR(i)=((phaseRED(i)/(2*pi))+r1(i)+c1(i))*(RED);
 transition_heightR_1(i)=transition_heightR(i)/2;% for drawing
i
end
%%%%%%%%%%
```

10. Appendix L. Simulation of Retrieved Service using Best-Match at Different SNR

(Matlab code)

```
clear
clc
close all;
a=100;  % interference biase
b=90;    % fringe contrast
TotalSampling=500;  % number of measurement point
hTrueRange=5000; %10000  % nm Upper limit of the measurement range
%hTrue=5000;
RED=639.2;       % RED was chosen  for best fit
GREEN=535;      %Green was chosen  for best fit
BLUE=460;       % Blue was chosen for best fit
% In this simulation 4 shifts are used to retrieve the phase information using Carre method.
% However, for experimental setup will use three phase shifts.
counter=1;
for k=100:-1:10
SNRarray(counter)=k;
%for i=1:TotalSampling
%-- Simulated phases to get intensities
% (1) RED colour
PhaseRED_0=(4*pi*hTrueRange)/RED+(0*(pi/180));     % first phase information
PhaseRED_90=(4*pi*hTrueRange)/RED+(90*(pi/180));   % second phase information shifted
by 45 degree
PhaseRED_180=(4*pi*hTrueRange)/RED+(180*(pi/180)); % third phase information shifted by
90 degree
PhaseRED_270=(4*pi*hTrueRange)/RED+(270*(pi/180)); % four phase information shifted by
135 degree
%-- From the practical setup, only intensities will be obtained
I_R_0=a+b*cos(PhaseRED_0);
I_R_90=a+b*cos(PhaseRED_90);
I_R_180=a+b*cos(PhaseRED_180);
I_R_270=a+b*cos(PhaseRED_270);
% I_RED_1=a+I_R_0;    % Intensity of the first phase
% I_RED_2=a+I_R_90;   % Intensity of the second phase
% I_RED_3=a+I_R_180;  % Intensity of the third phase
% I_RED_4=a+I_R_270;  % Intensity of the fourth phase
% %-- Determine the phase using Carre method
I_RED_1=awgn(I_R_0,k,'measured');    % Intensity of the first phase with added noise
I_RED_2=awgn(I_R_90,k,'measured');   % Intensity of the second phase with added noise
I_RED_3=awgn(I_R_180,k,'measured');  % Intensity of the third phase with added noise
I_RED_4=awgn(I_R_270,k,'measured');  % Intensity of the fourth phase with added noise
%-- Determine the phase using Carre method
phaseRED=ARIZONA(I_RED_1,I_RED_2,I_RED_3,I_RED_4);%-(67.5*(pi/180));
%Ired(i)=I_RED_1;        % Just for plot purpose (nothing to do with the algorithm at this stage of
research)
%----Repeat the above setups for (2) Green and blue colours
PhaseGREEN_0=(4*pi*hTrueRange)/GREEN+(0*(pi/180));
PhaseGREEN_90=(4*pi*hTrueRange)/GREEN+(90*(pi/180));
PhaseGREEN_180=(4*pi*hTrueRange)/GREEN+(180*(pi/180));
```

```
PhaseGREEN_270=(4*pi*hTrueRange)/GREEN+(270*(pi/180));
%PhaseGREEN_0(i)=PhaseGREEN_0;
I_G_0=a+b*cos(PhaseGREEN_0);
I_G_90=a+b*cos(PhaseGREEN_90);
I_G_180=a+b*cos(PhaseGREEN_180);
I_G_270=a+b*cos(PhaseGREEN_270);
%
% I_GREEN_1=a+I_G_0; % Intensity of the first phase
% I_GREEN_2=a+I_G_90; % Intensity of the first phase
% I_GREEN_3=a+I_G_180; % Intensity of the first phase
% I_GREEN_4=a+I_G_270; % Intensity of the first phase

I_GREEN_1=awgn(I_G_0,k,'measured'); % Intensity of the first phase with added noise
I_GREEN_2=awgn(I_G_90,k,'measured'); % Intensity of the first phase with added noise
I_GREEN_3=awgn(I_G_180,k,'measured'); % Intensity of the first phase with added noise
I_GREEN_4=awgn(I_G_270,k,'measured'); % Intensity of the first phase with added noise
phaseGREEN=ARIZONA(I_GREEN_1,I_GREEN_2,I_GREEN_3,I_GREEN_4);%-
(67.5*(pi/180));
%Igreen(i)=I_GREEN_1;    % Just for plot purpose (nothing to do with the algorithm at this
stage of research)

PhaseBLUE_0=(4*pi*hTrueRange)/BLUE+(0*(pi/180));
PhaseBLUE_90=(4*pi*hTrueRange)/BLUE+(90*(pi/180));
PhaseBLUE_180=(4*pi*hTrueRange)/BLUE+(180*(pi/180));
PhaseBLUE_270=(4*pi*hTrueRange)/BLUE+(270*(pi/180));

%PhaseBLUE_0(i)=PhaseBLUE_0;
I_B_0=a+b*cos(PhaseBLUE_0);
I_B_90=a+b*cos(PhaseBLUE_90);
I_B_180=a+b*cos(PhaseBLUE_180);
I_B_270=a+b*cos(PhaseBLUE_270);

% I_BLUE_1=a+I_B_0;  % Intensity of the first phase
% I_BLUE_2=a+I_B_90;  % Intensity of the first phase
% I_BLUE_3=a+I_B_180; % Intensity of the first phase
% I_BLUE_4=a+I_B_270; % Intensity of the first phase
I_BLUE_1=awgn(I_B_0,k,'measured');  % Intensity of the first phase with added noise
I_BLUE_2=awgn(I_B_90,k,'measured');  % Intensity of the first phase with added noise
I_BLUE_3=awgn(I_B_180,k,'measured'); % Intensity of the first phase with added noise
I_BLUE_4=awgn(I_B_270,k,'measured'); % Intensity of the first phase with added noise
phaseBLUE=ARIZONA(I_BLUE_1,I_BLUE_2,I_BLUE_3,I_BLUE_4);%-(67.5*(pi/180));
Iblue(k)=I_BLUE_1;     % Just for plot purpose (nothing to do with the algorithm at this stage of
research)

%----Best matching method to determine the fringe order for three colours ------
[nRED nGREEN
nBLUE]=BestMatchSimulation(phaseRED,phaseGREEN,phaseBLUE,RED,GREEN,BLUE);
%-------End of Best matching algorithm to find the fringe orders for RGB
   hREDCal(counter)=(phaseRED/(2*pi)+nRED)*(RED/2);          % surface height using red
   hGREENCal(counter)=(phaseGREEN/(2*pi)+nGREEN)*(GREEN/2);  % surface height
using green
```

```
   hBLUECal(counter)=(phaseBLUE/(2*pi)+nBLUE)*(BLUE/2);      % surface height using
blue
counter=counter+1;
end

plot(SNRarray,hREDCal/1000)

%%%%%%%%%%%%%%%%%%%%%%%%

function [phase]=ARIZONA(I1,I2,I3,I4)
%
num=(I4-I2);% ARIZONA
den=(I1-I3);% ARIZAONA
phase=atan(num/den);
phase=PhaseWraping(num,den,phase);
%%%%%%%%%%

function [phase]=PhaseWraping(num,den,phase);

if ((num > 0) && (den > 0))
   phase=phase;

elseif ((num > 0) && (den < 0))
   phase=pi+phase;

elseif ((num < 0) && (den < 0))
   phase=pi+phase;

elseif ((num < 0) && (den > 0))
   phase=(2*pi)+phase;

elseif ((num == 0) && (den > 0))
   phase=0;

elseif ((num == 0) &&(den < 0))
   phase=pi;

elseif ((num > 0) && (den==0))
   phase =0.5*pi;

elseif ((num < 0) && (den==0))
   phase =1.5*pi;

end

%%%%%%%%%

function [nR, nG, nB]=BestMatchSimulation(phaseR,phaseG,phaseB,RED,GREEN,BLUE)

nRange=450;        % Maximum fringe order that won't be exceeded during the measurement
%----Start----
nr=0;     % initial estimate for the Fringe order of RED colour
```

```
ng=0;   % initial estimate for the Fringe order of GREEN colour
nb=0;    % initial estimate for the Fringe order of BLUE colour
for j=1:(nRange+1)   % Investigate the height at 6 fringe order and then find best match
   hRED(j)=(phaseR/(2*pi)+nr)*(RED/2);          % surface height using red
   hGREEN(j)=(phaseG/(2*pi)+ng)*(GREEN/2);  % surface height using green
   hBLUE(j)=(phaseB/(2*pi)+nb)*(BLUE/2);      % surface height using blue
   nr=nr+1;        % incrementing the red fringe order
   ng=ng+1;    % incrementing the green fringe order
   nb=nb+1;      % incrementing the blue fringe order
end

nR=0;     % initial estimate for the Fringe order of RED colour
nG=0;   % initial estimate for the Fringe order of GREEN colour
nB=0;    % initial estimate for the Fringe order of BLUE colour
hMinValue= abs(hBLUE(1)-hGREEN(1))+abs(hBLUE(1)-hRED(1))+abs(hGREEN(1)-
hRED(1));
for jB=1:(nRange+1)           % counter for the blue fringe order (alwayes larger or equal the
others)
   for jG=jB:-1:1            % counter for the green fringe order (alwayes larger or equal the Red)
   for jR=jG:-1:1            % counter for the red fringe order (alwayes smaller or equal the others)
   NewValue= abs(hBLUE(jB)-hGREEN(jG))+abs(hBLUE(jB)-hRED(jR))+abs(hGREEN(jG)-
hRED(jR));
   if (NewValue <= hMinValue)
      hMinValue=NewValue;
      nB=jB-1;     % initial estimate for the Fringe order of RED colour
      nG=jG-1;    % initial estimate for the Fringe order of GREEN colour
      nR=jR-1;      % initial estimate for the Fringe order of BLUE colour
   end
   end
   end
end

%%%%%%%%%%%%%%%%%%
```

10. Appendix M. ISO 5436-1

‘’In accordance to the definition in ISO 5436-1, the step height is defined as the distance between two parallel planes, one of which is fitted to the upper surface and another is to the lower surface. The size of each fitted area is 200 × 100 pixels. Both planes are fitted by the least square method’’ Kitagawa (2010).

10. Appendix N. Measurement Result of DPI Mode

Two grating sample with step heights equal to 1264 ±4nm, 502.0 ±4nm and 185.9±2.3 nm have been measured using the dual wavelength combinations (DPI $_{red\text{-}green}$). The measurement has been done using 2X objective lens and evaluated using ISO 5436. The measurement results with these section profile are shown in Figure M. 1and Figure M.2.

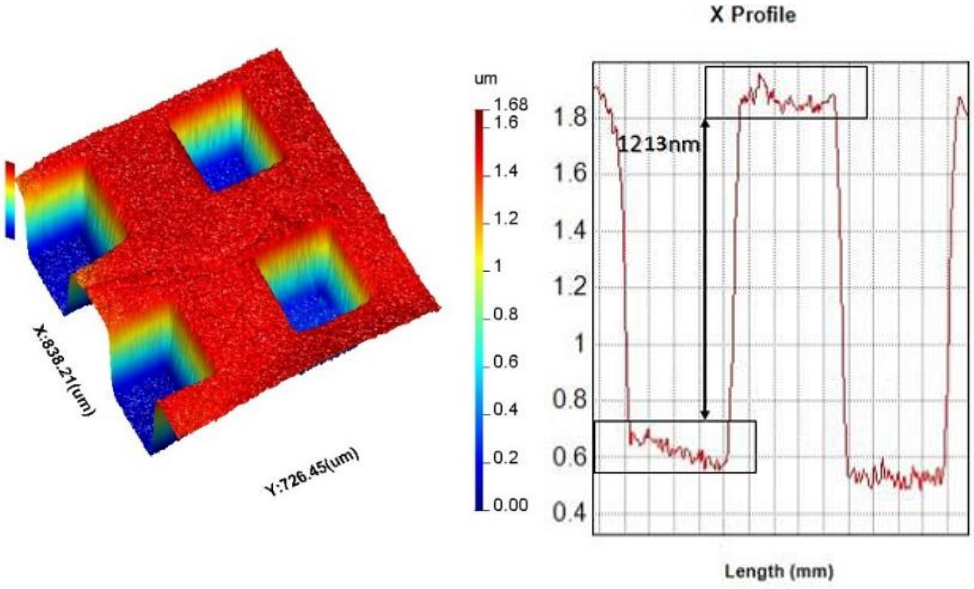

Figure N.1 Measured result for cross grating depth 1200_nm standard sample, illuminated by red and green sources. (b) Cross-sectional profile

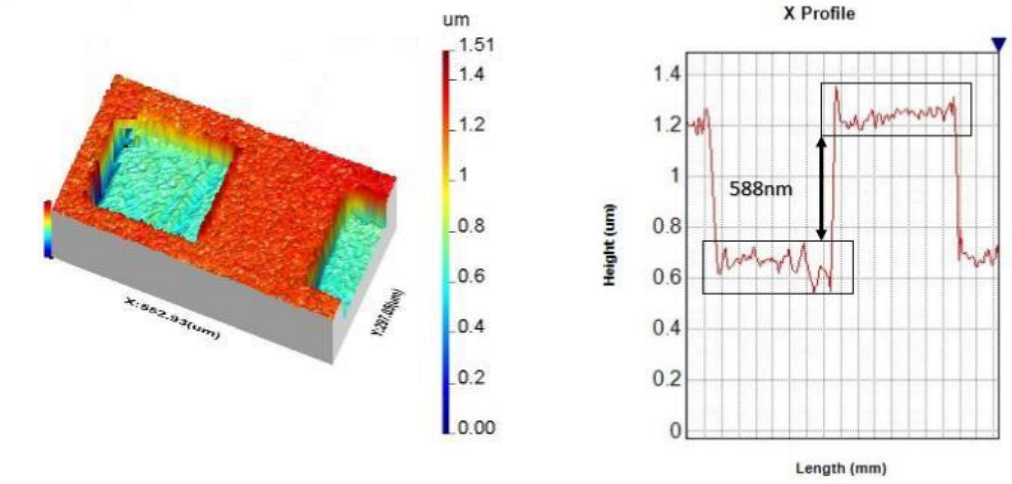

Figure N.2 Measured result for cross grating depth 500_nm standard sample, illuminated by red and green sources. (b) Cross-sectional profile

Publications and Awards

Refereed Conference Papers

1. Hussam Muhamedsalih, Saif Al-Bashir, Feng Gao, Xiangqian Jiang (6 Feb 2018) “Single Shot Dual Wavelength Polarised Interferometer’’, 2018 IEEE International Instrumentation and Measurement Technology Conference (I2MTC).
2. Saif Al-Bashir, Hussam Muhamedsalih, Feng Gao, Xiangqian Jiang (5 Jun 2018)’’ An investigate of single shot dual wavelength polarised interferometer which uses Carre and Four Step Phase Shift Algorithms’’, 18th International Conference and Exhibition, EUSPEN 2018.
3. Hussam Muhamedsalih, Saif Al-Bashir, Feng Gao, Xiangqian Jiang (18 Aug 2018)’’ Single-Shot RGB Polarising Interferometer’’, Proc. SPIE 10749.

Awards

1. Best presentation award from the in early career Research Symposium organised by EPSRC future metrology Hub, University of Huddersfield.